1966

The Fermi surface of tungsten

Robert Franz Girvan
Iowa State University

THE FERMI SURFACE OF TUNGSTEN

by

Robert Franz Girvan

A Dissertation Submitted to the
Graduate Faculty in Partial Fulfillment of
The Requirements for the Degree of
DOCTOR OF PHILOSOPHY

Major Subject: Physics

Approved:

Signature was redacted for privacy.

In Charge of Major Work

Signature was redacted for privacy.

Head of Major Department

Signature was redacted for privacy.

Dean of Graduate College

Iowa State University
Of Science and Technology
Ames, Iowa

1966

TABLE OF CONTENTS

ABSTRACT

Impulsive-field de Haas-van Alphen effect measurements have been carried out to study the Fermi surface of tungsten. An empirical model was constructed by fitting an equation for the shape of the Fermi surface to the results of this experiment combined with the Gantmakher size effect results of other investigators and with theoretical predictions for the Fermi surface shape. Good overall agreement is obtained between the predictions of the empirical model and experiment showing that a surface with the general features of the Lomer model can account for all of the experimental results. However, the empirical model is imprecise in certain respects, and small changes are indicated for a more precise description of the Fermi surface.

I. INTRODUCTION

A. General Considerations

The subject of this dissertation concerns one of the experiments which are carried out to increase our understanding of the properties of electrons in metals. Before attempting to define this study more precisely, it is necessary to begin with a brief description of the theoretical model which is usually used to discuss electrons in metals, that is, the one-electron approximation.

Since the electrons in a metal are a system of strongly interacting particles, an exact theoretical description of their properties has not been found. Quite useful results have been obtained, however, by considering an approximate model in which a single electron moves in the periodic potential $V(\underline{r})$ resulting from all the other electrons and ions in the metal. In this model, the single particle states are the solutions of the one-electron Schroedinger equation

$$\left(-\frac{\hbar^2}{2m}\nabla^2 + V(\underline{r})\right)\psi = E\psi. \qquad (1)$$

A fundamental result of the theory is that due to the translational symmetry of the lattice, these single particle states can be labelled by a wave vector $\underline{k}$ or by the corresponding crystal momentum $\hbar\underline{k}$. The energy eigenvalues $E(\underline{k})$ in Equation 1 are periodic functions of $\underline{k}$ so that $\underline{k}$ can be restricted to

lie within a unit cell of wave-vector space which is called the primitive Brillouin zone. An infinite number of discrete energy levels exists for each $\underline{k}$ within the primitive zone; each of these levels $E_i(\underline{k})$ is a periodic function in $\underline{k}$-space and represents a band of allowed energies.[1]

A great deal of effort has been expended over the last two decades in calculating $E(\underline{k})$ for many metals by first constructing a physically reasonable potential $V(\underline{r})$ and then solving Equation 1 numerically. Typical $E(\underline{k})$curves which result from such calculations are shown in Figure 1; these calculated curves are for the transition metal tungsten, about which this dissertation will be primarily concerned. Each of the curves gives the dependence of the one-electron energy on the wave-vector for a different band along a line from the center of the primitive Brillouin zone to the corner H. The sum total of curves like these for all directions in $\underline{k}$-space defines the band structure of the metal. Band structure calculations do not give really quantitative results since the potential $V(\underline{r})$ is not well-known. However, when it comes to accounting for most of the physical properties of a metal, it is not really necessary to know the entire band structure in detail. As we shall explain

---

[1]The basic concepts which are outlined in this introductory section are discussed in standard textbooks on solid state physics, e.g. Ziman (1964).

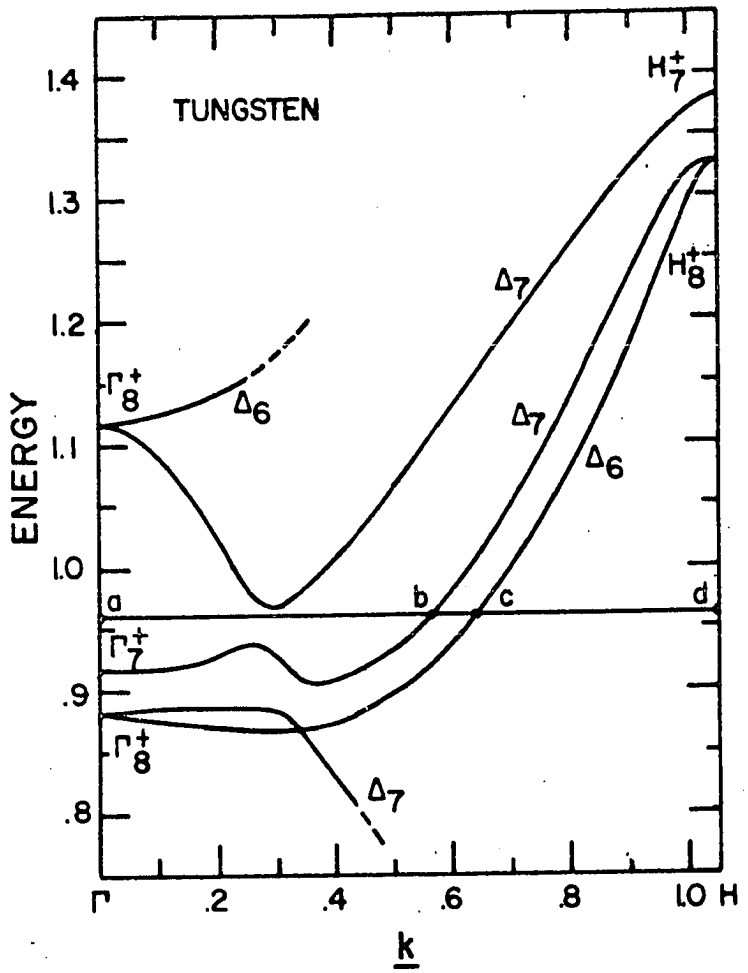

Figure 1. Relativistic electron dispersion curves for tungsten in the neighborhood of the Fermi energy. The ordinate is energy (Rydbergs) and the abscissa is distance in wave-vector space (reciprocal Bohr radii)(after Loucks 1965a).

below, certain features are much more important than others, and it is fortunate that these significant features can be determined experimentally. Nevertheless, the theoretical calculations are of vital importance since they provide a framework to guide the experimentalist in the interpretation of his observations.

The electronic contribution to many experimental phenomena can be understood by considering an ideal Fermi gas which is assumed to follow some dispersion law of the form $E(\underline{k})$ rather than by considering the system of electrons interacting with one another and with the lattice (cf. Pines 1963). Two fermions cannot occupy the same state so that at the absolute zero of temperature, all the lower energy states are occupied; the occupation number of the one-electron states drops discontinuously from 1 to 0 when all the electrons have been accommodated. The energy at which this discontinuity in the occupation number occurs is called the Fermi energy E_F and the locus of points in $\underline{k}$-space for which $E_i(\underline{k}) = E_F$ is the Fermi surface for the i^{th} band. The set of all such surfaces for the separate bands is the Fermi surface of the metal. Thus, if the Fermi energy in Figure 1 is given by the line a-d, we assume that all states with energies below this line are filled and all states lying above this line are empty. Then points b and c are points on two separate Fermi surfaces. (When

interactions are taken into account, the statement that the Fermi surface separates completely filled states from completely empty states is not rigorously true, but according to Migdal (1957) and Luttinger (1960) there is still a discontinuity of sorts in the occupation number of the electron states at the Fermi surface.)

The elucidation of both the shape of the Fermi surface and the dynamical properties of electrons occupying states near this surface is of primary importance in understanding the properties of a metal; most physical phenomena involve small energy transfers, and only those electrons close to the Fermi surface are energetically near unoccupied states. Thus, for example, it is only electrons at the Fermi surface which take part in electrical or thermal conduction or contribute to the electronic specific heat of a metal. At temperatures other than absolute zero, the Fermi surface is no longer perfectly sharp and the occupation number drops from 1 to 0 over an energy range of kT. However, even at room temperature the thermal energy ($kT \sim 1/40$ eV) is much less than the Fermi energy ($E_F \sim$ several eV), and for many purposes, e.g. calculation of the electrical conductivity, the surface can be taken to be sharp.

There are a number of experiments which can be carried out to measure both the shape of the Fermi surface and the dynamical properties of electrons on this surface, most of

which are discussed in a general review article by Pippard (1961). The three experiments which have yielded the most detailed information about the Fermi surface of tungsten are the de Haas-van Alphen effect, the Gantmakher size effect, and cyclotron resonance. These experiments are all carried out on single crystals of very pure metals which have been cooled to low temperatures so that the electronic mean free path between collisions is relatively long; furthermore, they are all carried out in a magnetic field. In each of these experiments, contributions from small groups of electrons on the Fermi surface can be separated out, so that very detailed information about the Fermi surface can be obtained. In the following section we will give a brief description of the Gantmakher size effect and cyclotron resonance. The de Haas-van Alphen effect, which is the experimental method used in this study, will be described in somewhat more detail in Section I-C.

B. The Gantmakher Size Effect and Cyclotron Resonance

Current understanding of the Gantmakher size effect and cyclotron resonance is based on a semiclassical treatment of the dynamical behavior of electrons in metals under the influence of an applied magnetic field. Provided that there are no interband transitions, it can be rigorously shown

that the Newtonian equations of motion for a free particle can be carried over to an electron moving in a periodic potential provided that the kinetic momentum $m\underline{v}$ is replaced by the crystal momentum $\hbar\underline{k}$.

In the periodic lattice we assume that the single-electron energies $E(\underline{k})$ are given by the solution of Equation 1. The energy levels of the electron in a magnetic field $\underline{B}$ can be found by using the equivalent Hamiltonian $\mathcal{H}_{eq} = E(\underline{K})$ where the wave vector $\underline{k}$ in $E(\underline{k})$ is replaced by the operator $\underline{K}$ given by

$$\hbar\underline{K} = -i\hbar\,\mathrm{grad} - e\underline{A}/c \qquad (2)$$

and $\underline{A}$ is the vector potential (Luttinger 1951, Blount 1962). Thus the motion of a wave packet describing an electron on the Fermi surface can be found from Hamilton's equations using the Hamiltonian $E(\underline{k})$. The well-known results for the velocity and acceleration are

$$\underline{v}_{\underline{k}} = \hbar^{-1}\,\mathrm{grad}_{\underline{k}} E(\underline{k}) \qquad (3)$$

and

$$\hbar\dot{\underline{k}} = e(\underline{E} + \underline{v}_{\underline{k}} \times \underline{B}/c) \qquad (4)$$

We see from Equation 3 that the velocity of an electron occupying a state $\underline{k}$ on the Fermi surface is normal to the surface at the point $\underline{k}$. Therefore, according to Equation 4, the magnetic field causes the vector $\underline{k}$ to move along the line of intersection of the surface $E(\underline{k})$ = constant with a

plane $\underline{k}.\underline{B}$ = constant. This path which is traced out by the tip of the vector $\underline{k}$ in the magnetic field is often referred to as an orbit.

We can set up curvilinear coordinates in the plane of the orbit such that for k_{tan} measured along the orbit and k_n measured normal to it, we have from Equation 4

$$\hbar \dot{k}_{tan} = \frac{eB}{\hbar c} \frac{\partial E}{\partial k_n}$$

or

$$dt = \frac{\hbar^2 c}{eB} \left(\frac{\partial E}{\partial k_n} \right)^{-1} dk_{tan}$$

so that the time required to traverse a closed orbit is

$$T_c = \frac{\hbar^2 c}{eB} \oint \frac{dk_{tan}}{\partial E / \partial k_n} \quad . \tag{5}$$

We define an orbit effective mass m* by

$$m^* = \frac{\hbar^2}{2\pi} \oint \frac{dk_{tan}}{\partial E / \partial k_n} \quad , \tag{6}$$

so that the cyclotron frequency ω_c, which is the frequency at which a closed orbit is traversed, can be written

$$\omega_c = \frac{2\pi}{T_c} = \frac{eB}{m^* c} \quad . \tag{7}$$

Furthermore, the integral in Equation 6 is the derivative of the orbit area A with respect to the energy so that we can write an alternative expression for the cyclotron mass

as

$$m^* = \frac{\hbar^2}{2\pi}\frac{\partial \mathcal{A}}{\partial E}. \qquad (8)$$

According to Equation 4, the projection of the r-space trajectory of an electron onto a plane perpendicular to the magnetic field will be similar to the orbit in k-space, but will be rotated by $\pi/2$.

Equations 4 and 7 are the basis for a qualitative understanding of the cyclotron resonance experiment and the Gantmakher size effect experiment. The Gantmakher effect (Gantmakher 1962) is studied in a thin metallic sample whose boundaries are represented by the lines a-b and c-e in Figure 2a. Also shown in the Figure are the relative orientations of a hypothetical orbit in k-space and the projection of the corresponding electron trajectory in r-space onto a plane perpendicular to the magnetic field; the magnetic field is parallel to both faces of the sample. An oscillatory electric field also lies in the plane of the sample surface, but at right angles to the magnetic field. The quantity δ represents the skin depth for the electric field whose frequency is typically $\sim 10^6$ Hz. If δ is much less than the orbit diameter in r-space and if the mean free path is sufficiently long, this configuration is appropriate for measurement of the calipered dimension 2p of the Fermi surface. The width 2p is an extremal calipered dimension with respect to planes k_y = constant through the sheet of the Fermi

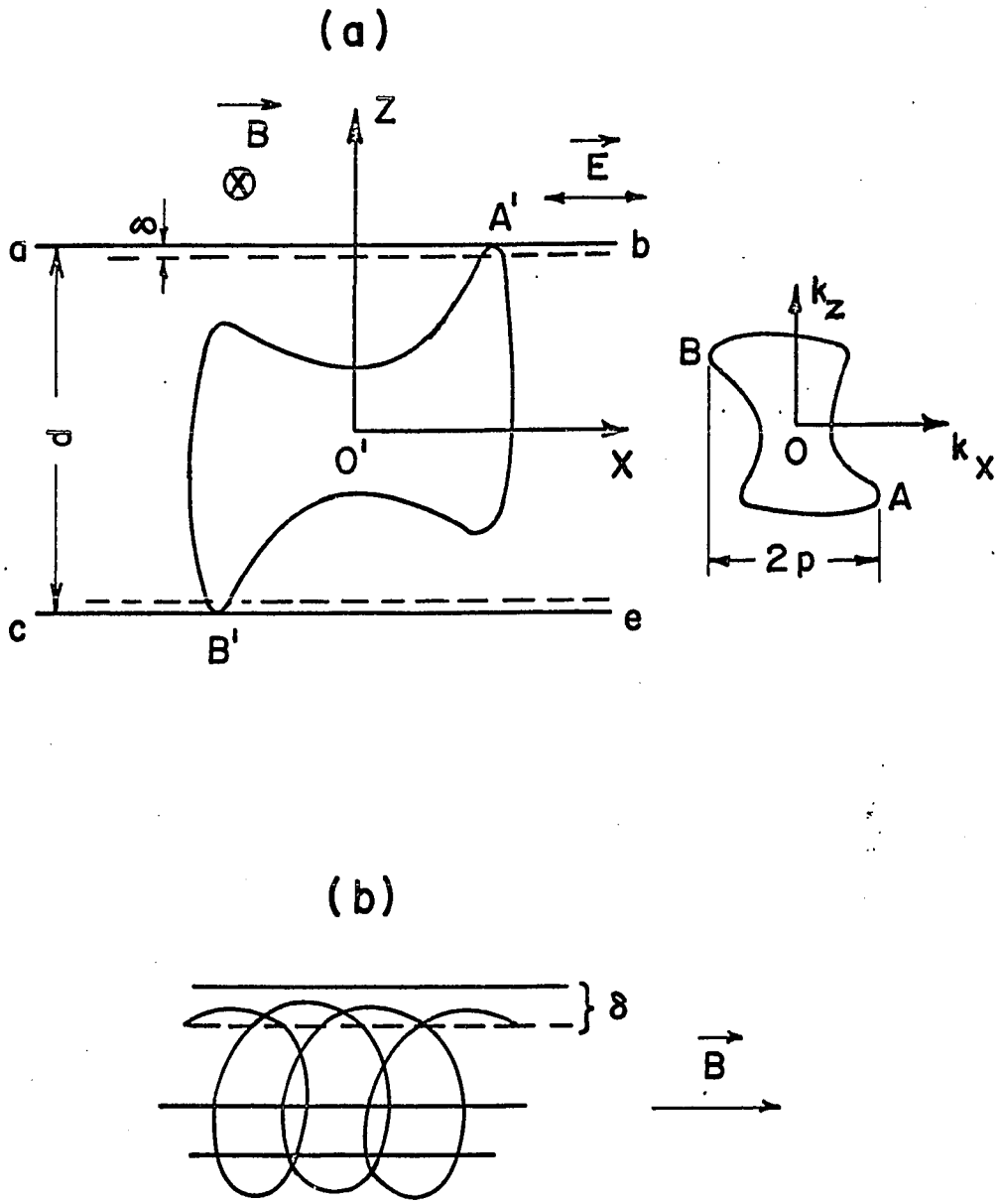

Figure 2. Illustrating electron trajectories and orbits for (a) the Gantmakher size effect experiment (after Gantmakher 1963) and (b) the cyclotron resonance experiment (after Azbel and Kaner 1956)

surface which is being considered.

In sufficiently high magnetic fields the dimensions of the electron trajectories will be smaller than the sample thickness d. As the magnetic field strength is reduced, the electron trajectories expand so that the number of electrons which pass through the skin layer and complete an orbit without colliding with the sample surface decreases. At some critical field value, the extremal calipered dimension of the trajectory just coincides with the sample thickness; and at this point, an anomaly is found in the field dependence of the resonant frequency of a coil containing the sample (Gantmakher 1962, 1963) or in the r-f transmission through the sample (Walsh and Grimes 1964).

The geometry for the observation of cyclotron resonance is the same as for the Gantmakher effect, except that only one surface of the sample is considered and the frequency ω of the electric field is substantially higher (typically 10^{10}-10^{11} Hz). The trajectories in $\underline{r}$-space which correspond to closed orbits on the Fermi surface are helices with their axes along the magnetic field direction (Figure 2b) so that an electron which passes through the skin depth at one point on its trajectory will do so again at intervals T_c until it suffers a collision. During each pass through the skin depth, the electron experiences an impulsive force from the electric field. If ω/ω_c is an integer, successive impulses

will be in phase and a resonance (change in the power absorption coefficient of the sample) will be observed. For sufficiently low values of the magnetic field these resonances are periodic in $1/B$ with period $\Delta(1/B) = \frac{e}{\omega m^* c}$.

The theoretical treatment of this effect (Azbel and Kaner 1956, 1957) shows that the effect is dominated by electrons on sections of the Fermi surface for which the quantity $m^*(k_B)$ is extremal with respect to k_B, the component of the wave vector along the magnetic field direction. However, if the magnetic field is tipped slightly out of the plane of the surface of the sample, most of the electrons will tend to drift out of the skin depth. Those which will not are those for which the average of the drift velocity $\bar{v}_z$ around an orbit is zero. Only this group will contribute to the resonance. Harrison (1960) has shown that the average drift velocity is zero for orbits which enclose an extremal (maximum or minimum) area in $\underline{k}$-space.

C. The de Haas-van Alphen Effect

From an experimental view point the de Haas-van Alphen effect can be described as the oscillatory behavior which is observed in the magnetization of single crystals of pure metals when they are cooled to liquid helium temperatures and placed in a strong magnetic field. When the field strength is changed, the oscillatory components are found to be periodic in $1/B$.

The importance of the de Haas-van Alphen effect as a tool for studying the Fermi surface stems from a relation found by Onsager (1952). For a uniform magnetic field B in the z-direction, electrons on a closed orbit in $\underline{k}$-space execute a periodic motion in the x-y plane. Onsager applied the Bohr-Sommerfeld quantization rule to this motion,

$$\oint \underline{p}.\underline{dr} = (n + \gamma)2\pi\hbar, \qquad (9)$$

where $\underline{p}$ is given by $\hbar\underline{k} + e\underline{A}/c$ and the integral is around an orbit. Here γ is an unspecified constant. He found that the orbits in the k_x-k_y plane enclose quantized areas which are given by the formula

$$A_n = (n + \gamma)\, 2\pi eB/c\hbar \, . \qquad (10)$$

Since k_z is not affected by the quantization, the quantized levels can be pictured as defining tubes in k-space (Figure 3). As the field strength is increased, the spacing ΔA between these allowed states increases in accordance with Equation 10 and as the outer levels are pushed through the Fermi surface the electrons become redistributed among other states. (It is assumed that sufficient collisions are present so that we can always define an equilibrium distribution function.)

According to Onsager (1952), the magnetization of the system oscillates with a frequency determined by the rate at which these levels pass through the Fermi surface. For a disk of thickness δk_z taken through the surface at k_z

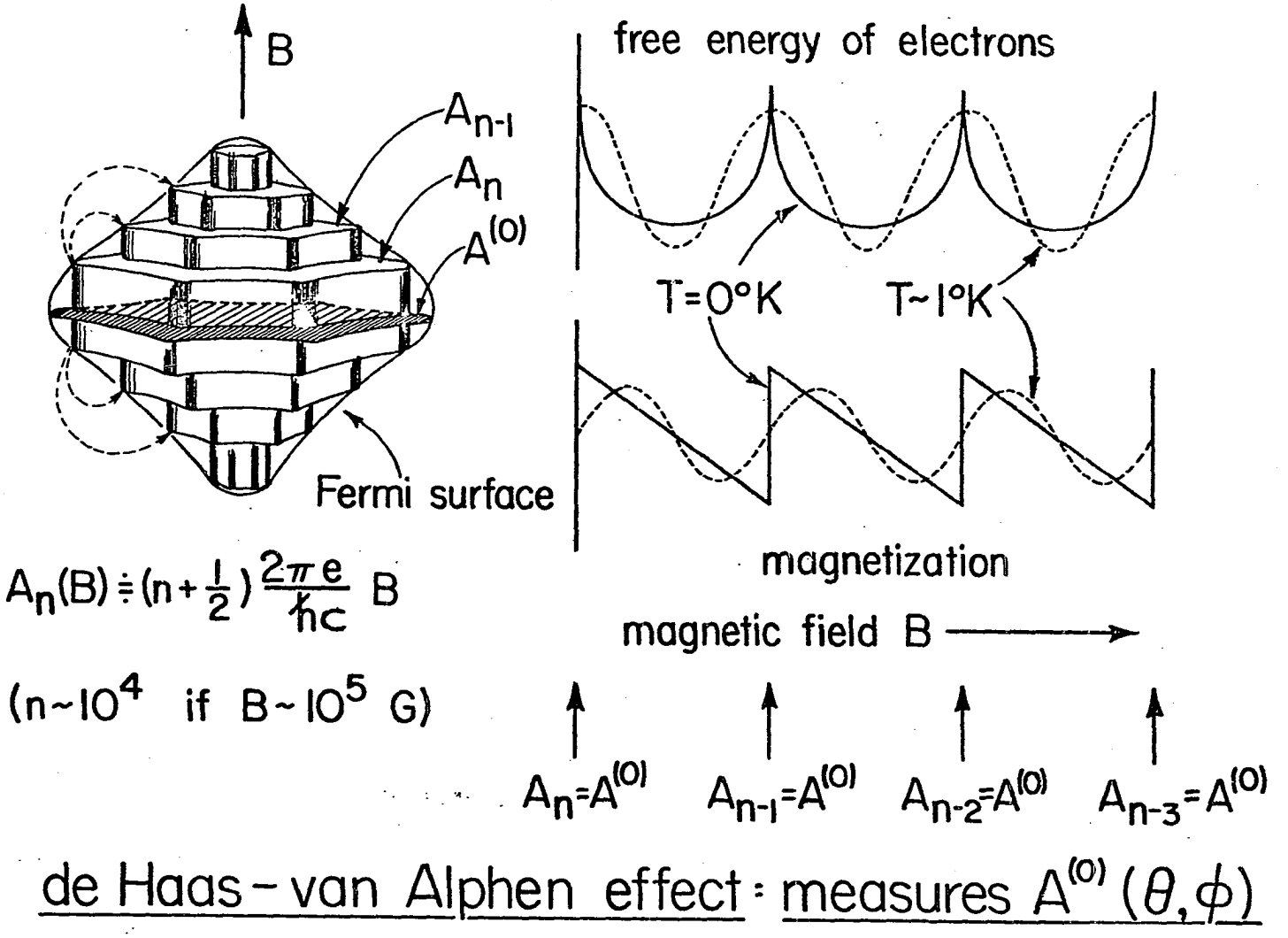

Figure 3. Illustrating the de Haas-van Alphen effect for a hypothetical Fermi surface

this frequency is

$$F = \frac{dn}{d(1/B)} = \frac{c\hbar A(k_z)}{2\pi e} , \qquad (11)$$

where we have taken n in Equation 10 to be a continuous variable. Pippard (1961) finds that at absolute zero, the magnetization δM of the disk has a sawtooth form as is shown in Figure 3. He expands δM in a Fourier series of the form

$$\delta M = \sum_r C(r,k_z) \sin\left(\frac{rch A(k_z)}{2\pi eB}\right) \delta k_z$$

The argument of the sine function is of magnitude 10^3-10^4 so that when δM is integrated over k_z to find the total magnetization, only the extremal areas A_o contribute to the integral.

At higher temperatures, the Fermi surface is no longer perfectly sharp and the de Haas-van Alphen oscillations are damped somewhat. The sawtooth wave form is rounded like the dashed wave form in Figure 3. Lifshitz and Kosevich (1955) have calculated the formula for the temperature dependence of the amplitude of the oscillations and we will use their final result, modified slightly to conform with the findings of later authors. We will include a spin splitting factor g since Cohen and Blount (1960) have argued that the spin splitting of the energy levels should be in general of magnitude $g\mu_B H/2$ whereas Lifshitz and Kosevich assume a g-value of 2. (Here μ_B is the double Bohr magneton.)

Usually an amplitude damping factor which arises due to the finite width of the Landau levels is also included.

An analysis by Dingle (1952) showed that for a quadratic dispersion law and further simplifying assumptions, the r^{th} harmonic in the Lifshitz and Kosevich formula should be multiplied by the factor $\exp(-4\pi^3 rm^*ckx/ehH)$ where x is an effective temperature related to the width of the Landau levels. Furthermore, it has been observed experimentally (Anderson and Gold 1963, Shoenberg 1962) that the de Haas-van Alphen oscillations are actually periodic in $1/B$ rather than $1/H$ as Lifshitz and Kosevich suggested. Thus each time that the applied field H appears in early theoretical papers it should be replaced by B.

In our experiment, we in fact observe not the oscillatory magnetization, but the oscillatory differential susceptibility χ_{osc}. If we include the additions which were noted above, this quantity can finally be written out as

$$\chi_{osc} = 4kTVF^2\left(\frac{2\pi e}{hc}\right)^{\frac{3}{2}}\left|\frac{1}{2\pi}\frac{\partial^2 A_o}{\partial k_z^2}\right|^{-\frac{1}{2}} B^{-\frac{5}{2}} \quad x \qquad (12)$$

$$\sum_{r=1}^{\infty}(-1)^r r^{\frac{1}{2}} \frac{\cos\left(\frac{\pi g rm^*}{2m_e}\right)\cos\left(\frac{2\pi rF}{B} \pm \frac{\pi}{4} - 2\pi r\gamma\right)}{2\sinh(4\pi^3 rcm^*kT/ehB)} e^{-4\pi^3 rm^*ckx/ehB}$$

Here m_e is the mass of a free electron. If there is more than one extremal section of the Fermi surface, each section will contribute an oscillatory signal according to Equation 12. Usually the argument of the hyperbolic sine in Equation 12 is somewhat greater than one so that only the first few harmonics in the sum need be retained and to a good

approximation $[2 \sinh(4\pi^3 cm^*kT/ehB)]^{-1}$ can be replaced by $\exp(-4\pi^3 rcm^*kT/ehB)$. When these steps are made, Equation 12 can be written

$$\chi_{osc} = \sum_i \chi_{oi}(B,T) \cos\left(\frac{2\pi F_i}{B}\right) , \qquad (13)$$

where $\chi_{oi}(B,T)$ is slowly varying. The sum is over the extremal sections and those harmonic components which have a significant amplitude. By sorting out the frequencies $F_i(\theta,\phi)$ as a function of the orientation (θ,ϕ) of the magnetic field direction with respect to the crystal axes, the orientation dependence $A_{oi}(\theta,\phi)$ of the extremal areas of the Fermi surface can be determined. From this information the shape of the Fermi surface can be inferred. This is the importance of the de Haas-van Alphen effect. Furthermore, by measuring the amplitudes $\chi_{oi}(B,T)$ as a function of temperature, the cyclotron masses can be obtained.

D. Outline of the Present Investigation

In this study we have used the de Haas-van Alphen effect to study the Fermi surface of tungsten. This work considerably extends an earlier study (Girvan 1964) which related only to the large portions of the Fermi surface. It is found that the general features of the Fermi surface of tungsten are in qualitative agreement with a crude model which was first proposed by Lomer (1964) and with more

elaborate models which were advanced by Loucks (1965b, 1966) on the basis of detailed band structure calculations (Loucks 1965a, 1965b). However, neither of these models give really quantitative agreement with our results. Therefore, we have constructed an analytical model for the Fermi surface of tungsten using both our results and the Gantmakher size-effect results (Walsh and Grimes 1964).

In tungsten it was found that some of the signals were quite complex and required special analysis techniques. The methods which were developed to perform the analysis on these complex signals are discussed in Chapter II along with the details of the apparatus and possible errors. In Chapter III we present the results of the frequency measurements together with some examples of the data. Cyclotron mass measurements were also made for most of the oscillatory components. The results of the cyclotron mass measurements which were carried out for the [100], [111], and [110] orientations are presented in the second part of Chapter III. In Chapter IV we discuss our data in terms of the models which were proposed by Lomer (1964) and Loucks (1965b, 1966), and then proceed to describe the experimentally-determined Fermi surface in terms of analytical functions. The chapter concludes with suggestions for further study.

II. EXPERIMENTAL PROCEDURE

A. The Impulsive Field Method

In this study measurements of the frequencies of oscillation of the magnetic susceptibility of small single crystals of tungsten were carried out using the impulsive-field method. This method was developed by Shoenberg (1957) and was later described by him in detail (Shoenberg 1962) so that a really detailed description will not be attempted here.

The sample is placed in a liquid-helium bath in the center of a solenoid, and a time-varying magnetic field $H(t)$ is produced by discharging a bank of capacitors through the solenoid. As the magnetization M changes with magnetic field, a voltage $dM/dt = (dM/dH)(dH/dt)$ is induced in the pickup coil. This voltage, which is due to the oscillations in the magnetic susceptibility, is filtered and displayed on one trace of a dual beam oscilloscope. For field measurement, the voltage developed across a standard resistor in series with the pulse coil is displayed on the second trace of the oscilloscope, and both traces are simultaneously photographed on Polaroid film. In order to make small changes in magnet current correspond to large deflections of the oscilloscope beam, most of the voltage developed across the standard resistor is bucked off by a calibrated

voltage supply and the small difference voltage is amplified by the oscilloscope.

After the capacitor discharge is completed, the second trace is again swept across the oscilloscope screen several times at known voltages which are produced by a calibration unit. The calibration lines which are produced by this procedure provide reference lines on the film for accurate field measurement. Some examples of the data which are obtained in this way are shown in Figure 4.

B. Experimental Apparatus

A block diagram of the apparatus is shown in Figure 5 and the physical arrangement of the components is shown in Figure 6.[1] The sample and pickup coil were located in a slender tail on one end of a glass-walled helium chamber, and the whole helium chamber was encased in a liquid-nitrogen dewar. A pulse solenoid fitted over the tail of the helium dewar and both the helium chamber and the solenoid were hung from brackets on a pumping line. By means of two large mechanical pumps, the temperature of the helium bath could be varied from 4.2°K to 1°K. A mercury and an oil manometer were connected to the helium chamber for temperature measurement.

The lower beam amplifier of the Tektronix 502

---

[1]The experimental apparatus has been described in more detail by Anderson (1962).

Figure 4. Some examples of impulsive-field deHaas-van Alphen effect data for tungsten

a. Overall picture with symmetric field pulse illustrating the effect of the resonant pickup circuit on the complicated dHvA frequency spectrum
H approximately midway between [00$\bar{1}$] and [11$\bar{1}$]
Temperature ~ 1°K
Resonant frequency ~ 155kHz
Filter passband ~ 140-170kHz
Bottom calibration line at 0kG; succeeding lines at intervals of 24.7kG
Pulse duration ~ 16ms

b. Expanded picture of α oscillations using the symmetric field pulse (The notation α is explained in Section III-A.)
H near [1$\bar{1}$0]
Temperature ~ 4°K
Resonant frequency ~ 100kHz
Filter passband ~ 70-140kHz
Bottom calibration line at 81.51kG; succeeding lines at intervals of 1.235kG
Time across picture ~ 1ms

c. Overall picture using the shunt ignitron (see caption for Figure 5)
H ~ 20° from [00$\bar{1}$] in the ($\bar{1}$10) plane
Temperature ~ 1°K
Resonant frequency ~ 50kHz
Filter passband ~ 30-70kHz
Bottom calibration line at 0kG; succeeding lines at intervals of 24.7kG
Time across picture ~ 50ms
(The resonance peaks for H>0 are off-scale and are not shown.)

d. Expanded picture of ϵ_u oscillations using the shunt ignitron (The notation ϵ_u is explained in Section III-A.)
H ~ 8° from [00$\bar{1}$] in the ($\bar{1}$10) plane
Temperature ~ 1°K
Resonant frequency ~ 50kHz
Filter passband ~ 25-75kHz
Bottom calibration line at 19,760kG; succeeding calibration lines at intervals of 1.235kG
Time across picture ~ 2ms

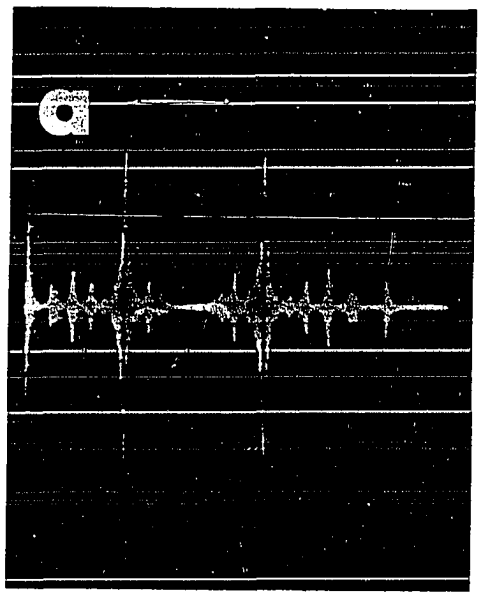
a

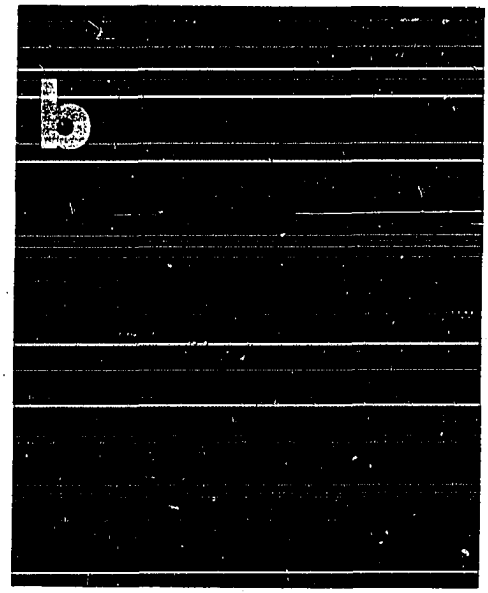
b

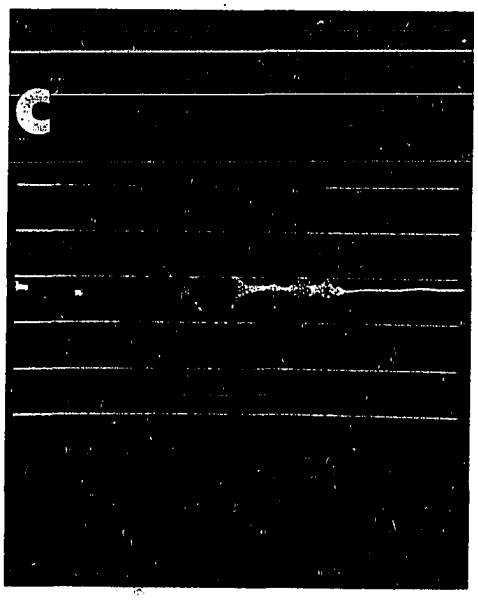
c

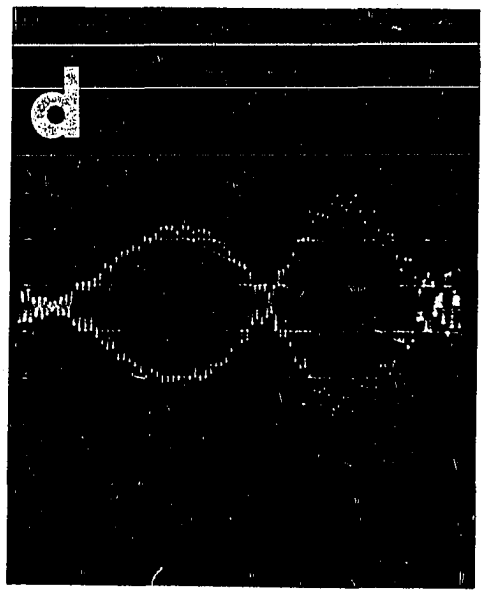
d

Figure 5. Block diagram of experimental apparatus (after Anderson 1962) Usually, the crowbar or shunt ignitron is not used (Figure 4a). When it is used, the field decays exponentially from its peak value (Figure 4c).

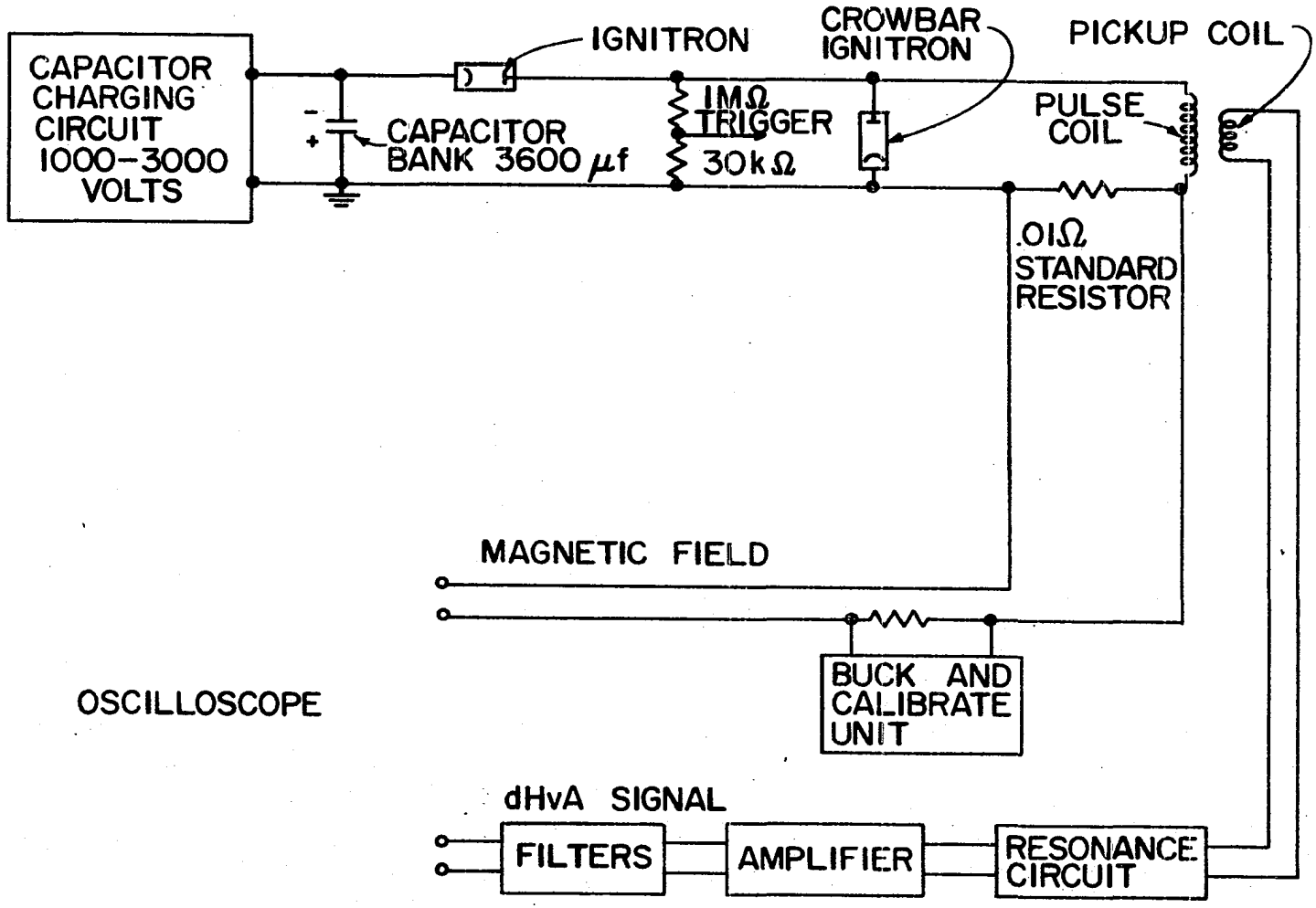
CAPACITOR CHARGING CIRCUIT 1000-3000 VOLTS
IGNITRON
CROWBAR IGNITRON
PICKUP COIL
CAPACITOR BANK 3600 μf
1MΩ TRIGGER
30kΩ
PULSE COIL
.01Ω STANDARD RESISTOR
MAGNETIC FIELD
BUCK AND CALIBRATE UNIT
OSCILLOSCOPE
dHvA SIGNAL
FILTERS
AMPLIFIER
RESONANCE CIRCUIT

Figure 6. The experimental apparatus (The liquid nitrogen dewar has been removed from its mounting and set on the floor.)

a. Pulse solenoid
b. Glass helium cryostat
c. Pumping line
d. Manometer
e. Capacitor charging unit
f. Capacitor
g. Bucking circuit
h. Oscilloscope
i. Electronic filter
j. Voltmeter to monitor signal induced in pickup coil by sample orienting coils
k. Sample orienting coils
l. Liquid nitrogen dewar

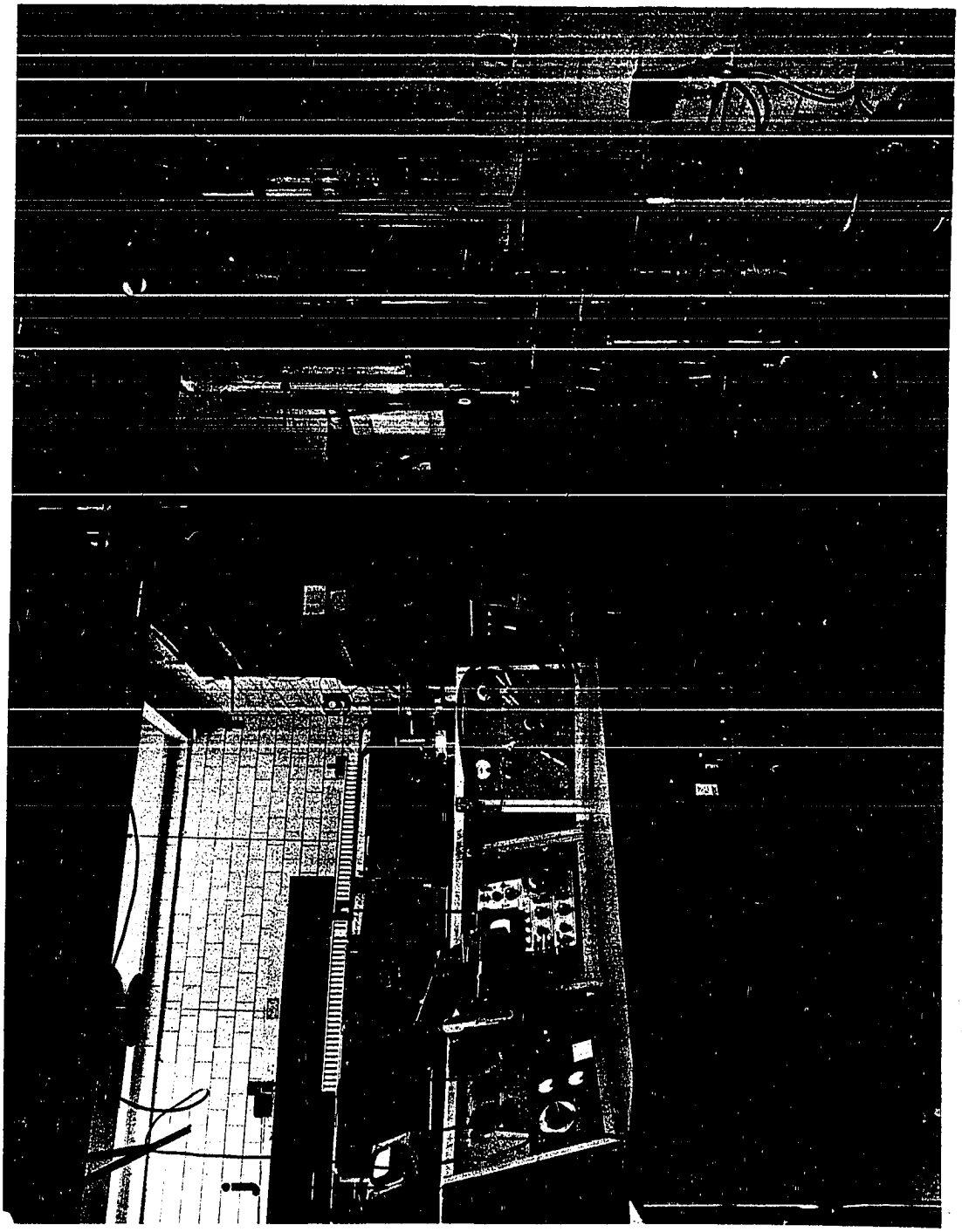

oscilloscope was connected differentially across a bucking circuit and the .01 ohm series resistor in the magnet circuit. This bucking circuit (see Anderson 1962) is a calibrated voltage supply which could be set to supply bucking voltages from zero to 15 volts in steps of 0.1 volts. The bucking circuit was also equipped with a polarity-reversing switch so that during a pulse it could be set to produce a voltage which opposed the voltage across the standard resistor. After the pulse the polarity could be reversed to supply voltages for the calibration lines.

Since the magnetic field direction is fixed in space by the physical arrangement of the helium cryostat and pulse coil, it is necessary to vary the orientation of the sample within the helium chamber in order to set the magnetic field along different crystallographic directions. Therefore, in each of the two sample holders which were used, the pickup coil was mounted in a small wheel with the axis of the pickup coil perpendicular to the axle of the wheel.

For the sample holder[1] which was used to gather most of the data, the axle of the wheel was held in Teflon bushings which were mounted in a nylon fork assembly at the bottom of the sample holder. The nylon holder was attached to a glass tube which in turn was connected to a stainless

---

[1]This sample holder was used by Anderson (1962) and has been described in more detail by him.

steel tube outside the high field region. The stainless steel tube was the physical support for the pickup coil assembly and extended to the top of the sample holder, which contained a winch assembly encased in a vacuum chamber. A loop of nylon fishing line was wrapped round the winch and the small wheel at the bottom end of the sample holder so that the wheel could be turned in the liquid helium chamber by turning the winch at the top of the sample holder. In the latter part of this study a second sample holder[1] was used in which the wheel was turned by a beveled gear arrangement.

Electrical connections to the pickup coil were led out of the helium chamber through the top of the sample holder to a variable capacitance and then via a band pass filter[2] to the terminals of the upper beam amplifier of a Tektronix 502 oscilloscope. The pickup coils[3] were wound on small nylon forms using about 1500 turns of either #50 or #52 AWG copper wire. The voltage induced in the pickup coils by the rapidly-changing field was minimized by winding inner layers and outer layers in opposite directions. Then, as described by Anderson (1962), turns were removed from the outer layers until the signal induced in the pickup

---

[1]This sample holder was put together by Mr. P.T. Panousis.

[2]Variable band-pass filter, Krohnhite Corporation, 580 Massachusetts Avenue, Cambridge 39, Massachusetts.

[3]The pickup coil which was actually used to gather most of the data was made by Mr. R. Phillips.

coil in a homogeneous alternating magnetic field was a minimum.

The 200 kG pulse magnets were constructed following the method described by Anderson (1962) and were calibrated by nuclear magnetic resonance (Girvan 1964). Most of the data which are reported here were taken using Solenoid F. The constant which related the field at the center of this solenoid to the current flowing through it was found to be 123.5 $\pm$ 0.2 Gauss/amp.

C. Sample Mounting and Orientation

The tungsten samples were three single crystals which were prepared by Metals Research Ltd., Cambridge, England, by spark-cutting from a zone-refined rod. The geometrical axes of these three crystals lay along the $[\bar{1}00]$, $[\bar{1}10]$, and $[\bar{1}1\bar{1}]$ crystallographic directions. As purchased, the samples were too thick to use in impulsive fields, and for this reason they were etched down to a final diameter of about 0.066 cm and a final length of about 0.5 cm in a mixture of 40% nitric acid and 60% hydrofluoric acid. Residual resistivity measurements were not carried out on the actual specimens, since such measurements invariably damage the crystals; however, ratios of $\rho(293°K)/\rho(4.2°K)$ in excess of 4,000 have been quoted for zone-refined tungsten by other authors (Fawcett 1962).

When one of these samples was inserted in the pickup

coil so that the crystallographic plane (h,k,l) was normal to the axle of the wheel, successive rotations of the wheel set the magnetic field along successive crystallographic directions in the plane (h,k,l).

Due to the small size of the samples, great care was necessary to orient a sample accurately with respect to the wheel. The detailed procedure for orienting a sample with respect to the string-driven sample holder differed slightly from that used for the geared sample holder, but both procedures used standard Laue back-reflection x-ray techniques (Cullity 1956). The sample was first glued in a small glass capillary (o.d. = 0.095 cm, i.d. = 0.065 cm) with Duco cement and the capillary was then inserted through a hole along the axis of a small nylon cylinder. In order to insure clear helium access to the sample, only one end of the sample was glued.

For the string-driven sample holder, a small mirror was first glued to a flattened place on the lateral surface of the nylon cylinder. The glass capillary containing the sample was turned about its axis until the directions along the normal to the mirror and along the axis of the nylon cylinder lay in the crystal plane in which it was desired to set the magnetic field. The detailed procedure for doing this has been described by Girvan (1964). After the sample and capillary had been correctly placed in the nylon

cylinder, the sample was put into the pickup coil by push-fitting the nylon cylinder into a cup-shaped cut in the end of the pickup coil form. Then a light beam directed normal to the axle of the wheel was shone onto the mirror. Using the reflected beam for reference, the nylon cylinder was turned until the mirror normal lay in a plane defined by the light beam and the axis of the pickup coil. This method of sample orientation had the advantage that the light beam and the nylon cylinder axis could quite accurately be set in a vertical plane by merely requiring that the reflected light spot move along a vertical line on the wall as the wheel was turned. Thus orientation errors in which the actual plane of rotation was twisted slightly from the desired plane of rotation were minimized.

The procedure which was used to orient a sample in the geared sample holder differed from that used for the string-driven sample holder in that the capillary and sample were first glued in their mounting and placed in the pickup coil. The geared sample holder was constructed with a short pickup coil so that one end of the sample stuck out of the end of the pickup coil; the entire pickup assembly was detachable and could be mounted on the x-ray camera. Thus to set the final orientation of the sample and its mounting with respect to the pickup coil, the protruding end of the sample was x-rayed through a hole in the side of the wheel.

The axle of the wheel could be set accurately parallel

to the x-ray beam by using a set of machined parallels. The Laue back reflection patterns produced in this manner were used to set the normal to the crystal plane (h,k,l) parallel to the axle of the wheel. The crystal was held firmly in the proper orientation by a coating of heavy Celvacene vacuum grease on the nylon mounting; the grease hardened when cooled to liquid helium temperature.

When rotation data were being taken, the angle made by the magnetic field in the plane (h,k,l) was determined by measuring the angle between the pickup coil axis and the axis of a set of coils which were mounted on the nitrogen dewar (see Figure 6). The tangent of the tilt angle of the pickup coil was found by setting the ratio of a-c currents in the two sets of coils to produce a minimum in the induced voltage in the pickup coil. The circuitry and detailed procedure for monitoring the pickup coil angle in this way have been discussed by Anderson (1962).

The geared sample holder was equipped with a mechanical revolution counter which was attached to the spindle used to turn the pickup coil. Since Mr. P.T. Panousis had shown that differences in pickup coil angle could be obtained from the revolution counter to within 0.1°, the angle monitoring coils were not used with this sample holder, and the angles between successive pickup coil positions were obtained directly from the calibrated revolution counter. Although

it was possible to obtain differences in angle very accurately from the revolution counter, there was some backlash in the gears. Therefore, the zero value for the angle scale was determined from the symmetry of the data.

D. The de Haas-van Alphen Signal

The de Haas-van Alphen signal in tungsten is found to consist of many frequency components F_i. In one sense the impulsive field method is well-suited to a study in which many frequency components are observed. Due to the rapid time variation of the magnetic field (pulse duration $\sim$ 15 ms), oscillations in the sample magnetization can be measured in the 100 kilohertz range, and thus standard filtering techniques can be used. In addition, the pickup signal can be further band-limited by connecting a small capacitor in parallel with the pickup coil. In actual practice, provision is made to switch different capacitors in parallel with the pickup coil in order to vary the resonant frequency of the pickup circuit. As the magnetic field changes, the frequency <u>in time</u> is given by

$$\omega_i = \frac{2\pi F_i}{H^2} \frac{dH}{dt} \tag{14}$$

for each de Haas-van Alphen component F_i. Therefore, resonance occurs for the i^{th} dHvA component when ω_i equals the resonant frequency ω_o of the pickup circuit.

The advantage of the resonant pickup circuit arrangement is illustrated by Figure 4a, which shows the pickup signal throughout the duration of the field pulse. Each peak in the pickup signal occurred when the resonance condition was satisfied for a particular F_i. Since the resonance condition for each F_i occurs at a different magnetic field value, the pickup signal from dHvA components which lie in successive frequency ranges is conveniently found to resonate during successive intervals of time along the field pulse. Thus a partial frequency analysis of the complicated dHvA spectrum is performed by the resonant pickup circuit. Usually, one or more electronic band pass filters were inserted in series with the pickup circuit to provide increased frequency discrimination.

Because of the enhanced amplitude near resonance, the measurements which are necessary to determine F_i for each of the dHvA components were necessarily made over a limited field range in which the pickup signal due to F_i was near resonance. In order to measure accurately the F_i which occurred in a particular resonance envelope, the oscilloscope trace was displaced and expanded as in Figure 4b so that the amplitude maximum and minimum of each cycle of the dHvA cycle could be resolved on an oscilloscope. The actual number of cycles of a component F_i which were recorded on an oscillogram

depended on the strength of the signal and the band width of the pickup circuit. For the very strong α oscillations, (see Section III-A) it was possible to obtain many more cycles than could be resolved on a single oscillogram. Usually from 30 to 80 cycles of the dHvA signal were recorded on one oscillogram, although as many as 130 cycles were used in certain cases for which it was necessary to separate nearly coincident frequencies.

E. Data Analysis

The data analysis consisted of accurately determining the F_i. Since the resonance technique could only give partial frequency resolution, it was necessary to find a higher resolution method to analyze some of the complex signals which we found in tungsten. Several methods were developed and tried, and only the final procedure will be described, even though not all of the results were obtained by this method.

The magnetic susceptibility in tungsten is so small that for purposes of determining the frequencies F_i, the magnetic induction field B which occurs in Equation 12 can be replaced by the applied field H. (The distinction between B and H will be discussed further in Appendix C.) The magnetic field values H at which cycle maxima and minima occurred were found by linear interpolation between

calibration lines using appropriate coordinates measured from the oscillograms. First the oscillograms were rephotographed onto 35 mm film, and then this film was projected onto a Teleducer[1] screen. The Teleducer was equipped with a crosshair which could be moved to any point on the projected image of the oscillogram, and a slidewire arrangement in the Teleducer produced an analog voltage proportional to the x or y coordinate of the crosshair. This voltage was automatically transferred to punched cards for computer analysis.

The preliminary phase of the computer analysis consisted of checking for errors in the coordinate readings from the oscillogram, smoothing the coordinate readings for the field trace and calibration lines, and setting up arrays corresponding to reciprocal field values and cycle numbers. The error checking consisted of requiring 1) that successive coordinates for the magnetic field trace be monotonically decreasing in value since the pictures were always read from the high field end to the low field end and 2) requiring that successive coordinates for the time axis be either monotonically increasing (falling field) or decreasing (rising field) in value. If there were no reading errors, a second order least squares smoothing procedure was applied

---

[1]Telecomputing Corporation, Burbank, California (now defunct)

to the field trace coordinates, and the calibration line readings were smoothed by averaging successive sets of 9 readings. After these steps had been completed, the linear interpolation necessary to find successive reciprocal magnetic field values was performed. The reciprocal field values, cycle numbers, and signal amplitudes corresponding to points read from the oscillogram were used for frequency analysis.

The two methods of frequency analysis used were least squares fitting of the points to straight lines and periodogram analysis. The first method depended solely on the fact that for a signal which is periodic in $1/H$, a plot of reciprocal field positions of cycle maxima and minima versus cycle numbers should be a straight line. The slope of the straight line gives the period of the dominant frequency contributing to the corresponding region of the oscillogram. Due to the limited bandwidth of the pickup circuit and to the field dependence of the amplitude of the dHvA signal, a particular oscillogram may contain distinct regions with different dominant frequencies F_i in each. In such a case, the plot of reciprocal field values of cycle maxima and minima versus cycle number will contain several straight line segments, one for each of the dominant frequencies. This situation is illustrated by Figure 7.

The slopes of these straight line segments were also

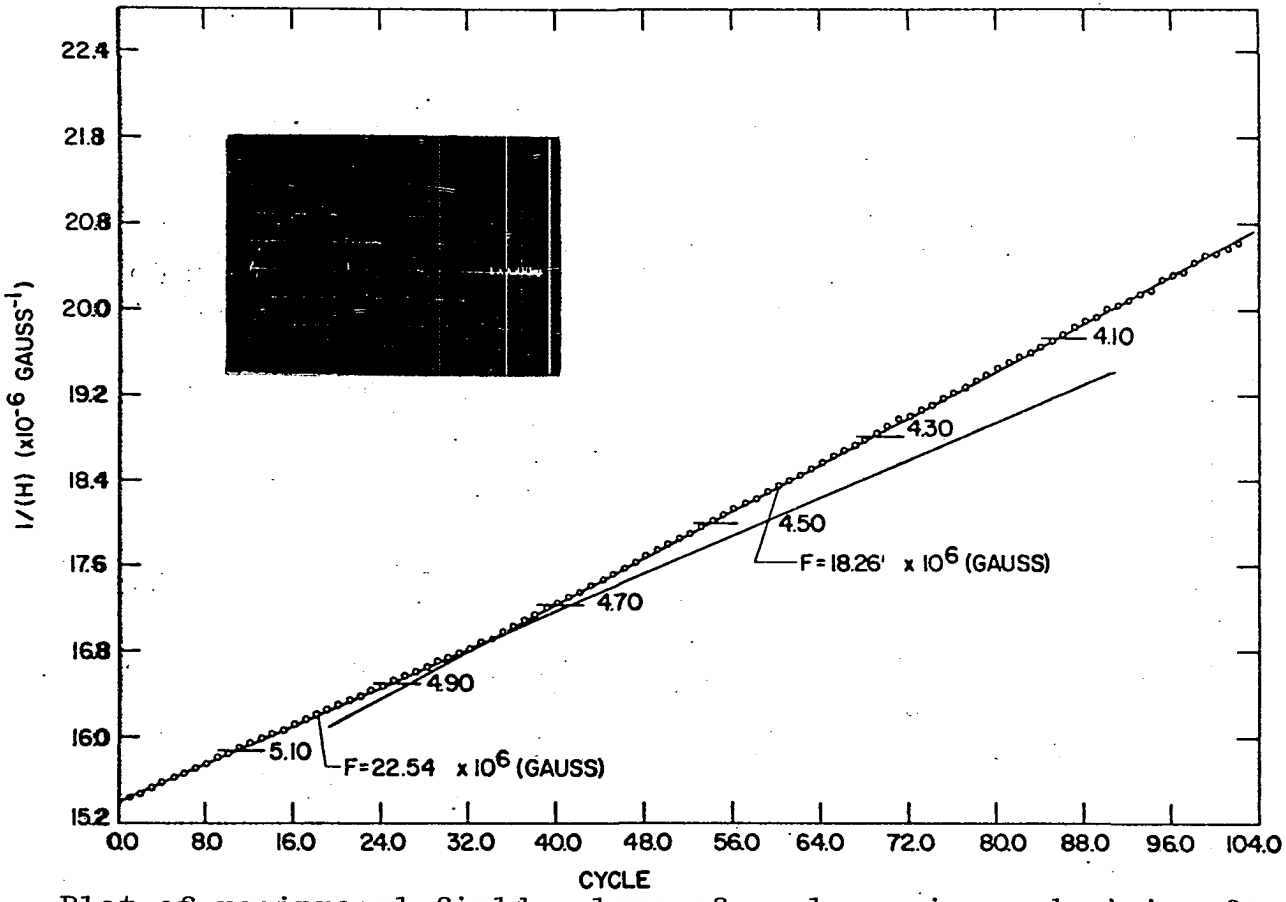

Figure 7. Plot of reciprocal field values of cycle maxima and minima for the data shown in the photograph (The numbers 4.1, 4.3,...,5.1 give the voltages of the calibration lines on the oscillogram, and the short line segments by these numbers are drawn whenever the field trace crosses a calibration line.

determined by computer analysis. The entire data analysis program is discussed in Appendix A, so we will give only a short description here. Short straight line segments of length N_i were fit to successive sections of the data by the method of least squares. Several passes were made through the data, each time using a slightly larger N_i.

In order to lessen the effects of possible reading errors at each step and to avoid calculating a mean slope when the N_i points being fitted lay on either side of a discontinuity in slope, the fitting procedure was carried out several times for each set of N_i points. After each of these fits, the deviation of each of the N_i points from the fitted line was checked; then a new least squares calculation was carried out, omitting those points which deviated from the fitted line by more than a certain multiple of the standard deviation.

Estimates for the de Haas-van Alphen frequencies were made from the slope and error calculations in two different ways: "long straight line" estimates for the frequencies were made by taking weighted averages of the "short straight line" slopes. Only points lying on a single linear section of the reciprocal field versus cycle number plot were used for each average. When the slopes of adjacent sections differed by less than a few percent, the resolution of this method was insufficient since the initial and final points

of each linear region could not be determined accurately.

In a variation of this method, the results of the least squares calculations were collected in a so-called ideogram, which is defined as a plot of I_j versus F_j, where I_j and F_j are defined as follows: If the frequency and error estimate derived from the i^{th} least squares fit are F_i and E_i respectively, and if N fits were performed for the data set, the ordinate (intensity) I_j at abscissa (frequency) F_j on the ideogram is given by

$$I_j = (dF/\sqrt{2}) \sum_{i=1}^{N} (1/E_i)\exp\left[-\tfrac{1}{2}(F_j-F_i)^2/E_i^2\right] \quad . \qquad (15)$$

Here dF is the interval at which ordinates are calculated. The de Haas-van Alphen frequencies are inferred from the frequencies at which peaks occur in the ideogram. Examples are given in Appendix B. However, this method fails when applied to a two-component beat pattern in which the constituent frequencies are quite close together. The reason for the failure is that when two frequencies are very close together and beating, the frequency at which the ideogram peak occurs depends not only on the frequencies of the beating components, but also on their amplitudes (Appendix B).

In order to separate more reliably the de Haas-van Alphen frequencies contained in beating patterns, a method

of periodogram analysis due to Whittaker and Robinson (1956) was used. This method is a variation of the Schuster (1898) method of testing a sequence of numbers $\{u_k\}$ to see if they contain a periodicity P. In our case, the sequence $\{u_k\}$ was constructed from an artificial dHvA signal. This signal was a triangular wave which was constructed mathematically by connecting successive points of amplitude maxima and minima of the actual dHvA signal with straight lines. The elements of $\{u_k\}$ were amplitudes of the triangular wave taken at equally-spaced values of reciprocal magnetic field.

A test period P (P is the reciprocal of F) was stepped from an initial value P_1 to a final value P_2 in steps of dP. At each step an appropriate subset of $\{u_k\}$ was selected to be tested for the periodicity P on the basis of the frequency results which had been found in the least squares calculations. No part of $\{u_k\}$ was tested for a periodicity P if it was clearly made up from a signal whose period differed from P by more than a certain percentage. The exact tolerance depended on the number of cycles of the strongest dHvA component in the oscillogram.

A relative intensity was calculated for each period P. The plot of intensity versus period which is found in this way is usually called a periodogram. We have plotted intensity I versus frequency F (rather than P). The frequencies of the dHvA components are inferred from the

frequencies at which peaks occur in the periodogram.

The periodogram analysis worked quite well when the de Haas-van Alphen signal was not too severely amplitude-modulated by filtering. One important series of data sets for which this condition was satisfied was the data which were taken to determine the orientation dependence of the low-frequency dHvA components in tungsten for field directions near [00$\bar{1}$] using the crowbar ignitron (see Figure 5). Since the rate of change of $\dot{H}/H^2$ after the field maximum was considerably less for this configuration than for the symmetric pulse configuration, (see Equation 14), the time-frequency of each dHvA component passed through the resonant frequency comparatively slowly so that many more dHvA oscillations could be observed in one resonance envelope (cf. Figure 4d). An example of a frequency spectrum obtained by this method for one of the data sets which were taken using the shunt ignitron is shown in Figure 8.

F. Measurement Errors

The measurement errors which can arise in this experiment can be divided into three categories. These are: (1) errors in determining the orientation of the crystal with respect to the magnetic field, (2) errors due to difficulty in analyzing complex waveforms, and (3) possible systematic errors in determining the field values at which

Figure 8. Periodogram for data shown in attached photograph This particular periodogram was selected because it illustrates the reliability of the periodogram analysis even for signals which have been severely attenuated by filtering and contain small noise bursts. The two large peaks and the small peak at a freqeuncy of about 70 x 10^5G give the correct dHvA frequencies. (By readjusting the filters, it was possible to make the term with frequency ~70 x 10^5G dominant and thus verify that the small peak at this frequency on the periodogram was not spurious.)

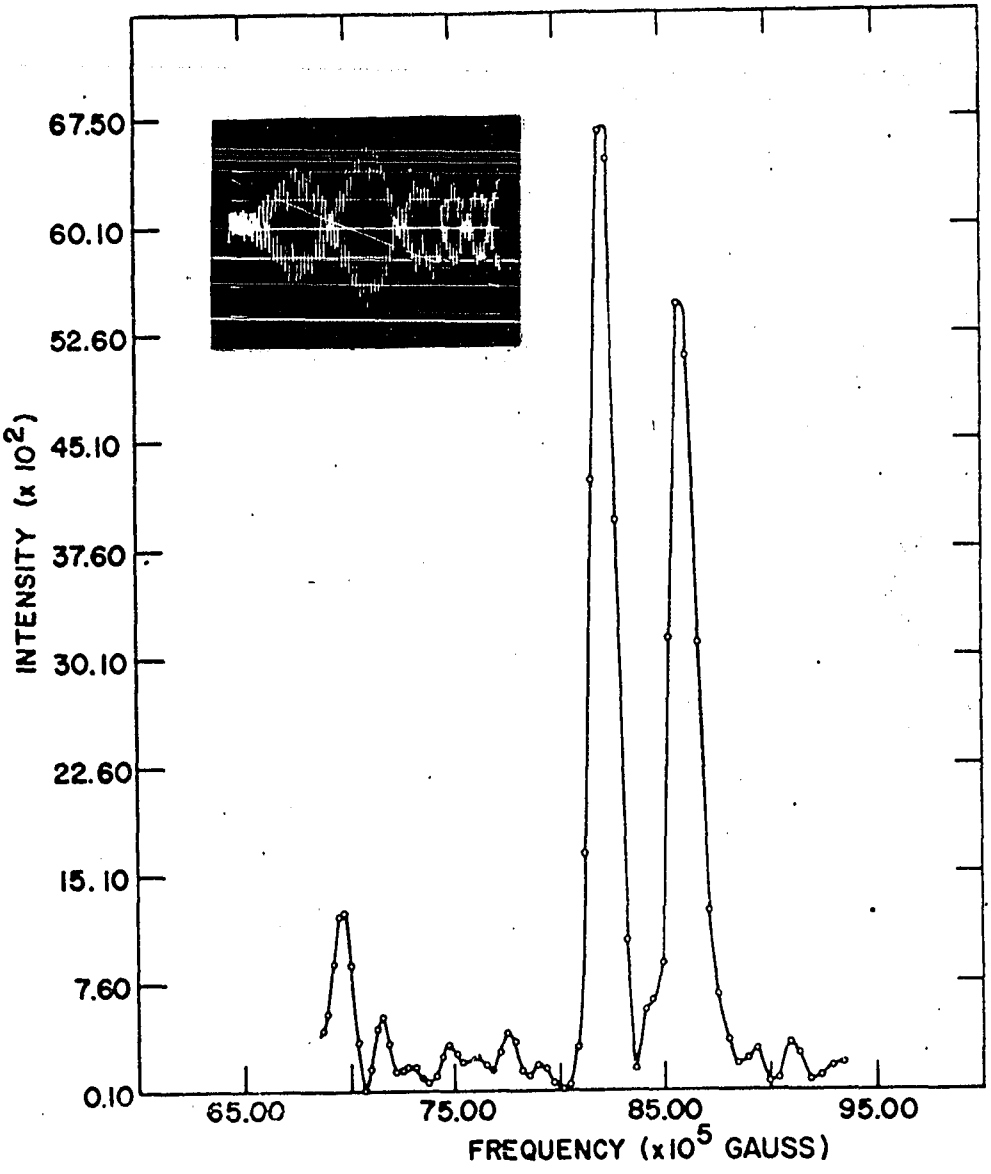
67.50
60.10
52.60
45.10
37.60
30.10
22.60
15.10
7.60
0.10
INTENSITY (x 10²)
65.00
75.00
85.00
95.00
FREQUENCY (x10⁵ GAUSS)

cycle maxima and minima occurred in the de Haas-van Alphen signal.

1. Errors in crystal orientation

The accuracy with which the orientation of the magnetic field is measured depends first of all on how accurately the sample is oriented with respect to the sample holder (see Section II-C); the tungsten samples were somewhat irregularly-shaped and quite small so that slight misorientations of this kind were difficult to avoid. Secondly, for the string-driven sample holder, the method which was used to determine the orientation of the pickup coil with respect to the magnetic field required that the axes of the solenoid, the angle-measuring coils, and the pickup coil could be made to coincide; these necessary alignments were carefully made.

The orientation dependence of the dHvA frequencies in the $(\bar{1}10)$ plane was mapped out by using the sample which had its geometrical axis along $[00\bar{1}]$ to study the orientation dependence for field directions near $[00\bar{1}]$, the $[\bar{1}11]$ sample for field directions near $[\bar{1}11]$, and the $[\bar{1}10]$ sample for field directions near $[\bar{1}10]$. There are several dHvA components in tungsten which vary quite rapidly with angle so that the angle corresponding to the symmetry direction in each of these sets of data could be found by examining the symmetry of the resulting plots of frequency versus angle. Usually an adjustment of between four and six

degrees was necessary to set the zero of the angle scale to coincide with the symmetry direction.

When the data from the different samples were combined in a manner consistent with cubic symmetry to give the orientation dependence of the frequencies throughout the $(\bar{1}10)$ plane, any serious orientation errors at large angles showed up as a mismatch between data taken using different samples. The worst such angular mismatch was about 10°. The best case showed negligible error.

2. Errors due to complex waveforms

It is felt that some of the data have not as yet been reliably analyzed, and the points which will be shown for these data represent only the present best estimate. It will be indicated which points are uncertain when the data are discussed. Most of the data could be analyzed reliably, and when these data were subjected to a detailed analysis, the results which were obtained from successive pulses agreed to considerably better than one percent.

3. Possible systematic errors

The most important systematic errors which are likely to occur in the impulsive field experiment are connected with the determination of the magnetic field values corresponding to each cycle maximum and minimum of the de Haas-van Alphen signal. The major unknown factor in this

determination is the shape of the solenoid at high fields. During a pulse, the magnet windings are subjected to enormous forces which may cause the solenoid to become slightly distorted. Any slight distortion of the magnet should cause cracking in the epoxy resin magnet coating, but such cracking has not been observed, and we have no other evidence that any significant distortion occurred.

Ideally, one would like to be able to measure the magnetic field directly during a pulse, but unfortuantely there are no accurate methods available for measuring large, rapidly-varying impulsive fields. Therefore, it is necessary to rely on a measurement of the coil current I and to determine H from the relation H=KI, assuming that distortion effects are small. The coil current is determined from the voltage across the standard resistor. The constant K which relates the current in the solenoid to the field at its center was determined from a proton resonance calibration (Girvan 1964). This measurement was made using a small direct current~12A which is, of course, considerably less than the peak pulse current (~1500A). Since the form of the actual pulse is a low-frequency, slightly-damped, half sine wave whose main frequency component is about 30 Hz. it is probable that no serious errors due to capacitive effect arose and that the d.c. calibration is adequate.

It is possible that a small error in frequency

measurement could have occurred due to the slow overload recovery of the oscilloscope amplifiers. Since it is often necessary to use large bucking voltages, these amplifiers are saturated during much of the pulse. Preliminary measurements of the recovery from a square wave overload indicated that there was some amplifier overshoot with a long settling time during overload recovery. However, when Mr. P.T. Panousis later checked this effect, using the actual sinusoidal field pulse, he found that errors due to the slow overload recovery of the amplifiers for the actual case are expected to be less than 0.4 percent.

Eddy currents induced in the sample by the impulsive field can in some cases contribute to a frequency difference between rising and falling field data. Fawcett (1962) has measured the low temperature transverse magnetoresistance of single crystals of tungsten and has found that the resistivity $\rho(H)$ in the magnetic field fits the expression $(\rho(H) - \rho(0))/\rho(0) = CH^m$ with an exponent m which is always greater than 1.94. Using his results for the orientation which yielded this lowest exponent and Gold's (1958) analysis of the effects of eddy currents on the de Haas-van Alphen frequencies, we find that frequency differences due to eddy currents are expected to be less than 0.03 percent.

Anderson (1962) has considered further systematic errors which can arise in this experiment. The conclusion

is that results obtained by the impulsive field method are quite reliable if the data for rising and falling field are averaged; there are several systematic errors in the raw data which are cancelled by this averaging. All data which we will quote will be averages of rising and falling field data.

Some of our results can be compared with the results obtained by other investigators (Sparlin and Marcus 1966, Brandt and Rayne 1963) using the torque method (oscillations are detected in the torque, $\underline{M} \times \underline{H}$). In most cases the agreement between the two different methods is better than one percent. However, for one low frequency component near [001], there is a four percent discrepancy which is not yet understood.

III. RESULTS

A. Frequency Results

The main part of this study consists of frequency data which were taken for magnetic field directions lying in a $(\bar{1}10)$ plane. Some data were taken for magnetic field directions lying in a (100) plane, but these data did not yield any results which could not have been predicted from the data in the $(\bar{1}10)$ plane and are therefore not discussed.

The points on Figure 9 show the overall frequency spectrum which was measured for magnetic field directions lying in the $(\bar{1}10)$ plane. We have plotted the results on a logarithmic scale in order to present all the data on one drawing. The points for magnetic field directions near $[00\bar{1}]$ were taken with a sample which had its geometrical axis along $[00\bar{1}]$. Similarly, the points near $[11\bar{1}]$ and $[\bar{1}10]$ were taken using samples which had their long axes along $[11\bar{1}]$ and $[\bar{1}10]$ respectively. Usually the bath temperature was about 1°K when these data were taken, and magnetic field strengths ranging from 12 to 160 kG were used.

In order to facilitate discussion of the data, each of the fundamental curves on the data plot has been labeled with a Greek letter. Smooth solid curves have been drawn through the fundamental terms $\alpha, \beta, \delta, \eta, \epsilon$. The orientation dependence of the upper and lower branches, ϵ_u and ϵ_l, of the low frequency ϵ oscillations near $[00\bar{1}]$,

Figure 9. Orientation dependence of all the frequencies found in tungsten for magnetic field directions in a $(\bar{1}10)$ plane; the frequencies have been plotted on a logarithmic scale. ∇ : $[00\bar{1}]$ axis sample, $\square$: $[11\bar{1}]$ axis sample, $\bigcirc$: $[1\bar{1}0]$ axis sample. Solid curves:fundamental terms; dashed curves:harmonic and combination terms predicted from fundamental curves. Shaded region:incompletely resolved data. Points lying in the dashed rectangular boxes will be plotted on an expanded scale on a later figure.

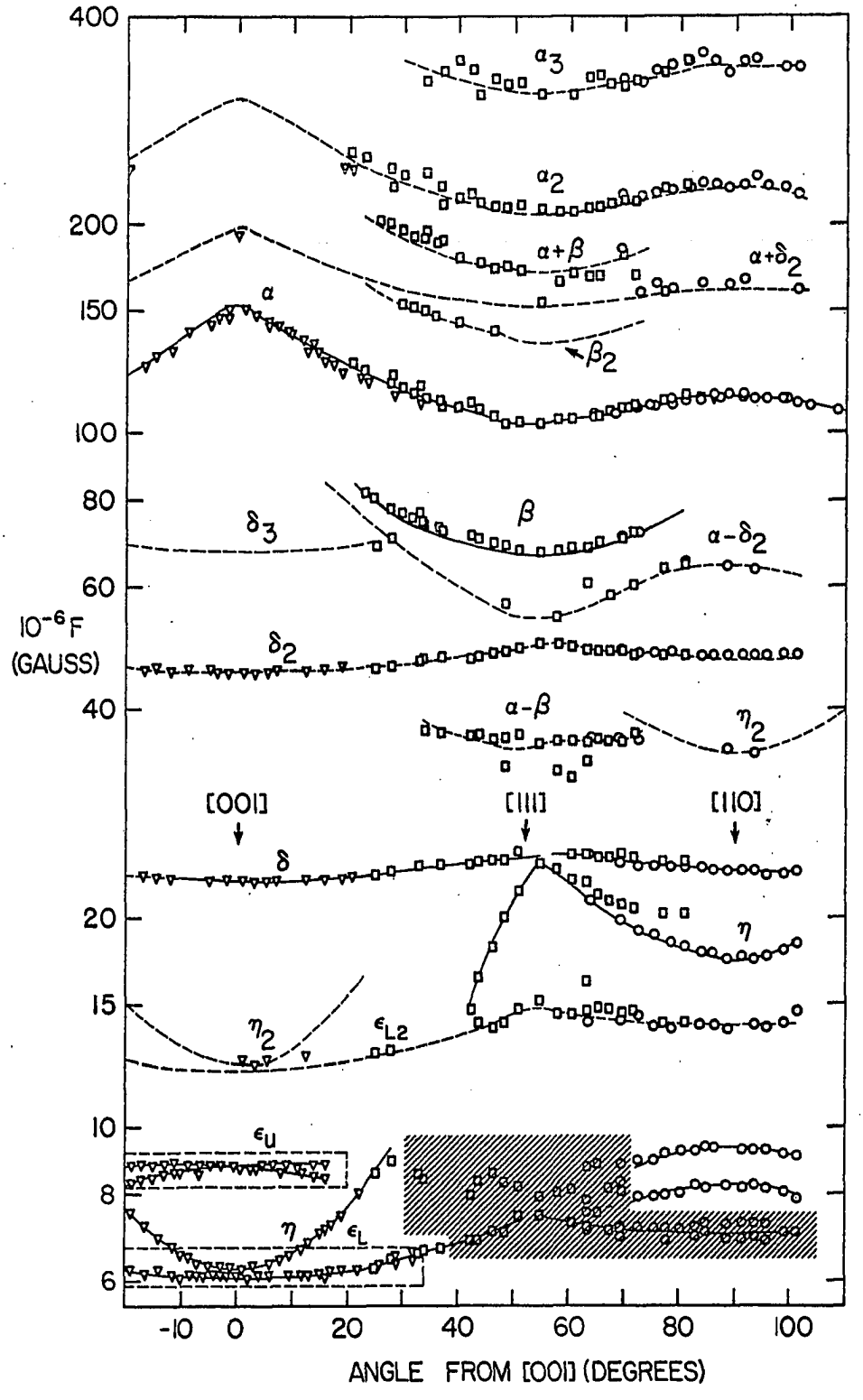
400
200
150
100
80
60
40
20
15
10
8
6
10^{-6}F
(GAUSS)
α_3
α_2
$\alpha+\beta$
$\alpha+\delta_2$
α
β_2
β
δ_3
$\alpha-\delta_2$
δ_2
$\alpha-\beta$
η_2
[001]
[111]
[110]
δ
η
ϵ_{L2}
ϵ_U
ϵ_L
-10
0
20
40
60
80
100
ANGLE FROM [001] (DEGREES)

(enclosed in dashed rectangles) does not show up very well on this plot. These data will be plotted later on an expanded scale (Figure 11).

Many of the fundamental terms in tungsten were quite strong so that harmonics of these terms were observed. In addition to harmonics, further nonfundamental terms are expected due to the basic nonlinearity of the magnetic properties of the crystal (Shoenberg 1962, Pippard 1963). The simplest of these are sum and difference combinations between the fundamental terms. In order to demonstrate which points on Figure 7 are due to nonfundamental terms, dashed curves have been drawn on the figure to represent either integral multiples of the fundamental terms or combination terms between strong components. Many of the observed points lie on these curves, and this is the basis for interpreting these terms as nonfundamental. For the sake of clarity, the complete set of dashed curves has not been shown. It will be noticed that there are terms $\alpha \pm \delta_2$, but that there are no terms $\alpha \pm \delta$. Due to the way in which the spectrum of frequencies appears on the oscilloscope screen, the terms $\alpha \pm \delta$ would have been swamped by the very strong α oscillations if they had occurred. We shall return to a further discussion of sum and difference terms in Appendix C.

The shaded regions in the low-frequency range for

field directions near [111] indicate regions in which signals were observed, but the resolution of the data processing procedure was not sufficient to separate the different beating components. It was possible, however, to obtain rough estimates of the frequencies from these data, and these estimates are plotted.

The slow-frequency data near [001] were also complex, but by the use of special techniques it was possible to analyze these data reliably. When our investigation of these slow frequencies was begun, they had been studied in two other investigations using the torque method (Brandt and Rayne 1963, Sparlin and Marcus 1964); these experimenters had given conflicting interpretations to their results. Since the interpretation of the small pieces of tungsten depends critically on the detailed orientation dependence of these slow frequencies near [001] (see Section IV-A), we will elaborate on these in some detail.

A special run was undertaken to study the orientation dependence of the slow frequencies near [001]. In order to obtain sufficient cycles to resolve these frequencies, it was necessary to connect the crowbar ignitron across the pulse coil circuit (Figure 5). The crowbar ignitron fired shortly after peak field so that the field decayed exponentially from its peak value (see Figure 4c). Because the rate of change of $\dot{H}/H^2$ is relatively slow during the

exponential decay of the field pulse, the time frequency of the dHvA components changes comparatively slowly with H, and it was possible to observe many cycles of a particular component F_i and yet use filtering to good advantage to separate neighboring frequencies. However, since the field pulse is not symmetric when the shunt ignitron is used, a straight average of the data taken for rising and falling field was not sufficient to find the correct frequency values. Therefore, for these data, measurements were first taken only on the falling side of the field during the exponential field decay. Then, when points had been taken for a sufficient range of magnetic field directions, the crowbar ignitron was removed, and the magnetic field was again set along different directions near $[00\bar{1}]$ in a $(\bar{1}10)$ plane. Using this configuration, data were taken for both rising and falling field, and the results were averaged. These averaged results were compared with the falling field data which had been taken using the crowar ignitron, and thus a correction factor could be determined for orientations near $[00\bar{1}]$; this correction factor was then used to scale all of the crowbar results.

Some examples of the beating patterns which were obtained in the slow frequency oscillations using the shunt ignitron are shown in Figure 10. Even with the pronounced

Figure 10. Some examples of impulsive-field dHvA data in tungsten taken at 1°K using the shunt ignitron

a. Beats between two components of ϵ_u oscillations
H about 10° from [00$\bar{1}$] in the ($\bar{1}$10) plane
Resonant frequency ~ 32kHz
Filter passband ~ 25-40kHz
Bottom calibration line at 24.7kG; succeeding calibration lines at intervals of 1.235kG

b. ϵ_L and η oscillations both dominant on one oscillogram (The η oscillations dominate at the high field end of the picture and the ϵ_L at the low field end.)
H ~ 13° from [00$\bar{1}$] in the ($\bar{1}$10) plane
Resonant frequency ~ 50kHz
Filters set to pass frequencies above 15kHz
Bottom calibration line at 13.585kG; succeeding lines at intervals of 1.235kG

c. ϵ_L oscillations beating with η oscillations, η oscillations dominant
H ~ 10° from [00$\bar{1}$] in the ($\bar{1}$10) plane
Resonant frequency, filter setting, and calibration line values the same as in b

d. η oscillations without noticeable beats
H ~ 8° from [00$\bar{1}$] in the ($\bar{1}$10) plane
Resonant frequency, filter settings, and calibration line values the same as for b
In later figures (Figures 32 and 33) we will show the strong beats which reappeared in the η oscillations when H was moved still closer to [00$\bar{1}$].

e. Showing beats between two terms of the ϵ_L oscillations
H ~ 29° from [00$\bar{1}$] in the ($\bar{1}$10) plane
Bottom calibration line at 14.820kG; succeeding lines at intervals of 1.235kG
Resonant frequency and filter settings the same as for b

f. Further example of beats between two components of ϵ_u oscillations
H ~ 19° from [00$\bar{1}$] in the ($\bar{1}$10) plane
Resonant frequency ~ 60kHz
Filter passband ~ 40-85kHz
Bottom calibration line at 17.290kG; succeeding lines at intervals of 1.235kG

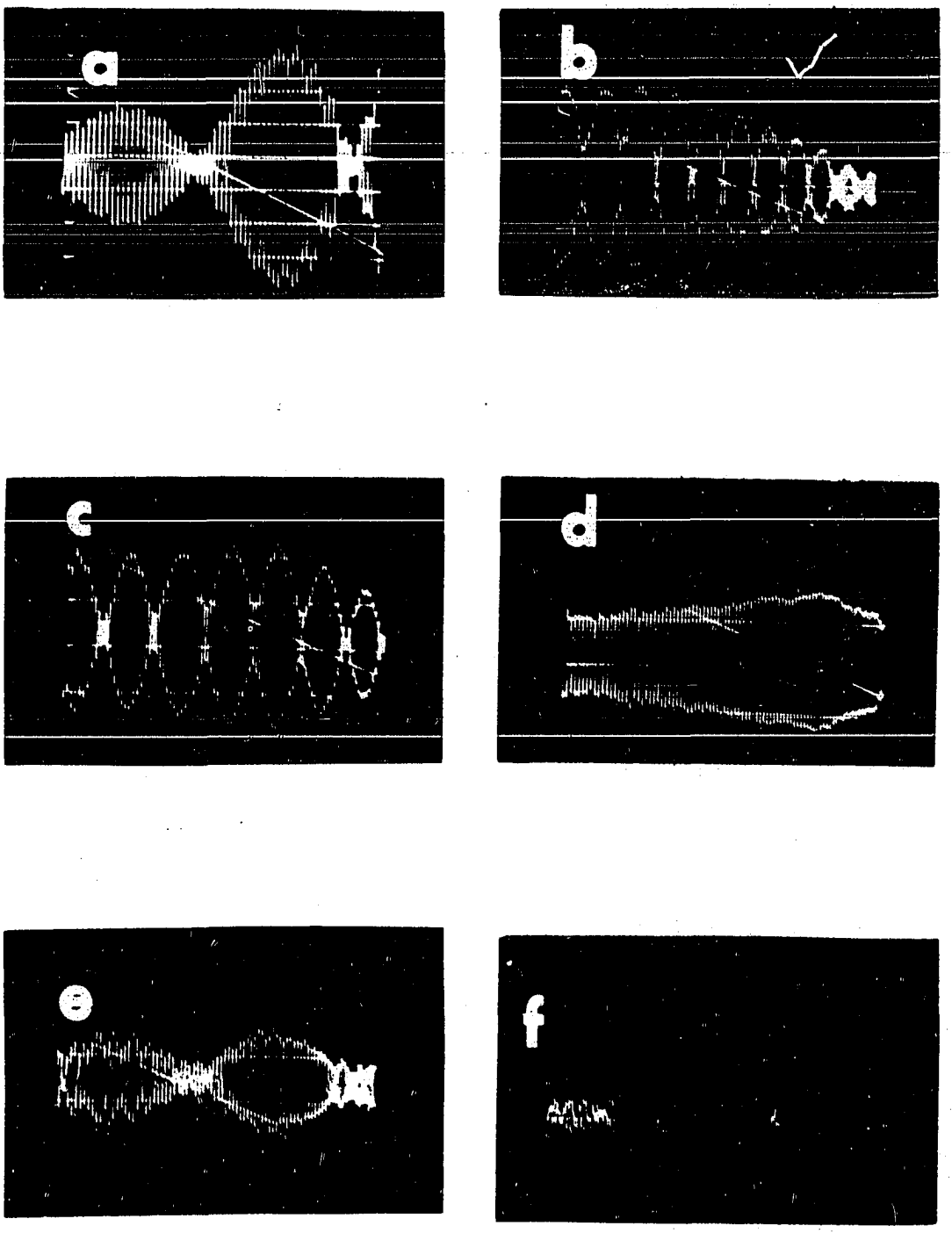
a
b
c
d
e
f

beating patterns and large number of cycles which were observed on pictures like these, it still proved difficult to determine the orientation dependence of the upper branch of these frequencies near [001] by straightforward beat analysis, and it was necessary to use the more reliable method of periodogram analysis (see Section II-E). The frequencies which were obtained by this method for the upper branch ϵ_u of the slow frequencies near [001] are shown on an expanded scale in Figure 11a.

The shunt ignitron data for the lower branch of the ϵ oscillations near [001] are shown on an expanded scale in Figure 11b. These data were processed by the standard method of finding the inverse slope of a line which was fitted to the reciprocal field positions of cycle maxima and minima. At about 12° from [001] both the η oscillations and the immediately slower ϵ_L oscillations could be brought into resonance on a single picture as is shown in Figure 8b. The frequencies for the two components in a case like this were determined from the reciprocals of the slopes of the two separate straight lines on the reciprocal field value plot for this picture. The strength of the η oscillations increased rapidly as the [001] direction was approached until at an angle of $\sim$10° from [001] they became so strong that they dominated over the whole low field range.

Since the ϵ_L oscillations appeared as a slightly slower

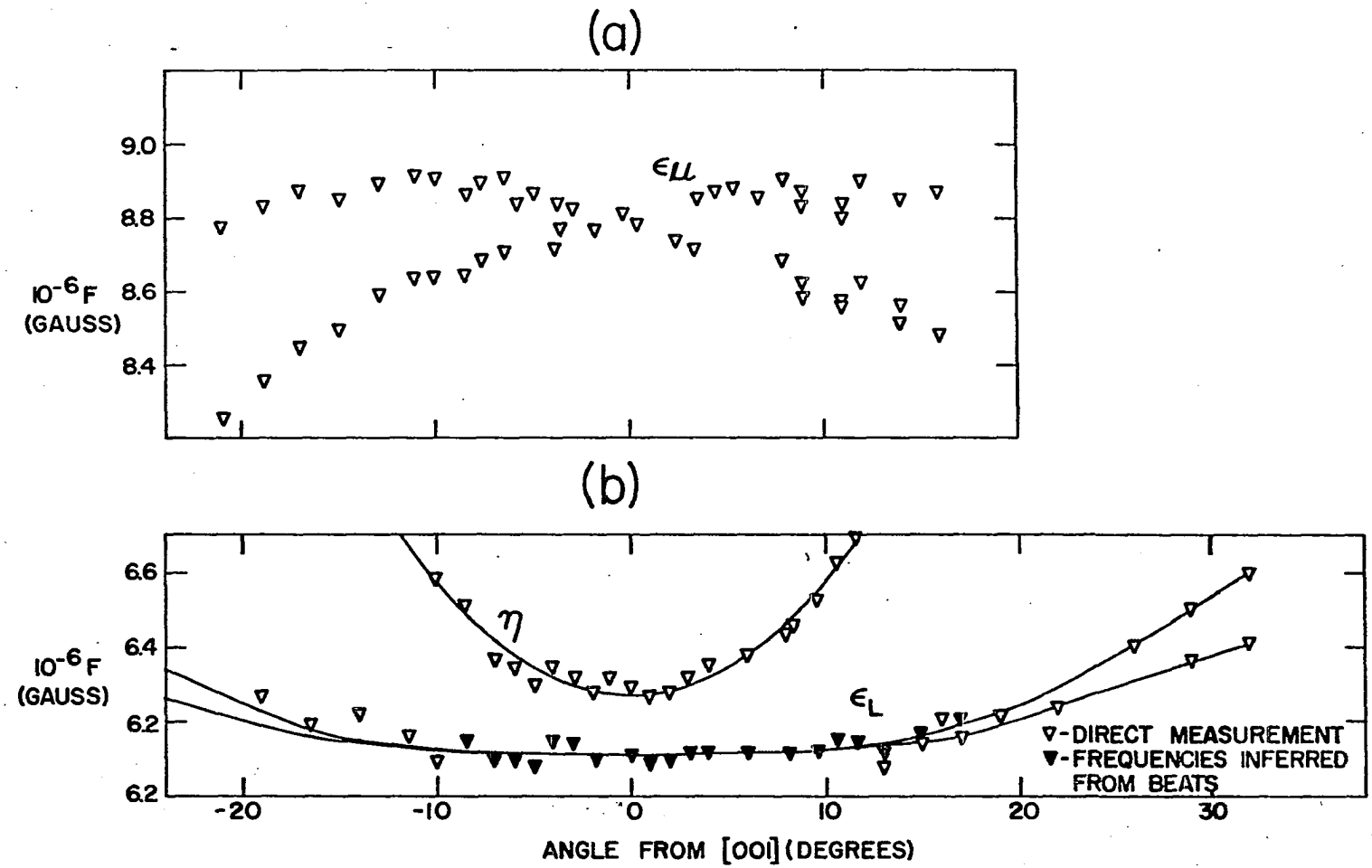

Figure 11. The orientation dependence of the ϵ_u and ϵ_L oscillations for field directions near $[00\bar{1}]$ in the $(\bar{1}10)$ plane; some measurements for the η oscillations are also shown

and weaker frequency than the η oscillations for H~10° from [001] , it was assumed that the beating pattern which was still apparent in the η oscillations when the field direction was moved closer to [001] was due to the ϵ_L oscillations which had now been almost completely swamped. However, when H was set about 8° from [001] , the beat pattern completely disappeared (see Figure 10d). Then, when the magnetic field direction was moved still closer to [001] , the beats reappeared. In spite of this peculiar disappearance of the beats due to the ϵ_L oscillations at about 8° from [001] , it was assumed that the beats in the η oscillations throughout the range of magnetic field directions near [001] were due to the ϵ_L oscillations, and a frequency for the ϵ_L oscillations was obtained from their beat frequency with the η oscillations. A subsequent check at [001] using the periodogram analysis program confirmed that the beating pattern in the η oscillations near [001] was indeed due to a lower frequency component.

At larger angles (H~29°) from [001] , sufficient cycles of the lower branches of the ϵ oscillations could be obtained to observe a beating pattern between two separate components (see Figure 10e). As is evident from Figure 11, it was possible to separate these two components only at two angles, namely 29° and 32° from [001] , although the effects of beating between them were evident over a slightly larger

range of angles.

The results on Figure 9 for frequencies lying in the range 6-10 x 10^6G for field directions near $[\bar{1}10]$ are not as reliable as those which we have just discussed for the same frequency range near $[00\bar{1}]$. These data near $[\bar{1}10]$ were taken using the symmetric field pulse (rather than the exponentially-damped field pulse as was used near $[00\bar{1}]$) so that signals from all of the terms with frequencies in the range 6-10 x 10^6G appeared on one oscillogram; the frequency resolution which could be obtained was therefore limited. We have shown the periodogram for one of these data sets in Figure 12. There are two small peaks on this plot at frequencies of about 7.7 x 10^6G and 8.8 x 10^6G. At nearby angles, two similar well-resolved peaks were always found in the frequency range corresponding to these two peaks. However, in the frequency range corresponding to these two large peaks on Figure 12, the terms were not always well-resolved. Nevertheless, we have used the frequencies at which peaks occurred in this lower frequency range as estimates of the true frequencies and have plotted these estimates in the shaded region near $[\bar{1}10]$ on Figure 9. We will see in Section IV-B that it is possible that there were a number of frequency terms in the range 6.5 - 7.5 x 10^6G; if this was the case, the uncertain results which were obtained from the lowest frequency range near $[\bar{1}10]$ would be

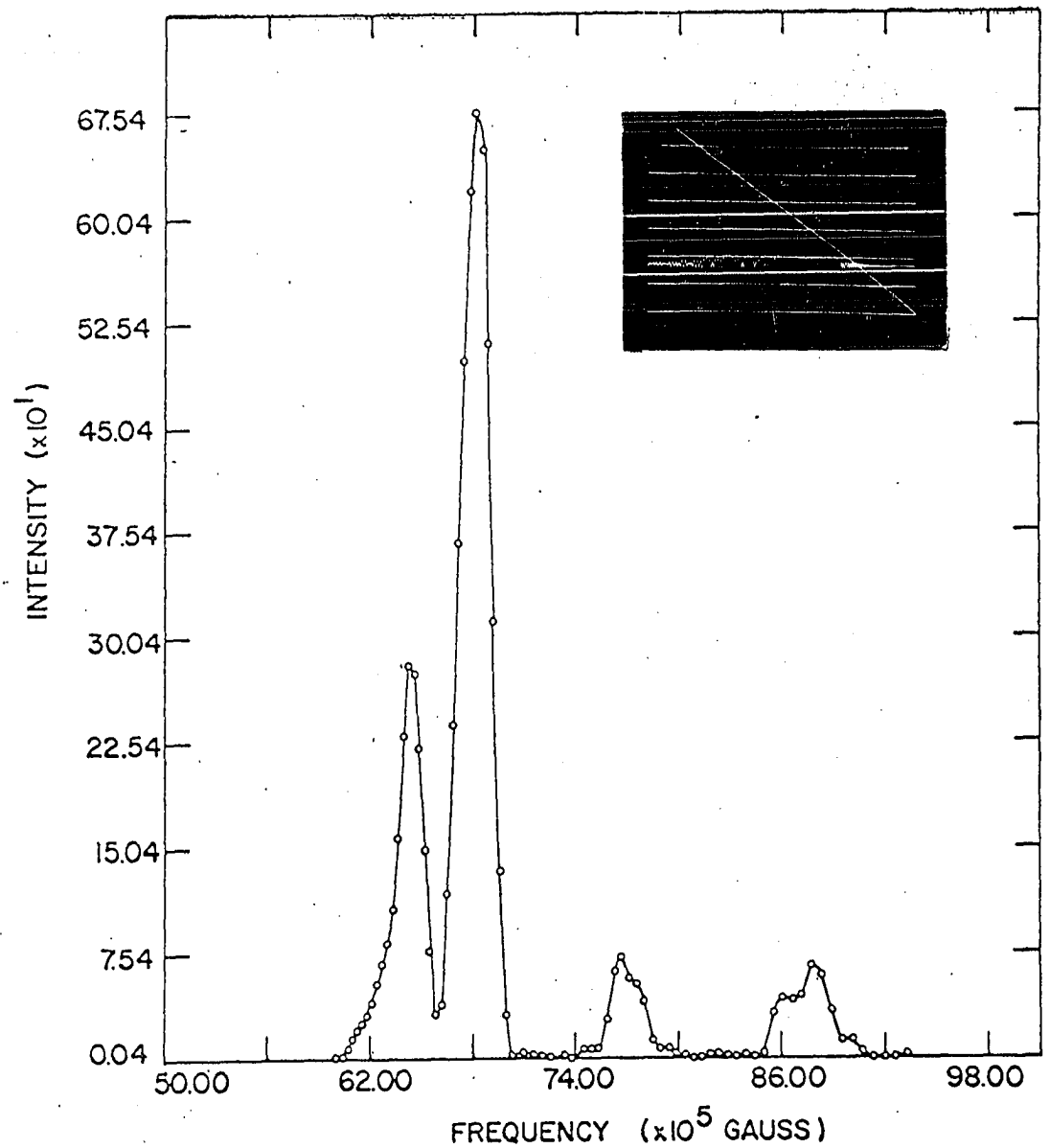

Figure 12. Periodogram for data shown in inset

explained.

Most of the remaining oscillatory terms on Figure 9 were separated quite well by the resonance technique so that it was usually not necessary to use periodogram analysis to find accurate frequency values for these terms. However, the frequency resolution for these terms was of course limited by the number of cycles which were obtained in a resonance envelope. In one important case, that of the β oscillations, this number was not large enough to tell whether this term was really a doublet or not. (We will see in Section IV-C that it is possible that there may really be two terms having frequencies very close to that of the β oscillations.) One of the better data sets which were obtained for the β oscillations is shown in Figure 13a. It is evident that there are not enough cycles on this oscillogram to tell whether the signal is due to two terms having very nearly the same frequency or not.

Examples of the data for some of the other terms are shown in Figures 13b, 13c, and 13d. (An oscillogram for the α oscillations has already been shown in Figure 4b.)

Figure 13. Examples of de Haas-van Alphen oscillations in tungsten at 1°K
Resonant frequency ~100kHz
Filter passband ~70-140kHz

a. β_- oscillations for H~35° from [001] in the $(\bar{1}10)$ plane
Bottom calibration line at 76.570kG; succeeding calibration lines at intervals of 1.235kG (The strong oscillations which are visible at the high field end of the oscillogram are the α oscillations.)

b. δ_- oscillations for H~35° from [001] in the $(\bar{1}10)$ plane
Bottom calibration line at 51.87kG; succeeding calibration lines at intervals of 2.47kG

c. oscillations and _ oscillations for H 48° from 001 in the $(\bar{1}10)$ plane (The oscillations dominate at the high field end of the oscillogram and the oscillations dominate at the low field end.) Bottom calibration line at 46.93kG; succeeding calibration lines at intervals of 2.47kG

d. δ_2 and $(\alpha-\beta)$ oscillations for H~33° from [001] in the $(\bar{1}10)$ plane

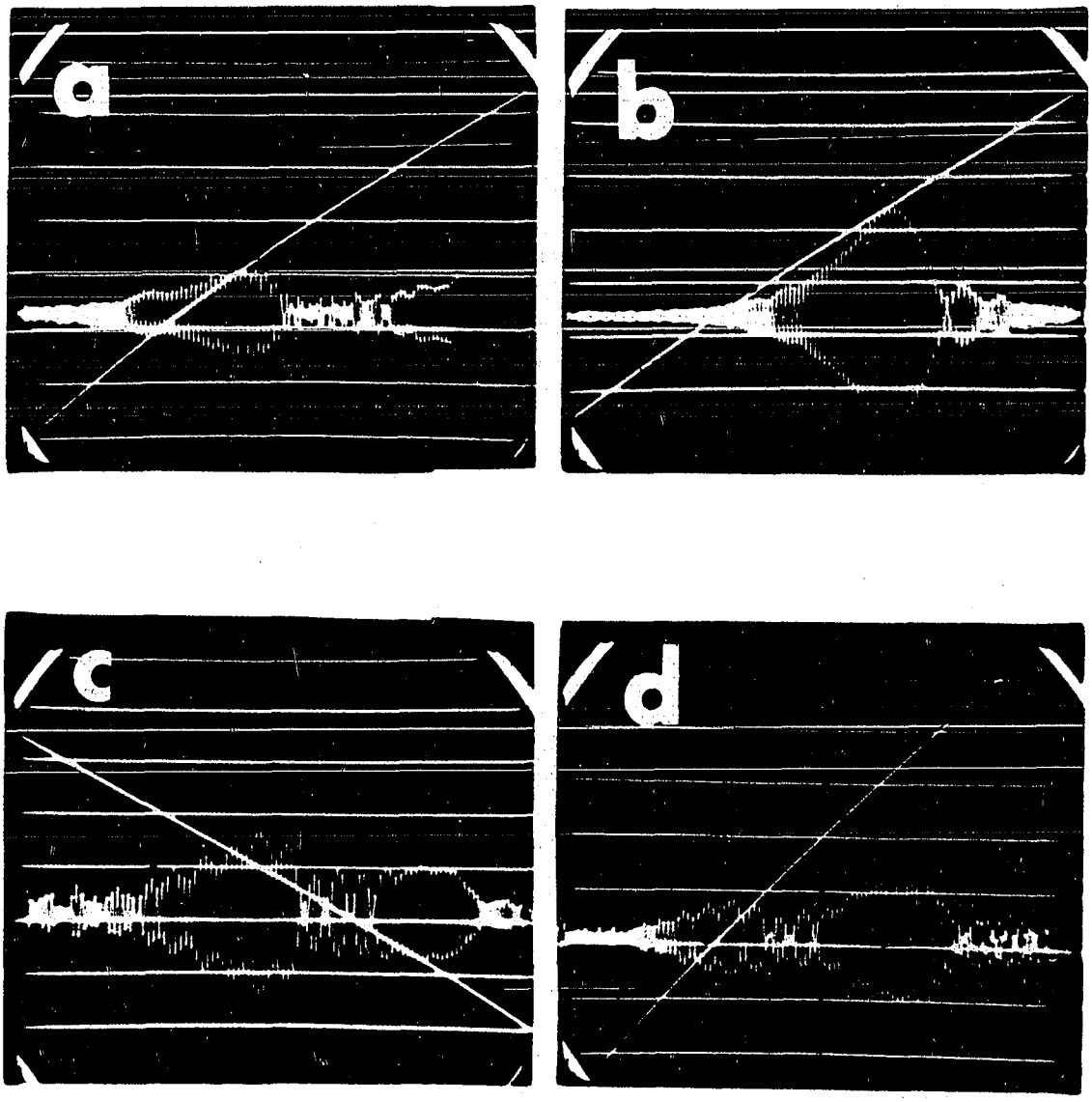
a
b
c
d

B. Cyclotron Mass Results

According to Equation 12, it should be possible to obtain the cyclotron mass corresponding to each orbit from a study of the variation of the amplitude A of the oscillations with temperature T. For all of our data, the condition $4\pi^3 m^* kT/ehH > 1$ holds so that to a good approximation, the hyperbolic sine in Equation 12 can be replaced by an exponential. The temperature dependence of the amplitude of the de Haas-van Alphen signal is then contained in the factor $T\exp(-4\pi^3 m^* ckT/ehH)$ so that the cyclotron mass can be found from the slope of a plot of log A/T versus T. This procedure for obtaining the orbit masses is much more tedious than direct cyclotron resonance, so that the complete orientation dependence of the cyclotron masses is usually studied by cyclotron resonance. The direct cyclotron resonance studies of the large orbits in tungsten (Walsh 1964) had received quite a complete interpretation; our dHvA results serve as a check on his interpretation since we can associate an area with our masses. The dHvA mass values for the lower mass orbits have also been measured by Sparlin and Marcus 1966) using the torque method.

Determinations of oscillation amplitudes from pulsed field signals are subject to considerable uncertainties (Shoenberg 1962), and precise values are possible only if extreme care is taken. Firstly, slight heating of the

sample can occur during a magnetic field pulse, and of course this heating is not detected by measuring the vapor pressure at the surface of the liquid helium bath. Shoenberg (1962) has considered this effect and has concluded that above the λ-point the sample temperature may be raised as much as 0.1°K, but that below the λ-point the heating is negligible. Secondly, the amplitude is sensitive to small changes in the shape of the field pulse which can occur from one data set to the next due to magnet heating during the pulse and to variations in the capacitor bank voltage at which the discharge is initiated. Care was taken to reproduce the field pulse as closely as possible for successive pulses, but small deviations are likely to have occurred. However, these deviations would result in a somewhat random scatter of the amplitude measurements about the straight line, and thus would affect only the precision with which the masses could be measured. Random errors can also arise from slight changes in the orientation of the specimen between successive pulses. Furthermore, Shoenberg (1962) has pointed out that if the position of the sample with respect to the pulse coil changes due to thermal expansion as the liquid helium level falls, the amplitude of the signal can be modified, since the field inhomogeneity over the length of the sample is changed.

The cyclotron masses for most of the terms were not

overly large and the signals were quite strong even at 4°K so that the temperature dependence of the amplitudes could usually be measured over the ~3°K temperature range from 4.2°K to 1°K. In spite of the possible uncertainties in these measurements, the plots of log A/T versus T were usually quite good straight lines for those terms which did not have an extremely large amplitude and were well separated from neighboring terms by the resonance technique. An example of a plot obtained for such data is shown in Figure 14.

For some of the terms the amplitude measurements were more uncertain because these terms were not well separated from neighboring terms by the resonance technique. This was the case for the β oscillations for H// $[1\bar{1}1]$. Two plots (Figures 15 and 16) are shown for the temperature dependence of the β oscillations. These plots are for the same data, but have been processed in two different ways in an attempt to evaluate the effects of beats in the β oscillations due to the very strong α oscillations. The duplicate processing was undertaken in an attempt to find a precise value for the cyclotron mass for the β oscillations at $[1\bar{1}1]$ so that this mass could be correlated with one or the other of two masses near this value which Walsh (1964) found in his cyclotron resonance study of tungsten. However, the dHvA mass results for the β oscillations do not seem to be sufficiently precise to make the correlation reliably. (The slopes of the mass

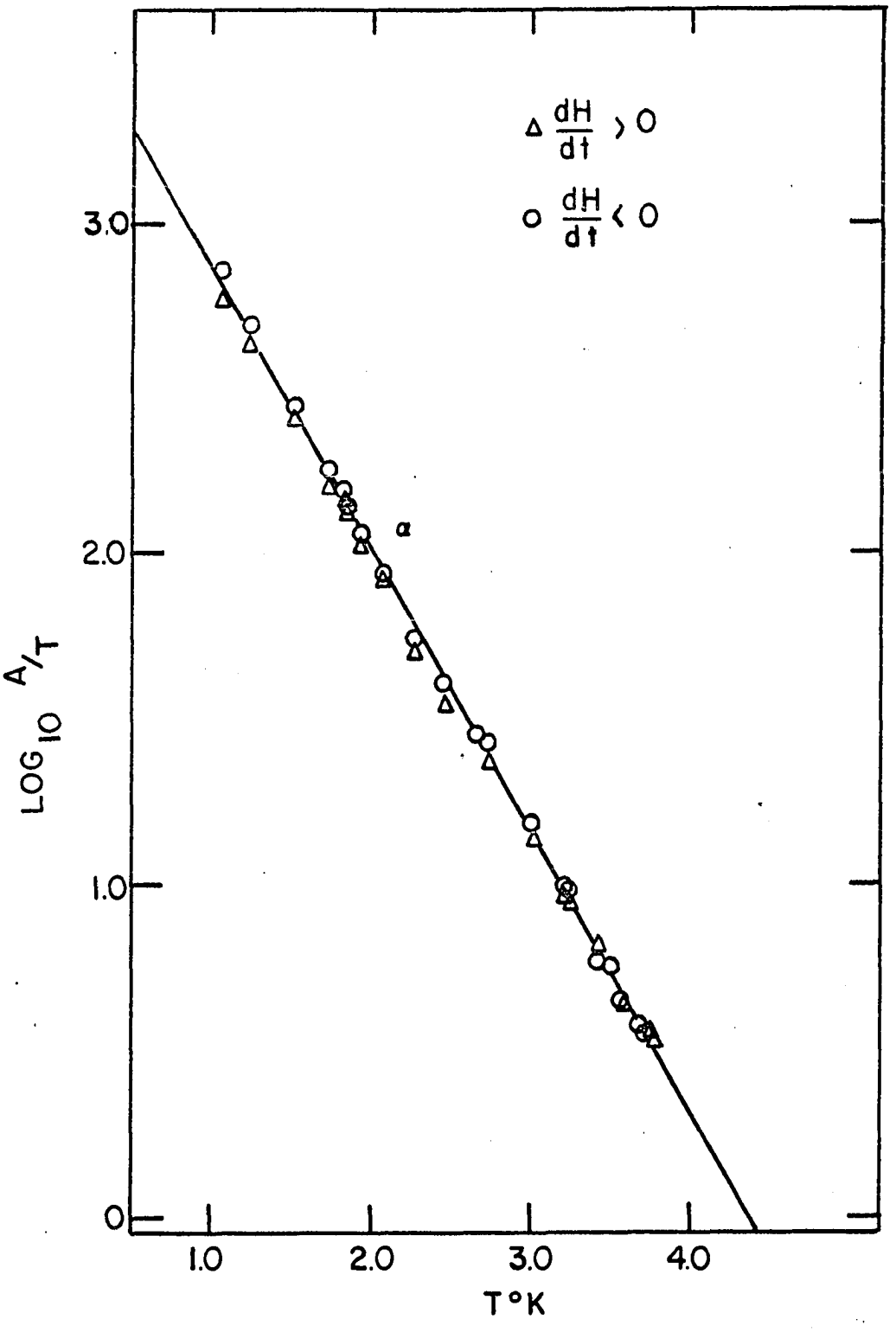

Figure 14. Temperature dependence of the amplitude of the α oscillations for H//[001] (m^*/m_e = 0.93)

Figure 15. Temperature dependence of the amplitude of the β and α oscillations for H// [1 1 $\bar{1}$] (for the α oscillations $m^*/m_e = 0.60$, for the β oscillations $m^*/m_e = 0.88$)

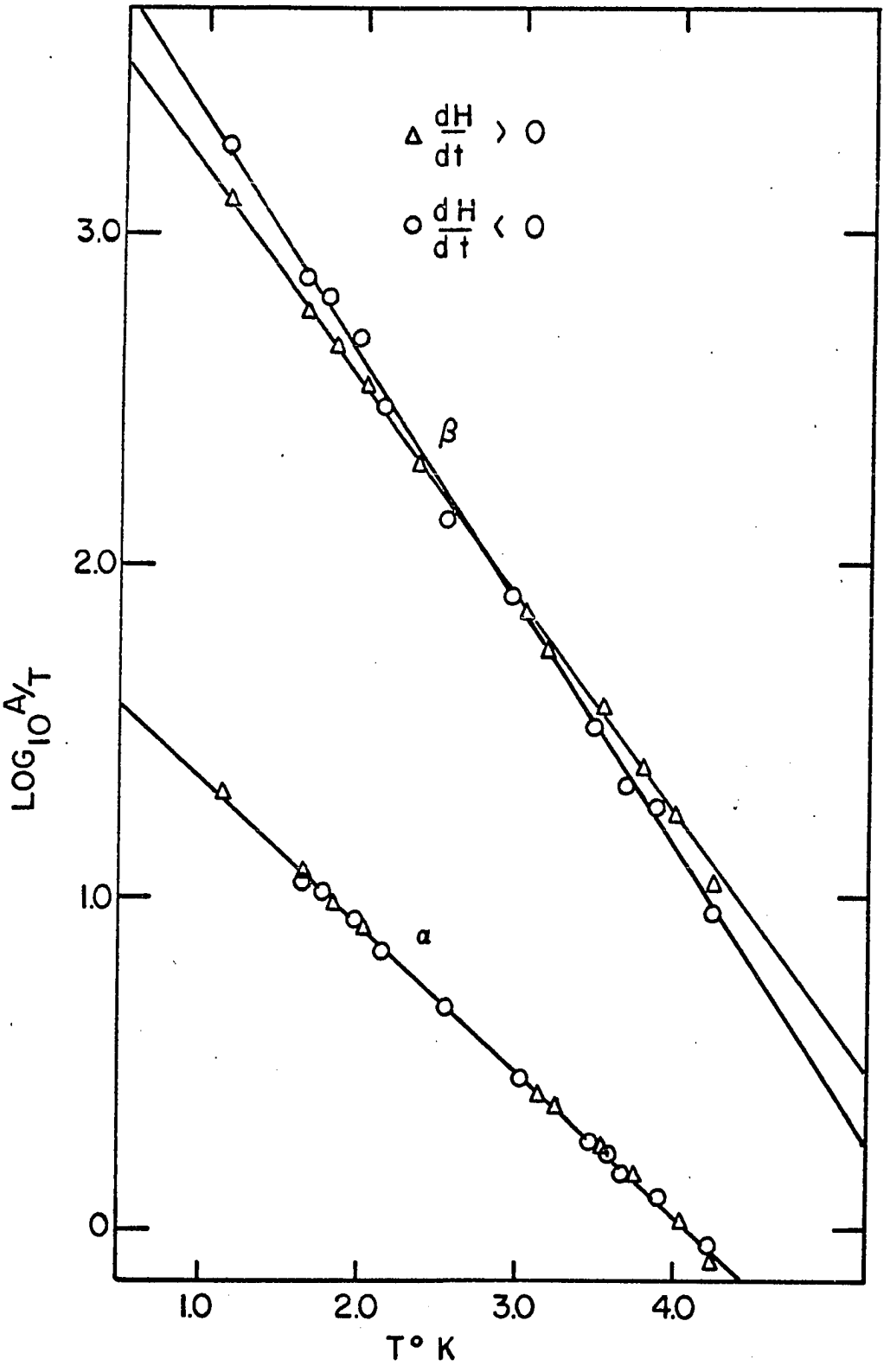
Δ dH/dt > 0
○ dH/dt < 0
β
α
3.0
2.0
1.0
0
LOG10 A/T
1.0
2.0
3.0
4.0
T° K

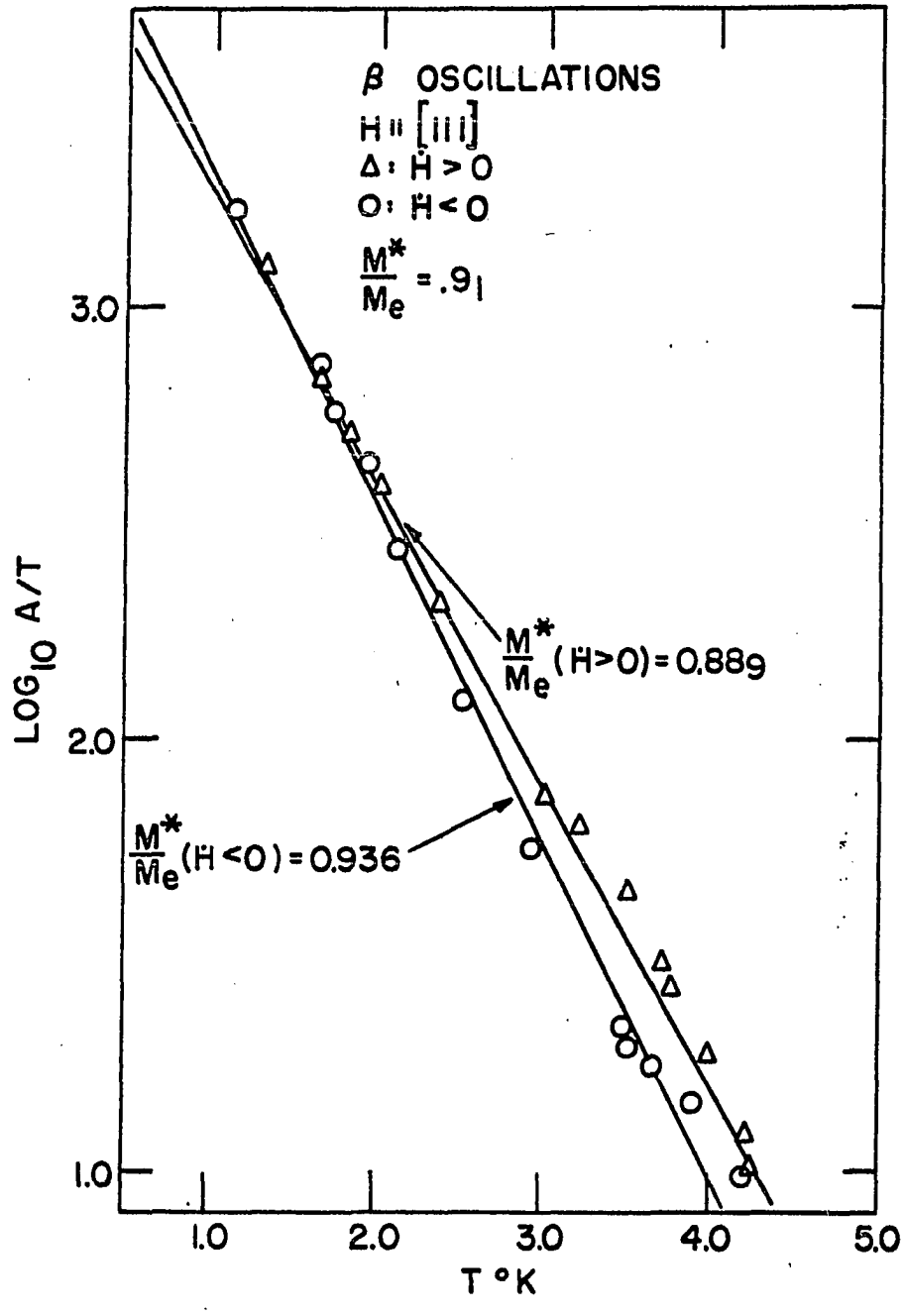

Figure 16. Temperature dependence of the sum of the amplitudes at beat maximum and beat minimum for the β oscillations at $[\bar{1}11]$

plots for rising and falling field are different because the rising and falling field resonance envelopes occur at different magnetic field values.)

Small adjustments could have been made to the lowest temperature points on some of the effective mass plots to correct for the exponential approximation, but this was not done since the correction was usually quite small. The largest correction would have been a ten percent lowering of the amplitude of the 1°K point for the α oscillations at $[11\bar{1}]$. On the semi-log plot of Figure 15 this corresponds to about twice the width of a plotting symbol.

Due to the difficulty in determining the best slopes for these mass plots, the overall accuracy of the results is no better than ten percent. In Section IV-C we will compare these results with the cyclotron resonance results and find that the results of the two experiments agree to within the experimental error.

The temperature dependence of the amplitude of some of the harmonic components was also measured in order to provide further evidence that these terms were indeed harmonics. According to Equation 12, the cyclotron masses for the harmonic terms should be integral multiples of the mass of the fundamental term.

Mass plots for the δ and δ_2 oscillations for H//$[00\bar{1}]$ are shown in Figures 17 and 18. Within the experimental

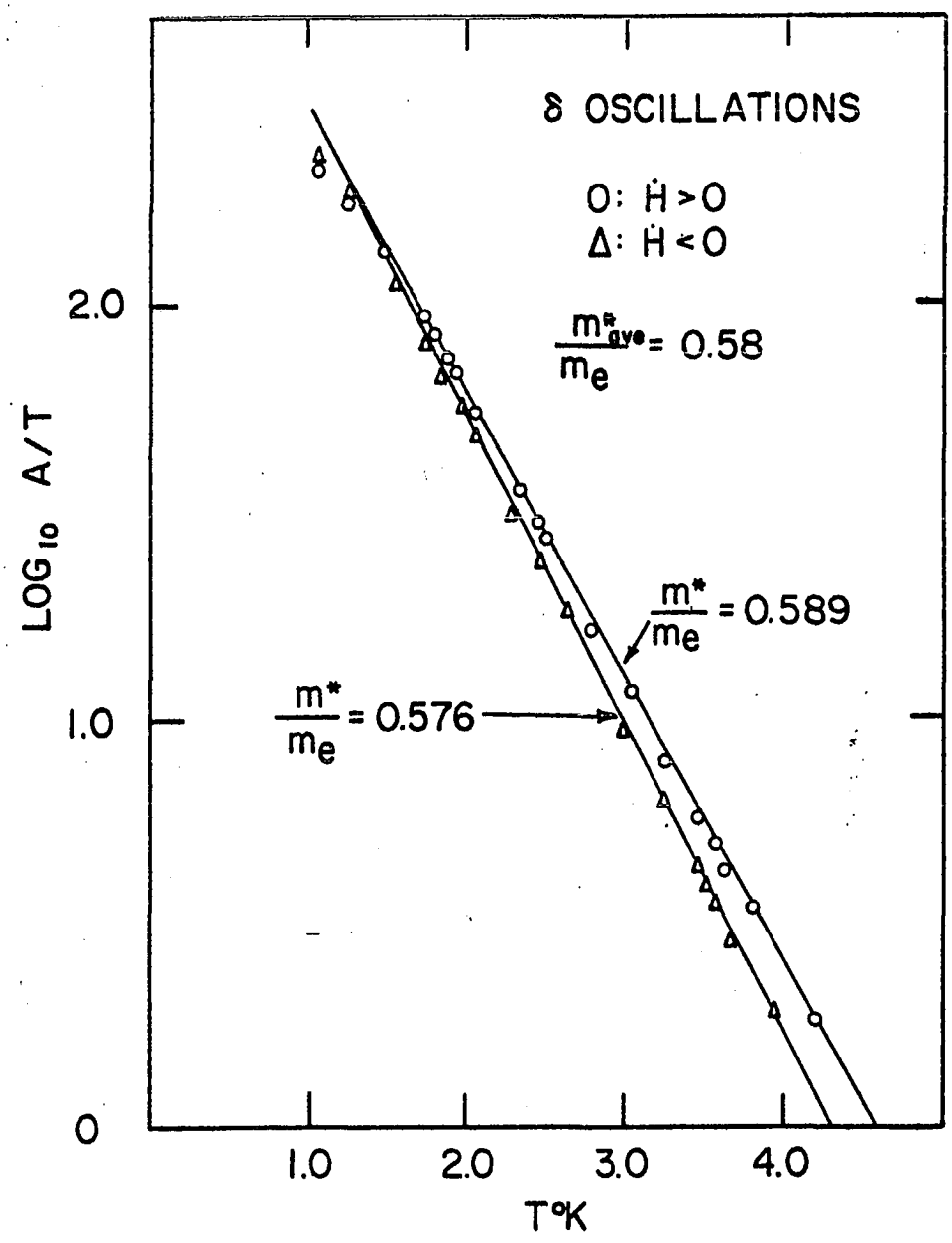

Figure 17. Temperature dependence of the amplitude of the δ oscillations for H// [00$\bar{1}$]

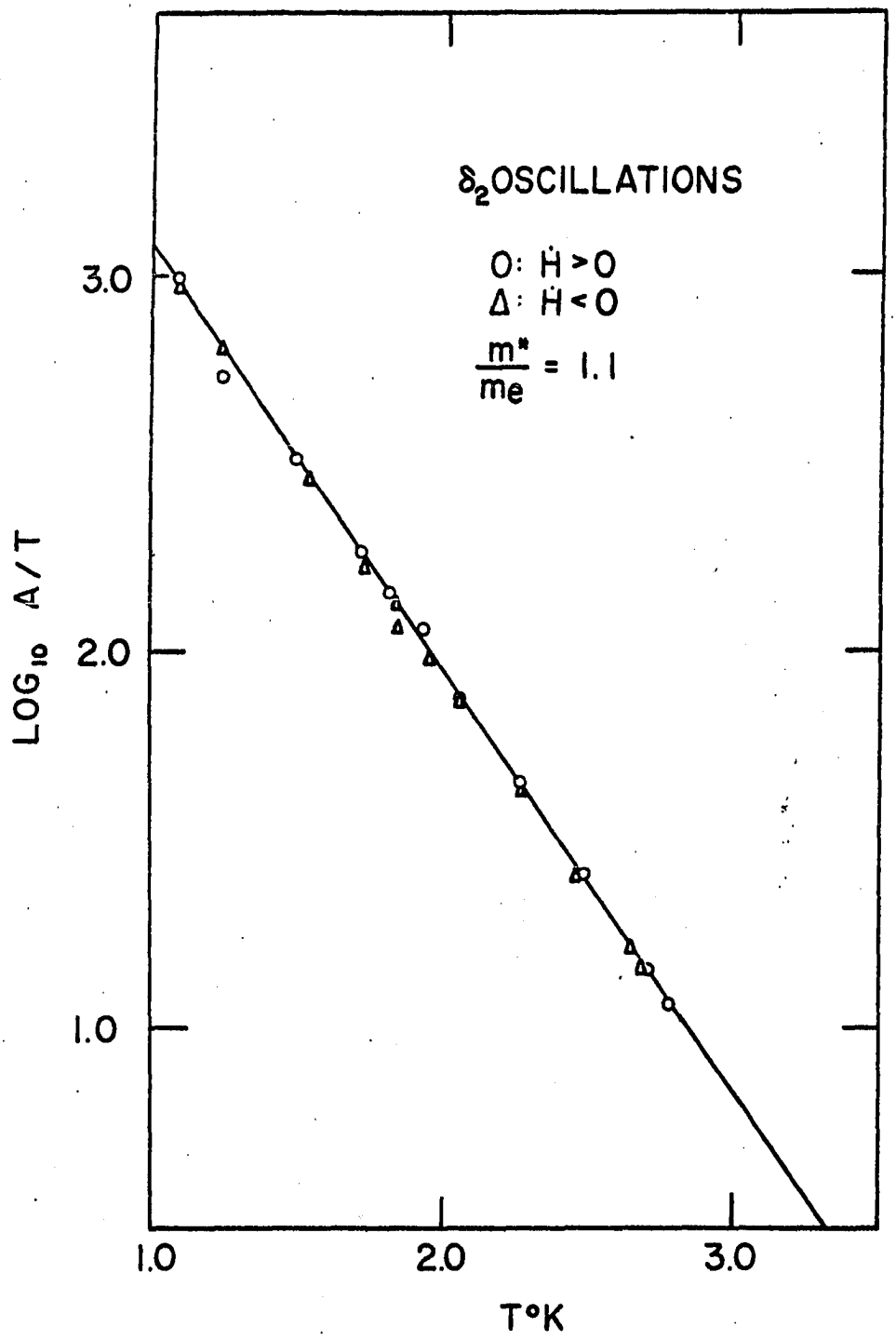

Figure 18. Temperature dependence of the amplitude of the δ_2 oscillations for H//[001]

error, the mass value for the δ_2 oscillations is twice that of the δ oscillations which is consistent with the interpretation of these oscillations as harmonics. The ratio of the masses of the δ_2 and δ oscillations for H// [110] was also consistent with the interpretation of the δ_2 oscillations as harmonics.

The temperature dependence of the amplitude of the and α_2 oscillations at the [110] orientation is shown in Figures 19 and 20. Each of these plots shows a low temperature saturation effect, but if the cyclotron mass values are derived from the high temperature slopes on these plots, the ratio of the mass of the α_2 oscillations to that of the α oscillations is almost two; the discrepancy from an integral ratio is not really outside the precision with which the masses can be measured. The bending over which is evident at the low temperature end of each of these two plots is thought to be due to effects of frequency modulation on the signal amplitude. The frequency modulation arises because B rather than H appears in the argument of the oscillatory factor in Equation 12 (Shoenberg 1962). We will discuss this effect in more detail in Appendix C.

At the [111] orientation, the mass values which were derived from the temperature dependence of the harmonics of the α oscillations (Figures 21 and 22) are somewhat less than integral multiples of the fundamental mass of $m^* = 0.6m_e$

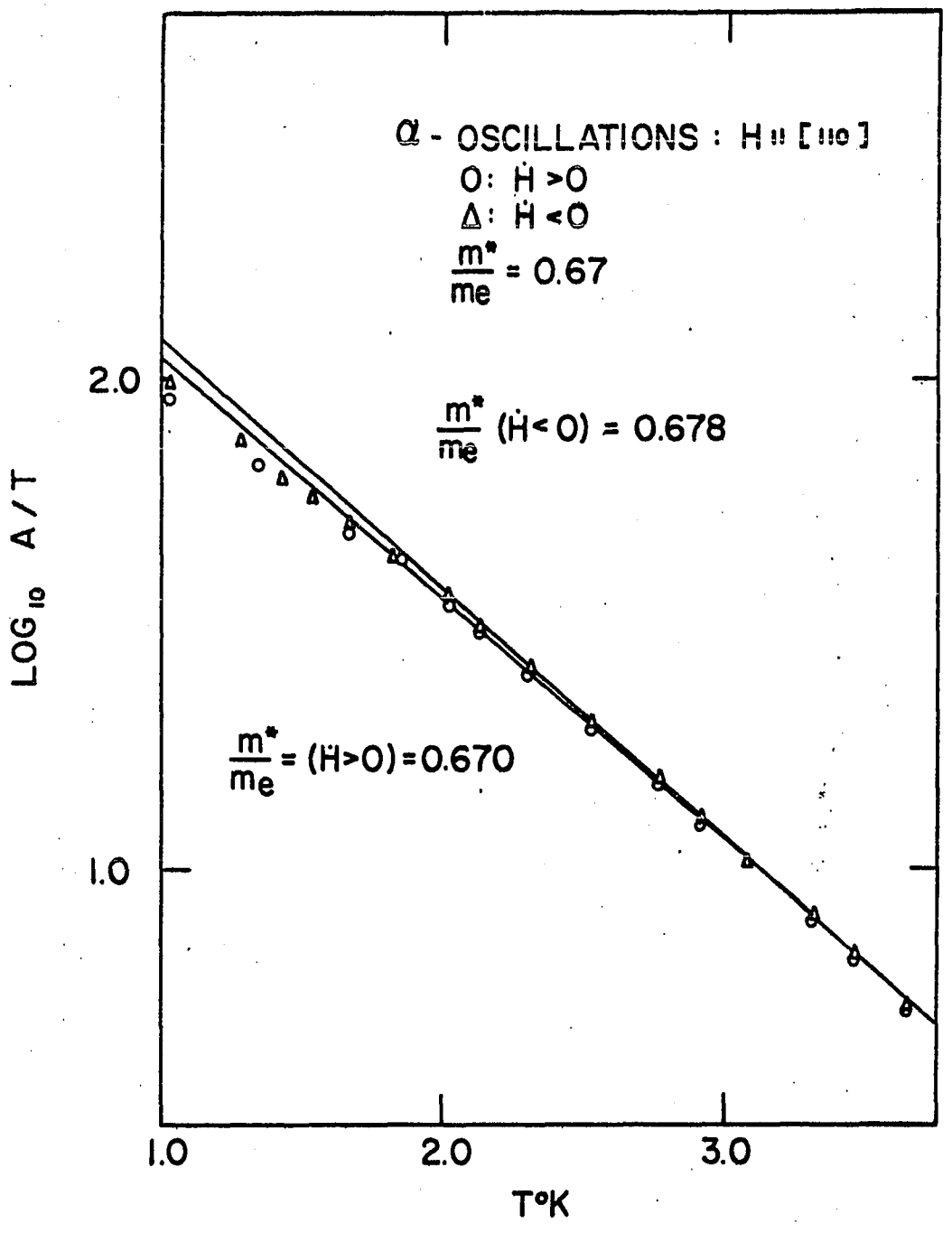

Figure 19. Temperature dependence of the amplitude of the α oscillations for H// [110]

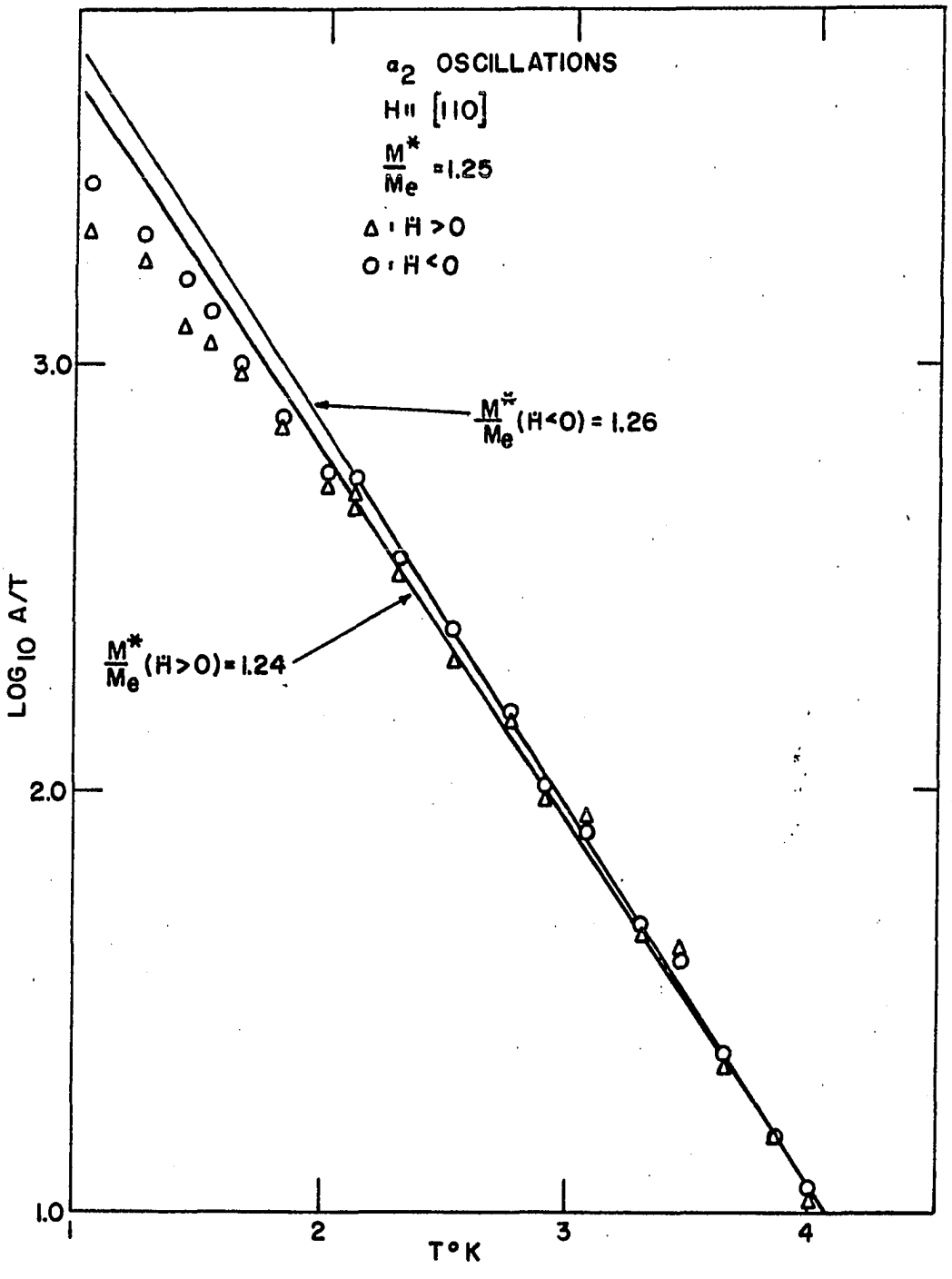

Figure 20. Temperature dependence of the amplitude of the α_2 oscillations for H// [110]

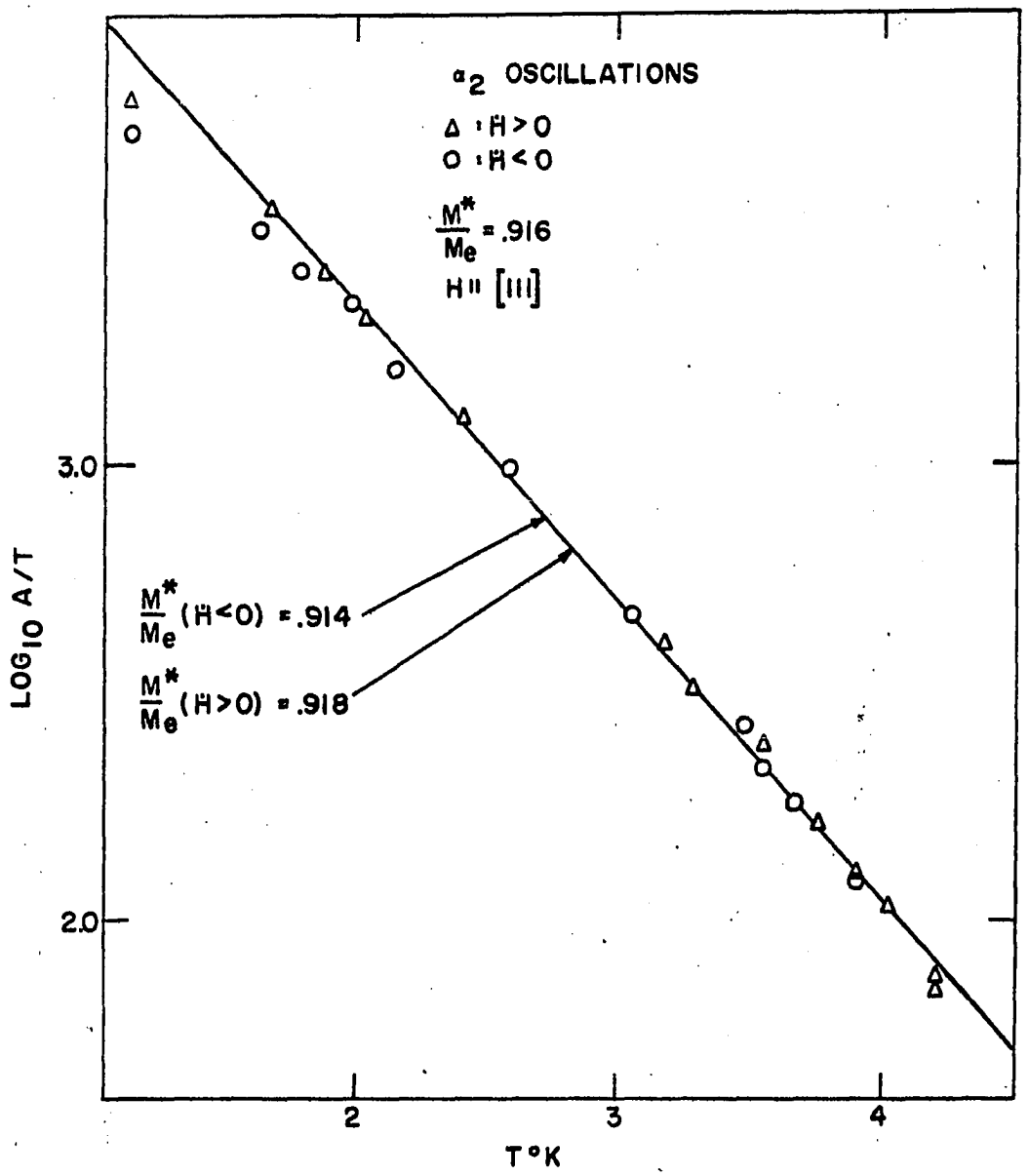

Figure 21. Temperature dependence of the amplitude of the α_2 oscillations for H// [11$\bar{1}$]

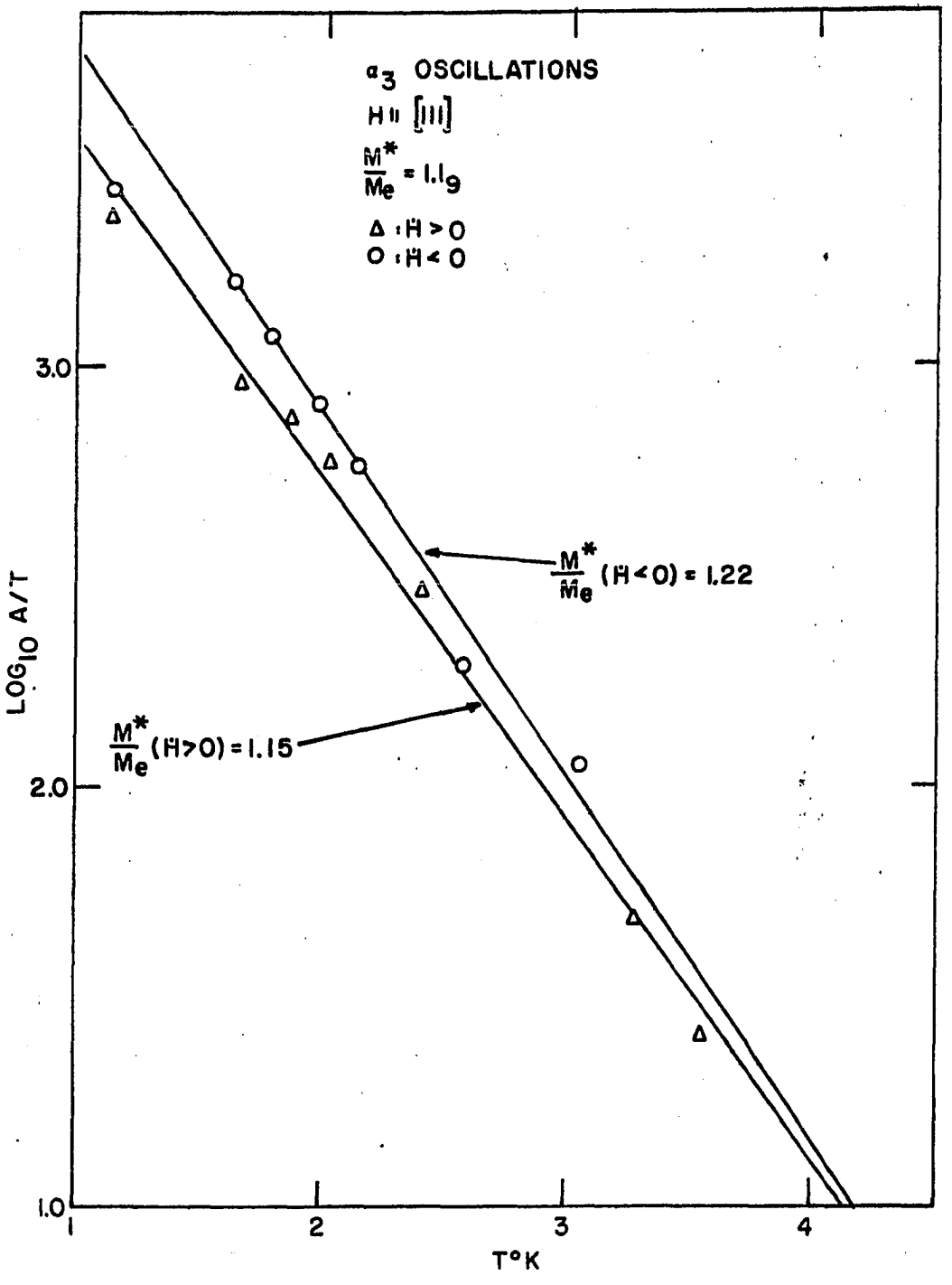

Figure 22. Temperature dependence of the amplitude of the α_3 oscillations for H// [111]

(Figure 15). However, as we shall discuss in Appendix C, the discrepancy may actually be due to systematic errors which can arise in the mass measurements when the signal amplitude is large enough so that the frequency modulation effect is important. Thus we believe that the α_2 and α_3 oscillations are in fact harmonics of the α oscillations, but that the determinations of the effective masses for these terms are in error.

IV. THE FERMI SURFACE

A. Theoretical Models for the Fermi Surface of Tungsten

1. The Lomer model

Some of the general features of the Fermi surface of tungsten were first sketched by Lomer (1962, 1964) in papers in which he modified the band structure found by Wood (1962) for b.c.c. iron so that it applied to the chromium group of transition metals (chromium, molybdenum, and tungsten). The model which he proposed has proved to be qualitatively correct so we will begin by discussing it briefly.

In Figure 23 we show a pictorial representation of the Lomer model. In this figure the various pieces of Fermi surface are approximated by octahedra and ellipsoids, and the pieces are properly positioned in the Brillouin zone. There is an electron surface at the center of the zone (the point labeled Γ) which can be roughly described as having an octahedrally-shaped body with ball-like protrusions at each corner of the octahedron. This surface has been named (Sparlin and Marcus 1964) the electron jack because of the similarity in shape to a child's jack. There is also an octahedrally-shaped hole surface centered at the corner H of the Brillouin zone. We will call this surface the hole octahedron. The other surfaces are a set of small elipsoidally-shaped hole surfaces centered about the points

Figure 23. Pictorial representation of the Lomer model for the Fermi surface of the chromium group of metals (This figure was kindly provided by Dr. W.M. Lomer, Solid State Physics Division, H.7, Atomic Energy Research Establishment, Harwell, Didcot, Berkshire, England.)

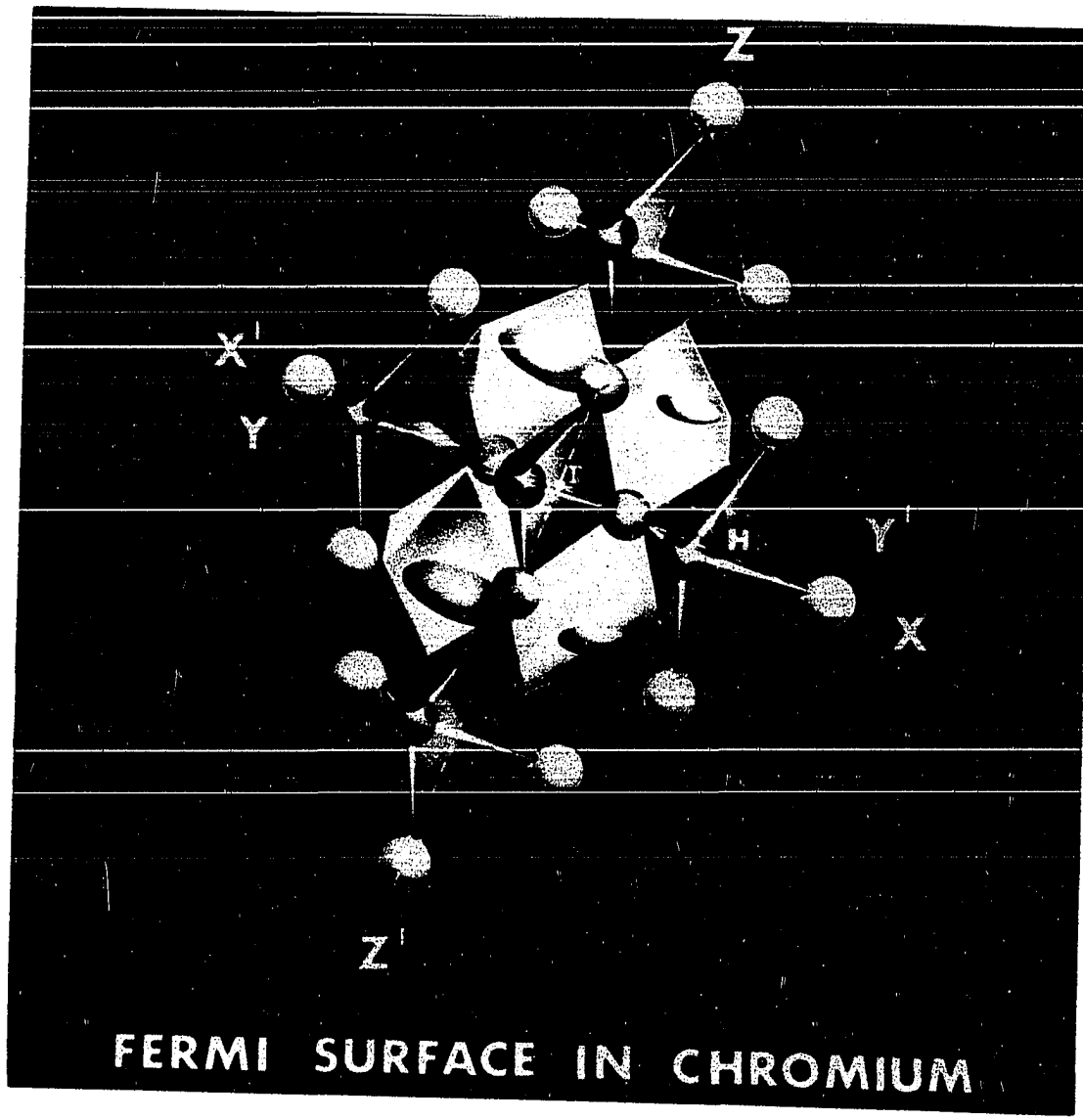

FERMI SURFACE IN CHROMIUM

N (the centers of the zone faces) and a set of small lens-shaped electron surfaces centered on the ⟨100⟩ axes. These lenses are not shown on the photograph, but they are illustrated in Figure 24 which is a central (100) section through the Lomer model. The lenses can be removed when spin-orbit coupling is taken into account.

2. Loucks' model

The results of later band calculations by Loucks (1965a, 1965b), Mattheiss (1964), and Mattheiss and Watson (1964) predicted that the shapes of the large pieces of the Fermi surface of tungsten did in fact consist of an electron surface which was shaped like a jack and a hole surface which had an octahedral shape. We will discuss the results of Loucks' two calculations since he has constructed geometrical models for the Fermi surface from them.

Loucks' first calculation (Loucks 1965b) was based on the APW method and did not take into account the effects of spin-orbit coupling. Some cross sections of the model which he found are shown in Figure 25a. These sections through the Fermi surface are the sections made by the tetrahedron HNP which is shown in Figure 25c. This non-relativistic model is qualitatively similar to the Lomer model.

In Loucks' second calculation (Loucks 1965a, also based on the APW method) relativistic effects were included.

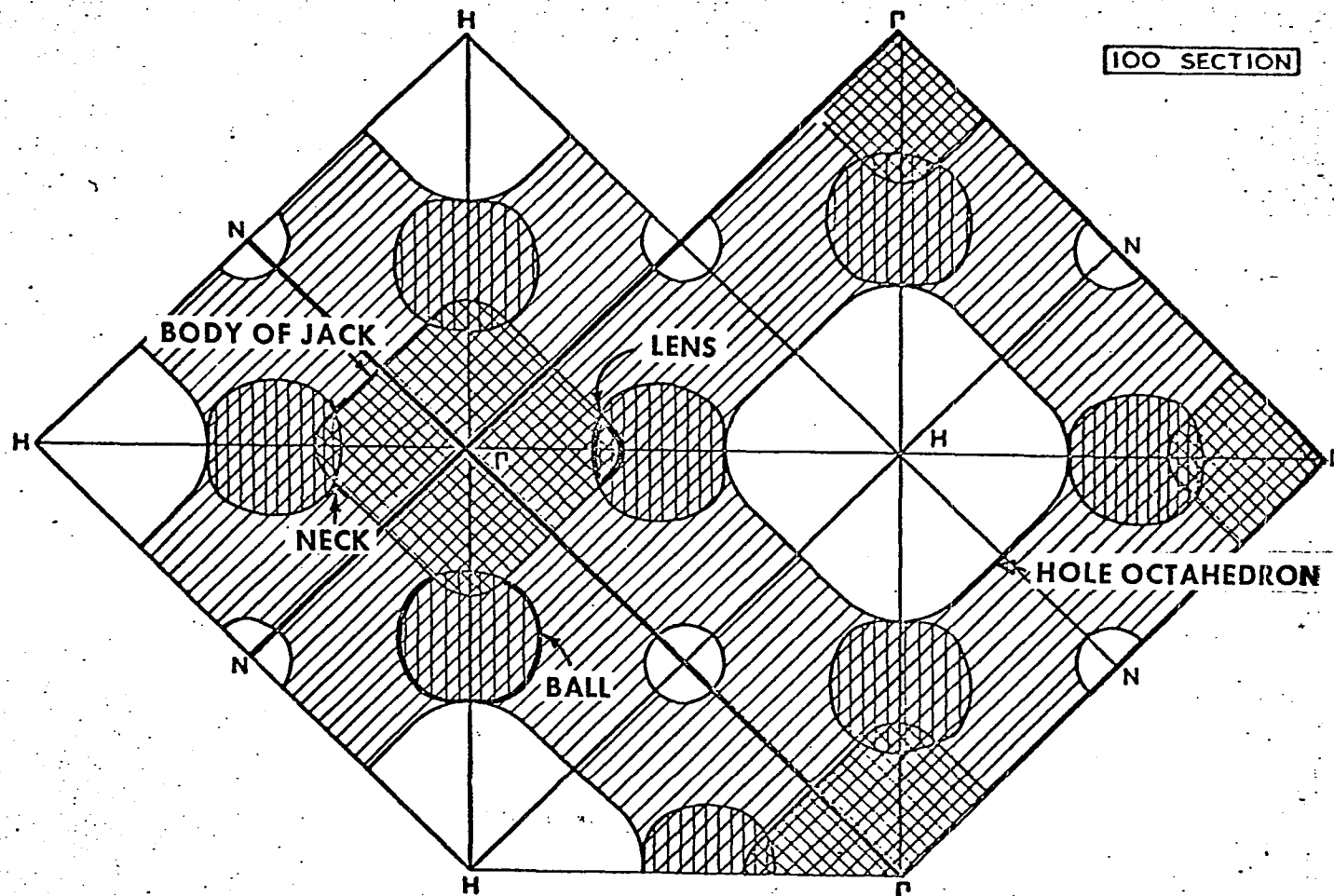

Figure 24. Central (100) section through the Lomer model (after Lomer 1964); the cross section of the fundamental zone is the square with corners H.

Figure 25. Some cross sections of Loucks' models for the Fermi surface of tungsten: a. Nonrelativistic model; b. Relativistic model; c. Brillouin zone for the body centered cubic structure showing the tetrahedron HNP which has been unfolded in a and b

(a)

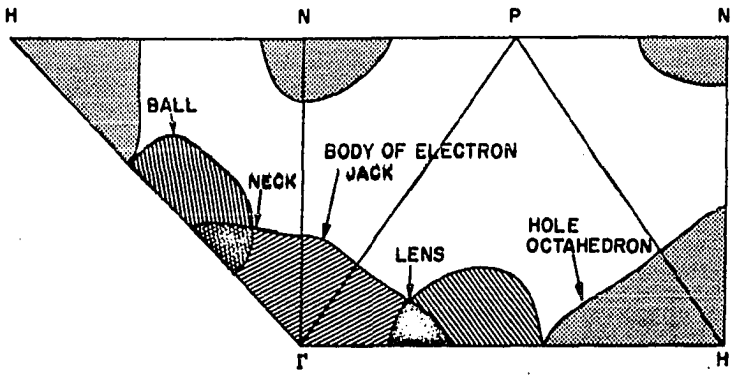
H
N
P
N
BALL
NECK
BODY OF ELECTRON JACK
LENS
HOLE OCTAHEDRON
Γ
H

(b)

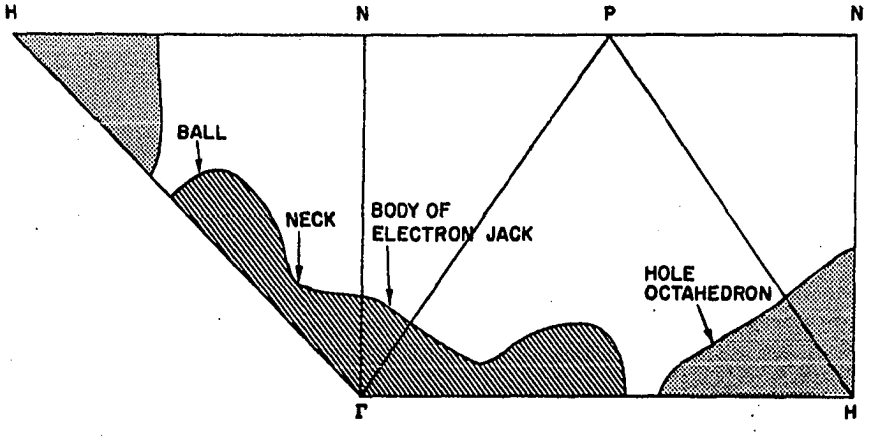
H
N
P
N
BALL
NECK
BODY OF ELECTRON JACK
HOLE OCTAHEDRON
Γ
H

(c)

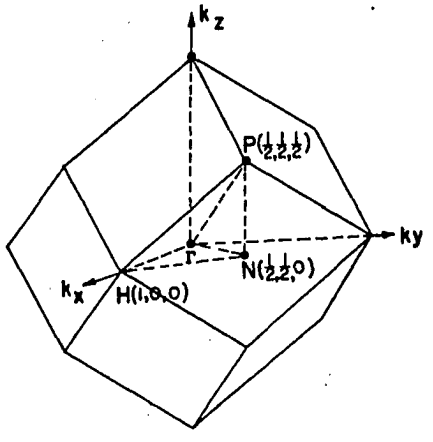
k z
P(1,1,1)
2,2,2
ky
Γ
N(1,1,0)
2,2,0
kx
H(1,0,0)

Both the lenses and the hole ellipses were found to disappear, and the neck region of the electron jack was smoothed out (Figure 25b). Furthermore, when the spin-orbit contribution to the relativistic terms is taken into account, the electron jack and hole octahedron surfaces are no longer required to touch along ⟨100⟩ axes, and in fact, Loucks found that there was a small separation between them. A similar prediction was made by Mattheiss and Watson (1964).

None of the theoretical models which we have outlined predicts all of the experimentally-determined features of the Fermi surface of tungsten correctly. However, we shall see that a combination of features from the different models seems to be in agreement with experiment.

B. Comparison of Some Previous Experimental Results with the Theoretical Models

1. Magnetoresistance and anomalous skin effect

Some of the earliest experimental results pertaining to the Fermi surface of tungsten were obtained from measurements of the transverse magnetoresistance of very pure single crystals of tungsten at low temperatures (Fawcett 1962). These measurements indicated that the Fermi surface of tungsten cannot support any open orbits and that tungsten is a compensated metal, that is, the volume enclosed by hole surfaces is equal to the volume enclosed by electron surfaces.

Each of these conclusions is in agreement with the predictions of a surface like the Loucks relativistic surface in which all portions of the Fermi surface are closed; the compensation requirement is automatically satisfied since Loucks found the Fermi level by requiring the electron and hole volumes to be equal.

The agreement of any of these models with the experimental results for the total surface area of the Fermi surface is not as satisfying. Measurements of the surface resistance of a polycrystalline specimen of tungsten under conditions in which the skin depth for a microwave electric field was much less than the electron mean free path (Fawcett and Griffiths 1962) yielded a total surface area which was less than the total surface area estimated by Loucks by about a factor of four. However, due to the relatively low accuracy ($\sim$30 percent) of the anomalous skin effect experiment and to the considerable departure of the Fermi surface of tungsten from a spherical shape, the anomalous skin effect may not give a reliable value for the surface area (Pippard 1960).

2. Gantmakher size effect and magnetoacoustic effect

The results of Gantmakher size effect measurements (see Section I-B) which were carried out in a $\{110\}$ plane by Walsh and Grimes (1964) are shown in Figure 26. The calipered dimensions yield shapes for $\{110\}$ projections of

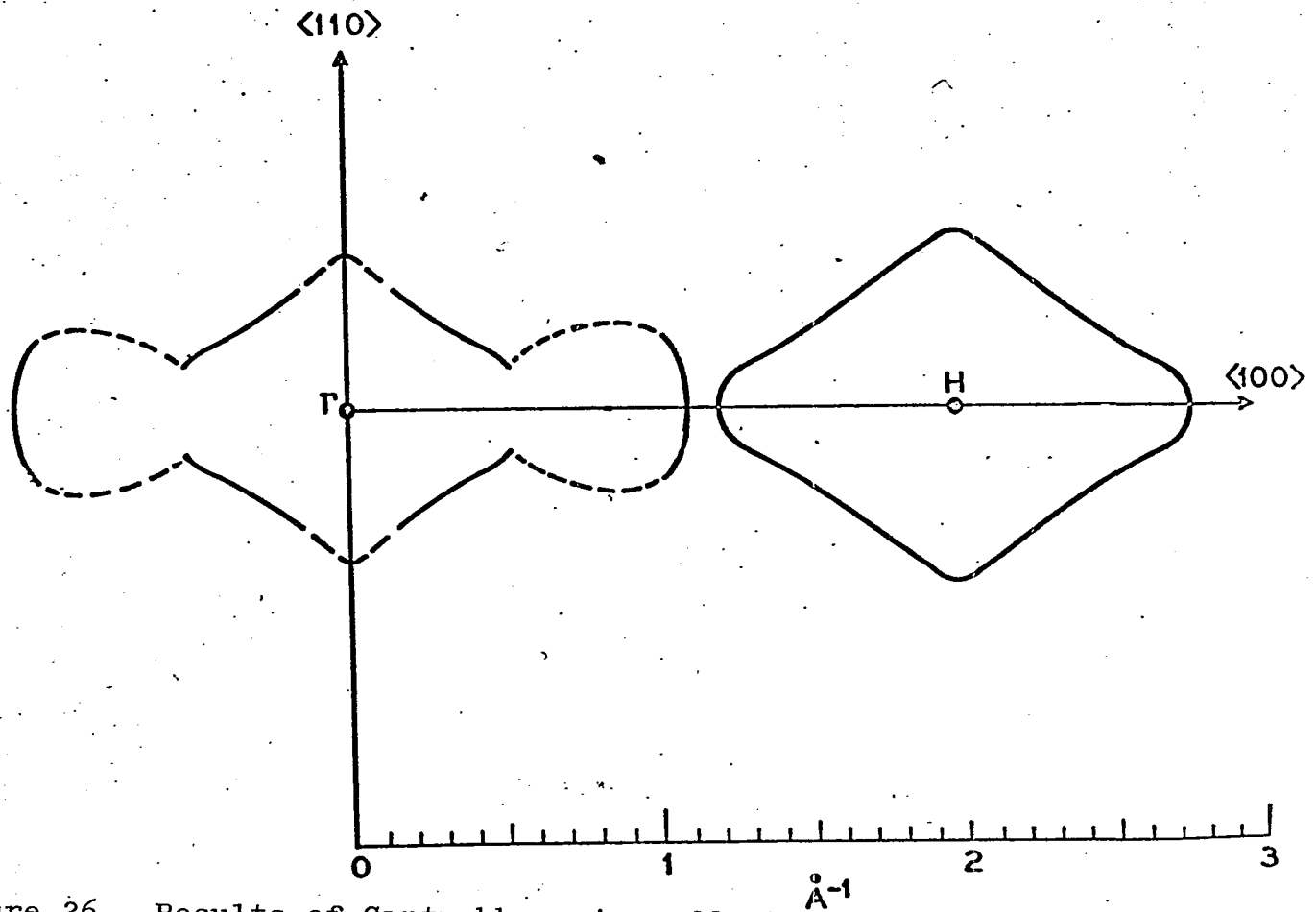

Figure 26. Results of Gantmakher size effect measurements in tungsten; ——— experimental k-vectors, ---- extensions implied by the model for the Fermi surface (after Walsh and Grimes 1964)

the electron jack and hole octahedron which are qualitatively quite similar in shape to those of the Loucks relativistic model (Figure 25b). Furthermore, they show that the electron jack and hole octahedron do not touch along ⟨100⟩ axes, which is in further agreement with the relativistic model. These authors state that in addition to the signals which were used to derive the cross sections shown in Figure 26, they also observed a number of other signals corresponding to smaller dimensions, but did not interpret them. Therefore, the absence of cross sections for small pieces of Fermi surface on Figure 26 should not be construed as meaning that none exist.

Extremal calipered dimensions of the Fermi surface can also be measured by observing oscillatory attenuation in sound waves traveling in a single crystal (magnetoacoustic effect). These measurements are carried out at low temperatures and in a magnetic field under conditions in which the electron mean free path is much longer than the sound wavelength. The oscillatory attenuation is approximately periodic in $1/H$, and for sound waves of wavelength λ which are propagating in a direction $\underline{q}$, an extremal orbit dimension Δk_{ext} in the direction $\underline{q} \times \underline{H}$ is determined from a period $\Delta(1/H)$ in the attenuation by the relation

$$\Delta k_{ext} = \frac{e}{\hbar c}\left[\lambda/\Delta(1/H)\right]$$

Rayne (1964) has carried out such measurements in tungsten and his results for extremal radii are shown in Figure 27. These results, although they show wave vectors which correspond with some of the dimensions on the theoretical models, do not seem to be in as clear cut overall agreement with the general features of the theoretical models as the size effect results are.

As a first step in setting up an analytical model for the Fermi surface, we have made considerable use of the calipered dimensions from the size effect. It is perhaps worthwhile to emphasize at this point why we prefer the size effect data to the magnetoacoustic effect data. The basic reason is that the resonances in the size effect can be translated into dimensions fairly unambiguously, whereas dimensions can be obtained from the magnetoacoustic effect only after a detailed frequency analysis. This analysis is difficult to perform in practice because of the limited number of oscillations which are usually observed.

In Figures 28a and 28b we show representative magnetoacoustic data which were published by Rayne (1964). Since only a few oscillations are observed, only limited resolution can be expected. Furthermore, the structure of these signals is expected to be quite complicated. Mackintosh (1960) has shown that even for the comparatively simple case of two spherical surfaces, the waveform of the oscillations is given by a Bessel function of double argument and that even the

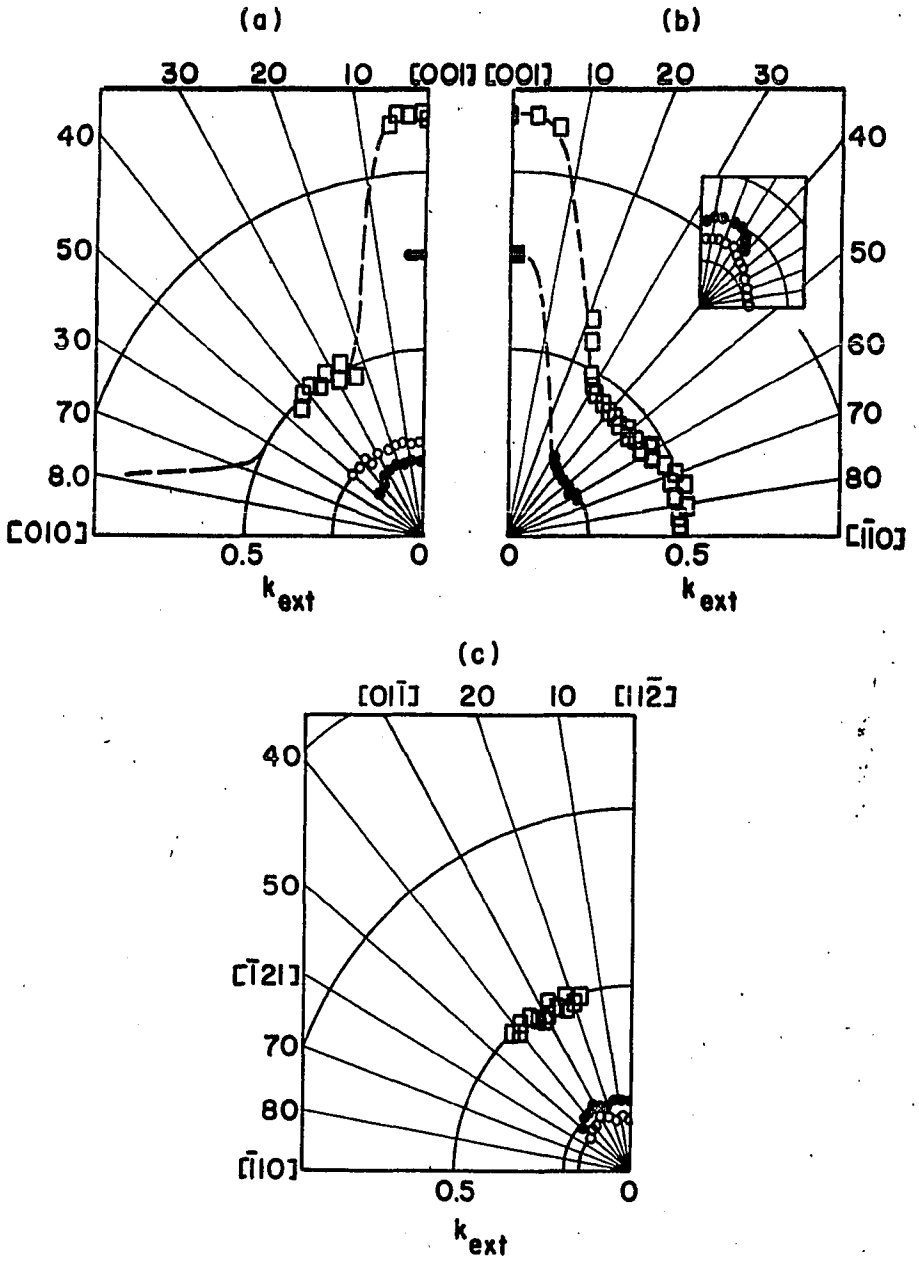

Figure 27. Angular dependence of extremal wave vectors for tungsten obtained from the magnetoacoustic effect: (a) (100) plane, (b) (110) plane, (c) (111) plane, (after Rayne 1964)

Figure 28. Examples of data related to extremal dimensions of the Fermi surface of tungsten

a. Recorder plot of a voltage proportional to the 390 MHz sound wave amplitude transmitted through a (111) plane tungsten sample versus 300/H
Temperature: 4.2°K
H// $[2\bar{1}\bar{1}]$
(after Rayne 1963)

b. Same as (a) except a (100) plane sample was used and H// $[0\bar{1}0]$

c. Recorder plot of the field derivative of the 4 MHz signal amplitude transmitted through a thin $(\bar{1}10)$ plane tungsten sample versus the magnetic field
Temperature: 4.2°K
H// $[11\bar{2}]$
(after Walsh, Grimes, Adams, and Rupp 1965)
(According to Gantmakher (1962b) the peaks at $H_h + H_e$, $2H_h$, $2H_h + H_e$, $3H_h$ arise from creation of current sheets within the bulk of the sample and consequent excitation of other orbits, the sum of the extremal dimensions just spanning the sample thickness.)

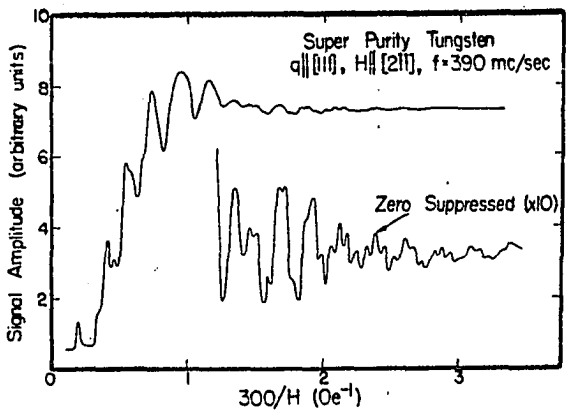
Super Purity Tungsten
q‖[1Ī], H‖[21̄], f=390 mc/sec
Zero Suppressed (x10)
Signal Amplitude (arbitrary units)
300/H (Oe⁻¹)

(a)

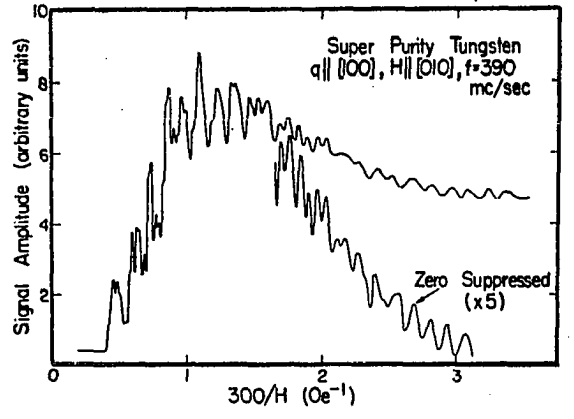
Super Purity Tungsten
q‖[100], H‖[010], f=390 mc/sec
Zero Suppressed (x5)
Signal Amplitude (arbitrary units)
300/H (Oe⁻¹)

(b)

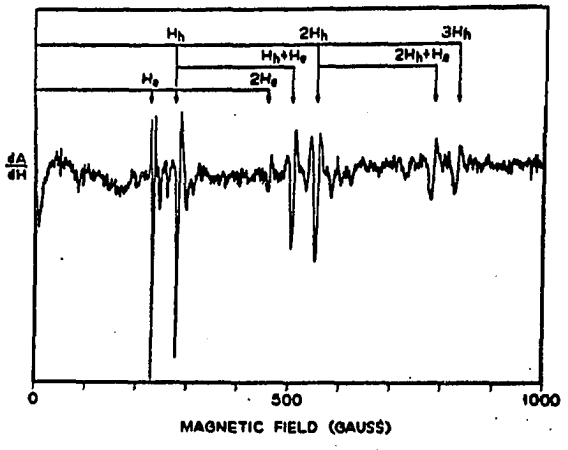
Hh
2Hh
3Hh
Hh+He
2Hh+He
He
2He
dΔ/dH
0
500
1000
MAGNETIC FIELD (GAUSS)

(c)

asymptotic form of this Bessel function is not simply the sum of two periodic terms. Thus it is felt that the interpretation of magnetoacoustic data is not as straightforward as that for the size effect data.

Representative size effect data which were published by Walsh, Grimes, Adams, and Rupp (1965) are shown in Figure 28c. These investigators obtain values for extremal calipered dimensions from the positions of the peaks using the formula

$$\Delta k_{ext} = \frac{et}{\hbar c} H_{peak}$$

where t is the sample thickness. As Koch and Wagner (1966)[1] have pointed out, the accuracy of this experiment is limited mainly by the uncertainty as to which feature of the observed peak in the signal corresponds to the orbit dimension just spanning the sample thickness. Since the peaks are very sharp, it would be expected that errors in the dimensions would not exceed ~ 5 percent. We shall later show that the model Fermi surface introduced in Section IV-C is not inconsistent with Rayne's magnetoacoustic data when one bears in mind the limited resolution in the magnetoacoustic experiment.

3. de Haas-van Alphen effect

Early measurements of the dHvA effect in tungsten (Sparlin and Marcus 1963, 1964; Girvan 1964) were consistent

---

[1] I am indebted to Dr. J.L. Stanford, Physics Department, Iowa State University, for bringing this study to my attention.

with the predictions of the theoretical models (Section IV-A) as far as the large pieces of the Fermi surface of tungsten were concerned. The impulsive-field results (Girvan 1964) showed that the orientation dependence of the frequency of the α oscillations was much like that expected for the central cross section of a regular octahedron (Figure 29). Furthermore, Walsh (1964), using circularly-polarized microwaves, was able to demonstrate that a [111] orbit with a cyclotron mass of $m^* = 0.83m_e$ was an orbit on an electron surface rather than a hole surface. He assigned this orbit to the central section of the electron jack. It was consistent to assign the β oscillations (Figure 29) to the same central section of the electron jack (Girvan 1964) since the frequency of these oscillations varies somewhat more rapidly than would be expected for the central cross sectional area of an octahedron and the mass value at [111] is not inconsistent with that found by Walsh (1964).

The orientation dependence of the δ and η oscillations (Figure 9) is also consistent with the theoretical models (Section IV-A) if the δ oscillations are interpreted as arising from the balls on the electron jack and the η oscillations are interpreted as arising from the necks. This interpretation was first suggested by Sparlin and Marcus (1964), and we will see in more detail in Section IV-C why this assignment comes about.

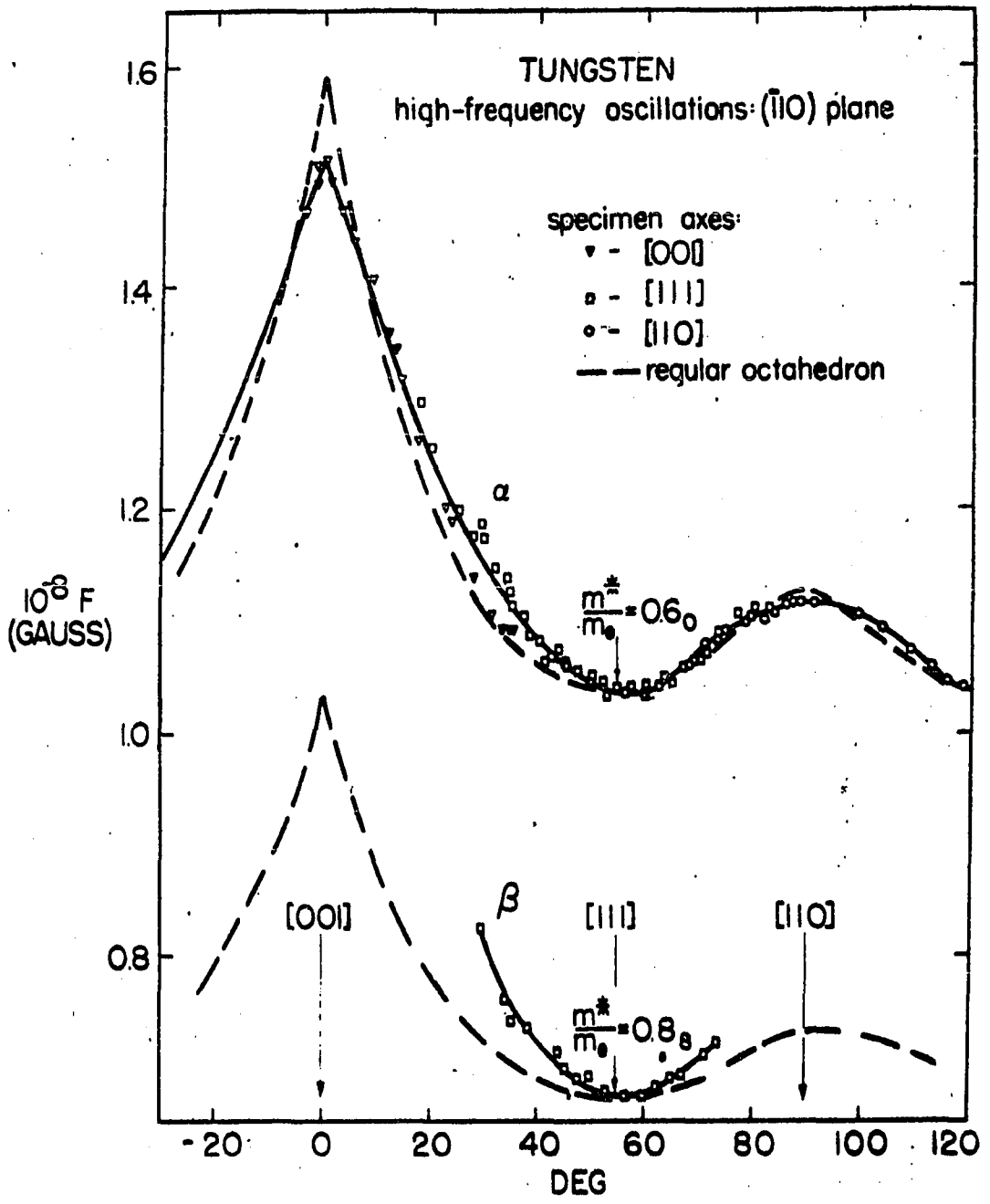

Figure 29. Orientation dependence of the frequencies of the α and β oscillations in the $(\bar{1}10)$ plane

The interpretation of the data for the remaining small pieces of the Fermi surface in terms of the theoretical models was not so straightforward. Some of the earliest low-frequency dHvA data related to very small portions of the Fermi surface were obtained by Brandt and Rayne (1963) using the torque method. Their results for the orientation dependence of these slow frequencies in the $(\bar{1}10)$ plane are shown in Figure 30. The term which varies with angle like a parabola near $[00\bar{1}]$ in this figure is the term which we have called the η oscillations on Figures 9 and 11; as we stated previously, this term is thought to give the orientation dependence of the cross sectional area of the extremal neck orbit on the electron jack. The orientation dependence given by the curves through the other frequency terms on Figure 30 is inconsistent with the theoretical models discussed in Section IV-A; this general orientation dependence is appropriate to two different sets of small surfaces on the $\langle 100 \rangle$ axes rather than one set as one might perhaps expect if the lenses indicated in Figures 24 and 25a were actually present. Brandt and Rayne (1963) have argued that the splitting of frequencies might be due to removal of the spin degeneracy of the energy levels by spin-orbit coupling. However, this argument violates the theoretical conclusion that in the absence of a magnetic field there must always be at least a double degeneracy at all points in the

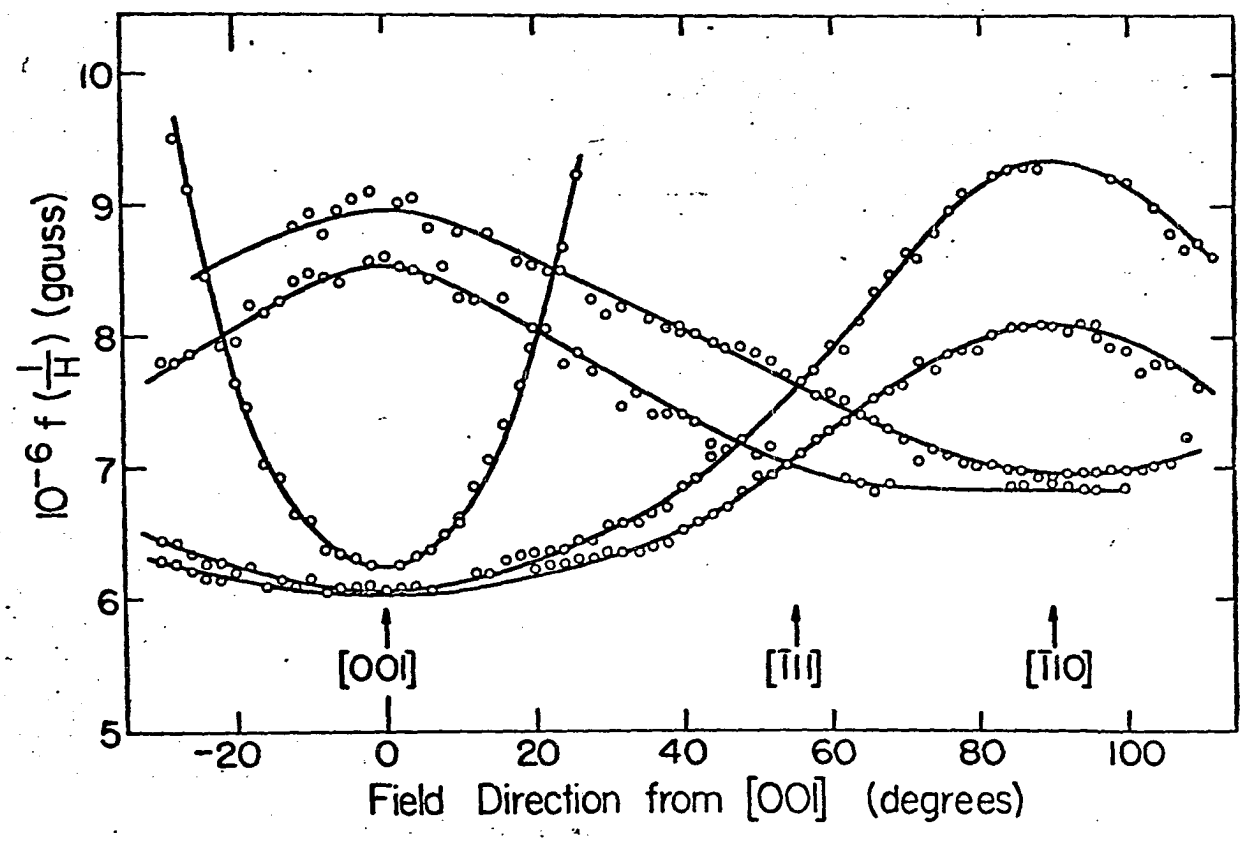

Figure 30. Torque method results for the orientation dependence of the low frequency dHvA components in tungsten in the $(\bar{1}10)$ plane (after Brandt and Rayne 1963)

Brillouin zone for any crystal in which the potential has a center of inversion (cf. Elliot 1954, Callaway 1964, p. 53).

It was noticed by Sparlin and Marcus (1964) that the data of Brandt and Rayne (1963) (excluding the parabola-like curve) differ only slightly from that which would be expected from a set of small ellipsoidally-shaped surfaces centered in the zone faces. The existence of such ellipsoids was in fact suggested by Lomer (see Figure 24); according to his model they would be hole ellipsoids.

In Figure 31a we have indicated one such ellipsoid and its relation to the diamond-shaped face of the Brillouin zone. The orientation dependence of the frequencies arising from such a set of ellipsoids in a $(\bar{1}10)$ plane is shown in Figure 31b; we have made a specific choice for the lengths of the three axes. It is seen that the only differences between the orientation dependence found by Brandt and Rayne (Figure 30) and that shown in Figure 31b is that in the latter figure, the upper two branches cross at $[001]$ and $[110]$ whereas the curves drawn by Brandt and Rayne in Figure 30 do not cross at these orientations.

There is thus a disagreement between Sparlin and Marcus (1964, 1966) and Brandt and Rayne (1963) in the interpretation of low-field de Haas-van Alphen data. In the following section we shall present evidence which makes it clear that the ellipsoidal hypothesis is the correct one.

Figure 31. Illustrating the expected orientation dependence of dHvA frequencies due to small ellipsoids centered in the Brillouin zone faces

a. Cross section through an ellipsoid centered on a point N in the face of the Brillouin zone; the semiaxes of the ellipsoids are $a = 6.415 \times 10^{-2}(2\pi/a)$ along ΓN, $b = 9.966 \times 10^{-2}(2\pi/a)$ along NP, $c = 7.265 \times 10^{-2}(2\pi/a)$ along NH. These are the dimensions used in our final model of the Fermi surface. (The de Haas-van Alphen effect can not distinguish between the cross section which is drawn with a solid line and the alternate (dashed) cross section which results when the ellipsoid is rotated 90° about the line NP.)

b. Expected orientation dependence of dHvA frequencies in the $(\bar{1}10)$ plane due to the ellipsoids

c. Expected orientation dependence in the plane which is shown dashed in the stereogram

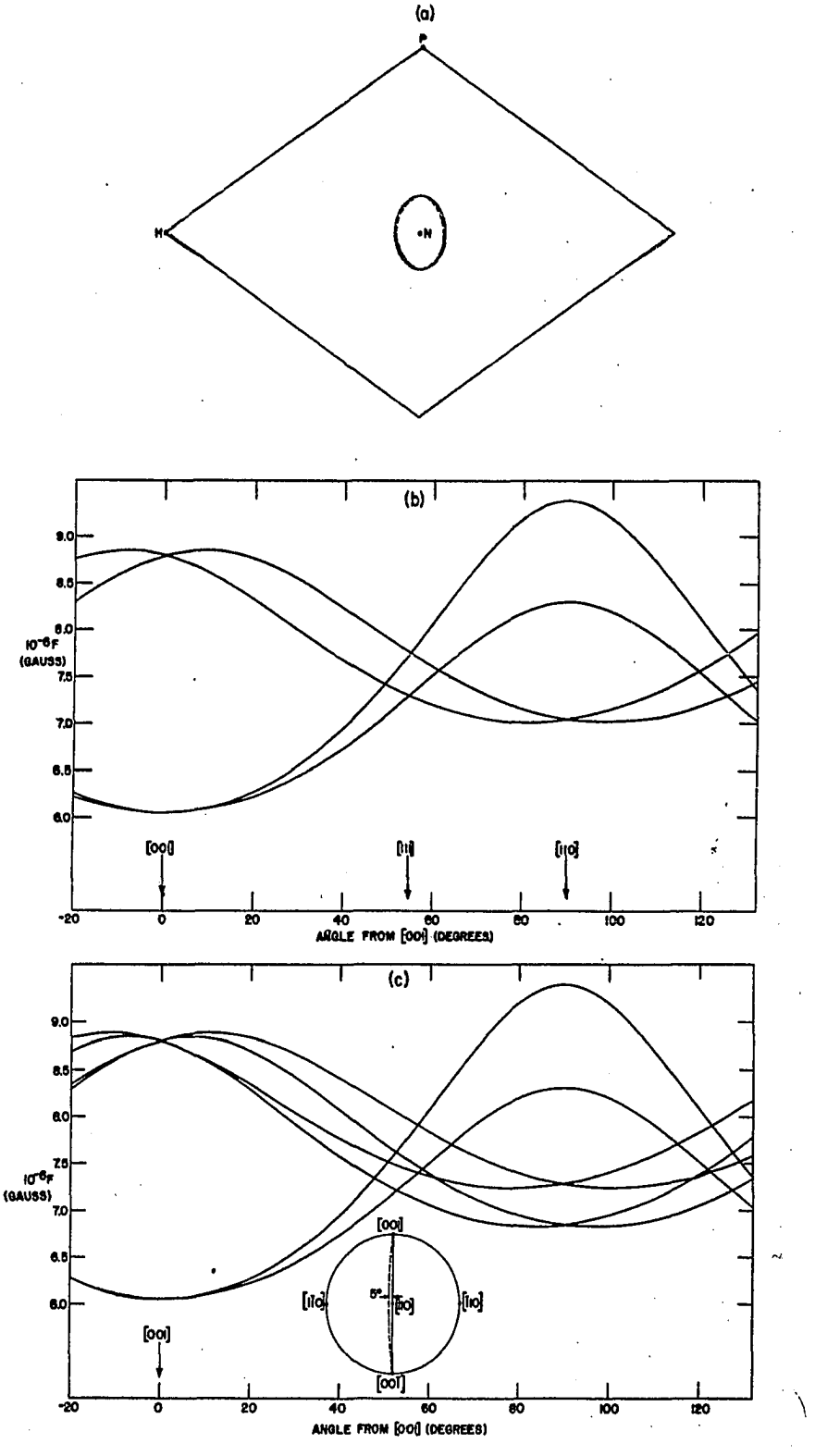
(a)
P
N
•N
(b)
9.0
8.5
8.0
10^{-6}F
(GAUSS)
7.5
7.0
6.5
6.0
[001]
[111]
[110]
-20
0
20
40
60
80
100
120
ANGLE FROM [001] (DEGREES)
(c)
9.0
8.5
8.0
7.5
10^{-6}F
(GAUSS)
7.0
6.5
6.0
[001]
[001]
[1$\bar{1}$0]
5°
[$\bar{1}$10]
[110]
[00$\bar{1}$]
-20
0
20
40
60
80
100
120
ANGLE FROM [001] (DEGREES)

C. Interpretation of the Small Pieces of the Fermi Surface from Impulsive-field dHvA Results

In view of the fact that Brandt and Rayne's (1963) results for the orientation dependence of the low frequency oscillations could not be fitted readily into a theoretical model for the Fermi surface of tungsten, it was felt to be important to check the orientation dependence of these slow frequencies near [001] using the impulsive field method. There are two features of the impulsive field method which would lead one to believe that such a check would be worthwhile. The first of these is that in the impulsive-field method, the amplitude of the pickup signal due to an oscillatory term F_i does not vanish when the slope $\partial F_i/\partial\Theta$ of the frequency versus rotation angle curve is zero, whereas in the torque method it does. Secondly, we were able to use considerable filtering during the actual experiment to partially separate neighboring frequencies. This filtering greatly simplified the task of extracting the component frequencies from the data.

In Figures 32 and 33 we show some examples of the original torque recordings which were obtained by Brandt and Rayne[1] for these slow frequencies when the magnetic field was near the [001] orientation; we have contrasted the torque

---

[1] Rayne, J.A., Carnegie Institute of Technology, Pittsburgh, Pennsylvania. We are indebted to Dr. Rayne for giving us the opportunity to examine the original data. Private communication (1965).

Figure 32. Examples of dHvA data for the slow frequencies in tungsten with the magnetic field direction set very close to the [001] orientation

Photograph on the left: Reproduction of original impulsive-field dHvA data for the ϵ_u oscillations, ϵ_u oscillations dominant
Bottom calibration line at 20.995kG; succeeding calibration lines at intervals of 1.235kG

Photograph on the right: Reproduction of original impulsive-field dHvA data for the η and ϵ_L oscillations, η oscillations dominant
Bottom calibration line at 13.585kG; succeeding calibration lines at intervals of 1.235kG

Recorder tracing: Reproduction of original torque data for terms in the frequency range of the ϵ_L, η, and ϵ_u oscillations

Field range: 13.9-16.1kG
(after Brandt and Rayne -- see footnote on page 103)

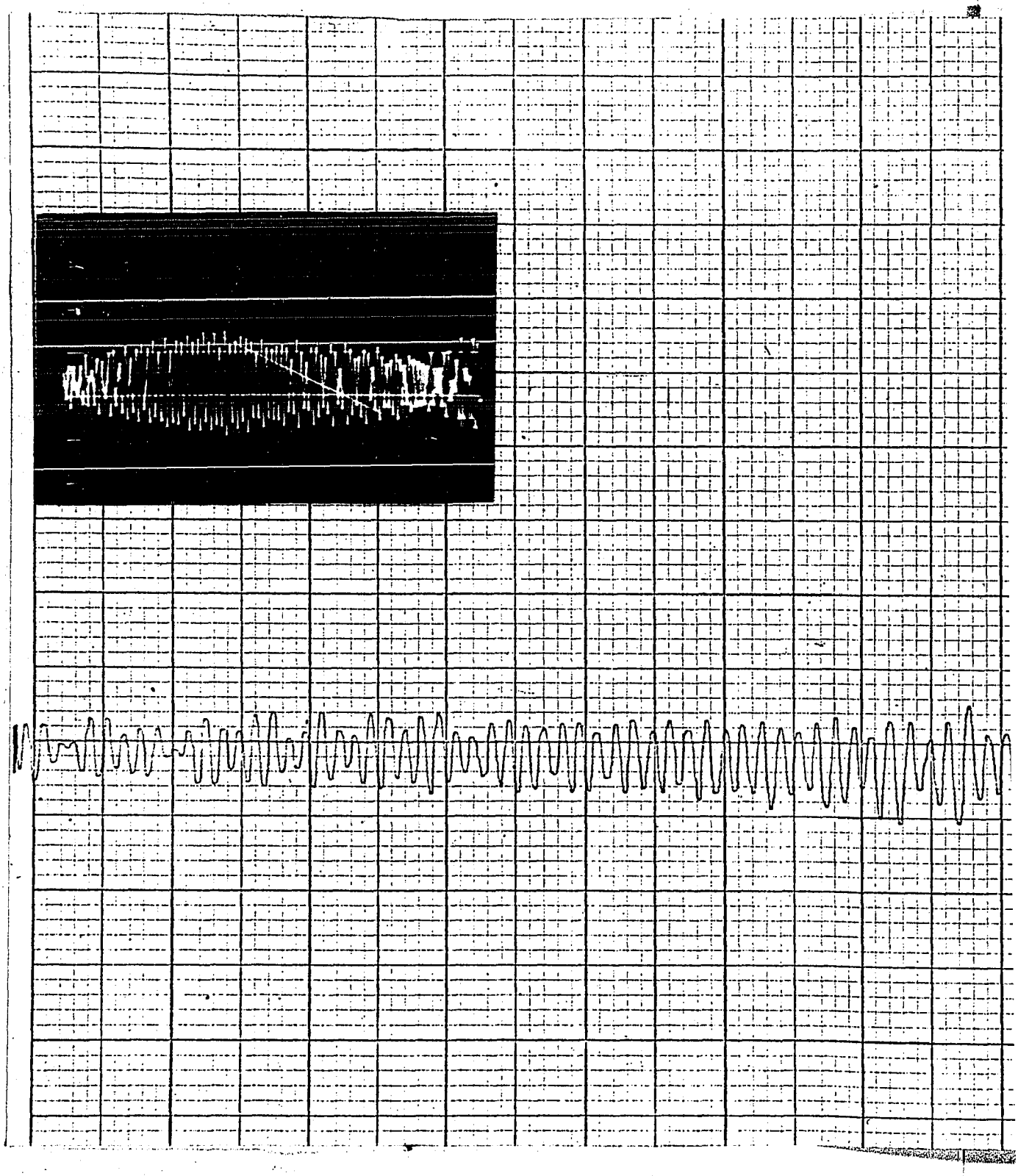

05:07 3-4-63 0 4/3 Z

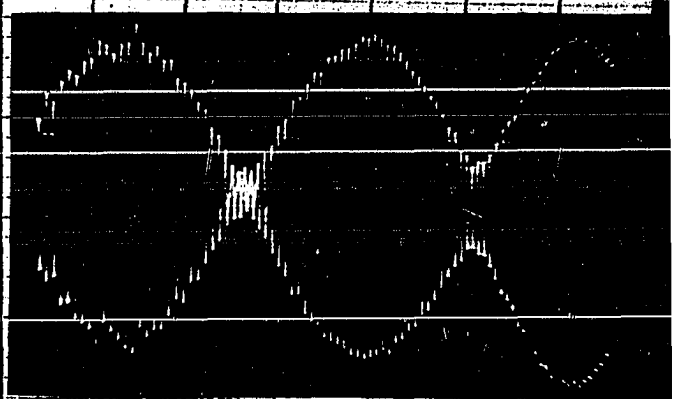

Figure 33. Examples of dHvA data for the slow frequencies in tungsten with the magnetic field orientation about 2° from [001] in the $(\bar{1}10)$ plane

Photograph on the left: Reproduction of original impulsive-field dHvA data for the ϵ_u oscillations, ϵ_u oscillations dominant
Bottom calibration line at 20.995kG; succeeding calibration lines at intervals of 1.235kG

Photograph on the right: Reproduction of original impulsive-field dHvA data for the η and ϵ_L oscillations, η oscillations dominant
Bottom calibration line at 13.585kG; succeeding calibration lines at intervals of 1.235kG

Recorder tracing: Reproduction of original torque data for terms in the frequency range of the ϵ_L, η, and ϵ_u oscillations

Field range: 13.9-16.1kG
(after Brandt and Rayne -- see footnote on page 103)

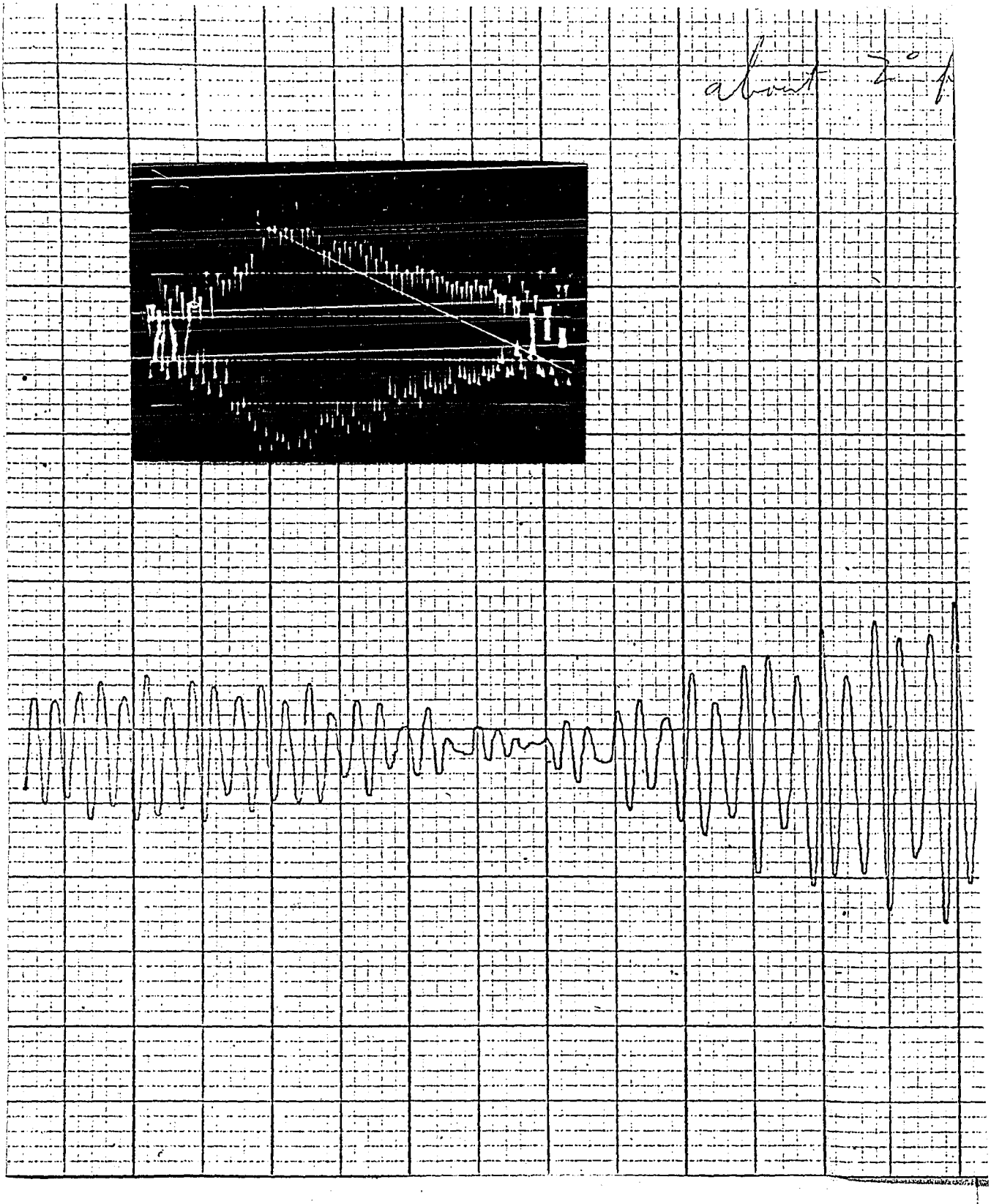
about 20 f

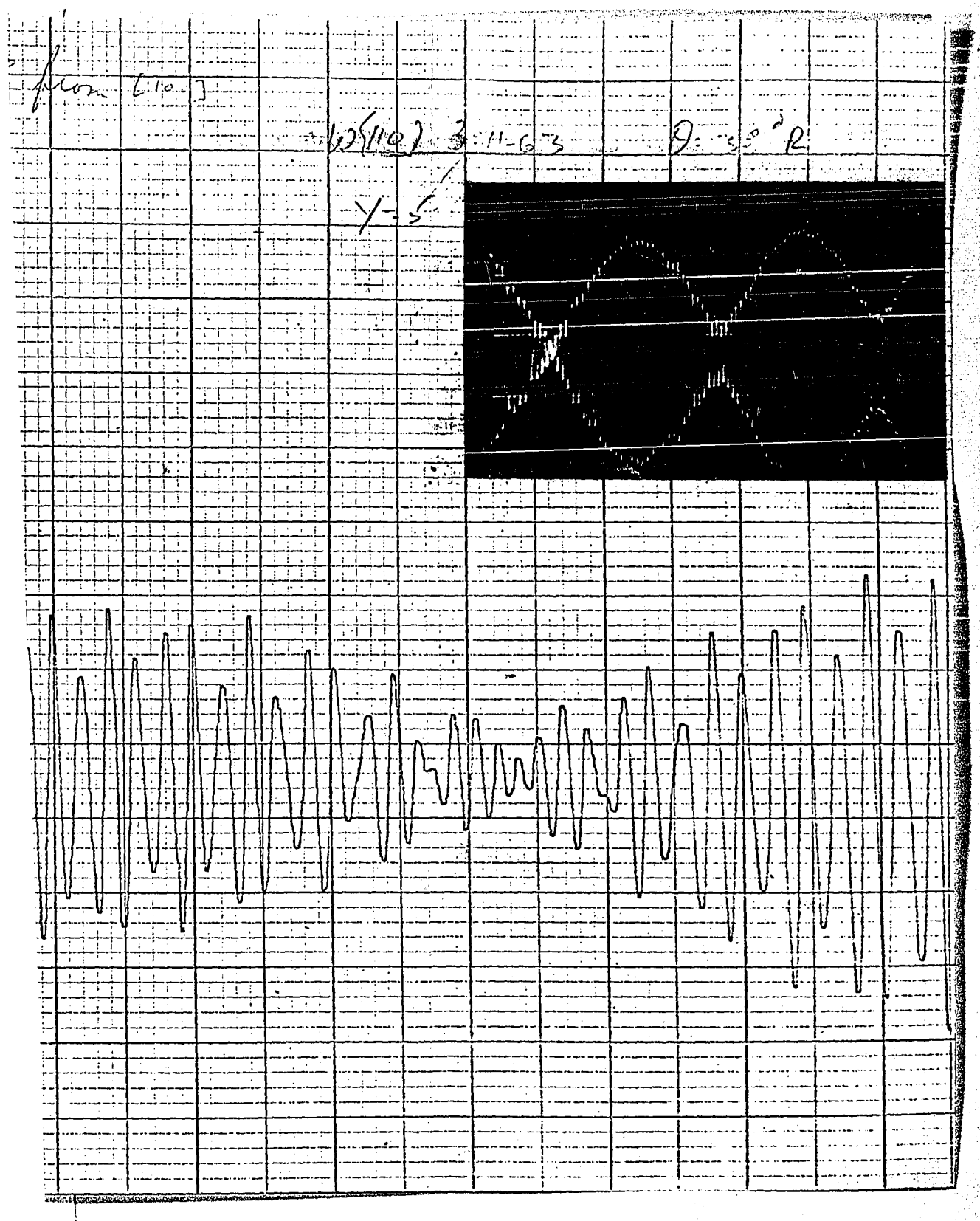
from [110]
Y-5

data with impulsive-field data which were taken near the [00$\bar{1}$] orientation using the shunt ignitron (inset photographs). Each torque recording is the sum of signals from the two terms ϵ_L, the η term, and the two terms ϵ_u[1]. In the impulsive field data, extensive filtering has been used to simplify the otherwise complicated signal which would result from the combination of all these frequency terms. To study the ϵ_u oscillations the filters were set so that these oscillations were dominant over most of the field range of an oscillogram (photographs on the left side of Figures 32 and 33). With a different filter setting the η oscillations (beating with the ϵ_L oscillations)dominated over the field range of one oscillogram (photographs on the right side of Figures 32 and 33). Thus, the analysis of the impulsive-field data would seem to be simpler than that of the torque data because the signals from all these frequency terms are combined in the torque data but are split up into two oscillograms in the impulsive-field data.

The impulsive-field results have already been shown in Figure 11, and we show them again in Figure 34. These data show an apparent crossing of the ϵ_u terms at [00$\bar{1}$] which is consistent with a model having small ellipsoids centered at

---

[1]Our results indicate that the two ϵ_u terms cross at [00$\bar{1}$] and we believe that the two ϵ_L terms coalesce at [00$\bar{1}$] so that at this particular angle only three frequency terms should be present. (See Figure 34).

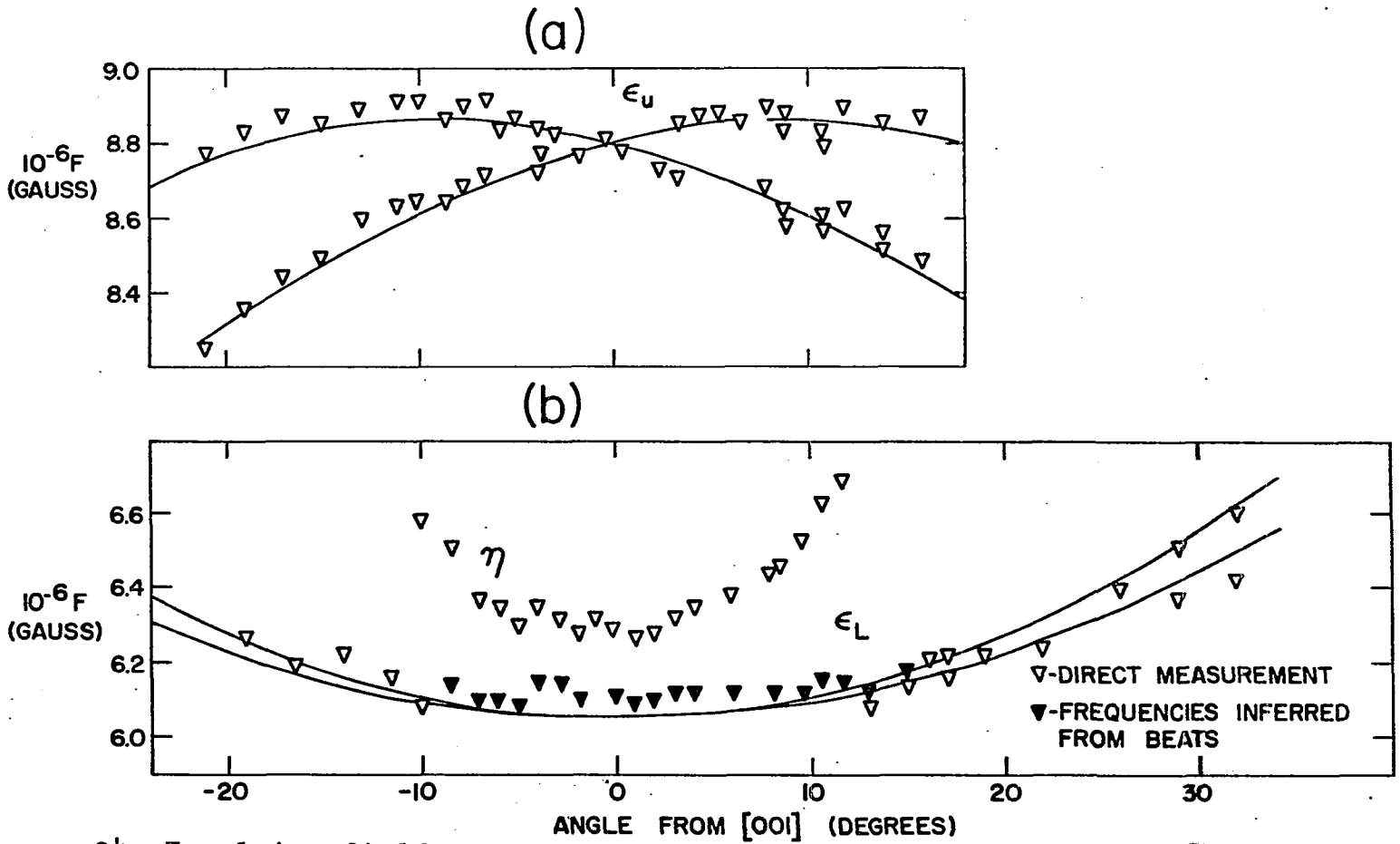

Figure 34. Impulsive-field results for the slow frequencies near $[00\bar{1}]$ in the $(\bar{1}10)$ plane. The solid curves give the orientation dependence expected from small ellipsoidal surfaces centered at points N. The dimensions of these ellipsoids are the same as those in Figure 31. (The data from which these results were derived were taken using the shunt ignitron.)

the points N. In fact, the solid curves on Figure 34 give the orientation dependence which would be expected from an appropriate set of ellipsoids centered on the points N in the Brillouin zone faces. The dimensions of the relevant ellipsoids were found by fitting to the observed frequencies at selected angles (shown in Figure 35), and the semiaxes were found to be $6.415 \times 10^{-2}(2\pi/a)$ and $7.265 \times 10^{-2}(2\pi/a)$ along $\langle 110 \rangle$ directions and $9.966 \times 10^{-2}(2\pi/a)$ along $\langle 100 \rangle$ directions. (These are the same ellipsoids which were used to calculate the orientation dependence in Figure 31.)

There is clearly a discrepancy between our results for the ϵ_u oscillations near $[00\bar{1}]$ and the corresponding results obtained by Brandt and Rayne (Figure 30); according to our results, the two branches of these oscillations cross at $[00\bar{1}]$ (Figure 34) whereas the torque results of Brandt and Rayne show a separation of about 5 percent between these two branches (Figure 30). Such a separation should show up in our data as beats in the ϵ_u oscillations, each beat containing about 20 cycles. No such beats are evident in the left hand insets in Figures 32 and 33, even though beat patterns with more than 20 cycles per beat appeared in these oscillations at other orientations. (See Figure 10a for an example with about 34 cycles per beat for H 10° from 001 .) Because the impulsive field data (when the shunt ignitron was used) are simpler to analyze than the torque data, we believe that the impulsive-field results are likely

to be more reliable.

In their recent paper Sparlin and Marcus (1966) also report the splitting in the ϵ_u oscillations at $[00\bar{1}]$. Nevertheless, they interpret these slow frequency oscillations in terms of ellipsoids at N on the basis of a nonzero $\partial F/\partial \theta\big]_H$ which they observed for the lower branch of the slow frequency oscillations as the magnetic field angle in the $(\bar{1}10)$ plane was rotated past the $[1\bar{1}0]$ direction. From this fact they inferred that the lower branches of the ϵ oscillations crossed at $[1\bar{1}0]$ rather than touched as the curves of Brandt and Rayne (Figure 30) suggest. Sparlin and Marcus have labeled the second term which they found in the ϵ_u oscillations at $[00\bar{1}]$ an "extra term" (see last sentence of footnote number 6 in Sparlin and Marcus 1966) and have not attempted to explain its origin. The fact that both torque studies report two frequencies for the ϵ_u oscillations at $[00\bar{1}]$ would seem to cast doubt on our results for the orientation dependence of these terms. However, as we have seen, the torque data of Brandt and Rayne were more complicated than our impulsive-field data, and it seems likely that the torque data obtained by Sparlin and Marcus were also complex. Therefore, we will use our impulsive-field results.

After the improved data analysis procedures had been developed to analyze the shunt ignitron data for the upper

branch of the slow frequency oscillations near [001], these procedures were tried on some of the older data for the slow frequencies near [110]. These older data had been taken without the benefit of the shunt ignitron, and the signals were more complex (cf. Figure 12) and more difficult to analyze than those which were obtained using the shunt ignitron. Nevertheless, using the improved procedures, it was possible to analyze some of the old data reliably. A plot of the points which have been obtained for the slow frequency oscillations including the data for field directions near [110] is shown in Figure 35. (The scaling factor for frequencies between 6 and 7 x 10^6G near [001] had not been found when this plot was made up so that the points which are plotted for these frequencies are too low by about three percent.) The old low-frequency impulsive-field data for field directions near [111] are so complex that a really adequate frequency analysis has not been obtained for these data, and therefore no points are plotted for the low frequency oscillations near [111].

As was explained in Section III-A, the data for the lowest frequencies near [110] were also not always well-resolved, and only rough estimates of these frequencies could be obtained. The question then arises as to why there should have been any difficulty in resolving the single term which is predicted for the lowest frequency oscillations at [110]

Figure 35. Expanded plot of impulsive-field results for the orientation dependence of the slow frequency oscillations in the $(\bar{1}10)$ plane The solid curves give the orientation dependence expected from ellipsoids at N (see Figure 31). The dashed curve gives the orientation dependence expected from a hyperboloid of revolution with its axis along $[00\bar{1}]$. Open circles: frequencies obtained by direct analysis. Filled circles: frequencies obtained by counting the number of cycles in a beat envelope. ↑: points which were used to find the semiaxes of the ellipsoids. Only the points for the upper two branches near $[00\bar{1}]$ and the upper two branches near $[1\bar{1}0]$ represent the frequencies correctly; the lower points are subject to small systematic errors which have been corrected in Figure 34 (see pages 112 and 60)

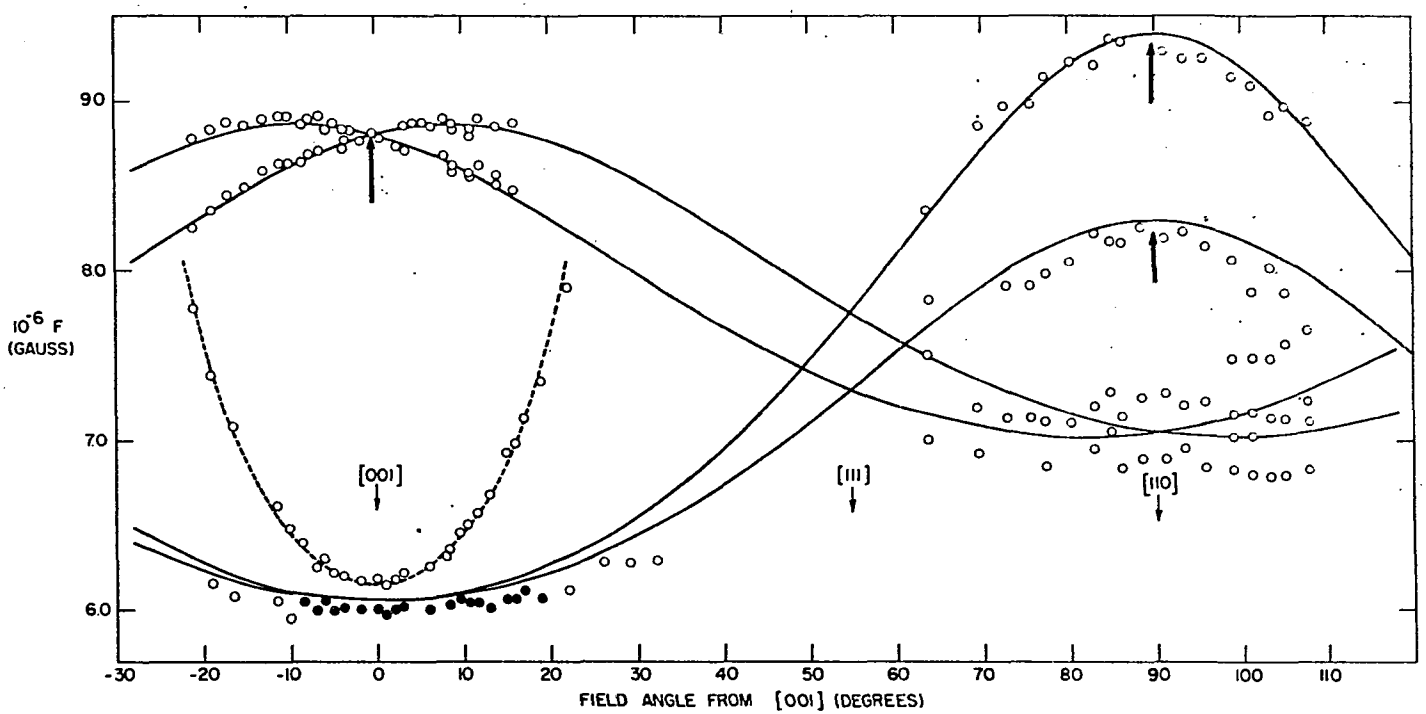
90
80
70
60
10^{-6} F
(GAUSS)
[001]
[111]
[110]
-30
-20
-10
0
10
20
30
40
50
60
70
80
90
100
110
FIELD ANGLE FROM [001] (DEGREES)

by the ellipsoid model. The estimates for these lowest frequency oscillations in fact indicate two terms in the frequency range 6.5-7.5 x 10^6G at $[1\bar{1}0]$ rather than one.

It is possible that the existence of these two frequencies is not a discrepancy with the ellipsoid at N model at all, but is actually due to a slight misorientation of the sample. The fact that the data for the η oscillations which were taken with the $[1\bar{1}0]$ axis sample do not quite match up with the data for the η oscillations which were taken with the $[11\bar{1}]$ axis sample (Figure 9) indicates that the magnetic field direction was not really set accurately in the $(\bar{1}10)$ plane when one or the other of these sets of data were taken. From the geometry of the orbit from which the η oscillations are thought to arise it is evident that sample misorientation near the $[1\bar{1}0]$ direction in the $(\bar{1}10)$ plane would lead to a lower frequency for the η oscillations. Thus it is reasonable to assume that the $[1\bar{1}0]$ axis sample was slightly misoriented when these data were taken.

If this misorientation in fact occurred, it would have affected the orientation dependence of frequencies due to ellipsoidally-shaped surfaces at N quite seriously. In Figure 31c we plotted the orientation dependence which would be expected from ellipsoids at N in a plane which is tilted 5° out of the $(\bar{1}10)$ plane. The frequency spectrum predicted by the ellipsoid model in this plane is complex, and analysis of such a frequency spectrum could certainly yield a doublet

for the lowest frequency branch at $[110]$.

D. Analytical Model for the Fermi Surface

1. Construction of the model

We have already discussed the ellipsoids at N, and we now turn to the electron jack and hole octahedron. The functions[1] to specify the shape of each of these surfaces will be written out in detail after a brief geometrical interpretation of the jack function. (The function for the hole octahedron is quite similar.) We make use of the fact that the surface on which the equation

$$|k_x|^n + |k_y|^n + |k_z|^n = 1$$

is satisfied is an octahedron for $n = 1$ and approaches a cube as $n \longrightarrow \infty$. A function

$$g_1(k_x,k_y,k_z) = |k_x|^{p_2} + |k_y|^{p_2} + |k_z|^{p_2},$$

with the adjustable parameter p_2 in the range $1 \leq p_2 < 2$, is used in making up an octahedral body for the jack. A similar function

$$g_2(k_x,k_y,k_z) = |k_x - A|^{p_8} + |k_y|^{p_1} + |k_z|^{p_1} \quad (p_1 > p_8 > 2)$$

$$+ \text{"exponential asymmetry term"}$$

is used to make up one of the balls on the electron jack.

---

[1]The basic form for the functions which were used was suggested by Dr. B.C. Carlson, Department of Physics, Iowa State University.

(The exponential term lifts the reflection symmetry which g_2 would otherwise exhibit in the plane $k_x = A$.) The functions g_1 and g_2 plus other g_i related to g_2 by cubic symmetry are combined with a "cube" function

$$g_3(k_x,k_y,k_z) = |k_x|^{p_6} + |k_y|^{p_6} + |k_z|^{p_6} \quad (p_6 > 2)$$

to give the jack function

$$F(k_x,k_y,k_z,p) = \sum_{i=1}^{8} \frac{K_i}{g_i(k_x,k_y,k_z)} - 1 \ .$$

Here the K_i are additional adjustable parameters and p stands for the whole set of parameters which can be varied to change the shape of the surface $F(k_x,k_y,k_z,p) = 0$. The "cube" term g_3 is used to make the faces of the octahedral body of the jack concave. (Due to the cube term, there are actually two surfaces $F(k_x,k_y,k_z,p) = 0$; one of these is a small cube about the origin inside the jack. This cube surface is never encountered during computation if the initial search for a point on the jack surface is not begun near the origin.) The neck of the electron jack arises naturally from the way in which the "ball terms" and the "body terms" are combined.

The explicit form for the function which was used to give the shape of the electron jack is

$$F(k_x,k_y,k_z,p) = \frac{p_5}{|k_x-p_3|^{p_8} + |k_y|^{p_1} + |k_z|^{p_{1+p_{12}}} \exp(-p_9|k_x-p_{11}|^{p_{10}})}$$

$$+\frac{p_5}{|k_x+p_3|^{p_8}+|k_y|^{p_1}+|k_z|^{p_1}+p_{12}\exp(-p_9|k_x+p_{11}|^{p_{10}})}$$

$$+\frac{p_5}{|k_x|^{p_1}+|k_y-p_3|^{p_8}+|k_z|^{p_1}+p_{12}\exp(-p_9|k_y-p_{11}|^{p_{10}})}$$

$$+\frac{p_5}{|k_x|^{p_1}+|k_y+p_3|^{p_8}+|k_z|^{p_1}+p_{12}\exp(-p_9|k_y+p_{11}|^{p_{10}})}$$

$$+\frac{p_5}{|k_x|^{p_1}+|k_y|^{p_1}+|k_z-p_3|^{p_8}+p_{12}\exp(-p_9|k_z-p_{11}|^{p_{10}})}$$

$$+\frac{p_5}{|k_x|^{p_1}+|k_y|^{p_1}+|k_z+p_3|^{p_8}+p_{12}\exp(-p_9|k_z+p_{11}|^{p_{10}})}$$

$$+\frac{p_4}{|k_x|^{p_2}+|k_y|^{p_2}+|k_z|^{p_2}}-\frac{p_7}{|k_x|^{p_6}+|k_y|^{p_6}+|k_z|^{p_6}}-1.$$

Final values for the 12 parameters in the function for the model electron jack surface were found by fitting the central (110) section of this surface to an empirical curve for this section. The empirical curve for this section was constructed first of all by using all of the size effect results of Walsh and Grimes (Figure 26). Gaps in the size effect data for the neck and the side of the ball on the electron jack were filled in by using results from Loucks' RAPW band calculations (see Figure 25b) and an empirical fit to the neck region derived from the orientation dependence

of the η oscillations near [001] (Figure 35). To fill in the empirical curve for the side of the ball, the size of the balls on the RAPW electron jack was scaled so that the area of the extremal (100) ball orbit agreed with the experimental dHvA area for this orbit. Then part of the central (110) section of this shape was used to make up the curve for the side of the ball. The shape of the (110) section of the neck region of the electron jack was approximated by part of a central (110) section of a hyperboloid of revolution. In Figure 35 the orientation dependence of the minimum cross-sectional area of this hyperboloid fits the orientation dependence of the η oscillations quite well over a range of about 20° on either side of [001] in the $(\bar{1}10)$ plane. (The size of the hyperboloid was first scaled to give the correct values for the η oscillations (Figure 34) rather than only the falling field values (Figure 35)).

A further criterion was used to fix the shape of the extremal (100) ball orbit. Loucks' calculation predicts that the shape of a cross section through one of the balls is not circular, but somewhat square. We attempted to arrive at the same shape for the cross section of one of the balls on the empirical model. The ratio of the width w of the ball cross section to the diagonal d was used to fit the degree of squareness (Figure 36). Loucks[1] found that this ratio

[1]Dr. T. Loucks, Department of Physics, Iowa State University, Private communication, 1965.

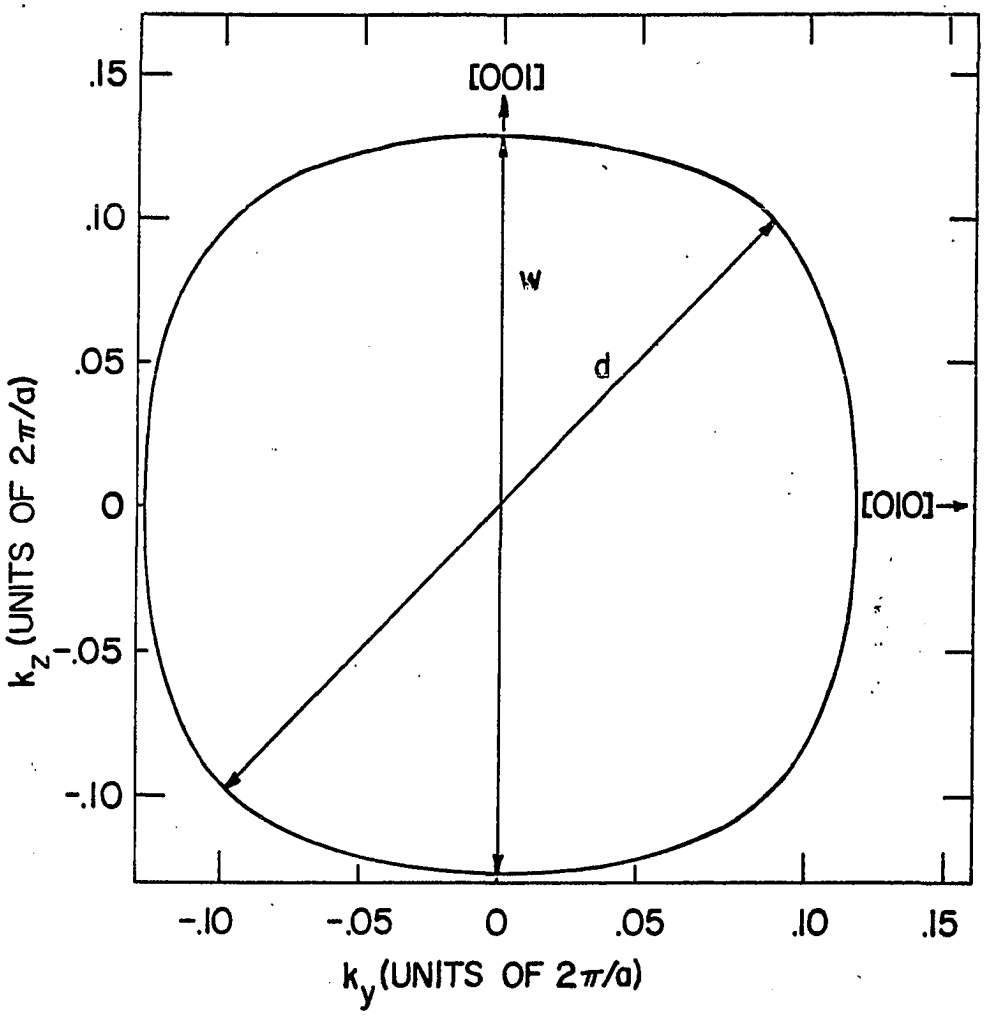

Figure 36. Shape of extremal (100) ball orbit ($k_x = .45(2\pi/a)$) The ratio of the width w to the diagonal dimension d is .918. Orbit area = $.0552(2\pi/a)^2$.

was 0.895. By setting the parameter p_1 in the jack function equal to three we were able to arrive at this same value for the ratio of the width of the cross section to the diagonal dimension in an early empirical model. However, when other parameters were changed to vary the shapes of other parts of the electron jack, the shape of the ball cross section was changed slightly. In the model which is reported here the ratio w/d is 0.918.

The final values for the parameters in the electron jack function were $p_1 = 3$, $p_2 = 1.1066$, $p_3 = .45395$, $p_4 = .27807$, $p_5 = 9.3869 \times 10^{-4}$, $p_6 = 4.5581$, $p_7 = 8.3675 \times 10^{-6}$, $p_8 = 2.6979$, $p_9 = 5.8337 \times 10^{2}$, $p_{10} = 1.9634$, $p_{11} = 0.39042$, $p_{12} = 3.9347 \times 10^{-4}$. With these values of the parameters, the function $F(k_x,k_y,k_z,p)$ defined a surface with the shape of the electron jack with radius vectors to points on the surface measured in units of $(2\pi/a)$.

The function which was used to generate the hole octahedron shape was

$$G(k_x,k_y,k_z,p)=\frac{p_5}{|k_x-p_3|^{p_8}+|k_y|^{p_1}+|k_z|^{p_1}+p_{12}\exp(-p_9|k_x-p_{11}|^{p_{10}})}$$

$$+\frac{p_5}{|k_x+p_3|^{p_8}+|k_y|^{p_1}+|k_z|^{p_1}+p_{12}\exp(-p_9|k_x+p_{11}|^{p_{10}})}$$

$$+\frac{p_5}{|k_x|^{p_1}+|k_y-p_3|^{p_8}+|k_z|^{p_1}+p_{12}\exp(-p_9|k_y-p_{11}|^{p_{10}})}$$

$$+ \frac{p_5}{|k_x|^{p_1} + |k_y + p_3|^{p_8} + |k_z|^{p_1 + p_{12}} \exp(-p_9 |k_y + p_{11}|^{p_{10}})}$$

$$+ \frac{p_5}{|k_x|^{p_1} + |k_y|^{p_1} + |k_z - p_3|^{p_8 + p_{12}} \exp(-p_9 |k_z - p_{11}|^{p_{10}})}$$

$$+ \frac{p_5}{|k_x|^{p_1} + |k_y|^{p_1} + |k_z + p_3|^{p_8 + p_{12}} \exp(-p_9 |k_z + p_{11}|^{p_{10}})}$$

$$+ \frac{p_5}{|k_x|^{p_2} + |k_y|^{p_2} + |k_z|^{p_2 + p_{14}} \exp\left[-p_{13}(\sqrt{k_x^2 + k_y^2 + k_z^2} - p_{15})^2\right]}$$

$$- \frac{p_7}{|k_x|^{p_6} + |k_y|^{p_6} + |k_z|^{p_6}} - 1 .$$

The final values for all of the parameters in the function for the hole octahedron were found by fitting the central (110) section of the surface defined by this function to the size effect data for the hole octahedron in Figure 26. The final parameter values for the octahedron were as follows: $p_1 = 2.5138$, $p_2 = 1.1084$, $p_3 = 0.34581$, $p_4 = .37179$, $p_5 = 4.6498 \times 10^{-5}$, $p_6 = 2.7257$, $p_7 = 1.165 \times 10^{-3}$, $p_8 = 2.1323$, $p_9 = 7.423 \times 10^{-4}$, $p_{10} = 1.7334$, $p_{11} = .45109$, $p_{12} = 1.4319$, $p_{13} = 3.043 \times 10^{5}$, $p_{14} = 6.3017 \times 10^{-2}$, $p_{15} = 0.41590$. The frequency values calculated from this shape were scaled by a factor of 1.0276 for comparison with the experimental dHvA frequencies, so that radius vectors to points on this surface must be multiplied by $\sqrt{1.0276}$ to

convert them to units of $(2\pi/a)$.

A (110) central section through the model surfaces which were obtained for the electron jack and hole octahedron is shown in Figure 37.

2. Comparison with the de Haas-van Alphen effect

After (110) sections of the model surfaces for the electron jack and hole octahedron had been fitted, the overall agreement of the shape of these surfaces with the de Haas-van Alphen effect data was tested for a number of magnetic field directions. Using the curve tracing program outlined in Appendix D, the extremal areas of cross section made by planes k_H = constant with the surfaces were calculated. The frequencies which were calculated from these areas are compared in Figure 38 with the fundamental frequencies found by experiment.

The solid curves in Figure 38 are drawn through points calculated from the empirical model. The curve through the points for the α oscillations gives the orientation dependence for frequencies arising from the central cross section of the hole octahedron. The solid curves which nearly fit the points for the ϵ_u and ϵ_L oscillations give the expected orientation dependence for the ellipsoidal surfaces centered at the points N. The other curves give the orientation dependence for frequencies arising from extremal sections of the electron jack. Thus, the δ oscillations, whose

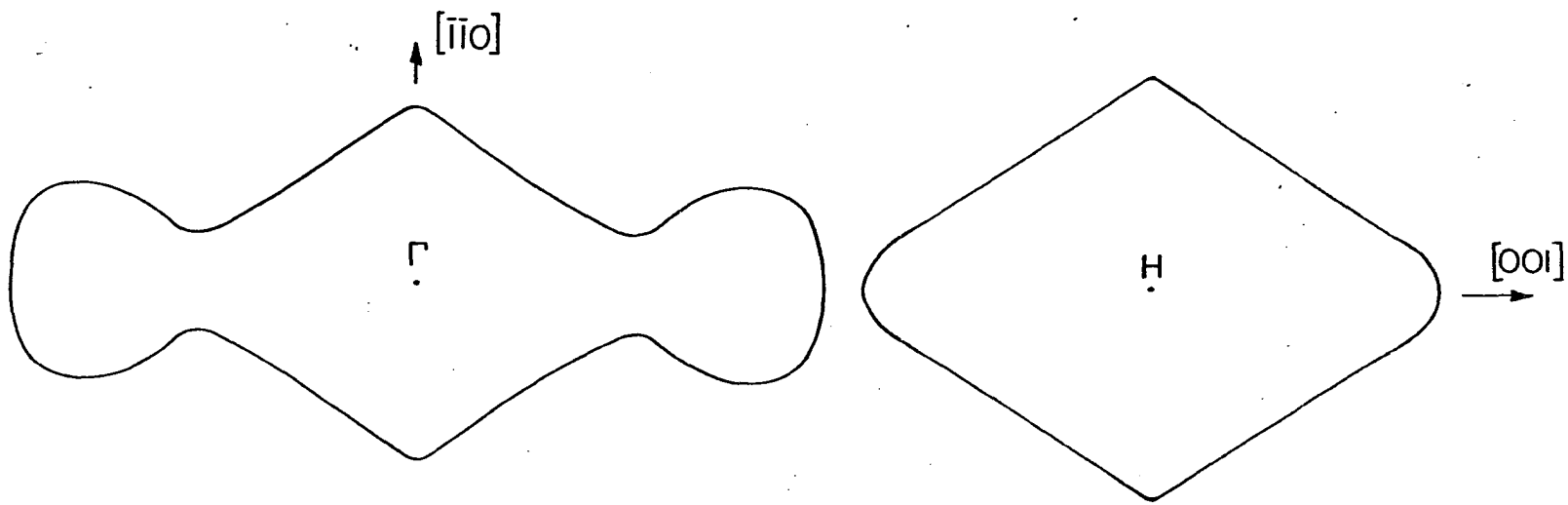

Figure 37. Central (110) section through the empirical surfaces for the electron jack and hole octahedron (These two surfaces would contact along the line Γ-H in the absence of spin-orbit coupling.)

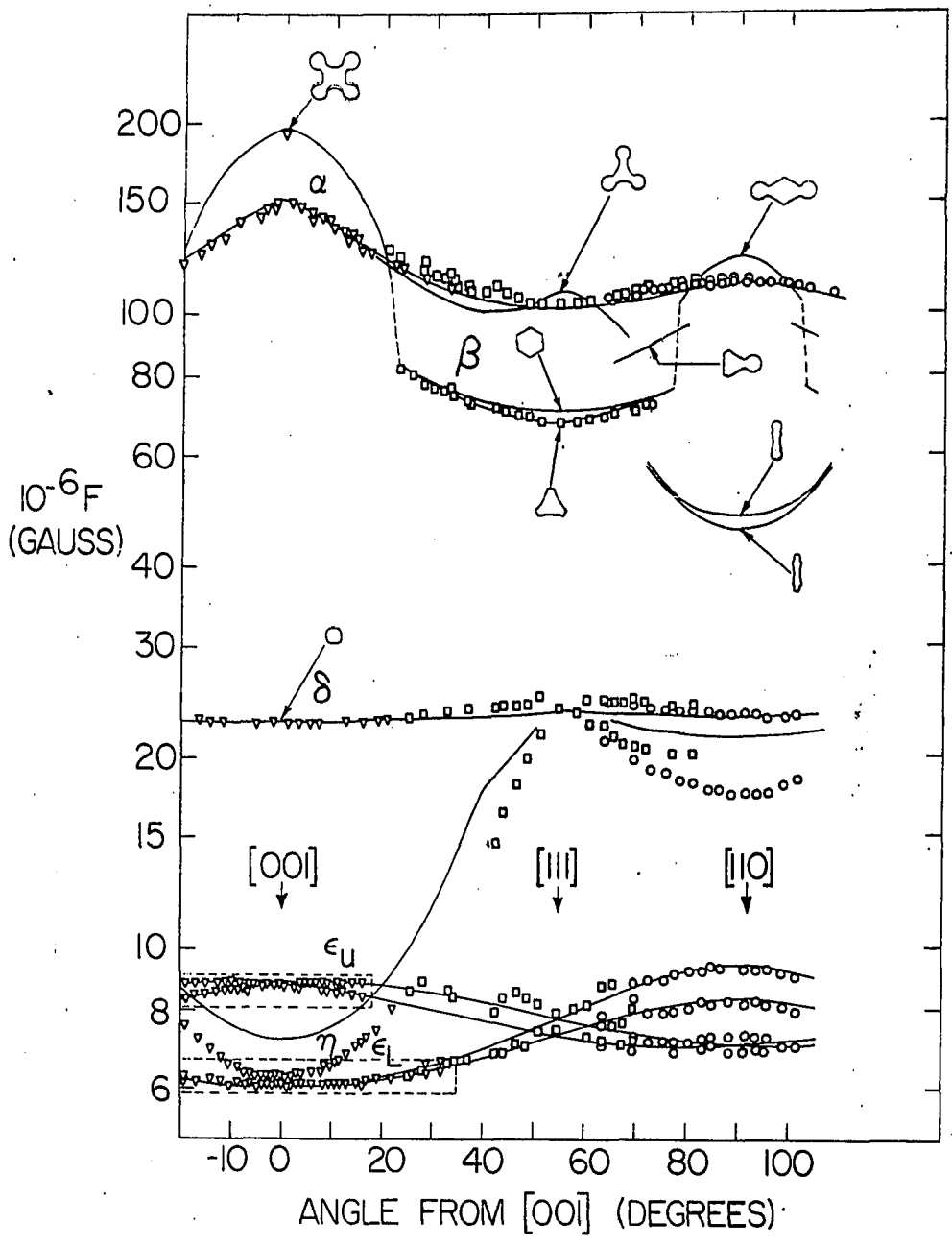

Figure 38. Comparison of the dHvA frequencies predicted by the model Fermi surface (solid curves) with the frequencies found by experiment (open plotting symbols) in the $(\bar{1}10)$ plane

frequency varies very slowly with angle give the orientation dependence of the area of an extremal ball orbit.

For field orientations near $[11\bar{1}]$, there are two extremal orbits on the body of the electron jack which predict frequencies which vary with angle much like the frequency of the β oscillations. There is a central orbit (which has a hexagonal shape at $[11\bar{1}]$) and a noncentral orbit with a slightly smaller area (which is shaped like a truncated triangle at $[11\bar{1}]$). The orientation dependence predicted by the triangle orbit fits the orientation dependence of the β oscillations quite well. However, it is difficult to decide which of these orbits the β oscillations should actually be assigned to. Walsh (1964) (see Figure 40) has reported that both of these orbits are observed in cyclotron resonance experiments, and he assigns the lower mass resonance to the central orbit on the electron jack. According to this interpretation, we would perhaps expect that the β oscillations should be assigned to the central orbit on the body of the jack rather than to the slightly smaller noncentral one.

As the field direction is tipped away from the $[11\bar{1}]$ orientation, the frequency predicted by either of the orbits for the β oscillations increases until at an angle of about 20° from $[001]$ the two branches coalesce and form a single central orbit. As the field orientation is moved still closer to $[001]$ this central orbit ceases to exist and a

new central orbit is formed which includes not only the body section of the electron jack but also four balls. According to the model, the first orbit which includes four balls as the field direction is rotated from $[11\bar{1}]$ toward $[00\bar{1}]$ is a self-intersecting orbit so that near the angle at which the four ball orbit first occurs, the cyclotron mass should increase tremendously (cf. Lifshitz and Kaganov 1959). Walsh (1964) in fact found such an increase in the cyclotron mass of the central jack orbit near the angle of changeover. At about 20° from $[00\bar{1}]$ the β oscillations disappear and, contrary to expectation, are not replaced within a few degrees by oscillations corresponding to the four ball orbit, presumably because of the strong damping associated with the large cyclotron mass.

Walsh (1964) found that the lowest value of the cyclotron mass of the four ball orbit, $m^*/m_e = 2.88$, occurred for $H//[00\bar{1}]$. Due to the large cyclotron mass for this orbit, the de Haas-van Alphen oscillations for this extremal section are expected to be heavily damped and therefore difficult to observe. We have, however, found a term with a frequency of 1.94×10^8 G for $H//[00\bar{1}]$. The single point for this term which is shown on Figure 38 lies on the predicted curve for the four ball orbit. This single point might also be a sum frequency of the α and δ_2 oscillations (see Figure 9). If we argue that the signal amplitude is determined to a large extent by the exponential damping factor (see Equation 12)

then the amplitude of the sum frequency $\alpha + \delta_2$ would be expected to be considerably larger than that of the four ball orbit, since the "effective mass" parameter for the $\alpha + \delta_2$ oscillations would be approximately $m^*_\alpha + m^*_{\delta_2} \cong 2m_e$ (see Appendix C), which is considerably less than Walsh's value of $m^* = 2.88m_e$ for the four ball orbit.

De Haas-van Alphen oscillations corresponding to many of the other large jack orbits which are predicted by the model were not observed. Because the cyclotron masses for many of the jack orbits are considerably larger than the masses for the α oscillations and the δ_2 oscillations (Walsh 1964), de Haas-van Alphen signals arising from the large orbits would probably have been swamped by signals from the terms α or δ_2.

The (110) central section of the electron jack near one of the necks is virtually indistinguishable from the generator of the hyperboloid of revolution which can account for the orientation dependence of the η oscillations (see Figure 35). However, the computed minimum area of the (001) neck section is about 15% too large. The reason for this misfit is that the computed (001) section through the neck actually turns out to be closer to a square than a circle. This is the most serious percentage discrepancy between the model and experiment.

A numerical comparison of the experimental de Haas-

van Alphen frequencies and the frequencies predicted by the model is carried out in Table 1. The frequencies F are related to extremal cross sectional areas of the Fermi surface A_0 (measured in units of $(2\pi/a)^2$) by the equation $F = 4.135 \times 10^8 A_0$. We have taken this opportunity to compare our results with the torque results of Sparlin and Marcus (1966) and of Brandt and Rayne (1963). In comparing the experimental results, it should be taken into account that in most cases the impulsive-field method provides considerably more frequency discrimination than the torque method; interpretation of these data should therefore be more straightforward.

3. Comparison of extremal dimensions of the empirical model with those found by experiment

The extremal $\langle 100 \rangle$ and $\langle 110 \rangle$ dimensions of the central sections of the models for the electron jack and the hole octahedron are compared with those found by experiment in Table 2. The agreement with the size effect results of Walsh and Grimes (1964) should be quite good since these results were used in finding the model. However, discrepancies have arisen for several reasons. The numerical values for the size effect k-vectors were obtained by measuring distances on a drawing which was like Figure 26, but 4/3 that size (about 100 points were measured for each surface). These extremal k-vectors were assumed to give the

Table 1: Comparison of Fundamental dHvA Frequencies Found by Experiment with Frequencies Predicted by the Empirical Model for the [001], [11$\bar{1}$], and [110] orientations

Orientation	Oscillation	Surface	Orbit	Frequency (x10^6 Gauss) Calculated	Experimental[a]	Experimental[b]	Experimental[c]
[001]		e_Γ[d]	4-ball	195.3	194[e]	---	---
	α	h_H	central	152.5	151	150.0	---
	δ	e_Γ	ball	22.79	22.7	22.7	---
	ϵ_u	h_N	central	8.805	8.80	8.78[f] 8.51	8.98 8.55
	η	e_Γ	neck	7.23	6.27	6.06-6.10	6.08-6.24
	ϵ_L	h_N	central	6.055	6.11	5.99-6.03	5.94-6.03
[11$\bar{1}$]		e_Γ	3-ball	108.2	---	---	---
	α	h_H	central	102.8	103.4	103.5	---
	β	e_Γ e_Γ	central truncated triangle	70.3 67.4	67.3[g]	---	---
	δ	e_Γ	ball	23.69	25.0[h]	24.7	25.8
	η	e_Γ	neck[i]	23.69	23.9	23.4	---
	ϵ	h_N	central	7.777	measurements unreliable	7.94	7.62
	ϵ	h_N	central	7.266	measurements unreliable	7.23	7.01
[110]		e_Γ	2-ball	122.8	---	---	---
	α	h_H	central	111.5	111.5	111.5	---
		e_Γ	non-central	47.6	---	---	---
		e_Γ	non-central	45.6	---	---	---
	δ	e_Γ	ball	23.11	23.5	23.8	24.2
	η	e_Γ	neck	21.42	17.3[j]	19.4	---
	ϵ	h_N	central	9.408	9.34	9.40	9.28
	ϵ	h_N	central	8.305	8.23	8.06	8.07
	ϵ	h_N	central	7.055	measurements unreliable	6.95	6.90

[a] The impulsive field results of this study
[b] Torque results of Sparlin and Marcus (1966)
[c] Torque results of Brandt and Rayne (1963)
[d] We use the notation of Sparlin and Marcus (1966) for the surfaces; e_Γ:electron surface at Γ (jack); h_H:hole surface at H (hole octahedron); h_N:hole surface at N (small ellipsoids).
[e] This term could also be the sum frequency of the α and δ_2 oscillations.
[f] Two terms were found for the ϵ_u oscillations at [001] in the torque method investigations.
[g] It is possible that the β oscillations are an unresolved sum of contributions from two extremal orbits on electron jack.
[h] The frequency of the δ oscillations could not be pinned down accurately at [11$\bar{1}$].
[i] The neck orbit and the ball orbit coincide at this orientation on the model.
[j] This frequency may be too low because of sample misorientation.

Table 2: Comparison of Extremal ⟨100⟩ and ⟨110⟩ Dimensions of the Empirical Model with Those Found by Experiment (for central sections of the electron jack and hole octahedron only)

Direction	Surface	Dimension	Length of radius vector (units of $\frac{2\pi}{a}$)[a]			
			Empirical Model	Experimental[b]	Experimental[c]	Experimental[d]
⟨100⟩	Electron jack	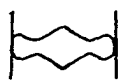	.555	$.55_9$	$.59_4$	$.52_3$
	Hole octahedron		.397	$.39_3$	$.39_3$	$.35_2$[e]
⟨110⟩	Electron jack		.250	xxxx	$.25_7$	$.29_7$
	Hole octahedron		.304	xxxx		
	Hole octahedron	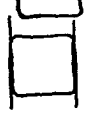	.310	$.30_2$		

[a] Both the size effect and magnetoacoustic results were originally quoted in units of A^{o-1}. We have changed them to units of $2\pi/a$ taking the distance Γ-H = $2\pi/a$ to be $1.987A^{o-1}$.
[b] Size effect results of Walsh and Grimes (1964)
[c] Magnetoacoustic effect results at 390MHz (Rayne 1964)
[d] Magnetoacoustic effect results at 930MHz (Jones and Rayne 1965)
[e] Obtained from analysis of beat pattern

shapes of central sections of the two surfaces. However, the faces of both the octahedral parts of the model electron jack and of the model hole octahedron turned out to be somewhat concave. Because of this concavity, there are some directions for which size effect calipered dimensions of these surfaces would not give the dimensions of the central sections, and to this extent, the fitting procedure is inconsistent. The shape of the central (001) section of the hole octahedron and the calipered dimension in the $[110]$ direction are shown in one of the sketches in Table 2. The central dimension of this section is $\sim$ 2% less than the calipered dimension. For field angles between $\sim$ 23° and $\sim$40° from $[001]$, central sections of the model electron jack are also concave, even though these sections do not include contributions from the balls; therefore the calipered dimension of each of these sections is also somewhat larger than the central dimension. The largest difference ($\sim$6%) between the calipered dimension and the central dimension of the body of the model electron jack occurs for H$\sim$23° from $[001]$ ($\underline{k}$-vector $\sim$23° from $[1\bar{1}0]$).

A further comparison can be made on the basis of the angles at which the central orbit on the electron jack ceases to exist. The size effect data indicate that in the $(\bar{1}10)$ plane this orbit exists between the angles of $\sim$18° and $\sim$75° from $[001]$, and it is very satisfactory that the model electron jack predicts that this orbit should exist between $\sim$23°

and 77° from [001].

A comparison between the magnetoacoustic effect results (Rayne 1964, Jones and Rayne 1965) and the predictions of the empirical model for some of the larger extremal dimensions in the (110) plane is carried out in Figure 39, and the comparison for symmetry directions is summarized in Table 2. The angular dependence for the complete set of extremal $\underline{k}$-vectors predicted by the model electron jack is rather complicated. Furthermore, in this study orbits on the electron jack were traced only at those slices k_H = constant which were necessary to find extremal areas, and not all of the orbits which are necessary to find extremal $\underline{k}$-vectors were traced, since this would have involved extensive additional computation. However, the predicted angular dependence of extremal $\underline{k}$-vectors which is shown does not appear to be in violent disagreement with the magnetoacoustic results, and may not be outside the experimental error (bearing in mind the difficulties in interpreting the magnetoacoustic results (page 91)).

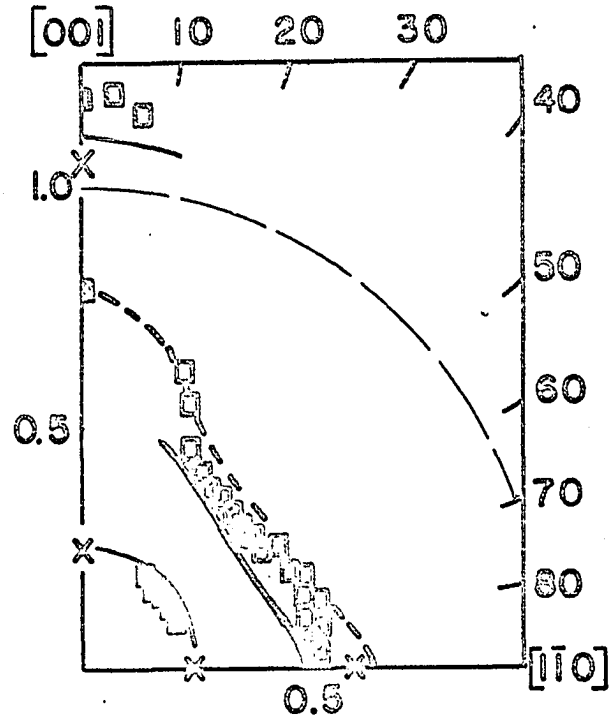

Figure 39. Comparison in the (110) plane of the magneto-acoustic results and some of the extremal k-vectors predicted by the empirical model. ◘, □: magnetoacoustic results at 390MHz (Rayne 1964); X : magnetoacoustic results at 930MHz (Jones and Rayne 1965); ——— some extremal dimensions on the electron jack; ---- central dimension of hole octahedron.

4. Orbit masses

We have delayed comparison of the dHvA orbit mass results with those of cyclotron resonance until after the Fermi surface models were discussed so that specific orbits could be defined. Walsh (1964) was able to assign many of his cyclotron resonance mass series to specific orbits without recourse to a comparison with the de Haas-van Alphen effect masses. His results in a {110} plane for some of the larger masses are shown in Figure 40 along with his assignment of these data to specific orbits on the electron jack and hole octahedron. It is evident that the orientation dependence shown in Figure 40 is consistent with that expected from surfaces having the general shapes of the electron jack and hole octahedron. For instance, the orientation dependence for the central orbit on the electron jack shows discontinuities when this orbit changes from the orbit which does not include any balls to the orbit which includes two balls or the orbit which includes four balls. (Walsh[1] has found other resonances, which yield in general lower masses than those shown in Figure 40 but thus far he has not arrived at a final interpretation for these masses.)

In Table 3 we have tabulated both the dHvA and cyclotron resonance mass results for the [001], [111], and [110]

[1] W.M. Walsh, Jr., Bell Telephone Laboratories, Murray Hill, New Jersey. Private Communication, 1964.

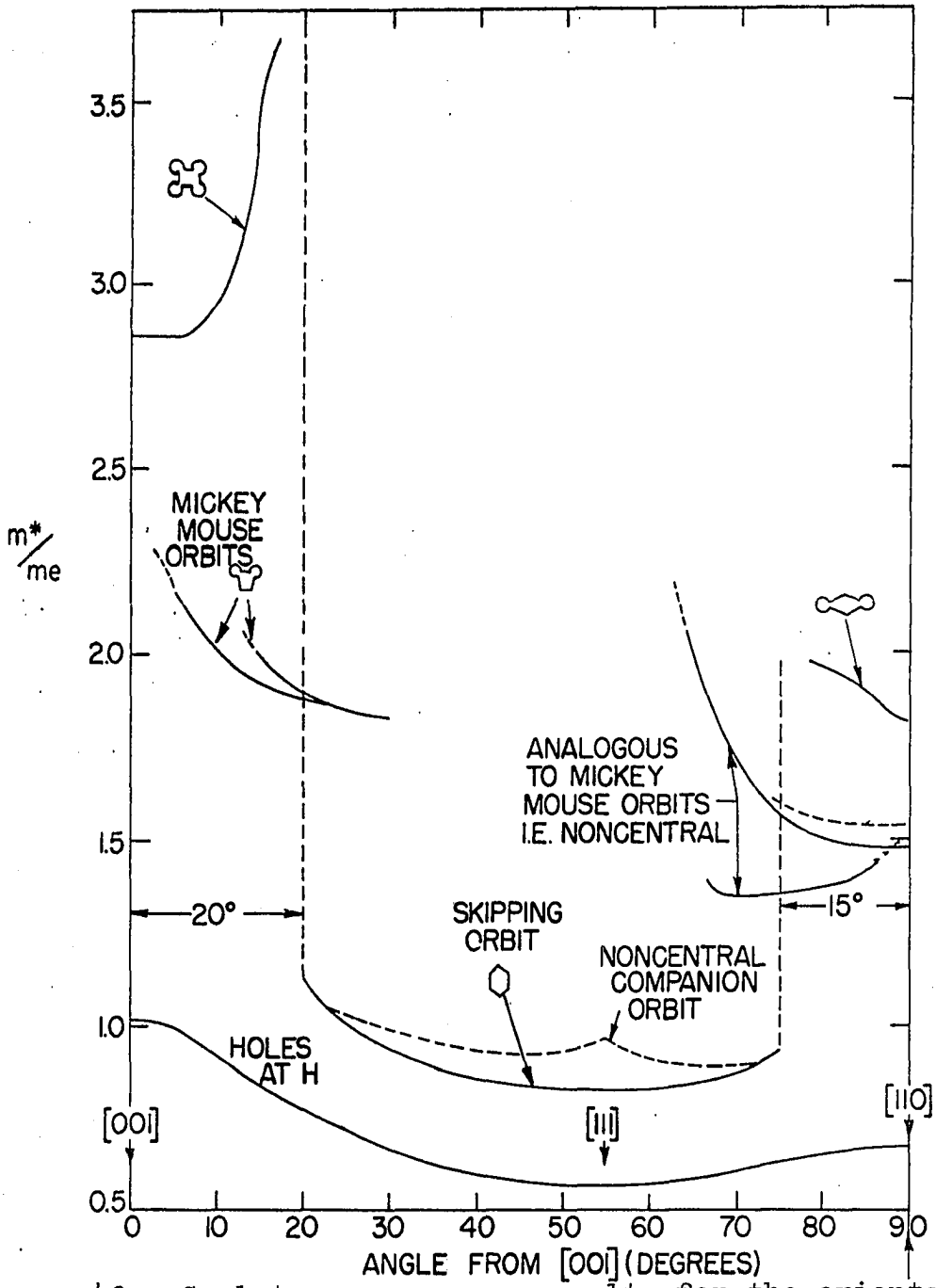

Figure 40. Cyclotron resonance results for the orientation dependence in the $(\bar{1}10)$ plane of the masses for some of the large jack orbits and the central hole octahedron orbit. (The original plot from which this figure was made was kindly provided by Dr. W.M. Walsh Jr., Bell Telephone Laboratories, Murray Hill, New Jersey. Private Communication 1964)

Table 3: Orbit Mass Results

Orientation	Surface	Orbit	dHvA oscillation	m^*/m_e dHvA[a]	m^*/m_e Cyclotron[b] Resonance	m^*/m_e dHvA[c]
[00$\bar{1}$]	electron jack	4-ball			2.86	
	electron jack	ball	δ	0.58	.55[d]	.505
	electron jack	neck	η	0.25[e]		.29 - .307
	hole octahedron	central	α	0.93	1.01	1.06 - 1.11
	holes at N	central	ϵ_u	0.37	.33[d]	.354 - .365
	holes at N	central	ϵ_L		.23[d]	.28
[11$\bar{1}$]	electron jack	triangle	β	0.9	.96[d,f]	
	electron jack	central			.83	
	electron jack	ball	δ			
	electron jack	neck	η			
	hole octahedron	central	α	0.60	.58[d]	.52
	holes at N	central	ϵ			.287
	holes at N	central	ϵ			.287
[110]	electron jack	2-ball			1.81	
	electron jack	ball	δ	0.60	.55[d]	
	electron jack	neck	η			.75
	hole octahedron	central	α	.67	.67	.63 - .65
	ellipsoids at N	central	ϵ		.36 - .37[d]	
	ellipsoids at N	central	ϵ		.32[d]	
	ellipsoids at N	central	ϵ		.27[d]	.262 - .276

[a] Orbit mass results of present study

[b] Orbit mass values picked off a plot of the cyclotron resonance results (Walsh 1964)

[c] Orbit mass results of Sparlin and Marcus (1966)

[d] The overall mass spectrum found by cyclotron resonance is rather complex. The mass assignments with superscript d may or may not correspond to Walsh's assignment. When the corresponding orbit is noncentral, it is necessary to assume that the cyclotron resonance results pertain to an orbit which has extremal area in order to make a direct comparison with the dHvA results.

[e] The η and ϵ_L oscillations were not resolved when these data were taken. The η oscillations had previously been found to dominate at this orientation so the orbit mass which was derived from the temperature dependence of the combined signal was assumed to be the mass for the η oscillations.

[f] The triangle orbit does not have extremal mass according to the empirical model. However, the model is not expected to predict mass values reliably, and this mass term has been assumed to correspond to the triangle orbit.

directions. Only the orbits having an extremal area are relevant to the dHvA effect so that in order to compare a dHvA mass value for a noncentral orbit with a similar cyclotron resonance mass value for a noncentral orbit, it is necessary to assume that the cyclotron resonance result also pertains to an orbit with extremal area. For instance, Walsh (Figure 40) has reported that there are two orbits with nearly the same mass as was found in the dHvA effect for the β oscillations. One of these orbits is noncentral and need not have extremal area. However, according to our empirical model (Figure 38) there are two orbits which predict dHvA frequencies near that of the β oscillations; we have therefore included in Table 3 both of the aforementioned cyclotron resonance mass values in case the noncentral orbit with extremal area might coincide with the noncentral orbit reported by Walsh. The overall agreement between mass results found by the two methods is extremely good. Unfortunately the dHvA mass for the β oscillations at [11] falls approximately midway between the two cyclotron resonance mass values; thus this mass measurement does not clarify the interpretation of these oscillations.

The mass values in Table 3 for the $\in$ oscillations can be combined with the corresponding frequencies for these oscillations (Table 1) to check the hypothesis that these oscillations arise from a set of ellipsoidally-shaped surfaces. For such a set of surfaces, the ratio

$m^*(\theta,\phi)/F(\theta,\phi)$ (where θ,ϕ give the orientation of the magnetic field) should be a constant. Sparlin and Marcus (1966) have carried out such a check, and for their measurements this ratio only varies by about 10 percent.

A direct comparison between the experimental orbit masses and the predictions of the empirical model is not carried out here; the masses depend on the slope of the $E(\underline{k})$ curves at the Fermi surface (cf. Equation 6), and although the surfaces $F(\underline{k},p) = 0$ and $G(\underline{k},p) = 0$ approximate the shape of the Fermi surface quite well, the slopes at which $F(\underline{k})$ and $G(\underline{k})$ intersect the surfaces are not necessarily similar to the slopes with which the curves $E_i(\underline{k})$ intersect the Fermi surface. (The experimental orbit masses are further complicated by electron-phonon interactions (cf. Ashcroft and Wilkins 1965).) We did, however, carry out calculations (Appendix F) to check whether the functions F and G would at least predict the anisotropy of the mass curves for the electron jack and hole octahedron respectively, and it was found that they did not.

5. Volume and compensation of the model Fermi surface

In spite of the fact that the computed neck area for the electron jack was too large, the model electron jack and hole octahedron were used to compute an estimate of the volume of the Fermi surface of tungsten, since the small discrepancy in the neck cross section should not have a very

large effect on the total volume. These calculations were carried out by first finding the cross sectional area A_i at about 250 slices k_H = constant. Then the volumes were computed according to the formula $V = \sum_i A_i \Delta k_{H_i}$. From the semiaxes given on page 110, the volume of one of the hole ellipsoids is $1.9453 \times 10^{-3}(2\pi/a)^3$. The final results are as follows:

Surface	Volume $(\frac{2\pi}{a})^3$
Hole octahedron	.11438
Six hole ellipsoids at N	.01167
Total hole volume	.12605
Electron jack	.1274

Here $a = 3.162 \times 10^{-8}$ cm is the estimated lattice constant for tungsten at 1°K (Nix and MacNair 1942; Cullity 1956, p. 484).

We know from the results of magnetoresistance measurements (Fawcett 1962) that tungsten is a compensated metal (equal electron and hole volumes). When the uncertainties in our fitting procedure are taken into account, our results for electron and hole volumes support this conclusion.

We have not computed the surface area of our model for the Fermi surface of tungsten and therefore cannot make a direct comparison with experimental estimate of the surface area of tungsten which has been obtained by anomalous skin effect measurements on polycrystalline samples by Fawcett

and Griffiths (1962). They found, to an accuracy of 30 percent, that their measured surface area could be accounted for by 0.078 hole per atom and 0.078 electron per atom, each occupying states in a hypothetical spherical Fermi surface. These results are to be compared with our estimate from our model Fermi surface of .127 electron per atom and .126 hole per atom.

The surface areas for spheres corresponding to the model electron and hole volumes would be about 40 percent larger than the anomalous skin effect areas, and the surface areas for the actual anisotropic model surfaces would be larger than the surface areas of the spheres. However, in view of the discussion on page 88 and in view of the fact that the anomalous skin effect samples were thought to be not perfectly polycrystalline, but to have a preferred orientation (for $\langle 100 \rangle$ directions along the normal to the sample surface) (Fawcett and Griffiths 1962) discrepancies between the experimental and model surface areas should be expected. However, since the discrepancy appears to be large, a re-examination of the accuracy of the anomalous skin effect surface areas would perhaps be worthwhile.

V. CONCLUDING DISCUSSION AND SUGGESTIONS FOR FURTHER STUDY.

The results of this study have not only confirmed the results of a torque method dHvA study in tungsten carried out by Sparlin and Marcus (1966) at low fields, but have also yielded other important groups of oscillations. Thus using high impulsive fields it was possible to detect and study the β oscillations and oscillations which probably arise from the central (001) section of the electron jack (the 4-ball orbit), whereas neither of these oscillations was observed in the torque studies. Moreover, because of its increased selectivity, we have been able to use the high-field method to resolve the disagreement between Sparlin and Marcus (1966) and Brandt and Rayne (1963) concerning the orientation dependence of the low frequency oscillations near [001] (see Section IV-C).

The simple empirical model has been shown to be in excellent agreement with a rich variety of experimental evidence. However, we recognize that it is imprecise in that it predicts an area for the neck on the electron jack which is 15 percent too large (see Table 1). A further change which may be required is a slight reduction in the size of the body of the electron jack. The orientation dependence of the area of an extremal noncentral orbit on the electron jack predicts the orientation dependence of the frequency of

the β oscillations quite well (Figure 38). However, it is difficult to believe that this is the correct assignment for these oscillations, in view of the fact that the central orbit is thought to have the lower cyclotron mass (Figure 40); since the curvature factors $\left|\partial^2 \mathcal{A}_o/\partial k_z^2\right|^{-\frac{1}{2}}$ for these two orbits do not appear to differ greatly (Appendix G), the central orbit would therefore be expected to contribute the larger dHvA signal. Furthermore, visual inspection of Loucks' solid 3-dimensional model for the electron jack combined with crude sketches on drawings of sections through our empirical model seems to indicate that simultaneous reduction in the area of the central [111] jack orbit and increase in the anisotropy of the orientation dependence of the area of the central section could be achieved by a mere reduction (roughly 5 percent) in the $\langle 110 \rangle$ dimensions of the electron jack; no size effect results were reported for this dimension so this change in the jack shape (to make the central orbit predict more closely the orientation dependence of the frequency of the β oscillations) could be made without destroying the agreement with the size effect results in other orientations.

It is unfortunate that there is not more direct experimental evidence available to determine the detailed shape of the electron jack. Due to the strength of the α oscillations, and the δ_3 oscillations, it is not altogether

clear that further impulsive-field studies of the β oscillations would yield any information regarding the existence of two extremal jack orbits with frequencies near that of the β oscillations, although further studies using the shunt ignitron should be carried out; perhaps these studies could also be carried out using the field-modulation technique (R.W. Stark, see Priestley 1966) since troublesome signal from the very strong α oscillations could possibly be nulled out using this method.

Another approach which should be pursued is to determine whether the term with frequency 1.94×10^8 G at [001] is due to the 4-ball orbit or arises from the combination of the α and δ_2 oscillations. This determination could perhaps best be carried out by a very careful simultaneous study of the orientation dependence of the term in question and the α and δ_2 oscillations. If this term turns out to arise from the 4-ball orbit, its frequency can be compared with the corresponding frequency predicted by the model (after the neck shape has been corrected) to determine whether a reduction in the $\langle 110 \rangle$ dimensions of the electron jack should be undertaken. Measurement of the frequency of the 2-ball orbit would of course also yield equally valuable information, but here again, the proximity of the strong α oscillations and the presence of combination frequencies are expected to complicate the measurements.

Precise Gantmakher size effect measurements of the $\langle 110 \rangle$ dimensions of the jack using a (100) plane sample rather than a (110) plane sample would also be of value. Such measurements might also be of value as a second experimental determination of the shape of the (100) ball cross section. (The magnetoacoustic results in Figure 27a might be interpreted as suggesting that the (100) ball cross section is more circular than the section which we showed in Figure 36. However, as we have pointed out earlier (page 91) it is difficult to derive such detailed information from the magnetoacoustic measurements.) Size effect measurements of the central (100) section of the hole octahedron could also be used to determine whether the sides of this section are concave or not and thus resolve the uncertainty as to whether the present $[110]$ size effect dimension for the hole octahedron (Figure 26) is the central dimension or not.

We should state explicitly that no evidence was found for the existence of the small lens-shaped surfaces which are predicted by the Lomer model and the Loucks nonrelativistic model (see Section IV-A), although such surfaces could have escaped detection in our experiment if they were very small. Sparlin and Marcus (1966) and Brandt and Rayne (1963) also do not report any evidence for the existence of these small surfaces (we have reinterpreted the data of Brandt and Rayne (1963) (see Section IV-C).

In connection with any further dHvA measurements in tungsten, an attempt should be made to make more reliable determinations of the absolute amplitude of the oscillations for use in gaining a further understanding of the origin and characteristics of the combination frequencies. It would be of great value to work out experimental conditions under which the strength of these combination signals might possibly be minimized while retaining fundamental oscillations of sufficient strength for study. In connection with any absolute amplitude measurements, the field dependence of the amplitude should also be studied so that the level broadening factor in Equation 12 can be determined; using curvature factors computed from the empirical model, a comparison could then be carried out between the amplitude predicted by Equation 12 and that observed experimentally to see if the seemingly large amplitudes which were found are really predicted theoretically. Serious complications are expected to arise in the interpretation of such measurements due to frequency modulation effects which seem to be evident in much of our data (see Appendix C).

A further measurement, which should be undertaken is a check of the temperature dependence of the amplitudes of the α, α_2, and α_3 oscillations at [111] to see if the discrepancy in the ratios of the orbit masses of these terms which was reported in Section III-B is reproduced; if the

discrepancy is again found, further mass measurements should be carried out at different field strengths in conjunction with determinations of absolute amplitudes to discover if there is any dependence of the measured mass ratios on amplitude.

VI. REFERENCES

Anderson, J. R. (1962) The Fermi surface of lead. Unpublished Ph. D. thesis. Ames, Iowa, Library, Iowa State University of Science and Technology.[1]

Anderson, J. R. and Gold, A. V. (1963) Phys. Rev. Letters 10, 227.

Anderson, J. R. and Gold, A. V. (1964) U. S. Atomic Energy Commission Report IS-762 Iowa State University of Science and Technology, Ames. Inst. for Atomic Research

Ashcroft and Wilkins (1965) Physics Letters 14, 285.

Azbel, M. and Kaner, E. A. (1955) J. Exptl. Theoret. Phys. (U.S.S.R.) 30, 811. [English transl. : Soviet Physics JETP 3, 772 (1956)]

Azbel, M. and Kaner, E. A. (1956) J. Exptl. Theoret. Phys. (U.S.S.R.) 32, 896. [English transl. : Soviet Physics JETP 5, 730 (1957)]

Barber, N. F. and Ursell, F. (1948) Phil. Mag. 39, 345.

Bartlett, M. S. (1955) Stochastic processes. New York, Cambridge University Press.

Blackman and Tukey (1959) The measurement of power spectra. New York, Dover Publications Inc.

Bloomfield, Phillip (1966) Bull. Am. Phys. Soc. 11, 170.

Blount, E. I. (1962) Phys. Rev. 126, 1636.

Brandt, G. B. and Rayne, J. A. (1963) Phys. Rev. 132, 1945.

Brunt, D. (1931) Combination of observations. New York, Cambridge University Press.

Callaway, J. (1964) Energy band theory. New York, Academic Press.

---

[1]The same information can be found in Anderson and Gold (1964).

Cohen, M. and Blount, E.I. (1960) Phil. Mag. 5, 115.

Cullity, B. D. (1956) Elements of x-ray diffraction. Reading, Massachusetts, Addison-Wesley Publishing Company, Inc.

Dingle, R. B. (1952) Proc. Roy. Soc. (London) A211, 517.

Elliot, R. J. (1954) Phys. Rev. 96, 280.

Fawcett, E. (1962) Phys. Rev. 128, 154.

Fawcett, E. and Griffiths, D. (1962) J. Phys. Chem. Solids 23, 1631.

Gantmakher, V. F. (1962), J. Exptl. Theoret. Phys. (U.S.S.R.) 42, 1416. [English transl. : Soviet Physics JETP 15, 982 (1962)]

Gantmakher, V. F. (1962b), J. Exptl. Theoret. Phys. (U.S.S.R.) 43, 345. [English transl. : Soviet Physics JETP 16, 247 (1963)]

Gantmakher, V. F. (1963) J. Exptl. Theoret. Phys. (U.S.S.R.) 44, 811. [English transl. : Soviet Physics JETP 17, 549 (1963).]

Girvan, R. F. (1964) High-frequency de Haas-van Alphen effect in tungsten. Unpublished M. S. thesis. Ames, Iowa, Library, Iowa State University of Science and Technology.

Gold, A. V. (1958) High field de Haas-van Alphen studies in lead. Unpublished Ph. D. thesis. Cambridge, England, Library, University of Cambridge.

Goldstein, H. (1953) Classical mechanics. Reading, Massachusetts, Addison-Wesley Publishing Company, Inc.

Harrison, W. A. (1960) Phys. Rev. 118, 1190.

Hok, Gunnar (1948) J. Appl. Phys. 19, 242.

International Telephone and Telegraph Corporation (1956) Reference data for radio engineers. New York, American Book-Stratford Press Inc.

Jenkins, Francis A. and White, Harvey E. (1957) Fundamentals of optics. New York, McGraw-Hill Book Company Inc.

Jones, C. K. and Rayne, J. A. (1965) Proceedings of the IXth International Conference on Low Temperature Physics p. 790. New York, Plenum Press.

Kendall, M. G. (1946) Contributions to the study of oscillatory time-series. New York, Cambridge University Press.

Koch, J. F., Stradling, R. A., and Kip, A. F. (1964) Phys. Rev. 133, A240

Koch, J. F. and Wagner, T. K. (1966) Radio frequency size effect studies in potassium. University of Maryland department of physics and astronomy technical report 547, College Park, Maryland.

Lifshitz, I. M. and Kaganov, M. I. (1959) Usp. Fiz. Nauk. 69, 419. [English Transl. : Soviet Physics Uspekhi 2, 831 (1960)]

Lifshitz, I. M. and Kosevich, A. M. (1955) J. Exptl. Theoret. Phys. (U.S.S.R.) 29, 730. [English Transl. : Soviet Physics JETP 2, 636 (1956)]

Lomer, W. M. (1962) Proc. Phys. Soc. (London) A80, 489.

Lomer, W. M. (1964) Proc. Phys. Soc. (London) A84, 327.

Loucks, T. L. (1965a) Phys. Rev. Letters 14, 693.

Loucks, T. L. (1965b) Phys. Rev. 139, 1181.

Loucks, T. L. (1966) Phys. Rev. 143, 506.

Luttinger, J. M. (1951) Phys. Rev. 84, 814.

Luttinger, J. M. (1960) Phys. Rev. 119, 1153.

Mackintosh, A. R. (1960) Ultrasonic absorption in metals. Unpublished Ph. D. thesis. Cambridge England, Library University of Cambridge.[1]

Mackintosh, (1963) The interaction of long-wavelength phonons with electrons. In Bak, T. A. ed. Phonons and phonon interactions: Aarhus summer school lectures. pp. 181-220. New York, W. A. Benjamin Inc.

---

[1]See also Mackintosh (1963)

Mattheiss, L. F. (1964) Phys. Rev. 134, A970.

Mattheiss, L. F. and Watson, R. E. (1964) Phys. Rev. Letters 13, 526.

Migdal, A. B. (1957) J. Exptl. Theoret. Phys. (U.S.S.R) 32, 399. [English transl. : Soviet Phys. JETP 5, 333 (1957)]

Munarin, J. A. and Marcus, J. A. (1966) Bull. Am. Phys. Soc. 11, 170.

Nix, F. C. and MacNair, D. (1942) Phys. Rev. 61, 74.

Onsager, L. (1952) Phil. Mag. 43, 1006.

Pines, David (1963) Elementary excitations in solids. New York, W. A. Benjamin, Inc.

Pippard, A. B. (1960) Reports on Progress in Physics 23, 176.

Pippard, A. B. (1961) The dynamics of conduction electrons. In DeWitt, C., Dreyfus, B., and De Gennes, P. G., eds. Low temperature physics: lectures delivered at Les Houches Summer School of Theoretical Physics. pp. 1-146. New York, Gordon and Breach, Science Publishers, Inc.

Pippard, A. B. (1963) Proc. Roy. Soc. (London) A272, 192.

Rayne, J. A. (1964) Phys. Rev. 133, A1104.

Rudra, A. (1955) Sankhyā 15, 9.

Schuster, A. (1900) Trans. Camb. Phil. Soc. 18, 107.

Shoenberg, D. (1957) The de Haas-van Alphen effect. In Gorter, C. J., ed. Progress in low temperature physics. Vol. 2, pp. 226-265. New York, Interscience Publishers Inc.

Shoenberg, D. (1962) Phil. Trans. Roy. Soc. (London) A255, 12.

Sondheimer, E. H. (1950) Phys. Rev. 80, 401.

Sparlin, D. M. and Marcus, J. A. (1963) Bull. Am. Phys. Soc. 8, 258.

Sparlin, D. M. and Marcus, J. A. (1964) Bull. Am. Phys. Soc. 9, 250.

Sparlin, D. M. and Marcus, J. A. (1966) Phys. Rev. 144, 484.

Terman, Frederick Emmons (1943) Radio engineers' handbook. New York, McGraw-Hill Book Company, Inc.

Walsh, Walter M. Jr. (1964) Phys. Rev. Letters 12, 161.

Walsh, W. M. Jr., and Grimes, C. C. (1964) Phys. Rev. Letters 13, 523.

Walsh, W. M. Jr., Grimes, C. C., Adams, G., and Rupp, L. W. Jr. (1965) Proceedings of the IXth International Conference on Low Temperature Physics, p. 756. New York, Plenum Press.

Whittaker, E. and Robinson, G. (1956) The calculus of observations. London, England, Blackie and Son Ltd.

Windmiller, L. R. and Priestley, M. G. (1965) Solid State Communications 3, 199.

Wold, Herman (1938) Study in the analysis of stationary time series. Uppsala, Sweden, Almquist and Wiksells.

Wood, J. H. (1962) Phys. Rev. 126, 517.

Ziman, J. M. (1964) Principles of the theory of solids. New York, Cambridge University Press.

VII. ACKNOWLEDGMENTS

The author wishes to express his gratitude to Dr. A. V. Gold for his guidance and support throughout the course of this investigation. Several helpful discussions with Dr. R. C. Young and Dr. T.L. Loucks are also acknowledged.

Many of the bookkeeping operations necessary for keeping track of all of the data and of the results of calculations were carried out by Mrs. Evelyn Blair. Mrs. Blair also kindly assisted in checking the preliminary results of many of the computations. Several persons have assisted in the analysis of the data at one time or another. The contributions of Mrs. Karen Stone, Mrs. Barbara Becker, and Mr. T. H. Koch in this respect are especially appreciated. Mrs. Becker also tabulated the final results of all the calculations for the model electron jack. Mr. O. M. Sevde provided helpful advice and assistance on many experimental problems.

Special thanks are extended to the author's wife Mary, who by her patience made continuation of this study possible.

VIII. APPENDIX

Appendix A: Further Discussion of Data Analysis Procedures

As we discussed in Section III-A most of the data in this study could be analyzed by the standard methods of either measuring magnetic field values at only two points or measuring the field value for every cycle and obtaining the frequency from the slope of a plot of the reciprocal field positions of cycle maxima and minima versus integers. However, these procedures were not sufficiently precise to determine the orientation dependence of the ϵ_u oscillations near [001] and further methods of analysis were therefore investigated. Several methods were tried and eventually the Whittaker and Robinson (1956 p. 343) method of periodogram analysis (see Appendix E) was adopted. Several authors (Whittaker and Robinson 1956, Brunt 1931, Kendall 1946, Wold 1938, Bartlett 1955) have discussed this or closely related methods of frequency analysis, and this method seems to be perfectly valid for finding the frequencies of pure sine waves making up a waveform. The data for the ϵ_u oscillations which were taken using the shunt ignitron (see Figure 10a) appear to almost satisfy the criterion of being a combination of sine terms having only weak field dependence of amplitude; in fact, the discussion in Appendix B which relates to pure sine waves may be more appropriate for these data than the discussion here. However, the justification

of the application of periodogram analysis to some of the other dHvA data is not so straightforward, and some of these data cannot be analyzed by other methods. Nevertheless, we believe we have made some progress even in analyzing complicated data. Part of the reason that improved results were obtained is probably due to systematic attempts to eliminate reading errors. A second reason for improved results is probably due to automatic computer determination of the straight line slopes so that a fairly comprehensive examination of the data can be rapidly undertaken without, for instance, replotting sections of reciprocal field versus cycle number plots on an expanded scale for accurate slope determination by hand. A third and important improvement is the use of periodogram analysis, since as we shall see below, this method may yield results even in some cases when considerable filtering has been used to produce sharp resonance envelopes but neighboring frequencies were not resolved by the filtering.

The problem at hand is the frequency analysis (in $1/H(t)$) of a signal $y(t)$ which results when oscillations which occur in the magnetization of our small crystals in the magnetic field $H(t)$ are detected using a pickup coil. The oscillatory e.m.f. is proportional to $dM/dt = (dM/dH)(dH/dt)$, and from Equation 12 we expect that dM/dH is of the form

$$\frac{dM}{dH} = \sum_i B_i(H,F_i)\sin\left(\frac{2\pi F_i}{H} + \gamma_i\right) \quad ,$$

where the B_i vary only slowly with H.

As was explained in Section II-D, the pickup circuit is made resonant by connecting a small capacitor across the pickup coil. In this case, the signal y(t) which is observed across the capacitor in the R-L-C pickup circuit would be given to within a constant factor by the solution of the equation

$$L\, d^2y/dt^2 + R\, dy/dt + y/C = dM/dt \quad , \qquad (16)$$

an equation which appears to be very difficult to solve explicitly, since the "frequency" ν_i of each of the oscillatory terms F_i in dM/dt varies with time ($\nu_i = F_i\dot{H}/H^2$). (For discussions of the form of y(t) when the frequency of the driving function varies linearly with time see Barber and Ursell (1948) and Hok (1948). Shoenberg (1962) has discussed some of the features of y(t) which are relevant to the de Haas-van Alphen effect.) The net effect of the circuitry is to produce a signal y(t) which is quite different from the original sum of sinusoidal terms in which each term had a rather slowly-varying amplitude and in which the argument varied with field exactly as $2\pi F_i/H$.

We can reproduce qualitatively some of the features of the signal y(t) by supposing that (by analogy to the case of a constant frequency driving function) it can be approximated

in the form

$$y(t) = \sum_i A_i((H(t),F_i)\sin(\frac{2\pi F_i}{H} + \phi_i(t)) \ .$$

By analogy to the forced harmonic oscillator, each A_i defines a resonant envelope when the time frequency ν_i of the corresponding dHvA term passes through the resonant frequency of the pickup circuit; as we mentioned in Section II-D, the partial frequency analysis which is performed in this way by the resonant pickup circuit is quite helpful in separating different frequency terms in the dHvA spectrum when these terms are well-resolved by the resonant circuit alone and each term is dominant over a sufficient range of cycles for accurate frequency measurements to be obtained. However, some of the same features of the resonant technique which are usually so helpful are somewhat of a hindrance to setting up analysis procedures to find the de Haas-van Alphen frequencies in a signal when it is not possible to obtain sufficient resolution to find all the dHvA terms using the resonant technique alone. For instance, due to the amplitude modulation and phase shift produced by the resonant circuit, it is often impossible to determine the subordinate frequencies in a complex waveform by examining those irregularities in amplitude which would have been regular beats, had the regularity not been destroyed by the amplitude variation and phase shift due to the resonant circuit. A further

complication arises due to the tendency towards ringing at the resonant frequency of the pickup circuit after the resonance maximum has been passed (Barber and Ursell 1948). Thus the effective frequency of the signal during some small interval of time after the resonance maximum has been passed may be the resonant frequency of the pickup circuit rather than the frequency appropriate to the de Haas-van Alphen signal. Finally, the periodogram of a signal in a sharp resonance envelope which has been achieved by considerable filtering is expected to show not only a term at the frequency of the fundamental dHvA term making up the resonance, but also side peaks at those frequencies which are necessary to construct the envelope shape.

In spite of the above complications, we chose to attempt a more detailed frequency analysis of the de Haas-van Alphen signal as it was rather than attempting a detailed evaluation of the effects of the circuitry on the form of dM/dt so that these effects could be compensated for. Only crude attempts were made to take into account the existence of the resonant pickup circuit. It was hoped that the effects of the resonant circuit (plus filters) were not so serious that they would prevent the detection of important periodicities in the data and that in spite of the effects of the circuitry, the regions of an oscillogram which would contribute most to the analysis would be those regions in which the basic

de Haas-van Alphen periodicity was least affected by phase shift and ringing. We have not worked out any explicit mathematical criteria for the validity of the periodogram analysis when applied to a signal which has been passed through filters to give a sharp resonance envelope. Instead, the success of the procedures was judged by analyses which were obtained both for actual de Haas-van Alphen data and for test signals which were constructed mathematically to approximate actual dHvA signals. Even though the procedures to be described are rather crude, more precise and better resolved results have been obtained than could have been hoped for using only the resolution of the resonant circuit.

The data analysis was carried out using an IBM 7074 computer. The input data to the computer program were coordinates which had been read from the oscillograms as described in Section II-D. After the error checking steps described in that section had been carried out, the coordinates for the field trace were smoothed by using the method of least squares (cf. Whittaker and Robinson 1956 p. 291) to fit a parabolas to successive sets of nine consecutive coordinates (x_i, y_i). Here x_i and y_i are the x and y coordinate respectively of the i^{th} point measured from the field trace. The y coordinate of each fitted parabola evaluated at the x-coordinate of the central one of the 9 points was used as the field trace coordinate to find the reciprocal

field value corresponding to this central point.

After all of the reciprocal field values had been calculated, a further check against reading errors was carried out by checking to see that the reciprocal field values formed a monotonically increasing sequence. (The oscillograms were always read from the high field end to the low field end.) If any reading errors were found by this check of if any reading errors had been found by the checks described on page 36, the data analysis procedure for this oscillogram was discontinued and all of the data cards were listed. An error message was typed for each card which contained a reading error so that the reading error could be found and corrected before further analysis was undertaken. Judging by the evenness of artificial waveforms which were plotted out as a function of reciprocal field, the smoothing procedure for the field trace coordinates (combined with the smoothing of the calibration lines described on page 36) worked quite well in averaging out some of the scatter inherent in reading the coordinates from the projected image of the oscillogram.

To test the overall effectiveness of the data analysis procedure, we used a modified version of the data analysis program which differed from the actual data analysis program only in that the data input steps in the original program were replaced by a subroutine[1] which generated the points of

[1]This subroutine was written by E.C. Clark, Ames Laboratory of the A.E.C., Iowa State University of Science and Technology.

amplitude maximum and minimum of a test signal. The test signal was of the form

$$y(H) = \sum_{i=1}^{N} A_i \sin\left(\frac{2\pi F_i}{H} + \phi_i\right) \qquad (17)$$

where

$$A_i = B_i\left[1 + \omega^2 Q^2/\omega_o^2)(1 - \omega^2/\omega_o^2)^2\right]^{-\frac{1}{2}}$$

and

$$\phi_i = \tan^{-1}\left[Q\frac{\omega_i}{\omega_o}(1 - \frac{\omega_o^2}{\omega_i^2})\right.$$

The quantity H was given by $H = H_o \sin\Omega t$ and ω_i was given by

$$\omega_i = \frac{2\pi F_i}{H^2}\Omega\sqrt{H_o^2 - H^2}$$

It was hoped that the frequency analysis of such a signal would give some indication of the validity of the analyses which were obtained for actual data. We will use a signal like that in Equation 17 as an example in discussing the data analysis program.

As a further aid to detecting errors (errors such as skipping a cycle are not detected by the previous steps), the waveform of the signal which was being analyzed was always displayed graphically using an IBM 1627 plotter. Such a plot for one of the test signals is shown in Figure 41a, and the plot of reciprocal field values at points of maximum and minimum amplitude of this signal are plotted versus cycle number in Figure 41b. Using the reciprocal field value

Figure 41. Test signal for data analysis procedures

a. Waveform constructed by connecting the points of amplitude maximum and minimum of a signal defined by Equation 17 with straight lines. We have chosen the four frequencies $F_1 = 8.78 \times 10^6$G, $F_2 = 7.66 \times 10^6$G, $F_3 = 6.75 \times 10^6$G, $F_4 = 6.43 \times 10^6$G with corresponding amplitudes $B_1 = .4$, $B_2 = .4$, $B_3 = 1.0$, $B_4 = .8$. The circuit quality factor Q is 30 and the resonant frequency is 10^5Hz. The magnetic field was varied as $(1.1 \times 10^5\text{G})\sin 200t$ from 35kG to 50kG.

b. Plot of reciprocal field values for amplitude maxima and minima versus integers. We have attempted to draw straight line segments through the points.

c. Frequency versus cycle curve found from weighted averages of linear least squares fitting calculations.

d. Smoothed frequency versus cycle curve found by taking weighted averages of the frequencies on the curve in Figure 41c. Only the middle frequency predicts one of the input frequencies correctly. (See page 39 for weaknesses of this method of predicting frequencies.)

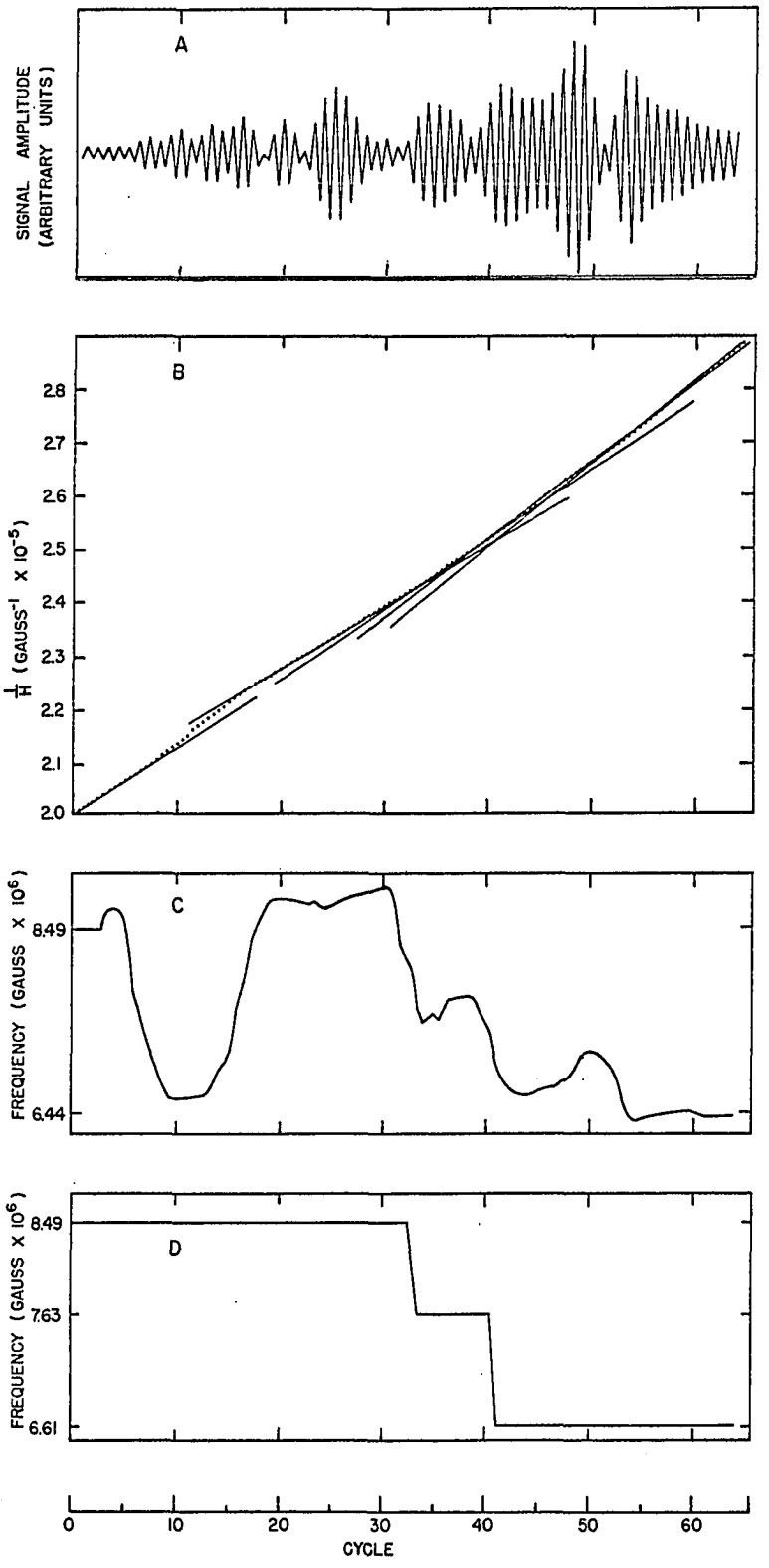
A
SIGNAL AMPLITUDE (ARBITRARY UNITS)
B
$\frac{1}{H}$ (GAUSS^{-1} x 10^{-5})
2.8
2.7
2.6
2.5
2.4
2.3
2.2
2.1
2.0
C
FREQUENCY (GAUSS x 10^6)
8.49
6.44
D
FREQUENCY (GAUSS x 10^6)
8.49
7.63
6.61
0
10
20
30
40
50
60
CYCLE

and cycle number coordinates like those on Figure 41b, linear least squares fitting calculations were carried out as is described on page 39.

The results of the least squares calculations were used in several ways. While least squares calculations were being carried out using the first fitting length N_i, the fastest frequency and the slowest frequency found were collected. If no frequency range had been read as input, the above maximum and minimum frequency were used to set the frequency range over which the ideogram and periodogram were calculated.

In some cases it was desirable to use the results of the least squares calculations directly. The result of the least squares calculation for each set of points for which the computed error estimate was minimal with respect to immediately adjacent sets of points was printed out for direct examination if the fitting length was greater than 30 half cycles.

The results of the least squares calculations were also displayed as an ideogram as was explained on page 40. An ideogram for the signal of Figure 41a is shown in Figure 42b. It is evident from this figure that the ideogram results cannot be relied on completely since the frequency at 7.63 x 10^6G is missing in the ideogram spectrum. The nature of the frequency spectra for actual de Haas-van Alphen data are quite variable however, and cases arise when an intercomparison of all the methods of analysis is necessary in

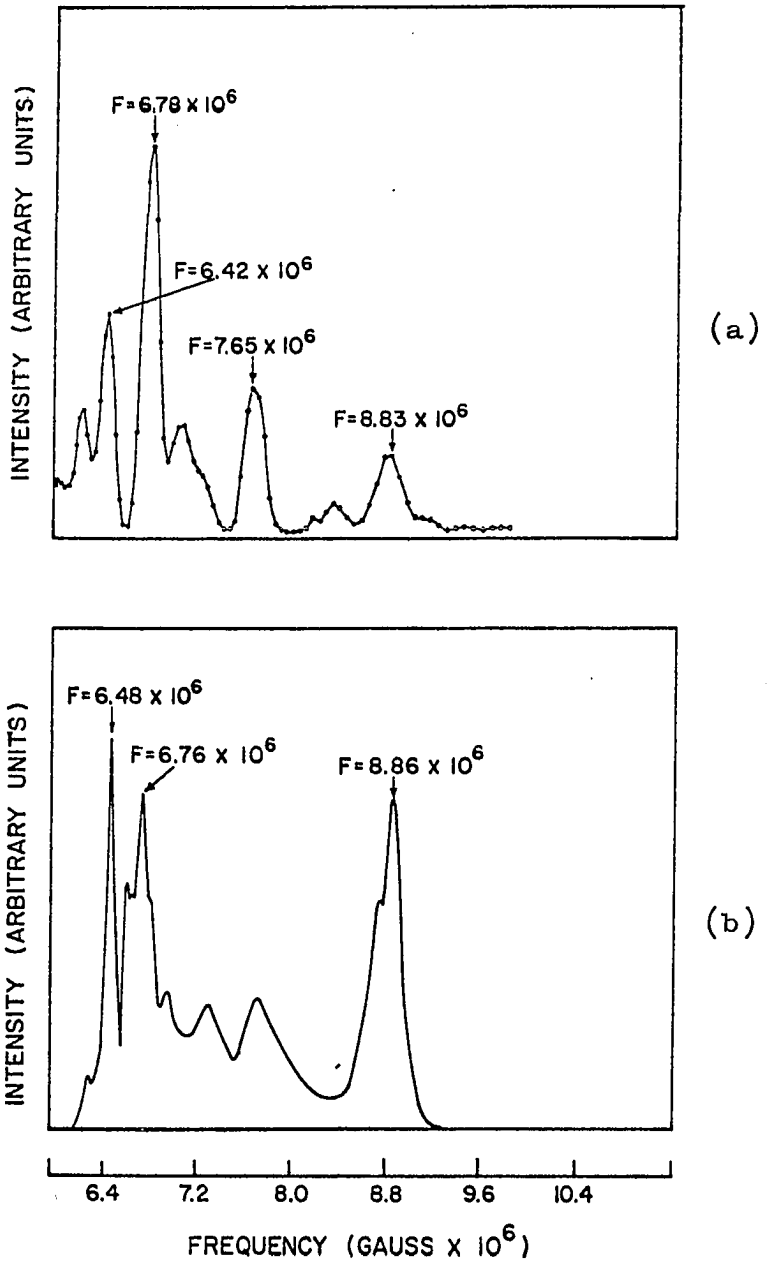

Figure 42. Computed estimates of the frequency spectrum of waveform of Figure 41a

a. Periodogram

b. Ideogram

order to find the dHvA frequencies in the data. For instance, in cases where some of the dHvA terms on an oscillogram are well-resolved by the resonance technique, we are quite certain that the ideogram predicts the frequencies correctly. One oscillogram may contain both terms which are resolved by the resonance technique and terms which are not; periodogram analysis is necessary to find the frequencies in the latter case, and the ideogram provides a convenient check on the periodogram in the former case.

A frequency versus cycle curve was constructed by assigning each frequency which was calculated by linear least squares fitting to the central one of the points which were used to calculate that frequency. Then as successive frequency calculations were made with different line lengths, a weighted average of the frequencies corresponding to each point on the reciprocal field versus cycle number plot was accumulated along with a total weight. The frequency versus cycle curve was used to obtain estimates of the initial and final points for the region of dominance of each frequency by converting it to a smoothed frequency versus cycle curve (Figure 41d).

For each oscillogram the first point on the frequency versus cycle curve was chosen as the initial point p_1 for the first horizontal line segment. Then the last point p_L on the frequency versus cycle curve with a larger frequency

value than the initial point was found. The final point p_{final} for the first horizontal line segment was the last point on the frequency versus cycle curve whose ordinate differed by less than one percent from that of point p_L. A weighted average F_{ave} of points p_1 to p_{final} on the frequency versus cycle curve was then computed, and the ordinates of these points were set equal to F_{ave}. Each point p_1 to p_{final} was given a weight equal to the computed weight for F_{ave}. Then the point $p_{final} + 1$ was defined as the initial point for line segment number two and the process was repeated until the last point had been used. Then the first point on the resulting new frequency versus cycle curve was defined as the first point for the first line segment and the preceding process was repeated, except that now p_{final} was taken to be the last point on the frequency versus cycle curve for which the frequency was within 100/N percent of p_L. Here N is the number of points in the longest horizontal line segment in the frequency versus cycle curve. This process was repeated until each of the line segments in the smoothed frequency versus cycle curve were separated by more than 400/N percent in frequency. When the data were well resolved by the resonance technique so that each dHvA term in the oscillogram dominated for a substantial number of cycles, the frequencies of the longer horizontal line segments in the resulting smoothed frequency versus cycle

curve were the frequency estimates which would be obtained by drawing straight lines through the reciprocal field versus cycle number points. One possible advantage of computing estimates for the slopes of long straight lines in this way is that by taking weighted averages, some account is taken of how well small groups of points used to calculate each frequency estimate actually fit a straight line. Therefore, regions in which there were reading errors or in which ringing was important should contribute less to the final frequency value than regions where the data were good.

For each oscillogram the plot of reciprocal field values versus cycle number (like Figure 41b) was always displayed automatically and the frequencies and end points for the horizontal lines of the smoothed frequency versus cycle curve (Figure 41d) were printed out. Furthermore the frequencies corresponding to the ten highest peaks in the ideogram were always printed out so that those peaks in the ideogram which predicted the frequencies reliably could be determined by inspection.

The final smoothed frequency versus cycle curve was also used to define specific portions of the data to be scanned through a certain range of frequencies in a succeeding periodogram analysis. As was explained on page 41, the periodogram analysis was performed on elements of an array $\{u_k\}$ and the elements of this array were the amplitudes of a

triangular wave taken at equally-spaced values of the reciprocal magnetic field. If the element u_m, say, of the array was to correspond to a reciprocal magnetic field value H_s and if $H_n^{-1} \leq H_s^{-1} < H_{n+1}^{-1}$ where H_n^{-1} and H_{n+1}^{-1} are reciprocal magnetic field values corresponding to successive amplitude maxima and minima, then u_m was calculated from the formula

$$u_m = \frac{A_{i+1} - A_i}{H_{i+1}^{-1} - H_i^{-1}}(H_s^{-1} - H_i^{-1}) + A_i \ .$$

Here A_i and A_{i+1} are the amplitudes read from the oscillogram at points i and i+1. About 10,000 elements u_m were calculated in this way, so that on the average, about 10,000/N elements were stored for each cycle of a picture which contained N cycles. Successive elements of the sequence $\{u_k\}$ differed by about $(H^{-1}(\text{last cycle}) - H^{-1}(\text{first cycle}))/10{,}000 = dH^{-1}$ which is the spacing in period at which ordinates are calculated on the periodogram. A smallest value of dH^{-1} was fixed by the storage capacity of the IBM 7074 computer,[1] and dH^{-1} was always set equal to this smallest value. In most cases the frequencies at which ordinates on the periodogram were computed were sufficiently closely spaced that the uncertainty due to the spacing between the computed ordinates in the frequency at which a peak in the periodogram occurred

---

[1]We are indebted to G.F. Covert, Experimental Physics Group XII for providing two autocoder subroutines by means of which the program could be run in the addstorage mode so that sufficient resolution could be obtained even though the FLAG monitor system was used.

was not important.

For the data which were taken using the shunt ignitron to determine the orientation dependence of the slow frequency oscillations near $[00\bar{1}]$, however, the spacing between frequencies at which ordinates were calculated on the periodogram was sometimes as large as 0.7 percent even though about 15,000 elements u_k were used when these data were being processed. (An earlier version of the data processing program in which more storage space was available for $\{u_k\}$ was used for these data.) This uncertainty is enough to show up as scatter on a plot such as Figure 11a. None of the standard methods for interpolating between two ordinates on either side of a periodogram peak to find a more accurate frequency for the peak (cf. Brunt 1931 p. 211, Whittaker and Robinson 1956 p. 354) were tried. Instead, more precise frequency values were estimated by sketching a curve through the periodogram for a sine wave (Appendix E), and by taking the frequency at which the peak occurred in this sketched curve as the frequency predicted by the periodogram. The position of this peak can certainly be estimated to at least 0.3 percent if the two calculated ordinates on either side of the peak are spaced by 0.7 percent.

The process by which certain parts of the data were selected to be analyzed for a certain periodicity p_o can be explained quite simply if it is remembered that because of

Equation 14 higher frequency terms are expected to dominate at higher fields. Thus, since oscillograms were always read from the high field end to the low field end, higher frequency terms are always expected to appear toward the beginning of the sequence of data points. We can picture the selection of the appropriate elements for the processing as sliding a fixed length line along straight lines connecting the mid-points of horizontal lines on a plot which is like Figure 41d except that the abscissa is reciprocal field rather than cycle number. For a scan carried out at frequency F_o the abscissa of the central point on the sliding line is the point for which the ordinate of the line connecting the centers of adjacent horizontal line segments in the frequency versus reciprocal field relationship is F_o. The length of the line was equal to the number of elements of the u array which corresponded to the longest horizontal line on the smoothed frequency versus cycle curve (with the addition of a sufficient number of elements so that all of the elements of the u array corresponding to the longest horizontal line on the smoothed frequency versus cycle curve were included for all scans carried out at frequencies which did not differ from the frequency of the longest line on the smoothed frequency versus cycle curve by more than $4/N \times 100$ percent.) Here N is the number of half cycles contained in the longest line on the smoothed frequency versus cycle curve.

Such a method of selecting only parts of the u array for periodogram analysis at each frequency is necessary for oscillograms which contain a wide range of frequencies since the periodogram analysis yields peaks for a term F_1 not only at the fundamental frequency F_1 but also at each subharmonic $F_1/2, F_1/3 \ldots$; if one of these subharmonic peaks were to fall in the midst of peaks from lower frequency terms, it would needlessly complicate the interpretation of the periodogram. It was thought that the addition of this feature would improve the periodogram analysis even when subharmonics were not important since at each position of the sliding line the data corresponding to field positions between the starting field and ending fields of the sliding line correspond more closely to a pure sine wave than do all of the data taken together. However, except for cases in which complications due to subharmonics were important, it was found that the data analyses were not significantly improved by the addition of this feature; those analyses which had previously been considered reliable again yielded peaks at the same frequencies, and the only change seemed to be that the relative strengths of peaks in the periodogram corresponding to low amplitude signals were increased. (This is because of the normalization discussed in Appendix E.) Those data for which the periodogram could previously not be interpreted still yielded periodograms which could not be interpreted.

While it is disappointing in one respect that the data selection procedures did not seem to be effective in improving the reliability of the analyses (except where subharmonic complications were eliminated), it is also encouraging that for analyses which were previously considered reliable the frequencies of the periodogram peaks were not shifted when only parts of the data were used to compute the periodogram ordinate at each frequency. Thus it would seem that the periodogram ordinate at frequency F_1 is not appreciably affected by the presence of data arising from a term with frequency F_2 which is well separated ($\sim$20 percent in the case of Figure 41a) in frequency from F_1. Such a conclusion could also be reached by examination of Figure 12. The periodogram in this figure was computed using all of the data and in spite of the fact that the amplitudes of lower frequency terms were quite large, periodogram ordinates between the two small higher frequency peaks are quite small.

Further examinations of the characteristics of the periodograms for signals which are amplitude modulated and contain a phase shift and in which the dominant frequency changes from one section of the data to the next were carried out by applying the periodogram analysis to signals defined by Equation 17. One of these tests was carried out by keeping all of the parameters in Equation 17 constant except Q. As Q was increased, small spurious peaks appeared in addition

to the main peaks and the periodogram became successively more difficult to interpret. The signal in Figure 41a represents the largest value of Q for which it was felt that the periodogram could be reliably interpreted since as Q was further increased, the spurious peaks became almost as large as the main peaks.

Appendix B: Two Component Beat Patterns

In this appendix we will consider the frequencies which would be obtained from an ideogram or straight line method if each cycle maximum and minimum of the signal

$$y = A_1 \cos\frac{2\pi F_1}{H} + A_2 \cos\frac{2\pi F_2}{H} \quad (A_1 > A_2 > 0) \tag{18}$$

were measured. The argument is a trivial extension of the argument used by Gold (1958) to the case of strong beating. It was never necessary to make quantitative use of these results, but a knowledge of their form was found to be useful in assessing the reliability of data analysis which were obtained.

Cycle maxima and minima occur when $\frac{dY}{d(1/H)} = 0$. If $x = 1/H$, we can write

$$-\frac{1}{2\pi}\frac{dy}{dx} = A_1 F_1 \sin 2\pi F_1 x + A_2 F_2 \sin 2\pi F_2 x \tag{19}$$

The frequencies which are measured by measuring cycle maxima and minima will depend on the rate at which zeros occur in the quantity (19). There are three cases to be considered.

Case 1: $A_1F_1 > A_2F_2$

If $\Delta F = F_1 - F_2$, we can write

$$-\frac{1}{2\pi}\frac{dy}{dx} = C \sin(2\pi F_1 x + \psi) \tag{20}$$

where

$$C = (A_1^2F_1^2 + 2A_1A_2F_1F_2\cos 2\pi\Delta Fx + A_2^2F_2^2)^{\frac{1}{2}} \tag{21}$$

and

$$\psi = \tan^{-1}\left(-\frac{A_2F_2\sin 2\pi\Delta Fx}{A_1F_1 + A_2F_2\cos 2\pi\Delta Fx}\right) \tag{22}$$

C is always greater than zero, so zeros in $\frac{dy}{dx}$ occur when $2\pi F_1 x + \psi = n\pi$, n = 0,1,2,3,..., and the repetition rate for cycle maxima is

$$\frac{1}{2}\frac{dn}{dx} = F_1 + \frac{1}{2\pi}\frac{d\psi}{dx}$$

The repetition rate written out in detail is

$$\frac{1}{2}\frac{dn}{dx} = F_1 + \frac{\Delta F(-A_1A_2F_1F_2\cos 2\pi\Delta Fx - A_2^2F_2^2)}{A_1^2F_1^2 + 2A_1A_2F_1F_2\cos 2\pi\Delta Fx + A_2^2F_2^2} \tag{23}$$

Beat waists occur in $\frac{dy}{dx}$ (and in y) when $\cos 2\pi\Delta Fx = -1$, and beat maxima occur when $\cos 2\pi\Delta Fx = 1$ so from Equation 23 we find that the effective frequency at beat minimum is

$$F_{min} = F_1 + \frac{\Delta FA_2F_2}{A_1F_1 - A_2F_2} \tag{24}$$

and the effective frequency at beat maximum is

$$F_{max} = F_1 - \frac{\Delta FA_2F_2}{A_1F_1 + A_2F_2} \tag{25}$$

Since $A_1F_1 > A_2F_2$, we must have $-\pi/2 < \Psi < \pi/2$ and in this case the frequency which will be found by counting a large number of cycles will be F_1, since the maximum counting error due to changes in Ψ is $\frac{1}{2}$ cycle.

Case 2: $A_1F_1 < A_2F_2$

We can rewrite Equation 20 as

$$-\frac{1}{2\pi}\frac{dy}{dx} = C\sin(2\pi F_2 x + \Psi') \tag{26}$$

where now $-\pi/2 < \Psi' < \pi/2$, and by the preceding argument, the frequency F_2 will be found by counting a sufficient number of cycles. For this case, the relations analogous to Equations 24 and 25 are

$$F_{min} = F_2 + \frac{\Delta F' A_2 F_2}{A_2F_2 - A_1F_1} \tag{27}$$

$$F_{max} = F_2 - \frac{\Delta F' A_1 F_1}{A_2F_2 + A_1F_1} \tag{28}$$

where $\Delta F' = F_2 - F_1$.

Case 3: $A_1F_1 = A_2F_2$

C becomes $2\cos\pi\Delta Fx$ and Ψ becomes $-\pi\Delta Fx$, so we can write

$$-\frac{1}{2\pi}\frac{dy}{dx} = 2\cos\pi\Delta Fx\sin\left[2\pi\left(\frac{F_1 + F_2}{2}\right)x\right] \tag{29}$$

The frequency which is measured in this case by counting a sufficient number of cycles is the average frequency.

In summary, if $A_1F_1 > A_2F_2$, the dominant frequency F_1

will be measured; and if $A_1F_1 < A_2F_2$, the subordinate frequency F_2 will be measured. In either case, if $F_{min} > F_{max}$, the second term is lower in frequency than the measured term; but if $F_{min} < F_{max}$, the second term is higher in frequency than the measured term.

In Figure 43 we have illustrated the sort of results which are obtained when different data analysis procedures are applied to a signal which is made up of two terms of nearly equal amplitude and frequency. In Figure 43a, the function

$$y = 20 \cos(2\pi 21x) + 19 \cos(2\pi 23x)$$

has been approximated by connecting successive points of amplitude maxima and minima with straight lines. The effective frequency which is found by taking one half the reciprocal of the difference between the x-values corresponding to successive points of maximum and minimum amplitude is plotted as a function of cycle number in Figure 43b. In this case $d\psi/dx$ is very nearly constant over most of the regions corresponding to the beat maxima in Figure 43a; in this case, the ideogram which is shown in Figure 43c contains a peak at the frequency 22.03 which is the effective frequency over the beat maxima. The periodogram, however, (also shown in Figure 43c) yields two peaks at the correct frequencies, and a straight line fit to all of the cycles yields the frequency 22.98 as is expected since this case

Figure 43. Illustrating the analysis of a signal with almost zero beat waists

a. Waveform constructed by connecting the points of amplitude maxima and minima of the signal
$$y = 20\cos(2\pi 21x) + 19\cos(2\pi 23x)$$
with straight lines.

b. Effective frequency F_{eff} versus half cycles. ($F_{eff} = 0.5/\Delta x$ where Δx = distance between adjacent cycle maxima and minima.)

c. Periodogram and ideogram for the signal in Figure 43a. The periodogram peaks occur at frequencies of 23.016 and 20.972. The ideogram peak occurs at a frequency of 22.032.

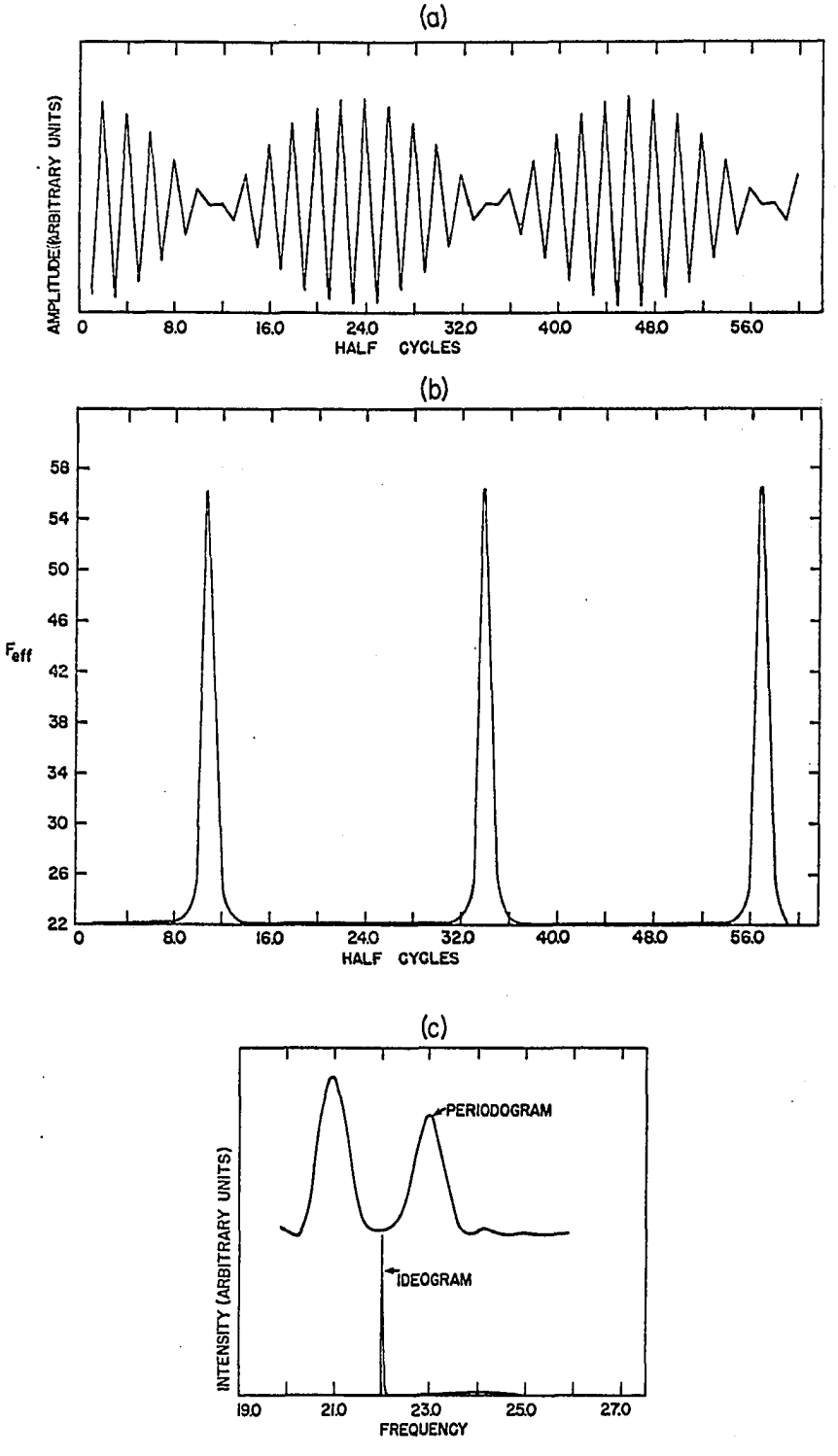
(a)
AMPLITUDE(ARBITRARY UNITS)
0
8.0
16.0
24.0
32.0
40.0
48.0
56.0
HALF CYCLES
(b)
F_{eff}
58
54
50
46
42
38
34
30
26
22
0
8.0
16.0
24.0
32.0
40.0
48.0
56.0
HALF CYCLES
(c)
PERIODOGRAM
IDEOGRAM
INTENSITY (ARBITRARY UNITS)
19.0
21.0
23.0
25.0
27.0
FREQUENCY

corresponds to case 2.

It is evident even from the simple case illustrated in Figure 43 that the frequencies at which peaks occur in the ideogram are not likely to give a reliable indication of the frequencies in a signal which is composed of two or more terms which are beating. An example of a case in which the ideogram is even more misleading is shown in Figure 44. In this case a peak occurs in the ideogram not only at the frequency corresponding to the effective frequency at beat maximum, but also at a frequency for which $d\psi/dx$ is nearly zero. The signal in Figure 44 corresponds to case 1 so that $d\psi/dx = 0$ when the effective frequency is equal to 10.

Consideration of simple cases like those shown in Figure 43 and Figure 44 is useful because it predicts some of the characteristics which are found in the analyses of actual de Haas-van Alphen data. In the actual data, signals which consist of several uniform beat envelopes are almost never obtained because of the resonant pickup circuit and the filters. Therefore the periodicity of the beat envelopes usually cannot be found by inspection, as it could be in the signals we have discussed here. Instead it is necessary in many cases to rely on the computer analysis and to judge the reliability af the analysis by comparing the results obtained by different methods of analysis. However, the above

Figure 44. Illustrating the analysis of a waveform containing beats (and a "reading error")

a. Waveform constructed by connecting the amplitude maxima and minima of the signal
$y = .01\cos(2\pi 10x) + .005\cos(2\pi 9x)$
with straight lines

b. Effective frequency F_{eff} versus half cycles ($F_{eff} = 0.5/\Delta x$ where Δx is the spacing between adjacent cycle maxima and minima.)

c. Periodogram and ideogram for signal of Figure 44a. The periodogram peaks occur at 9.997 and 8.945. The ideogram peaks occur at $F_1 = 9.719$ and $F_2 = 10.007$. The frequencies F_1 and F_2 are also indicated on Figure 44b.

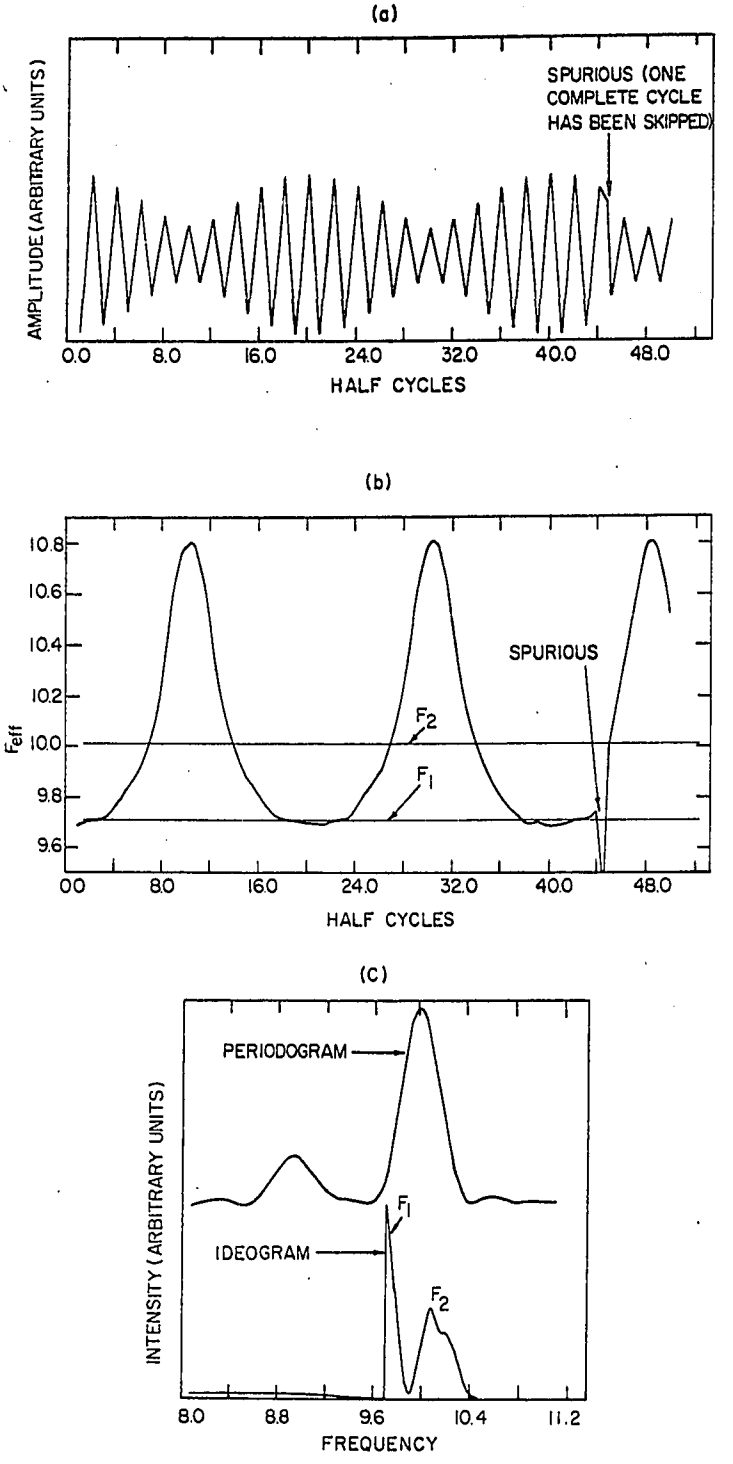
(a)
AMPLITUDE (ARBITRARY UNITS)
SPURIOUS (ONE COMPLETE CYCLE HAS BEEN SKIPPED)
0.0
8.0
16.0
24.0
32.0
40.0
48.0
HALF CYCLES
(b)
F_{eff}
10.8
10.6
10.4
10.2
10.0
9.8
9.6
SPURIOUS
F_2
F_1
00
8.0
16.0
24.0
32.0
40.0
48.0
HALF CYCLES
(C)
INTENSITY (ARBITRARY UNITS)
PERIODOGRAM
IDEOGRAM
F_1
F_2
8.0
8.8
9.6
10.4
11.2
FREQUENCY

discussion shows that we expect spurious peaks in the ideogram whenever two or more terms are beating although the periodogram yielded reliable analyses in these cases; therefore, when two closely-spaced peaks occur in the periodogram and one or more corresponding peaks occur in the ideogram, it is likely that only the frequencies predicted by the periodogram are correct if there is a discrepancy between the predictions of the two methods.

There is one further feature of Figure 44 which is of interest. One complete cycle of the test signal (Figure 44a) has been skipped between half cycle numbers 44 and 45. The computer program which was used to analyze the signal in Figure 44a was the same as the actual data processing program except that all of the input statements in the data processing program were removed and replaced by a subroutine which generated the test signal. Therefore the omission of a cycle between half cycle numbers 44 and 45 corresponds to skipping an amplitude minimum in reading an oscillogram. Even though this error is present in the test signal, the periodogram analysis (Figure 44c) still predicts quite accurately the frequencies which make up the test signal. Other similar tests have been carried out which indicate that the periodogram analysis results are relatively insensitive to minor reading errors. (Many of the major reading errors which can occur are taken care of by the error

checking steps in the input statements of the actual data processing program.)

Appendix C: Magnetic Interaction Effects

An effect which may be important in some of our data is a frequency modulation which occurs because the effective field acting on the electrons in a metal is the magnetic induction field $\underline{B} = \underline{H} + 4\pi\underline{M}$ and not the applied field $\underline{H}$ (Anderson and Gold 1963, Shoenberg 1962). The fact that replacing H by B in the argument of the sine function in Equation 12 could in some cases lead to serious frequency modulation effects was first realized by Shoenberg (1962). (The replacement of H by B in the expression for the magnetization was later justified by Pippard (1963) by a thermodynamical argument.)

Shoenberg considered a single dHvA term

$$M = M_0 \sin(2\pi F/(H + 4\pi M)) \tag{30}$$

Providing that $a = -4\pi dM/dH$ is sufficiently small, Shoenberg has shown that the susceptibility dM/dH can be written

$$dM/dH = -\frac{a}{4\pi}\left[(1 - a^2/8)\cos(2\pi F/H) - a\cos(2\cdot 2\pi F/H) + (9a^2/8)\cos(3\cdot 2\pi F/H) + \ldots\right] \tag{31}$$

(The condition $|4\pi M/H| << 1$ has been used.)

The various terms in Equation 31 represent harmonics which should not be confused with those of Equation 12. For $a \sim \frac{1}{2}$, the amplitudes of the harmonics in Equation 31 are

considerably greater than those predicted in most cases by Equation 12. In addition, as a increases with decreasing temperature, the amplitude of the fundamental term does not increase linearly with a due to the $a^2/8$ term. If the amplitude a is large enough, the $a^2/8$ term leads to a non-linear effective mass plot like those which were found for the α and α_2 oscillations for $H // [1\bar{1}0]$ (Figures 19 and 20).

We can make a crude estimate of the amplitude a for the α oscillations at 1°K when the effective mass data at $[1\bar{1}0]$ were taken by using the formula

$$a = \frac{V \times At \times 10^8}{N\pi r^2 \dot{H} Q} .$$

Here $r \sim .033$ cm is the sample radius and V is the amplitude of the observed signal in volts. The quantity $N \sim 1000$ is an effective number of pickup coil turns linked by the sample flux. $At \sim 2$ is the filter attenuation for 2 filters set to pass 70-140kHz, and Q is an effective pickup circuit quality factor by which the signal amplitude is enhanced at resonance. Studies of the response of our circuit to a time-varying signal by R. Phillips[1] lead to an estimate of $Q \sim 15$. For $V \sim 1$ volt and $\dot{H} \sim 10^7$ gauss/sec, we find $a \sim .2$ for the α oscillations at $[1\bar{1}0]$ so that the signal amplitude could have been affected by the frequency modulation effect and the tailing-off of the effective mass plot in Figure 19 could

[1]R. Phillips, Ames Laboratory of the A.E.C., Iowa State University. Private Communication, 1965.

be explained qualitatively in this way.

The tailing-off of the effective mass plots in Figures 19 and 20 could also be due to amplifier or filter saturation which might have occurred for the stronger low temperature signals. In fact, examination of the data suggests that saturation in the electronics could be important. In Figure 45 we have shown photographs of the α oscillations and of their harmonics at two different temperatures. The fact that the resonant envelope for each of these signals is distorted at the lowest temperatures would seem to indicate a saturation in the electronics. However, for a fixed-frequency input signal, the amplifiers and filters which were used in this experiment are linear over the range of input voltages which were used. The linearity of these components for a time-varying frequency has not been checked, but it seems unlikely that serious saturation effects could have occurred since our signals were well within the quoted range of acceptable input voltages.

The distortion effects which are evident in the shape of the resonance envelopes in Figure 45 could also be due to an amplitude fluctuation effect which was clearly evident in the α oscillations near [001] when they were studied using the shunt ignitron technique. A very long period fluctuation with a period extending over roughly 100 to 150 cycles is shown in Figure 46a. An intermediate length

Figure 45. Illustrating the deterioration of the resonance envelopes for the α oscillations and their harmonics as the temperature is lowered (All signals have been passed through two electronic filters set to pass frequencies in the range 70-140kHz, and the resonant frequency was 105kHz.)

a. α oscillations for H// [1$\bar{1}$0]
Temperature: 4.2°K
Baseline at 81.51kG
Calibration lines at intervals of 1.235kG

b. α oscillations for H// [1$\bar{1}$0]
Temperature: 1.02°K
Baseline at 81.51kG
Calibration lines at intervals of 1.235kG

c. α_2 oscillations
H// [1$\bar{1}$0]
Temperature: 2.53°K
Baseline at 86.45kG
Calibration lines at intervals of 1.235kG

d. α_2 oscillations
H// [1$\bar{1}$0]
Temperature: 1.02°K
Baseline at 86.45kG
Calibration lines at intervals of 1.235kG

e. α_2 oscillations
H// [11$\bar{1}$]
Temperature: 4.02°K
Baseline at 87.69kG
Calibration lines at intervals of 1.235kG

f. α_2 and α_3 oscillations
H// [11$\bar{1}$]
Temperature: 1.13°K
Baseline at 87.69kG
Calibration lines at intervals of 1.235kG

(The signals at the low field end of this oscillogram are due to the $\alpha + \beta$ oscillations. The α_3 oscillations appear at the high field end of the oscillogram.)

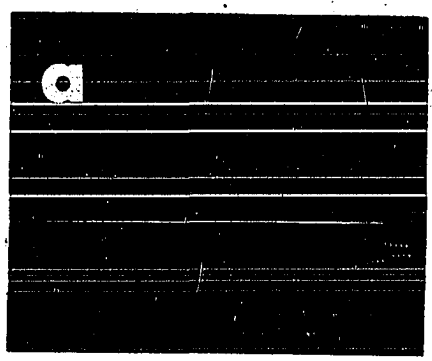
a

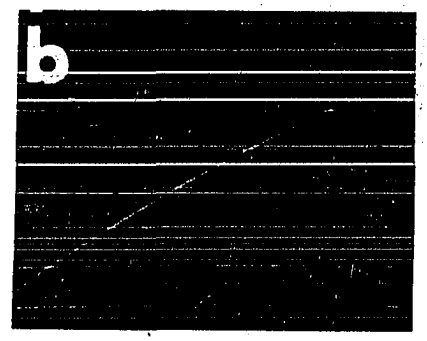
b


c

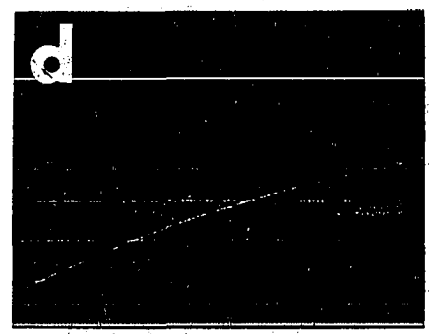
d

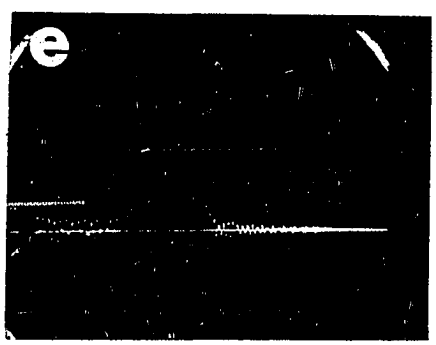
e

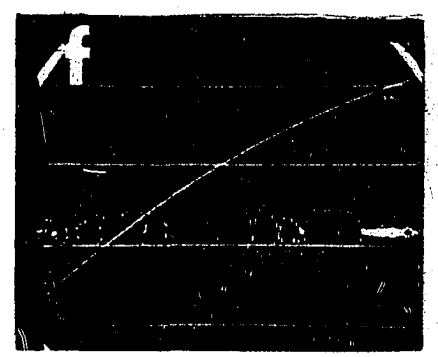
f

Figure 46. Beating patterns in the α oscillations (Each of these signals was observed while the pulse coil current was decaying through a shunt ignitron; and for each of these pictures, a cathode follower was used. The resonant frequency in all cases is about 200kHz and all signals have been passed through five electronic filters set to attenuate frequencies below 150kHz.)

a. Envelope of α oscillations
H near [001]
Temperature: about 1°K
Baseline at 67.93kG
Calibration lines at intervals of 6.175kG

b. Envelope of oscillations
H about 2° from [001]
Baseline at 56.81kG
Calibration lines at intervals of 2.47kG

c. α oscillations
H ~ 15° from [001] in the $(\bar{1}10)$ plane
Temperature about 1°K
Baseline at 55.575kG
Calibration lines at intervals of 1.235kG

d. Envelope of α oscillations
H ~ 15° from [001] in the $(\bar{1}10)$ plane
Temperature: about 1°K
Baseline at 43.225kG
Calibration lines at intervals of 1.235kG

e. Envelope of α oscillations
Temperature: about 1°K
Baseline at 38.29kG
Calibration lines at intervals of 6.175kG
H about 4° from [001]

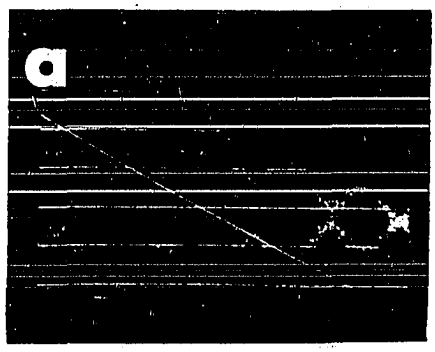
a

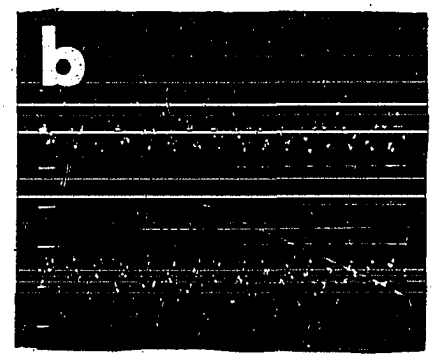
b

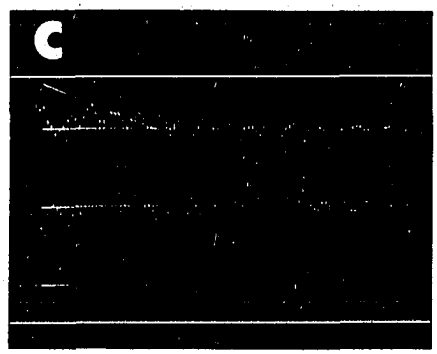
c

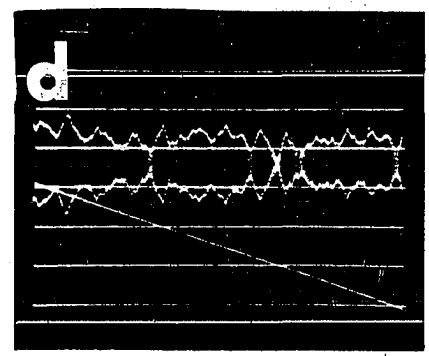
d

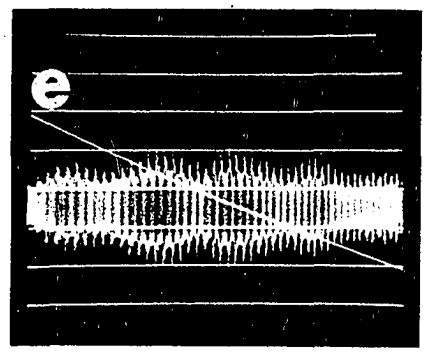
e

fluctuation, with a period of 25 to 30 cycles of the oscillations is shown in Figure 46b, and a much shorter period fluctuation is shown in Figure 46c. The amplitude fluctuations were not always regular, however, as is shown in Figure 46d. The various experimental factors which could give rise to amplitude fluctuations (Shoenberg 1962) have not been considered in detail since it was known that D.M. Sparlin[1] had also observed long beats in the α oscillations when he studied them by an entirely different method, i.e. the torque method.

A "beat frequency" for the intermediate length fluctuations was measured by plotting the reciprocal field positions at which beat maxima occurred versus integers (using data like that shown in Figure 46e). The points on these plots appeared to fall on straight lines, and it was found that the beat frequency is, to within the experimental accuracy, independent of magnetic field orientation for field directions near [001]. The characteristics of these amplitude fluctuations which have been examined to date are not inconsistent with an explanation based on an interaction with the slower ϵ and δ oscillations by means of which the amplitude of the α oscillations is modulated at the frequencies of these slower oscillations. Shoenberg has pointed out that such a

---

[1] D.M. Sparlin, now at Western Reserve University, Cleveland, Ohio. Private communication 1964.

modulation can arise when more than one frequency of oscillation is present and a low frequency term has a very large amplitude.

It is possible that modulation effects like those shown in Figure 46 could also explain the distorted resonance envelopes which were shown in Figure 45. Certainly these modulation effects would become more serious as the temperature is lowered if they are due to Shoenberg's frequency modulation effect.

When the side bands that arise from the frequency modulation effect are well separated in frequency from the fundamental terms, they are expected to appear as separate terms rather than as a beating effect in the fundamental term. The combination terms $\alpha + \beta$, $\alpha - \beta$, $\alpha + \delta_2$, and $\alpha - \delta_2$ in Figure 9 are thought to arise in this way. There is an argument which would seem to indicate that, to first order in amplitude, the strengths of the sum and difference frequencies are proportional to the product of the amplitudes of the corresponding fundamental terms. The amplitudes of the first order side band components of the signal

$$A_1 \sin\left(\frac{2\pi F_1}{H + 4\pi A_2 \sin\frac{2\pi F_2}{H}}\right) \simeq A_1 \sin\left(\frac{2\pi F_1}{H} - \frac{2\pi F_1}{H^2}\, 4\pi A_2 \sin\left(\frac{2\pi F_2}{H}\right)\right)$$

($|4\pi A_2| \ll H$) are proportional to $A_1 A_2$ (cf. Terman 1943 p. 578 and International Telephone and Telegraph Corporation

1956 p. 1085). A_1 and A_2 are of the form $A_i = B_i(H,F_i)T\exp(-Cm_i^*(T + x_i)/H)$ where C is a constant, so that we might expect the temperature dependence of either a sum or difference frequency to be given to first order in amplitude by $T^2\exp(-CT(m_1^* + m_2^*)/H$.

The results of some measurements of the temperature dependence of the amplitude A of the difference term $\alpha - \beta$ are shown in Figures 47 and 48. In Figure 47 we have plotted logA/T versus T as would be done for a fundamental term. In Figure 48 we have plotted log A/T^2 versus T, and the points on this plot may fit a straight line somewhat more closely than those in Figure 47. The mass for the β oscillations is about $0.9m_e$ and that for the α oscillations is about $0.6m_e$ so that the first order approximation predicts that a "cyclotron mass" value of $m^* \simeq 1.5m_e$ should be found from the slope of the plot in Figure 48 if the ideas of the previous paragraph are at all applicable.

There is one further observation which should be discussed here. As was pointed out in Section II-B, the orbit masses which were derived from the temperature dependence of the amplitude of the harmonics of the α oscillations at the [111] orientation (Figures 21 and 22) were considerably less than integral multiples of the fundamental mass of $m^* = 0.6m_e$ (Figure 16). In view of the considerable errors which were possible in the measurement of both the masses of the fundamental and of the harmonic terms, the discrepancy in the mass

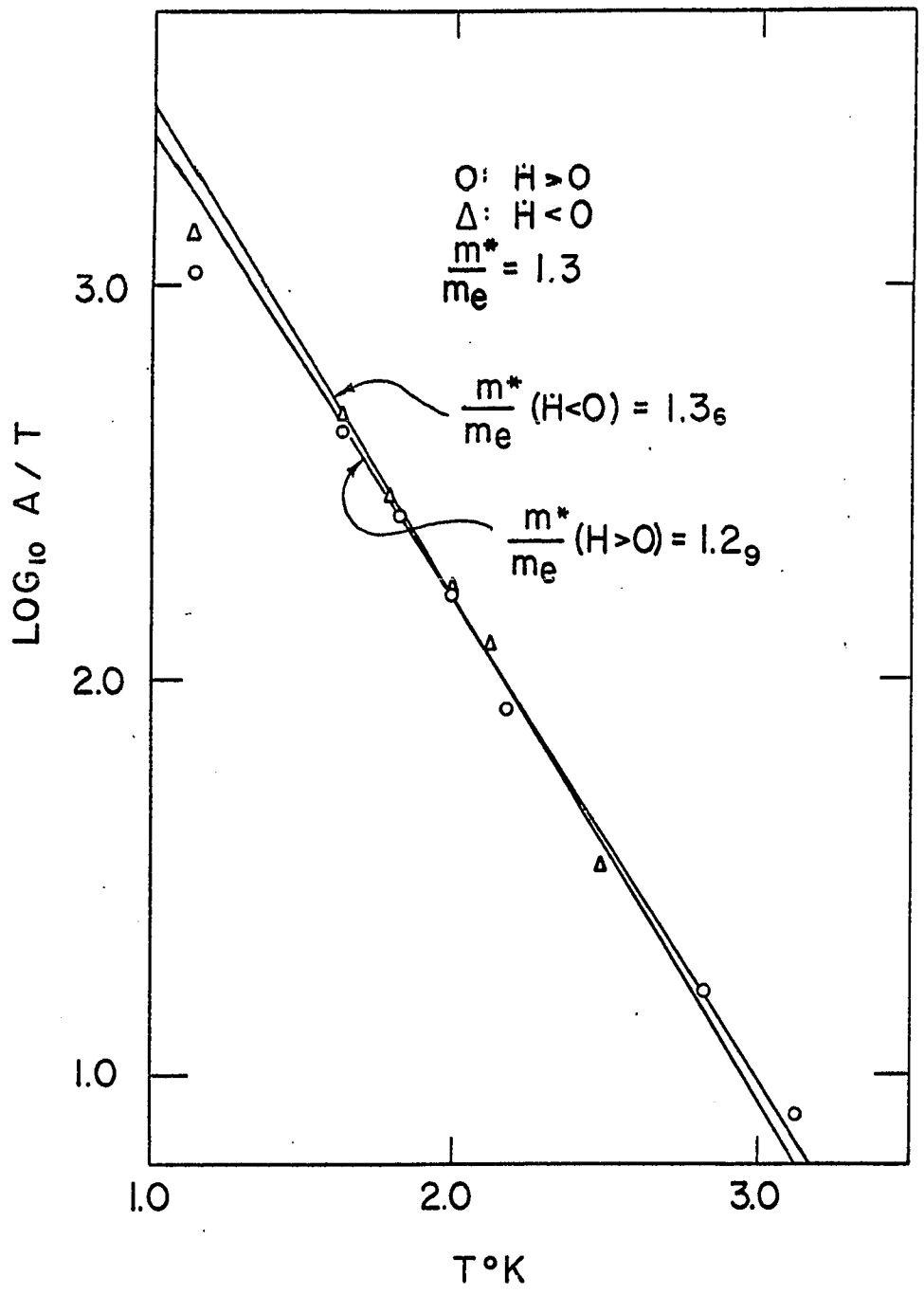

Figure 47. Temperature dependence of the amplitude of the $\alpha - \beta$ oscillations for H// [11̄1] .

Figure 48. Temperature dependence of the amplitude A of the $\alpha - \beta$ oscillations for H//[$\bar{1}11$] plotted as if the amplitude of these oscillations were proportional to the product of the amplitudes of the α and β oscillations

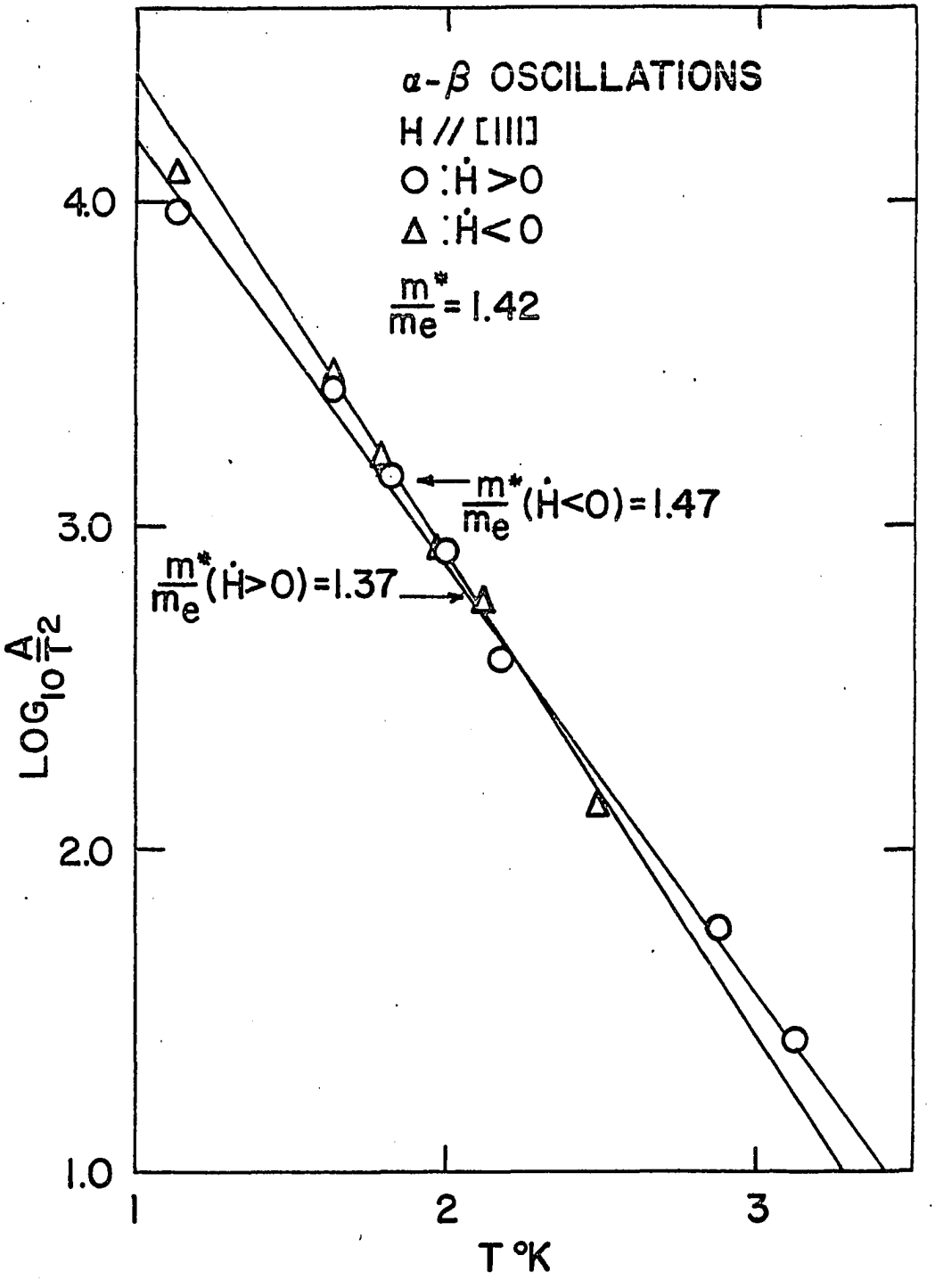
α-β OSCILLATIONS
H // [111]
O : Ḣ > 0
Δ : Ḣ < 0
m*/me = 1.42
m*/me (Ḣ<0) = 1.47
m*/me (Ḣ>0) = 1.37
LOG10 A/T2
4.0
3.0
2.0
1.0
1
2
3
T °K

ratio may not be as serious as is indicated. It does however, seem to be somewhat outside the experimental error.

One possible explanation for the observed mass ratios is that a distortion occurred in the electronics. For these data, the amplitude of the fundamental component was so large that at 1°K the output voltage of 15 volts peak-to-peak from an intermediate amplifier[1] exceeded the rated maximum peak output voltage by 5 volts. Therefore the response of this amplifier during the time immediately after the resonance envelope for the α oscillations, when the harmonics of the α oscillations resonated, may have been modified.

However, there are several indications that the effects of this large output signal may not have been really serious. The first of these is that for a constant-frequency signal, the amplifier in question does not begin to saturate until an output level of 90 volts is reached. The second is that even though the signal due to the α oscillations below 2°K was so large that the rated maximum peak output voltage rating for the amplifier was exceeded, no serious saturation effects are evident in the temperature dependence of the amplitude of these oscillations (Figure 16). Thirdly, from examination of the temperature dependence of the amplitude of the second harmonic for rising and falling field, it is evident either that recovery from any saturation effects

---

[1] Hewlett Packard Model 450A, Hewlett Packard Company, 275 Page Mill Road, Palo Alto, California

occurred with quite a long time constant or that saturation effects were not serious. The temperature dependence of the amplitude of the second harmonic of the α oscillations for $H \parallel [111]$ has been shown in Figure 21 and it is evident that the slopes of the rising and falling field data are not markedly different. Furthermore, the slope for the temperature dependence of the second harmonic seems to be already well-defined at higher temperatures where the electronic components were far from overload. It does not seem that the magnitudes of the discrepancies in the harmonic mass ratios which were observed for $H \parallel [111]$ can be explained by failure of the electronics.

Using a slight generalization of Equation 30, a further examination of the effects of frequency modulation was carried out in an attempt to see whether the anomalous mass results for the harmonics of the α oscillations at the [111] orientation could be explained in this way. We considered the formula

$$M = \sum_{j=1}^{3} M_j \tag{32}$$

where

$$M_j = A_j \sin\left(\frac{2\pi jF}{H + 4\pi M_1} - \frac{\pi}{4} - 2\pi j\gamma\right)$$

The quantities in the argument of the sine function appear in Equation 12. The M_j represent harmonic terms like those in Equation 12, and the A_j are defined as

$$A_j = j^{-\frac{1}{2}}\cos\left(\frac{\pi j m^*}{m_e}\right)NT\exp(-jST) \qquad (33)$$

like the amplitude factor (with g = 2) in the expression for magnetization from which Equation 12 was derived.

By using the condition $|4\pi M/H| << 1$ and by making repeated use of the Bessel function expansions

$$\cos(u\sin x) = J_o(u) + 2\sum_{n=1}^{\infty} J_{2n}(u)\cos 2nx$$

and

$$\sin(u\sin x) = 2\sum_{n=1}^{\infty} J_{2n-1}(u)\sin(2n-1)x$$

(International Telephone and Telegraph Corporation 1956 p. 1065), we arrived at the following expansion for the quantity $y = 8\pi^2 MF/H^2$:

$$\begin{aligned}
y = {} & \left[A_1\left(1 - \tfrac{1}{8}A_1^2\right) - \tfrac{1}{\sqrt{2}}A_2A_1 + \ldots\right]\sin\left(\tfrac{2\pi F}{H} - \tfrac{1}{4}\pi - 2\pi\gamma\right) \\
& + \left[\tfrac{1}{\sqrt{2}}A_2A_1 + \tfrac{3}{8}A_3A_1^2 + \ldots\right]\cos\left(\tfrac{2\pi F}{H} - \tfrac{1}{4}\pi - 2\pi\gamma\right) \\
& + \left[-\tfrac{1}{2\sqrt{2}}A_1^2 + A_2\left(1-A_1^2\right) + \tfrac{3}{2\sqrt{2}}A_3A_1 + \ldots\right]\sin\left(2\tfrac{2\pi F}{H} - \tfrac{1}{4} - 4\pi\gamma\right) \\
& + \left[\tfrac{1}{2\sqrt{2}}A_1^2 + \tfrac{3}{2\sqrt{2}}A_3A_1 + \ldots\right]\cos\left(2\tfrac{2\pi F}{H} - \tfrac{1}{4}\pi - 4\pi\gamma\right) \\
& + \left[-\tfrac{1}{\sqrt{2}}A_2A_1 + A_3\left(1 - \tfrac{9}{4}A_1^2\right) + \ldots\right]\sin\left(3\tfrac{2\pi F}{H} - \tfrac{1}{4}\pi - 6\pi\gamma\right) \\
& + \left[-\tfrac{3}{8}A_1A_1^2 - \tfrac{1}{\sqrt{2}}A_2A_1 + \ldots\right]\cos\left(3\tfrac{2\pi F}{H} - \tfrac{1}{4}\pi - 6\pi\gamma\right)
\end{aligned} \qquad (34)$$

(Terms to second order in A_1 were retained in the expansion of each of the harmonics in Equation 32.)

It is not altogether clear that the expansion in Equation 34 has been carried to high enough order to predict the amplitudes of the higher harmonics in Equation 32 reliably. Nevertheless, the temperature dependence predicted by this formula for values of m* and S appropriate to the α oscillations at [11$\bar{1}$] was found by direct computation for values of N (Equation 33) ranging from 2 to 6. For $m^*/m_e = 0.6$ and $S = 1.1$ these values of N correspond at T = 1°K to amplitudes of about .2 to .6 respectively for the quantity y. (Since the amplitude $|dM/dH|$ is equal to $|2\pi FM_o/H^2|$, the amplitude of the fundamental harmonic of y is a factor of 4π larger than that of the fundamental harmonic of dM/dH.

The amplitudes of the harmonic components of y were calculated for values of T between 1 and 4°K, and these amplitudes were then plotted on semi log paper just as the actual dHvA orbit mass data were. The slopes of straight lines on these plots were then calculated. Even for N = 5, the slope of the plot for the calculated temperature dependence of the amplitude for the second harmonic was reduced by only 8 percent below the value predicted without frequency modulation. For N = 5 the calculated amplitude for the fundamental component at 1°K lies about 30 percent below the amplitude predicted by a straight line through

the higher temperature points. Taken together, these two results are inconsistent with the experimental data which were shown in Figures 15 and 21. Thus the formula given by Equation 34 is not sufficient to account quantitatively for the low mass value measured for the α_2 oscillations at the [111] orientation. This fact is not too surprising, and may merely indicate that our approach is oversimplified. However, any further investigations to see how much the frequency modulation effect can affect mass measurements for harmonic components has been left for further study.

The values of m* and S for the orbit mass data for the α oscillations at [110] (Figure 19) are $0.67m_e$ and $1.2m_e$ respectively, and we compared the low temperature amplitude-damping effects predicted by the previous calculations with the damping observed experimentally for these oscillations. We previously estimated an absolute amplitude of 0.2 for the α oscillations at [110] and from a drawing like Figure 19, we estimate that the amplitude of the 1°K point is about 20 percent lower than is predicted by a straight line through the higher temperature points. The corresponding plot (N=2) for points calculated from Equation 34 only shows an 8 percent reduction in the amplitude at 1°K.

In summary, although it seems that the qualitative features of the anomalies in the mass measurements for the α oscillations and their harmonics at [111] and [110] can

be explained by the frequency modulation effect, further work would be required for a quantitative explanation.

Appendix D: The Electron Jack and Hole Octahedron Programs

The program which was used to calculate orbit areas on the electron jack and hole octahedron surfaces consisted of a main curve-tracing program and a function subroutine. The main program traced out the curve of intersection between the plane of the orbit and a surface defined by a relation $F(x,y,z) = 0$. The function subroutine evaluated $F(x,y,z)$ and its derivatives with respect to Cartesian coordinates y' and z' in the plane of the orbit.

The plane of the orbit was an $x' =$ constant plane of an $x'y'z'$ coordinate system which was rotated from the original xyz coordinate system by the Euler angles ϕ, θ, ψ (Goldstein 1953). The function $F(x,y,z)$ was evaluated at a point (y'_o, z'_o) (read as input) and then at successive points (y'_i, z'_o) where $y'_i = y'_o + i\Delta y'$. If the function changed sign between successive steps before forty steps had been taken, the curve tracing was initiated. The curve of intersection of the plane of the orbit with the surface $F(x,y,z) = 0$ was traced by steps along the tangent line. After each step, coordinates y', z' were found for which $F(x,y,z) \leq 2 \times 10^{-5}$ was satisfied. This was done by Newton's method using the component of the normal derivative to the surface which lay in the plane of the orbit.

The relations

$$y'_{i+1} = y'_i - \left[F(x,y,z)\frac{\partial F}{\partial y'}\Big/\sqrt{\left(\frac{\partial F}{\partial y'}\right)^2 + \left(\frac{\partial F}{\partial z'}\right)^2}\right]_{y' = y'_i, z' = z'_i}$$

$$z'_{i+1} = z'_i - \left[F(x,y,z)\frac{\partial F}{\partial z'}\Big/\sqrt{\left(\frac{\partial F}{\partial y'}\right)^2 + \left(\frac{\partial F}{\partial z'}\right)^2}\right]_{y = y'_i, z = z'_i}$$

were used to replace a point y'_i, z'_i by a point y'_{i+1}, z'_{i+1} which was closer to the surface. Steps along the tangent direction from a point y'_j, z'_j to a point y'_{j+1}, z'_{j+1} were made according to the formulas

$$y'_{j+1} = y'_j - s\left[\frac{\partial F}{\partial y'}\Big/\sqrt{\left(\frac{\partial F}{\partial z'}\right)^2 + \left(\frac{\partial F}{\partial y'}\right)^2}\right]_{y' = y'_j, z' = z'_j}$$

and

$$z'_{j+1} = z'_j - s\left[\frac{\partial F}{\partial y'}\Big/\sqrt{\left(\frac{\partial F}{\partial y'}\right)^2 + \left(\frac{\partial F}{\partial z'}\right)^2}\right]_{y' = y'_j, z' = z'_j}.$$

The step length $s \sim .002$ was read as input.

For the functions which we used to define the surfaces, $\left[F(x,y,z,p)\right]_{\text{inside surface}} > \left[F(x,y,z,p)\right]_{\text{outside surface}}$ so that the steps along the tangent vector define a counter-clockwise path around the orbit. Therefore the orbit areas were calculated from the formula

$$\text{Area} = \tfrac{1}{2}\left\{\sum_i \left[z'_{i+1}(y'_i - y'_{i+1}) + y'_{i+1}(z'_{i+1} - z'_i)\right]\right\}$$

The sum is over all points on the orbit.

Appendix E: Periodogram Analysis

The Whittaker and Robinson (1956) procedure to test a

sequence of numbers $\{u_k\}$ for a periodicity whose period extends over p consecutive elements of the sequence can be illustrated by arranging the elements of the sequence in a Buys-Ballot table. To test a sequence of m terms for a periodicity p, this table would be constructed as follows:

	u_1	u_2	u_3	u_p
	u_{p+1}	u_{p+2}	u_{p+3}	u_{2p}
	u_{2p+1}	u_{2p+2}	u_{2p+3}	u_{3p}
	.....	.....	.....	.....
	u_{mp-p+1}	u_{mp-p+2}	u_{mp-p+3}	u_{mp}
SUMS	U_1	U_2	U_3	U_p

If there is a component with periodicity p in the data, this component will pass through all phases of one complete period in the course of one horizontal row, and will be in the same phase at each of the terms in one vertical column. Therefore the part of the signal which is of period p will appear with m-fold amplitude in the column sums U_i. When a periodicity p exists in the data, the standard deviation of the means of the column sums will be much larger than when a periodicity of this period does not exist.

The periodogram analysis consisted of setting up a Buys-Ballot table for each test period p and then finding the standard deviations σ_p of the means of the column sums. Since different elements of the u sequence were used for each period test (see Appendix A), it was necessary to normalize

each σ_p by dividing by the standard deviation of the elements of the u sequence which were used at each step. When σ_p is plotted versus frequency $F = 1/p$ to make a periodogram, peaks in σ_p occur at frequency values corresponding to periodic components which exist in the data.

Whittaker and Robinson (1956) show that if the elements of the sequence $\{u_k\}$ are amplitudes of $A\sin(2\pi x/T)$ taken at equally-spaced values of x, the intensity distribution I(p) on the periodogram is given by

$$I(p) = \frac{1}{m^2} \frac{\sin^2 \frac{m\pi p}{T}}{\sin^2 \frac{\pi p}{T}}$$

The characteristics of this function are well-known from the theory of ideal diffraction gratings (cf. Jenkins and White 1957 p. 330).

In an attempt to improve our analysis procedures, several variations of the above method were tried. Kendall (1946) states that for periodogram analysis of his economic time series, the Whittaker periodogram was inferior to a periodogram defined by

$$I(p) = A^2 + B^2$$

where

$$A(p) = \frac{2}{mp} \sum_{j=0}^{p-1} U_{j+1} \cos \frac{2\pi j}{p}$$

and

$$B(p) = \frac{2}{mp} \sum_{j=0}^{p-1} U_{j+1} \sin \frac{2\pi j}{p}$$

(The U_j are the column sums in the Buys-Ballot table.) However, for our data, this method seemed to work no better than the Whittaker method.

Rudra (1955) has pointed out that the variance of the elements within each column of the Buys-Ballot table should be a minimum when the test period is near a true periodicity in the data and has suggested that periodocities might be better detected by dividing the variance of the column sums of the Buys-Ballot table by the variances of the elements within each column. For our data the minima in the within column variances turned out to be too shallow to be useful.

Periodogram analysis was used rather than the well-known power spectrum methods described by Blackman and Tukey (1959) because in an early power spectrum program we were not able to obtain reproducible results when the interval over which lagged products were calculated was changed. We did not investigate further the reason for this difficulty.

Appendix F: Orbit Masses for the Empirical Fermi Surface

As was discussed on page 139, there is no reason to believe that the functions F and G which were used to define the shape of the Fermi surface would also predict the masses correctly. There is, however, an argument which suggests

that it might be possible to calculate orbit masses to within a constant scaling factor if the shape of the Fermi surface were fitted exactly. The shape of the Fermi surface is given by the solutions of the equation

$$W = E(k_x,k_y,k_z) - E_F = 0$$

where $E(k_x,k_y,k_z)$ is the band structure. In the absence of any knowledge of E, let

$$F = H(k_x,k_y,k_z) - C = 0$$

(C = constant) represent a geometrical model for the Fermi surface which has been fitted to experimental data. If the surfaces W and F coincide, we must have

$$\frac{\partial E}{\partial k_y}\Big/\frac{\partial E}{\partial k_z} = \frac{\partial H}{\partial k_y}\Big/\frac{\partial H}{\partial k_z}$$

at all points on the surface at which $\partial H/\partial k_z \neq 0$. If we can assume that there is a differentiable function $K(k_x,k_y,k_z)$ such that

$$\frac{\partial E}{\partial k_y} = K(k_x,k_y,k_z)\frac{\partial H}{\partial k_y}$$

and

$$\frac{\partial E}{\partial k_z} = K(k_x,k_y,k_z)\frac{\partial H}{\partial k_z}$$

at all points on the surface, then

$$\frac{\partial E}{\partial k_\perp} = K(k_x,k_y,k_z)\frac{\partial H}{\partial k_\perp}$$

at all points on the surface. (Here $k_\perp$ is the k_n discussed

on page 8.) If $\frac{\partial^2 E}{\partial k_y \partial k_z}$ and $\frac{\partial^2 H}{\partial k_y \partial k_z}$ are continuous on the surface, then the tangential derivatives of $K(k_x,k_y,k_z)$ on the surface are zero so that $K(k_x,k_y k_z)$ takes on a constant value everywhere on the surface. If the conditions for this argument are actually satisfied, it should be possible to calculate masses for different orbits to within a scaling factor K = constant from integrals like those in Equation 6.

We did not investigate further the validity of the above argument, but instead put the usefulness of such an argument to an experimental test. The quantities

$$m' = \oint \frac{dk_t}{|\partial H/\partial k_\perp|}$$

were easy to compute so they were calculated as the orbits were traced to find the extremal areas. There are some features of the resulting m' versus k_H plots for the electron jack function which would be expected to be qualitatively similar to the true m* versus k_H plots if such plots could be obtained. These similarities arise because at many orientations a minimum number of m* minima is fixed by the nmmber of times a plane k_H = constant is tangent to a neck as k_H is varied from zero to its maximum value. A mass minimum should occur between two k_H values for which tangency occurs (unless one of these points of tangency occurs for $k_H = k_F$ where k_F is the extension of the Fermi surface along the field direction) (cf. Koch, Stradling, and Kip 1964).

Furthermore, both the experimental mass m* and the mass m' for the central orbit on the electron jack are expected to rise steeply as an angle is approached for which the central section through the electoon jack is tangent to a neck.

The orientation dependence of the extremal values of m' which were picked off the plots of m' versus k_H are shown in Figure 49b, and we have reproduced Figure 40 in Figure 49a. It is evident that except for qualitative similarities of the orientation dependence which are expected to follow from the shape of the jack, the orientation dependence of m' (Figure 49b) is not at all like that of m* (Figure 49a). It would seem that the argument that orbit masses can be calculated to within a scaling factor is invalid. One difficulty in the argument arises when saddle points occur. Again, we have assumed that the two functions describe precisely the same surface. Because of experimental uncertainties we should really assume that the function F would represent the surface in some least squares sense.

Appendix G: Some Noncentral Areas for the Electron Jack

Knowledge of the dependence of the cross-sectional area of the Fermi surface on distance in $\underline{k}$-space along the magnetic field direction is of interest for several reasons. The most important reason for this study is, of course, that the frequencies of de Haas-van Alphen oscillations are

Figure 49. Empirical and calculated orbit masses

a. Cyclotron resonance mass results of Walsh (1964) (See caption to Figure 40.)

b. Orientation dependence of some of the (scaled) "orbit masses" for the empirical model; heavy solid lines: orbits with both extremal area and extremal mass; light solid lines : orbits with extremal mass only; dotted lines : orbits having an extremal area for which m' is a relatively slowly-varying function of k_z. These orbits were included mainly to make this plot have somewhat the same form as Figure 50a, even though there are great differences between the two plots numerically. Quantities m' calculated using the electron jack function have been scaled so that m' for the central orbit on the electron jack at $[\tilde{1}11]$ is equal to the corresponding orbit mass as found by cyclotron resonance. Quantities m' calculated using the hole octahedron function were scaled so that m' for the central orbit on the hole octahedron at $[\tilde{1}11]$ agrees with Walsh's value for this orbit.

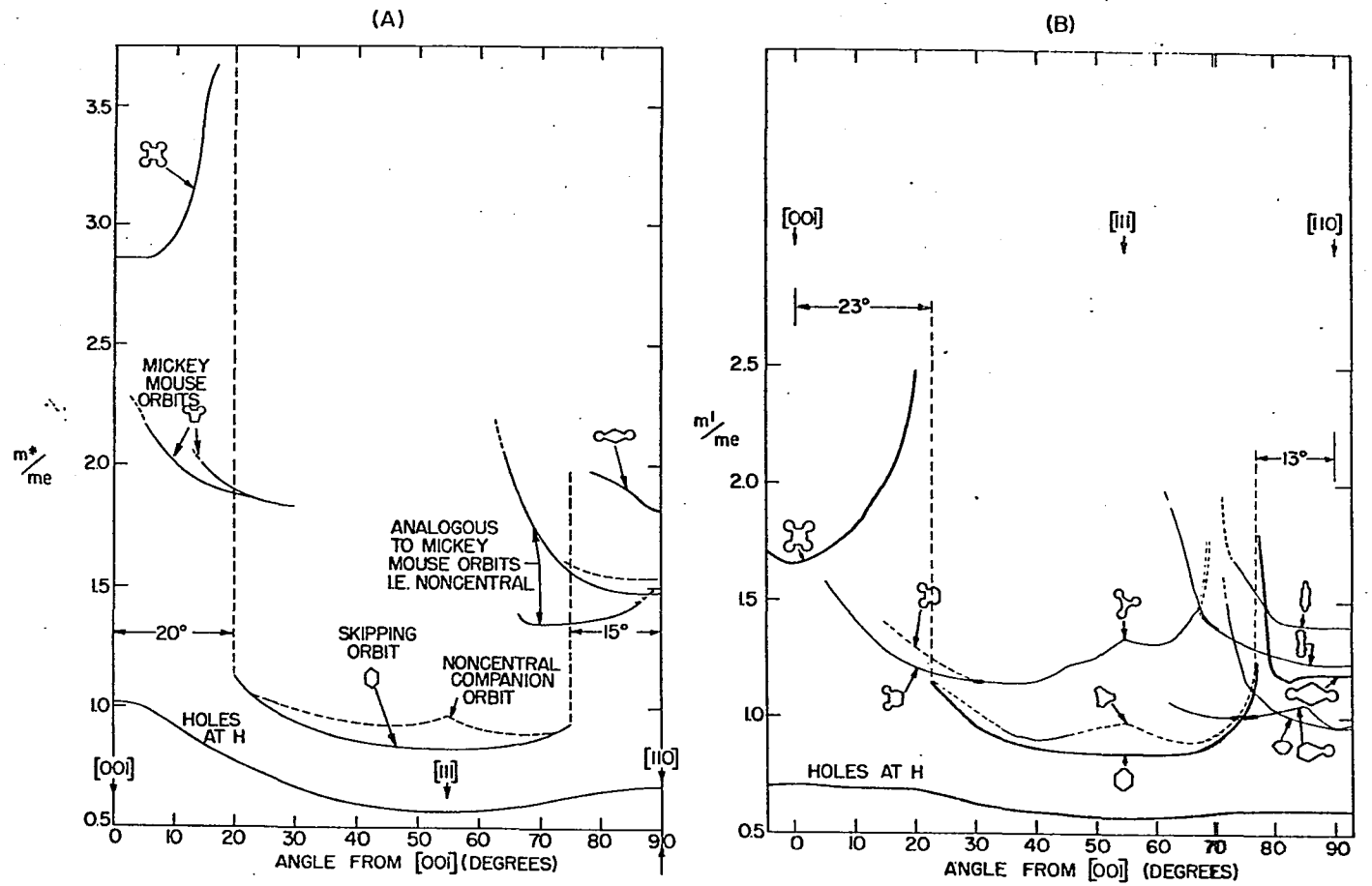
(A)
(B)
m*/me
m'/me
MICKEY MOUSE ORBITS
ANALOGOUS TO MICKEY MOUSE ORBITS I.E. NONCENTRAL
SKIPPING ORBIT
NONCENTRAL COMPANION ORBIT
HOLES AT H
20°
15°
23°
13°
[001]
[111]
[110]
ANGLE FROM [001] (DEGREES)

proportional to areas $A_o(k_H)$ for which $\partial A_o(k_H)/\partial k_H = 0$. In order to further illustrate the origin of some of the de Haas-van Alphen terms predicted by the empirical model (Figure 38), we have included in Figure 50 some examples of computed plots of $A(k_H)$ versus k_H. Using the frequency values which label the points with extremal area, areas on these plots can be correlated with predicted frequencies on Figure 38.

The plots in Figure 50 also give some idea of the relative magnitudes of the curvature factors $\left|\partial^2 A_o/\partial k_H^2\right|^{-\frac{1}{2}}$ (Equation 12) for the various orbits. As was discussed in Chapter V, there is some uncertainty as to which of two possible orbits on the electron jack corresponds to the β oscillations. The predicted curvature factors for these two orbits do not appear to be vastly different (Figure 50a) so that a choice for the appropriate orbit for the β oscillations cannot be made on the basis of the size of the curvature factor.

Munarin and Marcus (1966) have observed an oscillatory magnetoresistive size effect in gallium which is periodic in H rather than $1/H$. These so-called Sondheimer oscillations (Sondheimer 1950) have been interpreted (Munarin and Marcus 1966, Bloomfield 1966) in terms of orbits on approximately parabolic sheets of Fermi surface for which $\partial A/\partial k_H$ is constant. Loucks[1] has observed that there are also orbits on

[1]Dr. T. Loucks, Physics Department, Iowa State University of Science and Technology. Private Communication 1966.

Figure 50. Some plots of orbit area $\mathcal{A}(k_H)$ versus k_H for the model electron jack. Light solid lines have been drawn through the calculated points. Extremal areas are labeled with the corresponding dHvA frequencies F. Dashed lines give the estimated behavior of the curves where no calculations were carried out. Heavy solid lines are drawn where $\partial\mathcal{A}/\partial k_H$ is constant.

a. $k_H // [\bar{1}11]$. Rough values of the curvature factors are indicated for the two orbits which predict frequencies near that of the β oscillations.

b. $k_H // [\bar{1}10]$

c. k_H in $(\bar{1}10)$ plane 12° from $[\bar{1}10]$

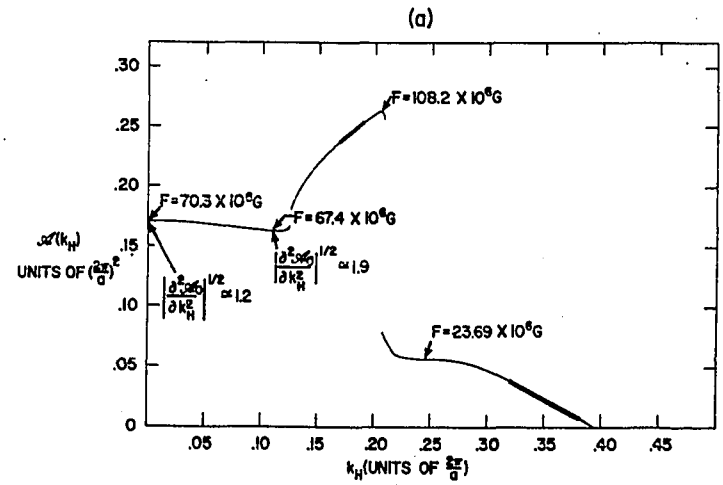
(a)
F=108.2 X 10⁶G
F=70.3 X 10⁶G
F=67.4 X 10⁶G
F=23.69 X 10⁶G
UNITS OF (2π/a)²
k_H(UNITS OF 2π/a)

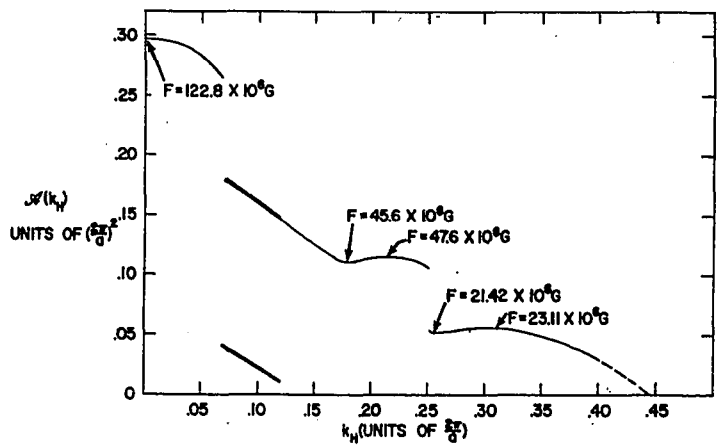
(b)
F=122.8 X 10⁶G
F=45.6 X 10⁶G
F=47.6 X 10⁶G
F=21.42 X 10⁶G
F=23.11 X 10⁶G
UNITS OF (2π/a)²
k_H(UNITS OF 2π/a)

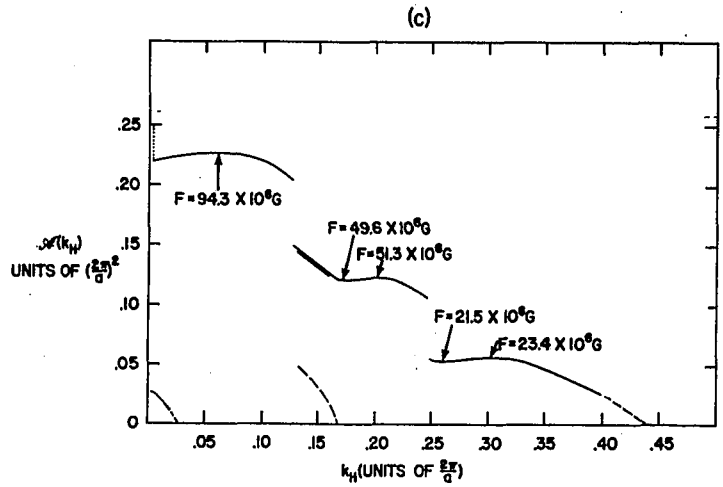
(c)
F=94.3 X 10⁶G
F=49.6 X 10⁶G
F=51.3 X 10⁶G
F=21.5 X 10⁶G
F=23.4 X 10⁶G
UNITS OF (2π/a)²
k_H(UNITS OF 2π/a)

his electron jack model for tungsten (Loucks 1966) for which $\partial A/\partial k_H$ = constant and has suggested that such oscillations could possibly be observed in tungsten.

There are orbits on our empirical model for which $\partial A/\partial k_H$ = constant also, and some of these are shown on Figure 50. Of course, for some of these orbits, the linear dependence of A on k_H may vanish if the $\langle 110 \rangle$ dimensions of the jack are reduced slightly (see Chapter 5). (However, the orbits on Loucks' model which correspond to orbits in the linear A versus k_H region of our model labeled "a" also have $\partial A/\partial k_H$ = constant.)

Appendix H: Data Analysis, Fortran Program for IBM 7074 Computer

```
 FORTRAN,COMPILE,       MAIN.
C                                                                              FT
C     PERIODOGRAM ANALYSIS FOR DE HAAS-VAN ALPHEN EFFECT DATA
C THIS PROGRAM WILL ONLY WORK IF EVERY HALF CYCLE OR MORE IS READ,  ANY
C     NUMBER OF READINGS MAY BE TAKEN BETWEEN THE MAX AND MIN OF THE CYCLES BUT
C     THE MAX AND MIN MUST BE READ.  ALSO ,THE FIRST TWO READINGS ON A PICTURE
C     MUST BE A MAX AND A MIN AND THE LAST TWO READINGS MUST BE A MAX AND MIN
C     NTAD IS THE NUMBER OF CYCLES WHICH ARE TO BE ADDED IN
C      SUCCESSION TO MAKE UP ONE TERM FOR THE PERIODOGRAM ANALYSIS
C     NL =NO. OF POINTS PER LINE
C
C      5    IDENTICAL NUMBERS CHANGES THE CALIBRATION LINE IN COMPUTING
C
C     10  IDENTICAL NUMBERS ENDS A DATA SET
C
      DIMENSION INDE(10),WERR(30)
      DIMENSION XLAB1(4),YLAB1(4),XLAB2(4),YLAB2(4),PIX(4),TITLE(4)
      DIMENSION U(1002),SM(500),NL(10),FACC(250),
     1HBOX(250),FLEV(30),NLEV1(30),NLEV2(30),WACC(250),SLMH1(275)
      DIMENSION CONA(250),CONC(250),POSA1(250),FLD1(250),POSB1(250),
     1XPOS1(250),CYCLE(250),RH(250),SAMP(250),RERR(250),HIL(250)
      DIMENSION FLD(3),POSA(3),POSB(3),FACA(3),FAC(3),FACB(3),AMP(3),
     1FACP(3),FACX(3),XPOS(3)
      EQUIVALENCE (U(1),RERR(1)),(U(251),POSA1(1)),
     1(U(501),FLD1(1)),(U(751),HIL(1)),(HIL(1),HBOX(1))
      EQUIVALENCE (SM(1),CONA(1)),(CONA(1),POSB1(1)),
     1(SM(251),CONC(1)),(CONC(1),XPOS1(1))
      CONP=.5
      NUPLI=1002
      READ 1179,XLAB1,YLAB1,XLAB2,YLAB2
 1179 FORMAT(16A5)
  118 READ 119,ALPHA,HILIN,COILK,HZERO,PIX,TITLE
  119 FORMAT (F3.1,F6.1,F8.2,F7.0,8A5)
      MSIG1=0
      MSIG2=0
      MTEST = 0
      M87 = 0
      RHTES=0.                                                          HISTCG
      DO 1190 I1=4,9
 1190 NL(I1)=I1+8
      IF (ALPHA) 120,117,120                                              FT 52
  117 STOP 88                                                             FT 46
  120 READ 1000,NL(1),NL(2),NL(3),NTAD,FL1,FL2,FL3,NINC,FMINR,FMAXR,MBOX
 1000 FORMAT(4I5,10X,3F5.0,I5,2E10.4,I3)
      CALL UPCOR(0,0)
      IF(NTAD)115,115,116
  115 NTAD=1
  116 FTAD=NTAD
      IF(MBOX)1161,1161,1162
 1161 MBOX=1
 1162 MBOX=MBOX
      PRINT 121, PIX,TITLE,ALPHA,COILK,HZERO,HILIN
  121 FORMAT(41HIDE HAAS-VAN ALPHEN COMPUTATIONS--PICTURE3X,8A5//
     19H  ALPHA =F5.1,8X,3HK =F10.2,7X,7HHZERO =F10.5,8X,8HHILINE =F6.1)
      FN = NINC
      HWP = FN/2.
      HILIN = HILIN - ALPHA
      NHWP = HWP
```

Fortran Program 1: Data analysis

```
      J1 = 0
      MSTO = 0
  122 READ 123,(POSA(I2),FACA(I2),FLD(I2),FAC(I2),POSB(I2),
     1FACB(I2),AMP(I2),FACP(I2),XPOS(I2),FACX(I2),I2 =1,3)
  123 FORMAT(15(F3.0,F2.0))
      IF(MSTO)1231,1233,1231
 1731 AP=POSA(1)*FACA(1)
      BP=POSB(1)*FACB(1)
      IF(AP-BP)1232,1241,1232
 1232 HILIN = HILIN -ALPHA
 1233 DO 1239  I3 =1,3
      AP=POSA(I3)*FACA(I3)
      BP=POSB(I3)*FACB(I3)
      IF(AP-BP)1238,1234,1238
 1234 IF(3 -I3)1235,1235,1236
 1235 MSTO = 1
      GO TO 122
 1236 M1 = I3 +1
      AP=POSA(M1)*FACA(M1)
      BP=POSB(M1)*FACB( M1)
      IF(AP-BP)1237,1241,1237
 1237 HILIN = HILIN - ALPHA
      GO TO 1239
 1238 J1= J1+ 1
      MSTO = 0
      POSA1(J1) = POSA(I3)*FACA(I3)
      FLD1(J1) = FLD(I3)*FAC(I3)
      POSB1(J1) = POSB(I3)*FACB(I3)
      SAMP(J1) = AMP(I3)*FACP(I3)
      XPOS1(J1)= XPOS(I3)*FACX(I3)
      HIL(J1)  = HILIN
      M87 = M87 + 1
      GO TO (1239,1308),M87
 1308 M87 = 1
      RERR(J1) = 0.
      K20 = J1-1
      IF(FLD1(J1) - FLD1(K20))1310,1309,1309
 1309 MTEST = MTEST + 1
      RERR(J1) = 1.
 1310 IF(XPOS1(J1) - XPOS1(K20))1311,1314,1312
 1311 MSIG1 = -1
      GO TO 1313
 1312 MSIG1 = +1
 1313 IF(MSIG1 + MSIG2) 1315, 1314, 1315
 1314 MTEST = MTEST + 1
      RERR(J1) = 1.
 1315 MSIG2 = MSIG1
 1239 CONTINUE
 1240 GO TO 122
 1241 NT = J1
      J2 = 0
      DO 1245 I4 = 1,NHWP
      NSTAR= I4
      NEND = I4 + NINC - 1
      FLP = 0.
      SUM1 = 0.
      SUM2 = 0 .
      DO 1244 I5 = NSTAR,NEND
      IF( HIL(I5) - HIL(I4))1243,1242,1243
 1242 FLP = FLP+1.
```

Fortran Program 1 (continued)

```
1243 SUM1 = SUM1 + ((HIL(I5)-HIL(I4))/ALPHA +1.)*POSA1(I5)
I244 SUM2 = SUM2 + ((HIL(I5)-HIL(I4))/ALPHA +1.)*POSB1(I5)
    1           + ((HIL(I4)-HIL(I5))/ALPHA)*POSA1(I5)
     SUM1 = SUM1/FLP
     SUM2 = SUM2/FN
     J2 = J2 +1
1245 RH(J2) = 1./(COILK*(HIL(J2)+ALPHA*((FLD1(J2)-SUM2)/(SUM1 - SUM2)))
    1+HZERO)
     NSTAR = NHWP+1
     NEND = NT - NHWP
     FNINC = NINC
     DO 1251 I6 = NSTAR,NEND
     SUM1 = 0.
     SUM2 = 0.
     FLP1= 0.
     SY1 = 0.
     SX1 = 0.
     SX2 = 0.
     SX3 = 0.
     SX4 = 0.
     SXY1= 0.
     SXY2= 0.
     NBOT = I6 -NHWP
     NTOP = I6 +NHWP
     FLP2 = 0.
     FLP3 = 0.
     DO 1250 I7 = NBOT,NTOP
     IF(HIL(I6)-HIL(I7))1246,1247,1248
1246 C1 = 1.
     C2 = 0.
     C3 = 0.
     FLP1 = FLP1 + 1.
     GO TO 1249
1247 C1 = 0.
     C2 = 1.
     C3 = 0.
     FLP2 = FLP2 + 1.
     GO TO 1249
1248 C1 = 0.
     C2 = 0.
     C3 = 1.
     FLP3 = FLP3 +1.
1249 SUM1 = SUM1 + C1 *POSB1(I7)+  C2* POSA1(I7)
     SUM2 = SUM2 + C3 *POSA1(I7)+  C2* POSB1(I7)
     XA = XPOS1(I7) -XPOS1(I6)
     SY1 = SY1 +FLD1(I7)
     SX1 = SX1 +XA
     X2 = XA*XA
     SX2 = SX2 + X2
     SX3= SX3 +X2*XA
     SX4 = SX4 + X2*X2
     SXY1 = SXY1 + FLD1(I7)*XA
1250 SXY2 = SXY2 + FLD1(I7)*X2
     SUM1 = SUM1/(FLP1+ FLP2)
     SUM2 = SUM2/(FLP3+ FLP2)
     SX22 = SX2*SX2
     SX32 = SX3*SX3
     SX12 = SX1*SX1
     SX23 = SX22*SX2
     Q1 = SY1*SX2*SX4 + SX1*SX3*SXY2 + SX2*SX3*SXY1
```

Fortram Program 1 (continued)

```
     1 -SY1*SX32 - SXY1*SX1*SX4 - SXY2*SX22
      C2 = FNINC*SX2*SX4 +2.*SX1*SX3*SX2 -FNINC*SX32 -SX12*SX4 -SX23
      FRAC = 01/C2
      J2 = J2 + 1
 1251 RH(J2) = 1./(COILK*(HIL(J2)+ALPHA*((FRAC - SUM2)/(SUM1 - SUM2)))
     1+HZERO)
      NSTAR = NT-NHWP+1
      NEND = NT
      DO 1257 I8 = NSTAR,NEND
      SUM1 = 0.0
      SUM2 = 0.0
      FLP1 = 0.0
      FLP2 = 0.0
      FLP3 = 0.0
      DO 1256  I9 = NSTAR,NEND
      IF(HIL(I8)- HIL(I9))1252,1253,1254
 1252 C1 = 1.
      C2 = 0.
      C3 = 0.
      FLP1 =FLP1+ 1.
      GO TO 1255
 1253 C1 = 0.
      C2 = 1.
      C3 = 0.
      FLP2 = FLP2 +1.
      GO TO 1255
 1254 C1 = 0.
      C2 = 0.
      C3 = 1.
      FLP3 = FLP3 + 1.
 1255 SUM1 = SUM1 +  C1*POSB1(I9)+ C2*POSA1(I9)
 1256 SUM2 = SUM2 +  C3*POSA1(I9)+ C2*POSB1(I9)
      SUM1 = SUM1/(FLP1 + FLP2)
      SUM2 = SUM2/(FLP3 + FLP2)
      J2 = J2 +1
 1257 RH(J2) = 1./(COILK*(HIL(J2)+ALPHA*((FLD1(J2)-SUM2)/(SUM1 - SUM2)))
     1+HZERO)
C                                                                        FT 86
C     PART TWO - MULTIPLE LINE FIT                                       FT 87
C                                                                        FT 88
C     NT=TOTAL NO. OF POINTS.                                            FT 89
      PRINT 1299,HILIN
 1299 FORMAT(16H  BOTTOM LINE = F6.1)
      K1=1
      K4=NT-1
      CYCLE(1) = 1.
      DO 1306 J=2,K4
 1300 IF(SAMP(J)-SAMP(J-1))1301,1303,1302
 1301 IF(SAMP(J)-SAMP(J+1))1303,1306,1306
 1302 IF(SAMP(J)-SAMP(J+1))1306,1306,1303
 1303 K2=J
      DO 1304 K=K1,K2
 1304 CYCLE(K) = CYCLE(K1) +(RH(K)-RH(K1))/(RH(K2)-RH(K1))
 1305 K1=K2
 1306 CONTINUE
      IF(K1-K4)7040,7050,7050
 7040 DO 7041 L1=K1,K4
 7041 CYCLE(L1)=CYCLE(K1)+(RH(L1)-RH(K1))/(RH(K4)-RH(K1))
 7050 CYCLE(NT)=CYCLE(K4)+1.
      DO 902 K = 1,NT
```

Fortran Program 1 (continued)

```
      IF(RH(K)-RHTES)1258,1258,1259                                    HISTCG
 1258 RERR(K)=1.
      MTEST=MTEST+1                                                    HISTCG
 1259 RHTES=RH(K)                                                      HISTCG
  902 CONTINUE
       IF(MTEST) 1322,1322, 1320
 1320 PRINT 833,MTEST
  833 FORMAT(12H THERE WERE   I4,15H READING ERRORS/6X,10HFIELD LINE
     18X,8HTOP LINE7X,11HBOTTOM LINE5X,11H X POSITION4X,16HRECIPROCAL FI
     2ELD)
      DO 1321 K=1,NT
      PRINT 9082,FLD1(K),POSA1(K),POSB1(K),XPOS1(K),RH(K)
      IF(RERR(K))1321,1321,1400
 1400 PRINT 9085
 9085 FORMAT(6H ERROR)
 9082 FORMAT(1H 5E16.4)
 1321 CONTINUE
       GO TO 118
 1322 KS=2600000000
      XMIN=CYCLE(1)
      YMIN=RH(1)
      CALL GRAPH(NT,CYCLE,RH,KS,7,15.,10.,0.,XMIN,0.,YMIN,XLAB1,YLAB1,
     1PIX,TITLE)
      CALL LLSID(CONP,FL1,FL2,FL3,MBOX,NT,NL,RH,CYCLE,FMIN,FMAX,1,FACC,
     1WACC,HBOX,NBO,OFBOX,JMDMI,JMDMA)
      RHMA=RH(NT)
      RHMI=RH(1)
      NRHC=1
      MLINS=0
      FTTM=.01
      FTM=FTTM
      JST=JMDMI
      JEN=JMDMA
 1405 MLINS=MLINS+1
      CALL WAVE(FACC,WACC,FLEV,NLEV1,NLEV2,JST,JEN,JC,FTM,NT,WERR)
      IF(MLINS-1)1411,1410,1411
 1410 CALL YMIMA(FACC,NT,FACCL,FACCB,INDE,NSSS,10,M1,1)
      PRINT 1406,FLEV(1),FLEV(JC)
 1406 FORMAT(58HK FIRST POINT ON FREQUENCY VS. CYCLE CURVE HAS FREQUENCY
     1= E12.5/57H  LAST POINT ON FREQUENCY VS. CYCLE CURVE HAS FREQUENCY
     2= E12.5)
      CON=.5*(RHMA+RHMI)
      CALL  SCLE(FACC,RHMA,RHMI,FACCB,FACCL,CON,NT,.5)
      CALL GRAPH(NT,CYCLE,FACC,KS,4,0.0)
 1411 LONG=0
      IF(MLINS-4)1412,1425,1425
 1425 PFTM=100.*FTM
      PRINT 1426,PFTM
 1426 FORMAT(36HK  FREQUENCY PROFILE ESTIMATES WITH   F8.4,20H PERCENT
     1RESOLUTION /6X,9HFREQUENCY9X,5HFIRST5X,4HLAST7X,5HERROR/24X,
     25HCYCLE5X,5HCYCLE)
 1412 DO 1440 J5=1,JC
      LEN=NLEV2(J5)-NLEV1(J5)
      IF(LEN-LONG)1435,1435,1430
 1430 LONG=LEN
      JLON=J5
      JFIRC=NLEV1(J5)
      JLASC=NLEV2(J5)
 1435 IF(MLINS-4)1437,1436,1436
 1436 IF(LEN-10)1437,1437,1427
```

Fortran Program 1 (continued)

```
1427 PRINT 1428,FLEV(J5),NLEV1(J5),NLEV2(J5),WERR(J5)
1428 FORMAT(1H E16.7,5X,I5,5X,I5,5X,E16.7)
1437 NST=NLEV1(J5)
     NEN=NLEV2(J5)
     DO 1438 J6=NST,NEN
     FACC(J6)=FLEV(J5)
1438 WACC(J6)=WERR(J5)
1440 CONTINUE
     JST=1
     JEN=NT
1441 XT=MLINS
     XDIFF=LONG
     XT=XT/XDIFF
     FTM=XT
     IF(MLINS-4)1405,1442,1442
1442 FPRO=RH(JLASC)-RH(JFIRC)
     IF(JLON-1)1444,1444,1443
1443 J5=JLON-1
     JBEG=NLEV1(J5)
     JEND=NLEV2(J5)
     RHCE1=0.5*(RH(JBEG)+RH(JEND))
     RHCE2=0.5*(RH(JFIRC)+RH(JLASC))
     AB=XT*FLEV(JLON)*(RHCE2-RHCE1)/(FLEV(J5)-FLEV(JLON))
     AB=ABSF(AB)
     FPRO=FPRO+AB
1444 IF(JLON-JC)1445,1446,1446
1445 J5=JLON+1
     JBEG=NLEV1(J5)
     JEND=NLEV2(J5)
     RHCE1=0.5*(RH(JBEG)+RH(JEND))
     RHCE2=0.5*(RH(JFIRC)+RH(JLASC))
     AB=XT*FLEV(JLON)*(RHCE2-RHCE1)/(FLEV(J5)-FLEV(JLON))
     AB=ABSF(AB)
     FPRO=FPRO+AB
1446 GO TO (1447,9902),NRHC
1447 PRINT 1429
1429 FORMAT(20HK IDEOGRAM ESTIMATES/9X,9HFREQUENCY12X,9HINTENSITY)
     FBOX=FMIN
     NSSS=1
     CALL YMIMA(HBOX,NBO,HBOXM,HBOXT,INDE,NSSS,10,M1,2)
     DO 1480 J5=1,M1
     IF=INDE(J5)
     FI=IF
     FI=FBOX+FI*DFBOX
1480 PRINT 1408,FI,HBOX(IF)
     DO 1409 J5=1,NBO
     FBOX=FBOX+DFBOX
     U(J5)=FBOX
1408 FORMAT(1H 2E20.8)
1409 CONTINUE
     CALL YMIMA(SAMP,NT,SAMPL,SAMPB,INDE,NSSS,10,M1,1)
     CON=RHMI
     CALL SCLE(SAMP,RHMA,RHMI,SAMPB,SAMPL,CON,NT,.5)
     CALL GRAPH(NT,CYCLE,SAMP,KS,4,0.0)
     XMIN=U(1)
     CALL GRAPH(NBO,U,HBOX,KS,4,8.,10.,0.,XMIN,0.,HBOXM,XLAB2,YLAB2,
    1PIX,TITLE)
     IF(FMAXR)81,81,801
 801 IF(FMINR)81,81,802
 802 FMIN = FMINR
```

Fortran Program 1 (continued)

```
      FMAX = FMAXR
      GO TO 803
   81 FMIN = FMIN
      FMAX = FMAX
  803 NC = NT - 1
C
C       PART 3 PERIODOGRAM ANALYSIS
C
 8032 DO 811 K=1,NC
      CONA(K) = (SAMP(K+1) - SAMP(K))/(RH(K+1) -RH(K))
      CONB = -CONA(K)*RH(K)
  811 CONC(K) = CONB + SAMP(K)
      PMIN = 1./FMAX
      PMAX = 1./FMIN
      NSTOR=NUPLI+9750
      ULIM = NSTOR
      QUA=(PMAX*ULIM   )/(RH(NT)-RH(1))
      IF(QUA-274.)8113,8113,8112
 8112 ULIM=(274.*(RH(NT)-RH(1)))/PMAX
      NSTOR=ULIM
      ULIM=NSTOR
 8113 DRH = (RH(NT)-RH(1))/ULIM
      FTMC=2.*DRH*FMAX
      IF(FTMC-FTM)9902,9901,9901
 9901 MLINS=MLINS-1
      FTM=FTMC
      NRHC=2
      GO TO 1405
 9902 FPRO=FPRO/DRH
      HFPRO=.5*FPRO
      NHPRO=HFPRO
      HFPRO=NHPRO
      NPRO=2*NHPRO
      RHS =RH(1) - DRH
      NP = NSTOR
      K = 1
      PRINT 8116,LONG,     NTAD,CYCLE(NT)
 8116 FORMAT(23HK PERIODOGRAM ESTIMATES/
     1         2HJ I5,33H CYCLES AT A TIME WERE CONSIDERED   /
     2  I5,57H CYCLES WERE ADDED TO MAKE A SINGLE TERM FOR THE ANALYSIS/
     322H THERE WERE A TOTAL OF F5.0,  7H CYCLES/
     49X,9HFREQUENCY12X,9HINTENSITY)
      DO 839 I = 1,NUPLI
      RHS = RHS + DRH
  813 DO 815 J = K,NT
      IF(RHS-RH(J+1))814,814,815
  814 K30 = J
      GO TO 841
  815 CONTINUE
  841 K = K30
  839 U(I)= CONC(K)+CONA(K)*RHS
      LU = NP - NUPLI
      DO 816 I = 1,LU
      RHS = RHS + DRH
      DO 8152 J = K,NT
      IF(RHS -RH(J+1))8151,8151,8152
 8151 K30 =J
      GO TO 8153
 8152 CONTINUE
 8153 K=K30
```

Fortran Program 1 (continued)

```
      MK = I
  840 A = CONC(K) + CONA(K)*RHS
      CALL UPCOR(A,MK)
  816 CONTINUE
      RHL = 0.0
      N1 = 0
      N2 = 0
      RHS = 0.0
      FLP1=1./FLEV(1)
      IF(FLP1-PMIN)8171,8171,817
 8171 PMIN=.95*FLP1
  817 DO 822 I = 1,9000
      RHL = RHL + DRH
      IF(RHL - PMIN)818,820,820
  818 N1 =N1+1
      N2 = N2 + 1
      RHS = RHS + DRH
      GO TO 822
  820 IF(RHL - PMAX)821,821,882
  821 N2=N2+1
  822 CONTINUE
  882 MSTE = 1
  883 RHS = RHS - DRH
      RHTES=RHS
      MF=0
      INTE=0
      J5=1
  823 DO 832 I = N1,N2 ,MSTE
      SFNUM=0.
      SUMU=0.
      SUMU2=0.
      MF=MF+1
      N3 = I
      RHS = RHS + DRH
      RRHL=1./RHS
      IF(RRHL-FLEV(J5))950,950,952
  950 IF(J5-JC)951,958,958
  951 J5=J5+1
      JBEG=NLEV1(J5-1)
      JEND=NLEV2(J5-1)
      RHCE1=(0.5*(RH(JBEG)+RH(JEND))-RH(1))/DRH
      JBEG=NLEV1(J5)
      JEND=NLEV2(J5)
      RHCE2=(0.5*(RH(JBEG)+RH(JEND))-RH(1))/DRH
      FACT1=(RHCE2-RHCE1)/(FLEV(J5)-FLEV(J5-1))
  952 IF(J5-1)958,958,953
  953 RHCEN=(RRHL-FLEV(J5-1))*FACT1+RHCE1
  954 NCEN=RHCEN
  955 IF(NCEN-NHPRO)958,958,956
  956 IF(NCEN+NHPRO-NSTOR)957,958,958
  957 INTE=NCEN-NHPRO
  958 DO 827 J=1,N3
      FNUM=0.
      SUMM = 0.0
      NBEG = J + INTE
      MQ = NBEG-I
      NUP = NBEG + NPRO - NUPLI
      IF(NUP)8241,8241,8242
 8241 NUP1 = NUP + NUPLI
      N40 = 2
```

Fortran Program 1 (continued)

```
      GO TO 825
 8242 NUP1 = NUPLI
      IF(NUP - LU)8244,8244,8243
 8243 NUP = LU
 8244 N40 = 1
      IF(NBEG - NUPLI)825,825,8492
  825 DO 8491 K = NBEG,NUP1,I
  849 SUMM = SUMM + U(K)
      SUMU2=SUMU2+U(K)*U(K)
      FNUM=FNUM+1.
 8491 CONTINUE
      MQ = K
      MK=MQ
      GO TO (8492,8261),N40
 8492 MQ = MQ+I
      MS = MQ - NUPLI
      DO 826 K = MS,NUP,I
      MK = -K
      IND=K
      A=GETU(IND)
C *** *** ***              SUBSCRIPTED VARIABLE NOT DIMENSIONED ; CHAR. 11  A=GETU(IND)
      FNUM=FNUM+1.
      SUMM = SUMM + A
      SUMU2=SUMU2+A*A
  826 CONTINUE
      MK=-MK
 8261 SM(J)=SUMM
      FNUM1=FNUM
      SUMU=SUMU+SM(J)
      SFNUM=SFNUM+FNUM
      IF(NTAD-1)8272,8272,8262
 8262 FNUM=1.
      A1=0.
      MFI=NBEG-2*I
      MLA=MK+2*I
      DO 8271 KIT=2,NTAD
      FNUM=FNUM+1.
      MRIF=MFI+KIT*I
      IF(MRIF-NUPLI)8263,8263,8264
 8263 T1=U(MRIF)
      GO TO 8265
 8264 MRIF=-MRIF
      CALL UPCOR(T1,MRIF)
 8265 MRIL=MLA-KIT*I
      GO TO (8266,8269),N40
 8266 IF(MRIL)8268,8268,8267
 8267 MRIL=-MRIL
      CALL UPCOR(T2,MRIL)
      GO TO 8270
 8268 MRIL=MRIL+NUPLI
 8269 T2=U(MRIL)
 8270 A1=(FNUM-2.)*A1/FNUM +(T1+T2)/FNUM
      SM(J)=SM(J)-A1
 8271 CONTINUE
 8272 SM(J)=SM(J)/(FNUM1+1.-FTAD)
  827 CONTINUE
      VARU=SUMU2/SFNUM-(SUMU/SFNUM)**2
      AVE = 0.0
  828 DO 829 J=1,N3
  829 AVE = AVE+SM(J)
```

Fortran Program 1 (continued)

```
      GN=J
      AVE = AVE/GN
      SUMN = 0.0
  830 DO 831 J = 1,N3
      SM(J) = SM(J) - AVE
  831 SUMN = SUMN + SM(J)*SM(J)
      SUMN = SUMN/GN
      SUMH1(MF)=SUMN/VARU
  832 CONTINUE
      DO 834 I=1,MF
      RHTES=RHTES+DRH
      RRHL=1./RHTES
  834 U(I)=RRHL
      XMIN=U(MF)
      CALL YMIMA(SUMH1,MF,YMIN,YMAX,INDE,NSSS,10,M1,2)
      DO 855 J5=1,M1
      IF=INDE(J5)
  855 PRINT 1408,U(IF),SUMH1(IF)
      CALL SCLE(SUMH1,HBOXT,HBOXM,YMAX,YMIN,HBOXT,MF,1.)
      CALL GRAPH(MF,U,SUMH1,KS,3,0.0)
      A = A
      A2 = A2
      MK = MK
      CONP=CONP
      FL1=FL1
      FL2=FL2
      FL3=FL3
      KS=KS
      XMIN=XMIN
      YMIN=YMIN
      JST=JST
      JMDMI=JMDMI
      JEN=JEN
      JMDMA=JMDMA
      JC=JC
      CON=CON
      NSSS=NSSS
      DFBOX=DFBOX
      NBO=NBO
      GO TO 118
      END                                                    FT139
```

Fortran Program 1 (continued)

```
      GN=J
      AVE = AVE/GN
      SUMN = 0.0
  830 DO 831 J = 1,N3
      SM(J) = SM(J) - AVE
  831 SUMN = SUMN + SM(J)*SM(J)
      SUMN = SUMN/GN
      SUMH1(MF)=SUMN/VARU
  832 CONTINUE
      DO 834 I=1,MF
      RHTES=RHTES+DRH
      RRHL=1./RHTES
  834 U(I)=RRHL
      XMIN=U(MF)
      CALL YMIMA(SUMH1,MF,YMIN,YMAX,INDE,NSSS,10,M1,2)
      DO 855 J5=1,M1
      IF=INDE(J5)
  855 PRINT 1408,U(IF),SUMH1(IF)
      CALL SCLE(SUMH1,HBOXT,HBOXM,YMAX,YMIN,HBOXT,MF,1.)
      CALL GRAPH(MF,U,SUMH1,KS,3,0.0)
      A = A
      A2 = A2
      MK = MK
      CONP=CONP
      FL1=FL1
      FL2=FL2
      FL3=FL3
      KS=KS
      XMIN=XMIN
      YMIN=YMIN
      JST=JST
      JMOMI=JMOMI
      JEN=JEN
      JMOMA=JMOMA
      JC=JC
      CON=CON
      NSSS=NSSS
      OFBOX=OFBOX
      NBO=NBO
      GO TO 118
      END                                                    FT139
```

Fortran Program 1 (continued)

```
FORTRAN,SCAN,          LLSID.

      SUBROUTINE LLSID(CONP,FL1,FL2,FL3,MBOX,NT,NL,RH,CYCLE,FMIN1,FMAX1,
     1JQ,FACC,WACC,HBOX,NBO,OFBOX,JMDMI,JMDMA)
      DIMENSION HBOX(250),NACT(250),ERR1(250),
     1FREQ1(251),NL(10),RH(250),CYCLE(250),FACC(250),WACC(250)
      EQUIVALENCE (FREQ1(2),NACT(1))
      JMDMA=0
      JMDMI=500
      ERR1M=10.**12
      MCOU=0
      M37=MBOX
      DO 1319 M=1,NT
      FACC(M)=0.
 1319 WACC(M)=0.
      GO TO (1320,1322),MBOX
 1320 DO 1321 M=1,400
 1321 HBOX(M)=0.
 1322 DO 500 KK=1,10
      J1=JQ
      NLK=NL(KK)
      IF(NLK)5001,5001,111
  111 JE=NLK
      DO 112  J = 1,JE
  112 NACT(J)=1
      FN=NLK
      SUMX2 = 0.0
      SUMX=0.0                                                    FT095
      SUMXY=0.0                                                   FT096
      SUMY=0.0                                                    FT097
      JF=J1
      JL=JE
   28 DO 3 J=JF,JL
      BJE=CYCLE(J)
      B2=RH(J)
      SUMX2=SUMX2+BJE**2
      SUMX=SUMX+BJE
      SUMY=SUMY+B2
      SUMXY=SUMXY+BJE*B2
    3 CONTINUE
   31 DEN=FN*SUMX2-SUMX*SUMX
      FM= (FN*SUMXY-SUMX*SUMY)/DEN                                FT104
      B= (SUMX2*SUMY-SUMX*SUMXY)/DEN                              FT105
      DIFM=0.
      SUM=0.
      DO 4 J=J1,JE
      ERR1(J)=RH(J)-(FM*CYCLE(J)+B)
      ERR1(J)=ABSF(ERR1(J))
      MGO=NACT(J)
      GO TO (4000,4),MGO
 4000 SUM=SUM+ERR1(J)*ERR1(J)
      IF(ERR1(J)-DIFM)4,4,4001
 4001 DIFM=ERR1(J)
    4 CONTINUE
      SD=SUM/FN
      SD=SQRTF(SD)
      MCOU=MCOU+1
      F1L=FL1*SD
      F2L=FL2*SD
```

Fortran Program 1 (continued)

```
      F3L=FL3*SD
      GO TO (4002,4002,4002,491),MCOU
 4002 IF(DIFM-F1L)4003,410,410
 4003 IF(DIFM-F2L)4004,44,44
 4004 IF(DIFM-F3L)491,47,47
   44 F1L=F2L
      GO TO 410
   47 F1L=F3L
  410 DO 43 J=J1,JE
      B1=CYCLE(J)
      B2=RH(J)
      NAC=NACT(J)
      IF(ERR1(J)-F1L)412,411,411
  411 GO TO (42,43),NAC
   42 NACT(J)=2
      SUMX2=SUMX2-B1**2
      SUMX=SUMX-B1
      SUMY=SUMY-B2
      SUMXY=SUMXY-B1*B2
      FN=FN-1.
      GO TO 43
  412 GO TO (43,413),NAC
  413 NACT(J)=1
      SUMX2=SUMX2+B1**2
      SUMX=SUMX+B1
      SUMY=SUMY+B2
      SUMXY=SUMXY+B1*B2
      FN=FN+1.
   43 CONTINUE
      GO TO 31
  491 RAD=((SUM/(FN-2.0))*FN)/ABSF(DEN)
      ERR1(J1)=SQRTF(RAD)/CONP
      FREQ1(J1)=CONP/FM
      ERR1(J1)=ERR1(J1)*(FREQ1(J1)**2)
      B1=CYCLE(J1)
      CYM=0.5*(B1+BJE)
      JMD=CYM
      FACC(JMD)=FACC(JMD)+FREQ1(J1)/ERR1(J1)**2
      WACC(JMD)=WACC(JMD)+1./ERR1(J1)**2
      IF(JMD-JMDMI)4910,4910,4911
 4910 JMDMI=JMD
 4911 IF(JMD-JMDMA)4913,4912,4912
 4912 JMDMA=JMD
 4913 IF(KK-1)492,492,498
  492 GO TO (493,494),M37
  493 M37=2
      FMIN = FREQ1(J1)
      FMAX = FREQ1(J1)
  494 IF(FREQ1(J1) - FMIN)495,496,496
  495 FMIN = FREQ1(J1)
  496 IF(FREQ1(J1)-FMAX)498,498,497
  497 FMAX = FREQ1(J1)
  498 J1=J1+1
      JE=JE+1                                                    FT115
      MCOU=0
      IF(JE-NT)4490,4490,5
 4490 NACT(JE)=1
      JF=JE
      JL=JE
      B2=RH(J1-1)
```

Fortran Program 1 (continued)

```
      SUMX2=SUMX2-B1**2
      SUMX=SUMX-B1
      SUMY=SUMY-B2
      SUMXY=SUMXY-B1*B2
      FNT=NLK
      IF(FNT-.1-FN)28,28,4495
 4495 J6=JE-1
      JB=J1-1
      DO 4497 J5=JB,J6
      NAC=NACT(J5)
      GO TO (4497,4496),NAC
 4496 FN=FN+1.
      B1=CYCLE(J5)
      B2=RH(J5)
      SUMX2=SUMX2+B1**2
      SUMX=SUMX+B1
      SUMY=SUMY+B2
      SUMXY=SUMXY+B1*B2
      NACT(J5)=1
 4497 CONTINUE
      GO TO 28
    5 JEND=NT-NLK+1
      IF(KK-1)5991,5991,599
  599 IF(NLK-30)800,800,600
 5991 IF(NLK-30)601,601,600
  600 PRINT 6,NLK
    6 FORMAT(47H LINEAR LEAST SQUARES ANALYSIS WITH FIT LENGTH  I4/
     111H  1ST CYCLE10X,5HERROR16X, 9HFREQUENCY)
  601 DO 71 J=1,JEND
      IF(ERR1(J)-ERR1M)60,60,61
   60 ERR1M=ERR1(J)
   61 IF(J-1)63,63,65
   63 IF(ERR1(J) - ERR1(J+1))7,7,71
   65 IF(J-JEND)67,66,66
   66 IF(ERR1(J) - ERR1(J - 1))7,7,71
   67 IF(ERR1(J) - ERR1 (J -1))68,68,71
   68 IF(ERR1(J) - ERR1 (J+1))7,7,71
    7 IF(NLK-30)71,71,700
  700 CYC=CYCLE(J)
      PRINT 8,CYC,ERR1(J),FREQ1(J)
    8 FORMAT(F8.1,2X,E20.8,2X,E20.8)
   71 CONTINUE
  800 GO TO (1400,1404),MBOX
 1400 MBOX=2                                                    HISTCG
      FMIN1=.9*FMIN
      FMAX1=1.1*FMAX
      FMIN=FMIN1
      FMAX=FMAX1
      DFBOX=ERR1M
      BOXT=(FMAX-FMIN)/DFBOX                                    HISTCG
      IF(BOXT-249.)1402,1402,1401
 1401 CFBOX=(FMAX-FMIN)/249.
 1402 NBO=0
      FBOX=FMIN1
      DO 1403 J4=1,400
      NBO=NBO+1                                                 HISTCG
      FBOX=FBOX+CFBOX
      IF (FBOX-FMAX)1403,1403,1404
 1403 CONTINUE                                                  HISTCG
 1404 DO 1410 J2=1,JEND
```

Fortran Program 1 (continued)

```
      ERR1(J2)=1.414213*ERR1(J2)
      FDIFF=(FMIN1-FREQ1(J2))/ERR1(J2)
      DFBC=DFBOX/ERR1(J2)
      DO 1407  J3=1,NBO
      FDIFF=FDIFF+DFBC
      IF(FDIFF-3.)1405,1405,1410
 1405 IF(FDIFF+3.)1407,1406,1406
 1406 EX=-FDIFF*FDIFF
      HBOX(J3)=HBOX(J3)+DFBC*EXPF(EX)
 1407 CONTINUE                                                    HISTCG
 1410 CONTINUE
  500 CONTINUE
 5001 DO 1413 J5=JMDMI,JMDMA
      B=1./WACC(J5)
      FACC(J5)=B*FACC(J5)
      WACC(J5)=SQRTF(B)
 1413 CONTINUE
      RETURN
      END
```

Fortran Program 1 (continued)

```
FORTRAN,SCAN,          WAVE.

      SUBROUTINE WAVE(FACC,WACC,FLEV,NLEV1,NLEV2,JMDMI,JMDMA,JC,FTM,NT,
     1WERR)
      DIMENSION WACC(250),FACC(250),FLEV(30),NLEV1(30),NLEV2(30),
     1WERR(30)
      JMDMS=JMDMI
1415  JMDMI=JMDMS
      J1S=1
      JC=0
      JMDMQ=JMDMI
1420  FTEST=FACC(JMDMQ)
      DO 1460 J5=JMDMI,JMDMA
      BF=FACC(J5)
      IF(BF-FTEST)1460,1450,1450
1450  FTEST=BF
1460  CONTINUE
      DF=FTM*FTEST
      JC=JC+1
      IF(JC-30)1417,1417,1416
1416  FTM=2.*FTM
      GO TO 1415
1417  DO 1422 J5=JMDMI,JMDMA
1419  CH=ABSF(FTEST-FACC(J5))
      IF(CH-DF)1421,1421,1422
1421  JIE=J5
1422  CONTINUE
      SUM=0.
      SUMW=0.
      DO 1423 J5=JMDMI,JIE
      BW=WACC(J5)
      SUM=SUM+FACC(J5)/BW**2
1423  SUMW=SUMW+1./BW**2
      SUM=SUM/SUMW
      FLEV(JC)=SUM
      NLEV1(JC)=J1S
      NLEV2(JC)=JIE
      BW=1./SUMW
      WERR(JC)=SQRTF(BW)
      JMDMI=JIE+1
      J1S=JMDMI
      JMDMQ=JMDMI
      IF(JMDMI-JMDMA)1420,1420,1425
1425  NLEV2(JC)=NT
      DO 1414 J5=1,JMDMS
1414  FACC(J5)=FLEV(1)
      DO 1424 J5=JMDMA,NT
1424  FACC(J5)=FLEV(JC)
      RETURN
      END
```

Fortran Program 1 (continued)

```
 FORTRAN,SCAN,          YMIMA.

      SUBROUTINE YMIMA(A,N2,AMIN,AMAX,IND,NSSS,NMIA,M1,MGO)
      DIMENSION A(275),XM(10),IND(10)
C     CALL YMIMA WITH MGO =1 IF ONLY THE MAXIMUM AND MINIMUM ELEMENTS
C     OF THE ARRAY A ARE DESIRED. MGO =2 IF RELATIVE EXTREMA ARE WANTED
C     CALL YMIMA WITH NSSS=-1 TO GET THE NMIA LOWEST RELATIVE
C    MINIMA IN AN ARRAY X(I) WITH N2ELEMENTS
C     CALL YMIMA WITH NSSS =+1 TO GET THE NMIA HIGHEST RELATIVE
C     MAXIMA IN AN ARRAY X(I) WITH N2 ELEMENTS
      AMAX=-10.**30
      AMIN=10.**30
      DO 3 I=1,N2
      IF(A(I)-AMIN)2,21,21
    2 AMIN=A(I)
   21 IF(A(I)-AMAX)3,22,22
   22 AMAX=A(I)
    3 CONTINUE
      GO TO (70,10),MGO
   10 NS=0
      NMIAT=NMIA-1
      NSS=0
      DO 1 J1=1,NMIA
      XM(J1)=0.
    1 IND(J1)=0
      DO 6 J=1,N2
      IF(A(J+1)-A(J))9,6,8
    9 NS=-1
      GO TO 4
    8 NS=1
    4 IF(NS+NSS)59,41,59
   41 IF(NSS-NSSS)59,42,59
   42 PM=A(J)
      DO 43 J1=1,NMIAT
      NUM=J1
      IF(NSSS)421,421,422
  421 IF(PM-XM(J1))44,44,43
  422 IF(PM-XM(J1))43,44,44
   43 CONTINUE
      GO TO 59
   44 NUP=NMIA-NUM
      DO 46 J1=1,NUP
      IT=NMIA-J1+1
       IB=NMIA-J1
      XM(IT)=XM(IB)
      IND(IT)=IND(IB)
   46 CONTINUE
      XM(NUM)=PM
      IND(NUM)=J
   59 NSS=NS
    6 CONTINUE
      M1=0
      DO 62 J1=1,NMIA
      IF(IND(J1))63,63,61
   61 M1=M1+1
   62 CONTINUE
   63 DO 69 I=1,M1
      IMIN=9999999
      DO 66 J5=I,M1


      IF(IND(J5)-IMIN)64,64,66
   64 IMIN=IND(J5)
      JC=J5
   66 CONTINUE
      IND(JC)=IND(I)
   69 IND(I)=IMIN
   70 RETURN
      END
```

Fortran Program 1 (continued)

```
FORTRAN,SCAN,          SCLE.

      SUBROUTINE SCLE(A,BB,BL,AB,AL,CON,N,SCF)
      DIMENSION A(325)
      FACT=SCF*(BB-BL)/(AB-AL)
      DO 1 I=1,N
    1 A(I)=FACT*(A(I)-AL)+CON
      RETURN
      END


AUTO,LIST,DECK,GETU
```

Fortran Program 1 (continued)

```
LINE  LABEL      OP    OPERAND                                          CO NO   LOC     C
PROGRAM  GETU    PAGE  00

01    EXECUTE    CNTRL 7                                                0001
02               DC
03                     @GETU      a
   X                                                                    0002   0325  A67
   X                                                                           0326  A00
04                     +0+0+1000+0+9100000002                                  0327  +0C
   X                                                                           0328  +0C
   X                                                                           0329  +0C
   X                                                                           0330  +0C
   X                                                                           0331  +91
05   ORIGIN      CNTRL  1000
06   *
07   *         FLAG FUNCTION GETU FOR OBTAINING NUMBERS STORED IN
08   *          UPPER CORE. USE - VALUE=GETU(INDEX) WHERE INDEX
09   *          .GT. ZERO AND .LT. OR .EQ. 9800
10   *
11   *         STORAGE NEEDED - 10 LOCATIONS
12   *
13   *         TIMING (INCLUDES BLX INTO GETU AND ZST1 AFTER IT)
14   *          108 MICROSEC.
15   *         WARNING - IF I/O IS OPERATING WHEN GETU IS ENTERED
16   *          GETU WILL WAIT FOR I/O TO CEASE AND TIMING IN THIS
17   *          IS UNPREDICTABLE.
18   *
19               ZA1    0+X94                                           0003   1000  +13
20               STD1   *(6,9)+1                                               1001  -12
21               XLIN   98,0                                                   1002  -48
22               BCB    1,*                                                    1003  +51
23               BCB    2,*                                                    1004  +51
24               DC
25                      +0400100000                                     0004   1005  +04
26               ZA1    9999+X98                                               1006  +13
27               DC
28                      +0400200000                                            1007  +04
29               B      2+X94                                                  1008  +01
30   END         CNTRL  1000
   X                                                                    0005          +01

INDEX WORDS USED INDICATED BY ZEROS
    11111111111111111111111111111111111111111111111111111111111111111111111111111111111111111111111111111111111111111111

SWITCHES USED INDICATED BY ZEROS
    11111111111111111111111111111111
```

Fortran Program 1 (continued)

```
AUTO,LIST,DECK,UPCOR

LINE  LABEL      OP     OPERAND                                  CD NO   LOC     C
PROGRAM  UPCOR   PAGE   00

01    EXECUTE    CNTRL  7                                        0001
02               DC
03                      @UPCOR     @
                                                                 0002   0325   A84
   X                                                                    0326   A0C
   X                                                                    0327   +0C
04                      +0+0+1000+0+9100000002                           0328   +0C
   X                                                                    0329   +0C
   X                                                                    0330   +0C
   X                                                                    0331   +91
05    ORIGIN     CNTRL  1000
06               ZA1    1+X94                                    0003   1000   +13
07               STD1   *(6,9)+1                                        1001   -12
08               ZA1    0                                               1002   +13
09               BZ1    ZERO                                            1003   +1C
10               BM1    GET                                             1004   -1C
11    PUT        ZST1   98(0,5)                                  0004   1005   -11
12               ZA1    0+X94                                           1006   +13
13               STD1   *(6,9)+1                                        1007   -12
14               ZA1    0                                               1008   +13
15               BCB    1,*                                             1009   +51
16               BCB    2,*                                      0005   1010   +51
17               DC
18                      +0400100000                                     1011   +04
19               ZST1   9999+X98                                        1012   -11
20               DC
21                      +0400200000                                     1013   +04
22               B      3+X94                                           1014   +01
23    GET        ZST1   98(0,5)                                  0006   1015   -11
24               MSP    98                                              1016   -03
25               ZA1    0+X94                                           1017   +13
26               STD1   *(6,9)+6                                        1018   -12
27               BCB    1,*                                             1019   +51
28               BCB    2,*                                      0007   1020   +51
29               DC
30                      +0400100000                                     1021   +04
31               ZA1    9999+X98                                        1022   +13
32               DC
33                      +0400200000                                     1023   +04
34               ZST1   0                                               1024   -11
35               B      3+X94                                    0008   1025   +01
36    ZERO       XL     98,+0100000000                                  1026   +45
37               ZA1    +0                                              1027   +13
38               BCB    1,*                                             1028   +51
39               BCB    2,*                                             1029   +51
40               DC
41                      +0400100000                              0009   1030   +04
42               ZST1   0+X1                                            1031   -11
```

Fortran Program 1 (continued)

```
LINE  LABEL      OP     OPERAND                                          CD NO.  LOC     C
PROGRAM  UPCOR   PAGE   00

43               RS     98,RDW                                                   1032   +65
44               DC
45                      +0400200000                                              1033   +04
46               B      3+X94                                                    1034   +01
47   RDW         NOP    9799(0,1)                                         0010   1035   -01
48   END         CNTRL  1000
   X                                                                             1036   +01
   X                                                                             1037   +00
   X                                                                       0011         +01

INDEX WORDS USED INDICATED BY ZEROS
    01111111111111111111111111111111111111111111111111111111111111111111111111111111111111111111111111111111111111111111

SWITCHES USED INDICATED BY ZEROS
    11111111111111111111111111111111

     OBJECT

     OBJECT

     STAR


    F C R T R A N  J O B
    MAINPROG   1500 RELOCATED BY   0500 LOCATIONS
         REQUESTS SUBROUTINE UPCOR       BRANCH AT 3672
         REQUESTS SUBROUTINE GRAPH       BRANCH AT 3673
         REQUESTS SUBROUTINE LLSID       BRANCH AT 3674
         REQUESTS SUBROUTINE WAVE        BRANCH AT 3675
         REQUESTS SUBROUTINE YMIMA       BRANCH AT 3676
         REQUESTS SUBROUTINE SCLE        BRANCH AT 3677
         REQUESTS SUBRCUTINE GETU        BRANCH AT 3678
    LLSID      7118 RELOCATED BY   6118 LOCATIONS
         REQUESTS SUBROUTINE SQRTF       BRANCH AT 7863
    WAVE       8464 RELOCATED BY   7464 LOCATIONS
         REQUESTS SUBROUTINE SQRTF       BRANCH AT 8644
    YMIMA      8682 RELOCATED BY   7682 LOCATIONS
    SCLE       8952 RELOCATED BY   7952 LOCATIONS
    GETU       9004 RELOCATED BY   8004 LOCATIONS
    UPCOR      9013 RELOCATED BY   8013 LOCATIONS
    GRAPH      9051 RELOCATED BY   8051 LOCATIONS
         REQUESTS SUBROUTINE SMUT        BRANCH AT 9170
    SMUT       9201 RELOCATED BY   8201 LOCATIONS
    LIBRARY ROUTINES
    SQRTF      9399 RELOCATED BY   9074 LOCATIONS
         REQUESTS SUBROUTINE ERRTYPE     BRANCH AT 9443
    ERRTYP     9444 RELOCATED BY   8444 LOCATIONS
    MISSING SUBROUTINES
    NONE
    COMMON     9499
    LAST LOCATION USED   9465
```

Fortran Program 1 (continued)